

METALLIC NANOPARTICLE SYNTHESIS WITHIN REVERSE MICELLAR
MICROEMULSION SYSTEMS

Except where reference is made to the work of others, the work described in this dissertation is my own or was done in collaboration with my advisory committee. This dissertation does not include proprietary or classified information.

Christopher Lawrence Kitchens

Certificate of Approval:

Gopal Krishnagopalan
Professor
Chemical Engineering

Christopher B. Roberts, Chair
Professor
Chemical Engineering

Ram B. Gupta
Professor
Chemical Engineering

Charles A. Eckert
Professor
Georgia Institute of Technology
Atlanta, Georgia

Stephen L. McFarland
Dean
Graduate School

METALLIC NANOPARTICLE SYNTHESIS WITHIN REVERSE MICELLAR
MICROEMULSION SYSTEMS

Christopher Lawrence Kitchens

A Dissertation
Submitted to
the Graduate Faculty of
Auburn University
in Partial Fulfillment of the
Requirements for the
Degree of
Doctor of Philosophy

Auburn, Alabama
December 17, 2004

VITA

Christopher Lawrence Kitchens, son of Larry and Anita Kitchens, was born on August 9, 1977 in Boone, NC. He graduated from Watauga High School in Boone, NC in 1995. He attended Appalachian State University in Boone, NC on full academic scholarship and graduated with a Bachelor of Science degree in Chemistry with a Certified Chemist concentration in December of 1999. He entered graduate school in the Department of Chemical Engineering at Auburn University in Auburn, AL in May of 2000. Following the completion of his Doctor of Philosophy in Chemical Engineering from Auburn University, he will begin Post Doctorial Studies for Dr. Charles A. Eckert in the School of Chemical and Biological Engineering at Georgia Institute of Technology.

DISSERTATION ABSTRACT
METALLIC NANOPARTICLE SYNTHESIS WITHIN REVERSE MICELLAR
MICROEMULSION SYSTEMS

Christopher Lawrence Kitchens

Doctor of Philosophy, December 17, 2004
(B.S., Appalachian State University, 1999)

Directed by Christopher B. Roberts

The synthesis of metallic nanoparticles is integral for the advancement of the field of nanotechnology. Solution based nanomaterial synthesis is an effective method for the production of nanomaterials, particularly with the use of surfactants and other materials for directed assembly allowing control over the nanomaterials' physical properties.

This dissertation presents research performed to study the synthesis of metallic nanoparticles within reverse micelle systems. A fundamental approach has been taken to carefully examine the role of each component of the reverse micelle system, specifically the surfactant, bulk solvent, and the aqueous micelle core. The role of the sodium bis(2-ethylhexyl) sulfosuccinate (AOT) surfactant is two fold. Initially, the surfactant forms reverse micelles, nano-sized water pools dispersed within the bulk organic solvent which act as nano-reactors for the chemical reduction of the metallic precursors and metallic nanoparticle synthesis. The surfactant also acts as a stabilizing agent, effectively dispersing synthesized particles in solution, preventing agglomeration. Previously it was thought that spherical reverse micelles acted as templates for nanoparticle synthesis

despite the negligible effect of the initial micelle diameter on the on the diameter of nanoparticles synthesized. Rather the initial micelle diameter influences the nanoparticle growth rate. In contrast, the properties of the bulk organic solvent do influence the nanoparticle diameter.

The nature of solvent interactions with the AOT surfactant tails in various liquid alkane solvents, compressed propane, and supercritical ethane demonstrates that steric stabilization of the metallic nanoparticles by the AOT surfactant determines the particle sizes synthesized, rather than the previously accepted templating effect. Time resolved UV-vis spectroscopy was used to study the kinetics of particle synthesis, Neutron Spin Echo spectroscopy and Small Angle Neutron Scattering were used to determine the bending elasticity of the reverse micelle AOT monolayer as a measure of the micelle rigidity, a total interaction energy model was developed to determine the thermophysical effects by predicting the synthesized particle diameters and electron microscopy was used to analyze the synthesized particles. The nature of anionic interactions on metallic nanoparticle synthesis was also investigated with impacts on microemulsion stability and nanoparticle surface properties. The presence of chloride ions within compressed propane results in the formation of diamond-shaped copper nanoparticle assemblies.

Compressed and supercritical fluids have been demonstrated as effective media for the production of nanomaterials by taking advantage of their novel, tunable properties. This investigation of metallic nanoparticle synthesis within the AOT reverse micelle system has provided an increased understanding of the controlling factors of microemulsion based nanoparticle synthesis with applications in the production of novel yet practical nanomaterials and the advancement of nanotechnology.

ACKNOWLEDGMENTS

I wish to begin by expressing my deepest appreciation to Dr. Christopher B. Roberts for his expertise, guidance and support throughout my studies at Auburn. I can clearly remember my first meeting with Dr. Roberts when I was an undergraduate looking at potential graduate schools. Dr. Roberts is more than an excellent advisor; he is an inspiration and a true friend.

I would also like to thank my fellow group members and undergraduate students who have contributed to the research done in our lab. In particular I would like to thank Chandler McLeod whose research has paralleled my own work and has been available for invaluable collaboration and discussion of our research in order to further our knowledge. The financial support of the Department of Energy, Basic Energy Sciences Division (Grant DE-FG02-01ER15255) is greatly appreciated in addition to the support of our Program Manager, Paul Maupin.

I owe a special thanks to my parents, Larry and Anita, my brothers Joseph and Stephen, and my sister Carolyn; for without their unconditional love and guidance I would not be where I am today. I would also like to thank my father for his help on the statistical analysis of my results described in this thesis. I would like to thank my wife's parents, Don and Dorothy Bell, who have provided encouragement and support.

Most importantly I would like to thank my wife, Ashley. Her love, devotion and friendship have helped me throughout my graduate studies and to her I am most thankful.

Style manual or journal used: Journal of the American Chemical Society (JACS)

Computer software used: Microsoft Office, Scion Image, ImageJ, Minitab, IGOR Pro 5, Solid Edge, and EndNote.

The following publications were a product of this dissertation:

1. Kitchens, Christopher L., McLeod, M. C., Roberts, C. B.; Solvent Effects on the Growth and Steric Stabilization of Copper Metallic Nanoparticles in Liquid Alkane/AOT Reverse Micelle Systems. *J. Phys. Chem. B*; 107(41); 2003.
2. Kitchens, Christopher L., McLeod, M. C., Roberts, C. B.; Synthesis and Modeling of Metallic Nanoparticles in Compressed Liquid and Supercritical Fluid Based Reverse Micelles. *6th International Symposium on Supercritical Fluids*. Versailles, France; April 2003.
3. Kitchens, Christopher L., Roberts, C. B.; Copper Nanoparticle Synthesis in Compressed Liquid and Supercritical Fluid Reverse Micelle Systems. *I&EC Research*; Accepted and to be published ASAP.
4. Kitchens, Christopher L., McLeod, M. C., Roberts, C. B.; Chloride Ion Effects on Synthesis and Assembly of Copper Nanoparticles in Liquid and Compressed Alkane Microemulsions. (To be submitted)
5. Kitchens, Christopher L., Bossev, D., Roberts, C. B.; Solvent Effects on AOT Reverse Micelles in Liquid and Compressed Alkanes Investigated by Neutron Spin Echo Spectroscopy. (To be submitted)

TABLE OF CONTENTS

CHAPTER 1	1
1. Introduction and background material	1
1-1. Nanomaterials	1
1-2. Emulsion Based Synthesis of Particles	5
1-3. Metallic Nanoparticle Production	13
1-4. Supercritical Fluids	21
1-5. Chapter overview	25
1-6. References	28
 CHAPTER 2	 35
2. Solvent Effects on the Growth and Steric Stabilization of Copper Metallic Nanoparticles in AOT Reverse Micelle Systems	35
2-1. Introduction	35
2-2. Experimental	38
2-2a. Materials	38
2-2b. Particle Synthesis	39
2-3. Results and discussion	42
2-3a. Solvent Effects on Copper Nanoparticle Synthesis	43
2-3b. Water Content Effect on Copper Nanoparticle Synthesis	48
2-3c. Salt Effect on Copper Nanoparticle Synthesis	53
2-3d. Temperature Effect on Copper Nanoparticle Synthesis	61
2-3e. Reducing Agent Effect on Copper Nanoparticle Synthesis	62
2-3f. Effects of Surfactant / Cosurfactant Concentration	63
2-4. Steric Stabilization of Particles by Surfactant	65
2-5. Conclusions	66
2-6. References	68
 CHAPTER 3	 70
3. Interaction Energy Model for Sterically Stabilized Metallic Nanoparticles	70
3-1. Introduction	70
3-2. Modeling	73
3-3. Experimental	83
3-4. Modeling Results	83
3-4a. Liquid Phase Results	83
3-4b. Compressed Propane Results	93
3-4c. Compressed and SCF Ethane Results	100
3-4d. Compressed Ethane + Cosolvent Results	103

3-5. Conclusions.....	107
3-6. References.....	108
CHAPTER 4	110
4. Copper Nanoparticle Synthesis in Compressed and SCF Phase Reverse Micelle Systems	110
4-1. Introduction.....	110
4-2. Experimental.....	113
4-2a. Materials	113
4-2b. Phase Behavior Measurements	113
4-2c. Particle Synthesis.....	114
4-3. Particle Synthesis Results	117
4-3a. Compressed Propane / AOT Reverse Micelle System	117
4-3b. Compressed and SCF Ethane / AOT Reverse Micelle System.....	124
4-3c. Ethane + Alkane Cosolvent / AOT Reverse Micelle System	128
4-4. Conclusions.....	133
4-5. References.....	135
CHAPTER 5	137
5. Solvent Effects on AOT Reverse Micelles in Liquid and Compressed Alkanes Investigated by Neutron Spin-Echo Spectroscopy	137
5-1. Introduction.....	137
5-2. Reverse Micelle Microemulsion Background	139
5-3. Neutron Scattering Background.....	143
5-4. Experimental.....	147
5-4a. SANS Measurements	148
5-4b. NSE Measurements.....	149
5-5. Results and Discussion	149
5-5a. SANS Measurements	149
5-5b. Liquid Phase NSE Measurements.....	156
5-5c. Compressed Propane Phase NSE Measurements	165
5-6. Conclusions.....	169
5-7. References.....	170
CHAPTER 6	173
6. Chloride Ion Effects on Synthesis and Directed Assembly of Copper Nanoparticles in Liquid and Compressed Alkane Microemulsions.....	173
6-1. Introduction.....	173
6-2. Experimental Methods.....	176
6-3. Results and Discussion	178
6-3a. Particle Synthesis in Liquid Phase AOT Reverse Micelles	178
6-3b. Particle Synthesis in Compressed Propane – AOT Reverse Micelles	188
6-4. Conclusions.....	203
6-5. References.....	205

CHAPTER 7	208
7. Conclusions and recommendations of Future Work.....	208
7-1. Conclusions.....	208
7-2. Future Work.....	213
7-2a. Continued Investigation of Synthesis within Tunable Solvents	213
7-2b. Particle Deposition Applications	215
7-2c. Anion Effects on Nanomaterial Synthesis within Compressible Fluids ..	216
7-2d. Nanoparticle Functionalization.....	217
7-2e. Initial Stages of Copper Nanoparticle Synthesis	219
 APPENDIX A.....	 221
A. Research Methods.....	221
A-1. Synthesis of Cu(AOT) ₂ and AgAOT	221
A-1a. Synthesis of Cu(AOT) ₂ Batch Method	221
A-1b. Synthesis of Cu(AOT) ₂ Using Columns	222
A-1c. Column Regeneration	223
A-1d. Synthesis using an Anion Exchange Resin.....	224
A-1e. Synthesis of Silver AOT using Columns.....	224
A-1f. Synthesis of Cu(AOT) ₂ by the Eastoe Method	225
A-1g. Method for Determining Conversion.....	225
A-2. Results.....	225
A-3. Research Methods for Copper Nanoparticle Synthesis	230
A-3a. Copper Nanoparticle Synthesis in Liquids	230
A-3b. Copper Nanoparticle Production in Compressible Solvents.....	231
A-4. Particle Collection Methods.....	232
 APPENDIX B.....	 233
B. Synthesis of Copper Metallic Nanoparticles in AOT Reverse Micelle Systems...	233
B-1. Experimental Growth Curves	233
B-1a. Effects of W Value on Particle Growth	233
B-1b. Effects of Various Bulk Solvent Types on Particle Synthesis.....	234
B-1c. Effects of Copper Salt Precursor on Particle Synthesis	236
B-2. Synthesis of Copper Metallic Nanoparticles in AOT Reverse Micelle Systems	
Experimental Growth Curves Regression Analysis.....	237
B-2a. Effects of Bulk Solvent Type on Particle Synthesis with W =5	237
B-2b. Effects of Bulk Solvent Type on Particle Synthesis with W = 10	239
B-2c. Effects of W Value on Particle Growth for Isooctane Bulk Solvent	241
B-2d. Effects of Copper Salt on Particle Synthesis	243
 APPENDIX C.....	 245
C. UV-Vis Absorbance Data Tools	245
C-1. Details on the Ocean Optics SD2000 Fiber Optic Dual Spectrometer	245
C-2. UV-Vis Time Resolved Measurements using the Ocean Optics Fiber Optic	
Spectrometer Method.....	245
C-3. Data Compiler and Reducer.....	246

C-4. Visual Basic Applications for Excel Code for Reducing Data from Varian Cary 3 UV-Vis Spectrometer.....	248
APPENDIX D.....	249
D. High Pressure Vessels for Compressed and Supercritical Fluid Reactions	249
D-1. Variable Volume View Cell Apparatus	249
D-2. High Pressure View Cell.....	260
D-3. High Pressure Neutron Spin Echo Cell.....	265
D-4. High Pressure Fiber Optic Probe Assembly	273

LIST OF FIGURES

Figure 1-1a. Molecular structure of sodium bis(2-ethylhexyl) sulfosuccinate (AOT) surfactant. The dotted lines represent the cone-like packing structure of the twin tail surfactant.	7
Figure 1-1b. Reverse micelle formed by the self-assembly of AOT surfactant molecules which disperse nano-sized water droplets within the bulk oil phase, creating a thermodynamically stable microemulsion.	7
Figure 1-2. Phase diagram of the Water – Surfactant – Oil microemulsion system demonstrating various surfactant aggregate geometries consisting of 1. Spherical micelles. 2. Rod-like micelles. 3. Irregular bicontinuous phase. 4. Reverse cylindrical micelles. 5. Reverse micelles. 6. Hexagonal phase. 7. Cubic phase. 8. Lamellar phase. 9. Reverse cubic phase. 10. Reverse hexagonal phase. (Obtained from Zhang et al., 2003) ²	8
Figure 1-3. Relationship between the surfactant shape, critical packing parameter R, and the surfactant aggregate structures formed within the microemulsion. (Obtained from Hiemenz and Rajagopalan, 1997, p.371.)	9
Figure 1-4. Mechanism for intermicellar exchange of the water cores within the AOT reverse micelles which mediates the chemical reaction between water soluble reactants A and B to form reactant C.	13
Figure 1-5. Reaction mechanism for the synthesis of copper nanoparticles via chemical reduction of the copper functionalized AOT surfactant followed by particle growth through the dynamic intermicellar exchange of the micelle contents.	15
Figure 1-6. Characteristic UV-Vis absorbance bands for Copper and Silver nanoparticles in solution.	18
Figure 1-7. Pressure - Temperature phase diagram demonstrating the supercritical fluid region at the culmination of the vapor – liquid equilibrium curve.....	23
Figure 2-1. Copper nanoparticle growth curves measured in-situ by plotting the UV-vis absorbance ratio (Abs_{500}/Abs_{566}) as a function of time using various alkane bulk solvents with $W = 5$, $[AOT] = 0.1106$ M, $[CuAOT_2] = 0.01106$ M, $N_2H_4 = 3 X [Cu]$. The even carbon number alkanes are shown for clarity.	44
Figure 2-2. Cu nanoparticle growth curves measured in-situ by (Abs_{500}/Abs_{566}) as a function of time using various alkane bulk solvents with $W = 10$, $[AOT] = 0.1106$ M, $[CuAOT_2] = 0.01106$ M, $N_2H_4 = 3 X [Cu]$. The even carbon number alkanes are shown for clarity	49

Figure 2-3. Cu nanoparticle growth curves measured in-situ by (Abs_{500}/Abs_{566}) as a function of time using an isooctane bulk solvent and adjusting the W value with $[AOT] = 0.1106 \text{ M}$, $[CuAOT_2] = 0.01106 \text{ M}$, $N_2H_4 = 3 \times [Cu]$	51
Figure 2-4. Cu nanoparticle growth curves measured in-situ by (Abs_{566}/Abs_{500}) as a function of time through the reduction of $Cu(NO_3)_2$ dissolved in AOT reverse micelle cores with W values of 5 and 10. a) Hexane and isooctane as the bulk alkane solvent and concentrations of $AOT = 0.133 \text{ M}$, $Cu(NO_3)_2 = 0.011 \text{ M}$, and $N_2H_4 = 3 \times [Cu]$. b) Cyclohexane as the bulk alkane solvent and concentrations of $AOT = 0.265 \text{ M}$, $Cu(NO_3)_2 = 5.5 \times 10^{-3} \text{ M}$, and $N_2H_4 = 3 \times [Cu]$	56
Figure 2-5. In Situ UV-Vis absorption measurements of copper nanoparticle growth in AOT/Cyclohexane reverse micelle system with $W = 5$. a) Particle synthesis via $Cu(AOT)_2$ reduction with $[AOT] = 0.11 \text{ M}$, $[Cu(AOT)_2] = 0.011 \text{ M}$ with each scan at 30 minute intervals. b) Particle synthesis via $Cu(NO_3)_2$ reduction with $[AOT] = 0.265 \text{ M}$, $[Cu(NO_3)_2] = 5.5 \times 10^{-3} \text{ M}$ with each scan at 15 minute intervals. The characteristic peak at 566 nm continues to grow and shifts slightly toward 600 nm with the formation of copper particle network.....	59
Figure 2-6. TEM image of copper nanoparticle network synthesized in an AOT reverse micelle system with cyclohexane as the bulk solvent, $[AOT] = 0.265 \text{ M}$ and $W = 5$. Copper particles were synthesized by reduction of $Cu(NO_3)_2$, $5.5 \times 10^{-3} \text{ M}$, using hydrazine, $[N_2H_4] = 3 \times [Cu]$	60
Figure 3-1. Contributions to the Total Interaction Energy Model for 8 nm diameter copper nanoparticles coated with AOT dispersed in hexane at 25°C and 1 bar.....	75
Figure 3-2. Attractive van der Waals contribution to the total interaction energy calculated for spherical copper nanoparticles coated with AOT surfactant and dispersed in hexane at 20°C for various particle diameters as a function of the separation distance.....	77
Figure 3-3. Plot of the ligand volume fraction as a function of the distance from the particle surface for various sized particles. At a distance of 9.1 Å corresponds to the length of the AOT surfactant.....	79
Figure 3-4 . Plot of the Total Interaction Energy, $\Phi_{total}/k_B T$, curves calculated for 4nm to 20nm diameter Cu nanoparticles coated with AOT and dispersed in hexane at 20°C and 1 bar. The model predicts an ultimate particle size of ~9 nm in diameter for hexane.....	84
Figure 3-5. Plot of the $\Phi_{total}/k_B T$ curves calculated for 10 nm diameter Cu nanoparticles coated with AOT and dispersed in hexane at 1 bar and temperatures ranging from 25°C to 65°C . The model predicts that 10 nm diameter Cu particles would be sterically stabilized in hexane at 25°C , however as the temperature is increased to 65°C the particles would agglomerate and precipitate out of solution.....	88
Figure 3-6. a) Plot of the $\Phi_{total}/k_B T$ curves calculated for 6nm to 12nm diameter Ag nanoparticles coated with AOT and dispersed in hexane at 25°C and 1 bar. b,c) TEM image and size distribution for Ag particles synthesized in	

liquid hexane–AOT– water reverse micelle system with 1.0×10^{-3} M AgAOT, 9.9×10^{-2} M AOT, and $W = 10$	90
Figure 3-7. Plot of the $\Phi_{\text{total}}/k_B T$ curves calculated for 8 nm diameter Ag nanoparticles coated with AOT and dispersed in hexane at 20°C and 1 bar with decreasing surface coverage of AOT on the Ag particles. The model predicts that as the percent surface coverage decreases, the ability to stabilize particles in solution also decreases	92
Figure 3-8. Chi interaction parameter, χ , for AOT in compressed propane as a function of temperature and pressure. Typically values of χ less than 0.5 are characteristic of good solvent conditions.....	95
Figure 3-9. Hamaker constant A_{131} for copper nanoparticles interacting through compressed propane as a function of temperature and pressure.....	96
Figure 3-10. Plot of the $\Phi_{\text{total}}/k_B T$ curves for Cu nanoparticles coated with AOT and dispersed in compressed propane. 3a) Shows the effect of particle diameter from 6nm to 15 nm at 310 bar and 25°C. 3b) shows the effects of pressure on 10nm diameter Cu particles at 25°C and in the range of 150 to 450 bar. 3c) Shows the effect of temperature on a 10nm diameter Cu particle at 310 bar and pressures ranging from 25°C to 65°C.	98
Figure 3-11. Plot of the $\Phi_{\text{total}}/k_B T$ curves for 9 nm diameter Cu nanoparticles coated with AOT and dispersed in SCF ethane at 35°C as a function of separation distance and pressure.....	101
Figure 3-12. Plot of the $\Phi_{\text{total}}/k_B T$ curves for Cu nanoparticles coated with AOT and dispersed in compressed ethane at 25°C for various particle diameters and pressures.....	102
Figure 4-1. High pressure reaction vessel equipped with a modified piston displacement hand pump, opposing windows for in-situ UV-Vis measurements, a face plate window, RTD temperature control, and flush mount pressure transducer.....	115
Figure 4-2. Copper nanoparticle size distribution for synthesis in compressed propane with $[AOT] = 5.5 \times 10^{-2}$ M, $[CuAOT_2] = 5.5 \times 10^{-3}$ M and $W = 1.5$ at 21°C and pressures of 241, 276, and 317 bar.	118
Figure 4-3. TEM image of copper nanoparticles synthesized in propane / AOT / $W=1.5$ reverse micelle system at 241bar $T=21^\circ\text{C}$, $[CuAOT_2] = 5.53 \times 10^{-3}\text{M}$, $[AOT] = 5.53 \times 10^{-2}\text{M}$. Particles collected by spray techniques through capillary tubing.	122
Figure 4-4. TEM images of copper nanoparticles synthesized in propane / AOT / $W=2$ reverse micelle system at bar $T=21^\circ\text{C}$, $[CuAOT_2] = 5.53 \times 10^{-3}\text{M}$, $[AOT] = 5.53 \times 10^{-2}\text{M}$. Images A and B were synthesized at $P=275$ bar, Image C at 241 bar and Image D at $P=345$ bar.....	123
Figure 4-5. Copper particle growth curves plotted as the average particle diameter in solution as a function of time, measured by in-situ UV-Vis absorption techniques. The particle growth curves demonstrate the effects of temperature and cosolvent presence on particle synthesis in the AOT – ethane reverse micelle system.....	125

Figure 4-6. TEM image of copper nanoparticles synthesized in SCF ethane – AOT reverse micelle system with $[\text{CuAOT}_2]=5.5 \times 10^{-3}$, $[\text{AOT}]=5.5 \times 10^{-2}$ and $W=1.5$ at 35°C and 517 bar. Particles were collected by spray deposition through 0.1 micron capillary tubing.....	127
Figure 4-7. Demixing pressures for the ethane – cosolvent microemulsion system as a function of temperature, cosolvent mol fraction and water content with $[\text{CuAOT}_2] = 6.0 \times 10^{-3}$ M and $[\text{AOT}]=6.0 \times 10^{-2}$ M.....	129
Figure 5-1. SANS results for liquid phase AOT reverse micelle microemulsion with $[\text{AOT}] = 0.137$ M and varying bulk solvent, W value and octanol additive. The solid lines represent the PCF-HS modeling fit of the data points.	150
Figure 5-2. SANS results for the AOT reverse micelle microemulsion in compressed propane with $[\text{AOT}] = 0.6$ M at various temperatures and pressures. The lower curves are the measured backgrounds for the pure d-propane.....	154
Figure 5-3. The Intermediate Scattering Function decay curves measured by NSE for the liquid phase AOT microemulsions for a) d-cyclohexane $W = 10$, b) d-cyclohexane $W = 5$ and c) d-hexane $W = 10$. The solid lines are to guide the eye.....	157
Figure 5-4. Q -dependant diffusion results obtained by NSE for the liquid phase AOT reverse micelle microemulsion. The solid lines represent the fitting of the data points with equations 4 and 5.....	158
Figure 5-5. Q -dependant diffusion results obtained by NSE for the compressed d-propane / AOT / $W=8$ reverse micelle microemulsion.....	166
Figure 6-1. Copper nanoparticle growth curves measured in situ by the absorbance ratio of the intensity at $\lambda = 566$ nm relative to $\lambda = 500$ nm. The time resolved UV-vis absorbance measurements demonstrate the kinetics of spherical copper nanoparticle synthesis within the isooctane / AOT – $\text{Cu}(\text{AOT})_2$ / H_2O reverse micelle microemulsion with varying W value and HCl concentration within the micelle core.	180
Figure 6-2. TEM image of copper nanoparticles synthesized in isooctane / AOT – $\text{Cu}(\text{AOT})_2$ / $W = 10$ reverse micelle microemulsion with $[\text{HCl}] = 4.2 \times 10^{-2}$ M within the micelle core. The copper particles are stabilized by dodecylamine, and the AOT surfactant was removed prior to particle collection. The image displays the uniformity of particle deposition and details of particle agglomerates with increasing magnification.....	182
Figure 6-3. Particle size distributions obtained from TEM analysis of copper nanoparticles synthesized within isooctane / AOT – $\text{Cu}(\text{AOT})_2$ / $W = 10$ reverse micelle microemulsion with HCl concentrations within the micelle core of a) 0.0 M, b) 4.2×10^{-3} M, c) 4.2×10^{-2} M.....	185
Figure 6-4. Total interaction energy of two spherical copper nanoparticles coated with dodecylamine and dispersed in isooctane as a function of the particle diameter and separation distance.	187
Figure 6-5. TEM image of copper nanorods synthesized in isooctane / AOT – $\text{Cu}(\text{AOT})_2$ / $W = 3$ reverse micelle microemulsion with $[\text{HCl}] = 4.2 \times 10^{-2}$ M.....	189

Figure 6-6. In situ UV-vis absorbance spectra of copper nanoparticles, synthesized in compressed propane / AOT – Cu(AOT) ₂ / W = 3 reverse micelle microemulsion. Spectrum a was measured in situ, 3 hours after copper reduction with [HCl] = 4.2 x 10 ⁻³ M at 20°C and 310 bar. Spectrum b was measured from the organic isooctane phase after the liquid – liquid extraction step of the particle collection methods for the experiment corresponding to spectrum a. Spectrum c was measured in situ, 3 hours after copper reduction with [HCl] = 4.2 x 10 ⁻² M at 20°C and 310 bar.	191
Figure 6-7. TEM Images of diamond shaped assemblies of copper nanoparticles synthesized in compressed propane / AOT – Cu(AOT) ₂ / W = 3 reverse micelles with [HCl] = 4.2 x 10 ⁻² M within the micelle core. Particles were collected by a,b) spray process from the propane system and c,d) droplet method for particles re-dispersed in isooctane + 0.01 M dodecylamine.	193
Figure 6-8. TEM image of diamond shaped aggregates of copper particles collected as a precipitate at the aqueous – oil interface during the liquid – liquid extraction of the AOT surfactant followed by re-dispersion in acetone. Synthesis was performed in compressed propane / AOT – Cu(AOT) ₂ / W = 3 reverse micelles with [HCl] = 4.2 x 10 ⁻² M.	194
Figure 6-9. EDS spectra measured from diamond shaped assemblies of copper nanoparticles collected by a) spray technique following synthesis in compressed propane, on a nickel TEM grid (Figure 7a) and b) by the droplet method on a copper grid of particles re-dispersed in acetone following precipitation during the liquid – liquid extraction of the AOT surfactant (Figure 10c).	200
Figure 6-10. TEM images of copper nanoparticles synthesized in compressed propane / AOT – Cu(AOT) ₂ / W = 3 reverse micelles with [HCl] = 4.2 x 10 ⁻³ M and collected by a) spray process, b) re-dispersion in isooctane + 0.01 M dodecylamine, and c,d) by precipitation during the liquid – liquid extraction of the AOT surfactant and re-dispersed in acetone.	201

LIST OF TABLES

Table 2-1. Experimental results of the relative particle growth rates and ultimate particle sizes obtained for Copper nanoparticles synthesized in various alkane bulk solvents with $[\text{CuAOT}_2] = 0.01106 \text{ M}$, $[\text{AOT}] = 0.1106 \text{ M}$ and $W = 5$ and 10 .	45
Table 2-2. Experimental results of the relative particle growth rates and ultimate particle sizes obtained for Copper nanoparticles synthesized in an isooctane reverse micelle system with $[\text{CuAOT}_2] = 0.01106 \text{ M}$ and $[\text{AOT}] = 0.1106 \text{ M}$ for W values ranging from 3 to 15.	46
Table 2-3. Experimental results of the relative particle growth rates, maximum absorbance ratio and ultimate particle size obtained for copper nanoparticles synthesized in AOT reverse micelles by the reduction of $\text{Cu}(\text{NO}_3)_2$ salt.	57
Table 3-1. Experimental results of the relative particle growth rates and ultimate particle sizes obtained for Copper nanoparticles synthesized in various alkane bulk solvents with $[\text{CuAOT}_2] = 0.01106 \text{ M}$, $[\text{AOT}] = 0.1106 \text{ M}$ and $W = 5$ and 10 . The calculation results obtained from the total interaction energy model show excellent agreement with the ultimate particle sizes obtained experimentally.	86
Table 3-2. Table of thermophysical properties of the copper nanoparticle – liquid alkane – AOT system for various bulk alkane solvents.	87
Table 3-3. Table of thermophysical properties of the copper nanoparticle – alkane – AOT system for various compressed, SCF, and compressed + cosolvent alkane solvents.	97
Table 3-4. Maximum copper nanoparticle diameters predicted by the total interaction energy model for various ethane – AOT systems as a function of pressure, temperature and the addition of hexane, isooctane and cyclohexane cosolvents at different mol fractions. The predicted particle sizes demonstrate the effects of the bulk solvent properties on particle synthesis. The – indicates a prediction of the inability to synthesize particles of any size.	104
Table 4-1. Descriptive statistics of experimental particle size distributions obtained from TEM analysis for copper nanoparticles synthesized in compressed propane, ethane + cosolvent, and SCF ethane at various temperatures, pressures, cosolvent mol fractions and water contents. The predicted particle sizes by the total interaction energy model are listed for comparison.	119
Table 5-1. Results obtained from the PCF-HS model fit of the SANS data for the liquid phase AOT microemulsions	153

Table 5-2. NSE results for the liquid phase microemulsions and comparison of the reverse micelle radius determined by SANS, NSE and the Correlation Length. The values for the bending elasticity modulus are determined by two different methods.	160
Table 5-3. NSE results for the compressed d-propane / AOT / W=8 microemulsions as a function of temperature and pressure. The values for the bending elasticity modulus are determined by two different methods..	167

LIST OF ABBREVIATIONS

A_{131}	Hamaker constant
AOT	Sodium bis(2-ethylhexyl) sulfosuccinate
AR	Absorbance Ratio
CFD	Chemical Fluid Deposition
CMC	Critical Micelle Concentration
CTAB	Cetyltrimethylammonium Bromide
Cu	Copper
d	center to center separation
D ₂ O	deuterium oxide (heavy water)
$D_{\text{def}}(Q)$	deformation diffusion coefficient
D_{eff}	effective diffusion coefficient
DLS	dynamic light scattering
DLVO	Derjaguin-Landau-Verwey-Overbeek
D_{tr}	translational diffusion coefficient,
E_3^{coh}	cohesive energy density
EDS	Energy dispersive X-ray spectroscopy
ϕ	ligand volume fraction
fcc	face centered cubic
FWHM	full width at half max
GXL	Gas Expanded Liquid
h	separation distance
h	Planck's constant
$I(Q)$	scattered intensity
$I(Q,t) / I(Q/0)$	intermediate scattering function
IQR	interquartile range
k	bending elasticity constant
k_B	Boltzmann's constant
k_{ex}	intermicellar exchange rate constant
n	refractive index
NSE	Neutron Spin Echo

p	polydispersity
$P(Q)$	form factor
P_c	critical pressure
PEG	poly(ethylene glycol)
PVA	poly(vinyl alcohol)
PVP	poly(vinyl pyrrolidone)
Q	momentum transfer function
R or r	micelle hydrodynamic radius
R	Ideal Gas Constant
R	particle radius
RESS	rapid expansion of supercritical solvents
$S(Q)$	structure factor
SAED	selected area electron diffraction
SANS	Small Angle Neutron Scattering
SAXS	Small Angle X-ray Scattering
SCF	Supercritical Fluid
SDS	Sodium Dodecylsulfate
SLD	scattering length density
T	Temperature
T_c	critical temperature
TEM	Transmission Electron Microscope
UCSC	Upper Critical Solution Concentration
UV-Vis	Ultra Violet - Visible
W	Water Content
2θ	scattering angle
$\langle \alpha_2 ^2 \rangle$	damping amplitude
δ_i	Hildebrand solubility parameters
ϵ	dielectric constant
η	viscosity
λ	wavelength
λ_2	damping frequency of the droplet deformation
ξ_r	correlation length
Φ_{elas}	elastic interaction force
Φ_{osm}	osmotic interaction force
$\Phi_{\text{total}}/k_B T$	total interaction energy force
Φ_{vdW}	van der Waals interaction force
χ	Flory-Huggins interaction parameter
\bar{k}	saddle-splay elasticity constant

CHAPTER 1

1. INTRODUCTION AND BACKGROUND MATERIAL

1-1. NANOMATERIALS

Nanotechnology is the study and implementation of nanomaterials, defined by length scales less than 100 nanometers, and has emerged as an influential area of research and development for future technologies¹⁻¹¹. A majority of the state-of-the-art technologies that are in use today operate on the micro-scale, such as microelectronics. As technology advances the trend is to operate on an even smaller level, leading to the development of a variety of nanomaterials with unique properties and characteristics as well as an unlimited potential of applications. Postulations on the future of nanotechnology include the formation of nanocomputers and nanomachines which act as assemblers and replicators of virtually any conceivable material or device by tailored atomic scale production. Potential applications range from materials necessary to make space travel feasible to the hypothetical “breadbox assembler” present in every household which will consist of atomic raw materials used to produce a desired object or material¹⁰⁻¹². The synthesis of many nanomaterials consists of a “bottom up” mechanism beginning with atomic building blocks, as opposed to the conventional methods of micro scale synthesis consisting of “top down” mechanisms^{4-7,10-12}. The every-day usage of such nanodevices lies in the distant future, however current research in the production of

nanomaterials lies in controlling these tailored assemblies, particularly isolated nanoparticles of specific size and morphology.

Current applications of nanoparticles include optical, electronic, magnetic, sensor, superconducting, biological, catalytic and biomedical materials as well as coatings, films, and seeded growth of micro/macro scale materials^{6,7,11,13}. Nanoparticle properties have the potential to differ significantly from conventional materials thus allowing for the development of novel and innovative materials. Composition, structure, interfacial properties, defects, flaws and other physical aspects of these materials are the key ingredients which mold these materials for their potential applications yielding new and innovative materials. In order to take advantage of these physical aspects, synthesis of nanomaterials must be understood and controlled. Control of nanoparticle synthesis lies in manipulation of the physical properties, thermodynamics and kinetics of the system, thus allowing for tailored assembly down to the atomic level. The arrangement of atoms on the nanoscale directly influences the material properties, such as strength, uniformity, chemical activity and performance. Without a fundamental understanding of the surface chemistry, thermodynamics and kinetics of nanoparticle synthesis, the full potential for application will not be achieved.

Synthesis of nanoparticles has been achieved in the solid, liquid, gas and supercritical phases, each with its advantages and drawbacks. Solid state synthesis is a conventional method consisting of mechanical deformation under shear conditions⁴⁻⁶. This method is typically diffusion limited and energy intensive resulting in high temperatures and large size distribution and non-uniformity of the product. Liquid, gas

and supercritical phase synthesis provides increased diffusion of reactants, allowing for better kinetics and more favorable operating conditions as compared to solid state synthesis^{2,13-18}. This is necessary for the synthesis of many thermodynamically sensitive materials and also yields more uniform and mono-dispersed materials. A majority of synthesis techniques performed in fluid media involve atomic and molecular synthesis from the bottom up in a nucleation and growth type mechanism, regardless of the material composition. This is true for metallic, organic, organometallic, or composite materials and due to the nanoscale synthesis, misplacement of a single atom or the smallest defect in the crystal lattice or grain structure can potentially affect the performance of the material, either advantageously or detrimentally^{5,6,11,13}. The “bottom up” synthesis is typically achieved by one of three methods, acid/base reaction, precipitation, or reduction/oxidation reaction. Each of these methods can be used to initiate particle growth followed by a nucleation and growth mechanism. Particle nucleation can be achieved either homogeneously by temperature or pressure adjustment or heterogeneously by the addition of a reducing agent, antisolvent or some other type of initiator. The particle growth is governed by the thermodynamics of the system, including temperature, pressure, density, pH, and dielectric constant^{2,6,11}.

Particle nucleation and growth play an important role in determining the physical properties of the resulting material however; other thermodynamic and kinetic factors such as stabilization and diffusion can be influential in determining particle morphology and structure. Certain phenomena such as coagulation, the formation of strong compact aggregates, and flocculation, formation of a loose network of particles, can be either

advantageous or detrimental depending on the materials application. Attractive interactions between nanoparticles synthesized in a fluid phase can arise from electrostatic or van der Waals forces, leading to undesired agglomeration. In many cases colloidal stabilization provides efficient means to prevent unwanted agglomeration. In the case of metallic nanoparticles, entropic stabilization of the particles by a protective layer of surfactant has proven effective in preventing degradation, oxidation and agglomeration. Surfactants have also been shown to act as dispersants to stabilize particles through steric or electrostatic repulsion^{6,13,19}.

Metallic nanoparticles have found applications in electronics, magnetic materials, sensors, explosives, catalysts, pharmaceuticals, powder metallurgy, thin films and coatings. Metallic nanoparticles have been produced in a variety of morphologies^{2,5,7,13,18,20-35} (spheres, rods, fibers, cubes, and hollow cubes) and compositions^{17,36-54} (metallic, intermetallic, organometallic, alloys, and composites). Some of the more popular solution synthesis techniques include aqueous, non-aqueous, sono-chemical, organometallic precursor, chemical vapor deposition, gels and microemulsion methods^{2,5,6,13,16,55,56}. Synthesis of metallic nanoparticles has potential as an extremely innovative research area due to the interesting properties they exhibit. The high surface to volume ratio provides high reactivity for surface active materials such as catalysts as well as applications involving thin films and coatings. Metallic nanoparticles have the ability to go through tailored synthesis to produce various desired particle morphologies and compositions. The various metallic materials, consisting of a wide range different metals and metal composites, allow for interesting metal lattice and

conductivity properties. Surface properties and reactive sites make these materials attractive for biomedical applications and as seeded growth initiators^{17,22,35,57}. Nanoparticle applications cover many areas of research due to the high activity and versatility of the materials. However, in many cases the high surface activity results in metal nanoparticle susceptibility to oxidation, hydrolysis or some other form of degradation. Stabilizing ligands and other surface conditioning substances, such as surfactants, are necessary for the preservation of these materials^{6,13,19}. Surfactants and other stabilizing ligands, such as thiol compounds, create a thin protective monolayer on the surface of the nanoparticles^{58,59}. These thin monolayers are also used to functionalize nanoparticles for nanomaterial assembly applications^{55,60}. Surfactants play an important role in the synthesis of metallic nanoparticles with the application of an emulsion based method.

1-2. EMULSION BASED SYNTHESIS OF PARTICLES

A typical emulsion consists of a single phase consisting of three components, water, oil and an amphiphilic molecule such as a surfactant^{1,61-63}. Normally oil and water are immiscible but with the addition of a surfactant, the oil and water become miscible because the surfactant is able to bridge the interfacial tension between the two fluids^{1,62}. The molecular structure of surfactants affords it the ability to immerse polar and non-polar compounds such as oil and water. Surfactants consist of two main entities, a hydrophilic head group, which prefers an aqueous environment and a hydrophobic (or lyophobic) tail group, which prefers an organic, non-polar environment. There are four main classes of surfactants determined by the ionic charge of the head group which

include cationic surfactant (positive charge), non-ionic surfactant (neutral charge), anionic surfactant (negative charge) and zwitterionic surfactant (both positive and negative charge). An example surfactant used throughout this work is sodium bis(2-ethylhexyl) sulfosuccinate, also known as Aerosol-OT or AOT seen in Figure 1-1a. AOT is a twin tailed, anionic surfactant with a sulfosuccinate head group stabilized as a salt by a sodium cation. The AOT molecule has an inverted conical shaped structure and has proven to be an effective emulsifier, thus finding a wide range of applications as well as numerous intensive studies.

One class of emulsion is a microemulsion. Microemulsions are distinct from other emulsions in that they are transparent, spontaneously self-assemble, more stable with respect to phase separation, and consist of aggregates are on the length scale of less than 100 nm. The geometry of surfactant aggregates within a microemulsion can take on a variety of forms based on the location in the water – surfactant – oil phase diagram shown in Figure 1-2 as well as the molecular geometry of the surfactant. The geometry of the surfactant molecule can be defined by the critical packing parameter⁶⁴ defined with examples in Figure 1-3. AOT has an inverted cone shape with a critical packing parameter greater than one allowing for preferential formation of reverse micelle surfactant aggregates. An oil-in-water microemulsion, o/w, located in the bottom left corner of the phase diagram, consists of water as the bulk fluid with small amounts of surfactant and oil. For an o/w microemulsion, the surfactant and oil components will self assemble to form a minimum free energy entity know as a micelle. Micelles are composed of nano-scale oil droplets encased in a monolayer of surfactant with the

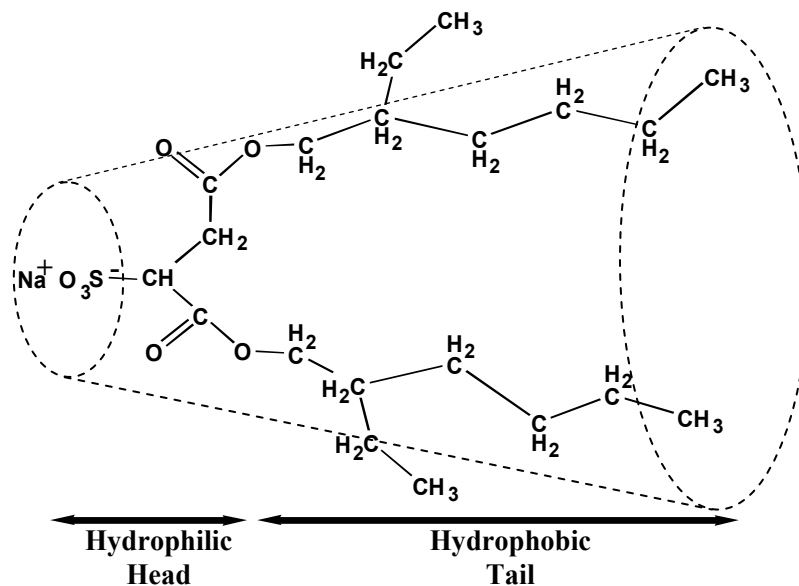


Figure 1-1a. Molecular structure of sodium bis(2-ethylhexyl) sulfosuccinate (AOT) surfactant. The dotted lines represent the cone-like packing structure of the twin tail surfactant.

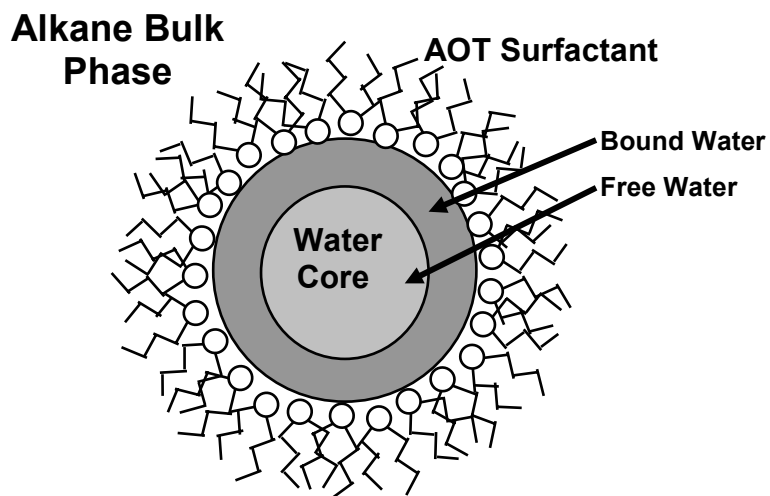


Figure 1-1b. Reverse micelle formed by the self-assembly of AOT surfactant molecules which disperse nano-sized water droplets within the bulk oil phase, creating a thermodynamically stable microemulsion.

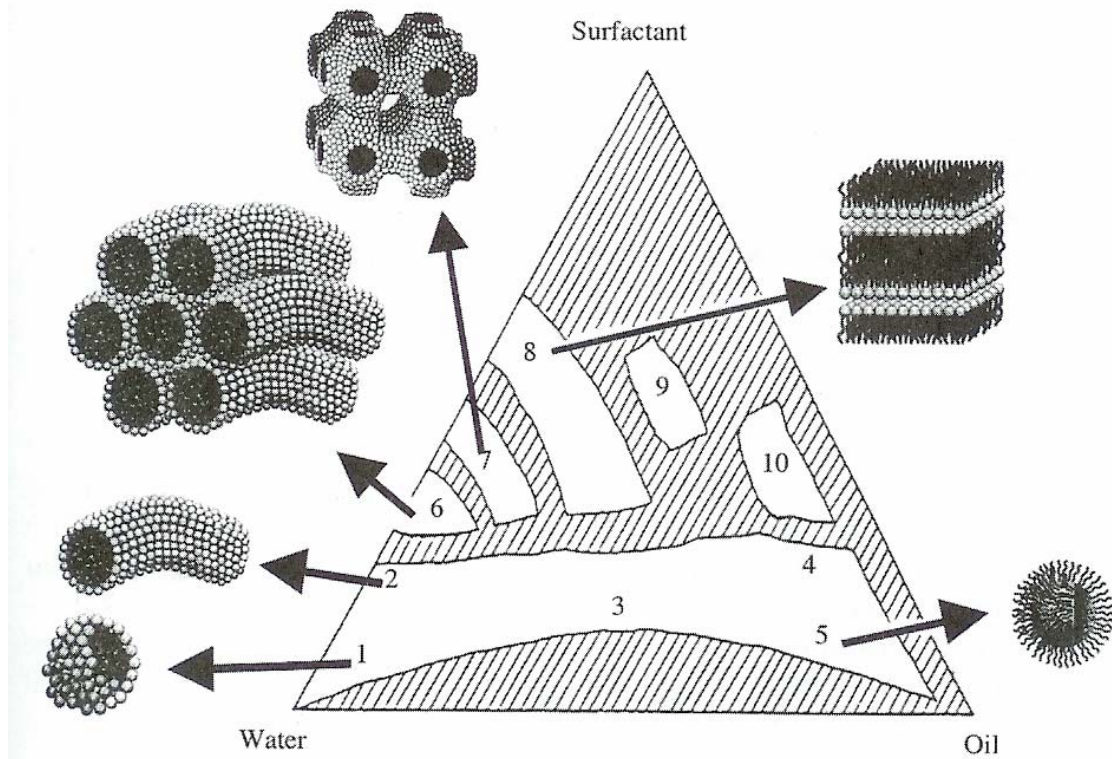


Figure 1-2. Phase diagram of the Water – Surfactant – Oil microemulsion system demonstrating various surfactant aggregate geometries consisting of 1. Spherical micelles. 2. Rod-like micelles. 3. Irregular bicontinuous phase. 4. Reverse cylindrical micelles. 5. Reverse micelles. 6. Hexagonal phase. 7. Cubic phase. 8. Lamellar phase. 9. Reverse cubic phase. 10. Reverse hexagonal phase. (Obtained from Zhang et al., 2003)²

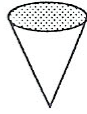
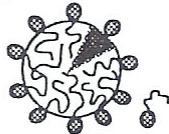

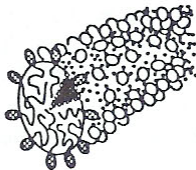

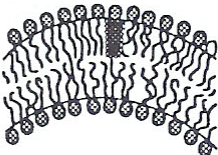

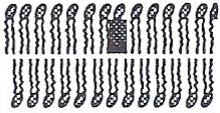
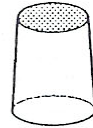
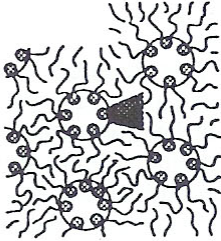
Lipid	Critical packing parameter	Critical packing shape	Structures formed
Single-chained lipids (surfactants) with large head group areas: SDS in low salt	$< 1/3$	Cone 	Spherical micelles 
Single-chained lipids with small head group areas: SDS and CTAB in high salt, nonionic lipids	$1/3-1/2$	Truncated cone 	Cylindrical micelles 
Double-chained lipids with large head group areas, fluid chains: phosphatidyl choline (lecithin), phosphatidyl serine, phosphatidyl glycerol, phosphatidyl inositol, phosphatidic acid, sphingomyelin, DGDG, ^a dihexadecyl phosphate, dialkyl dimethyl ammonium salts	$1/2-1$	Truncated cone 	Flexible bilayers, vesicles 
Double-chained lipids with small head group areas, anionic lipids in high salt, saturated frozen chains: phosphatidyl ethanolamine phosphatidyl serine + Ca^{2+}	~ 1	Cylinder 	Planar bilayers 
Double-chained lipids with small head group areas, nonionic lipids, poly (cis) unsaturated chains, high T: unsaturated phosphatidyl ethanolamine, cardiolipin + Ca^{2+} phosphatidic acid + Ca^{2+} cholesterol, MGDG ^b	> 1	Inverted truncated cone or wedge 	Inverted micelles 

Figure 1-3. Relationship between the surfactant shape, critical packing parameter R , and the surfactant aggregate structures formed within the microemulsion. (Obtained from Hiemenz and Rajagopalan, 1997, p.371.)¹

hydrophilic surfactant tails preferentially oriented on the oil droplet surface and the hydrophilic head group extending into the bulk water phase. A water-in-oil, w/o, microemulsion located in the bottom right corner of the phase diagram, consists of an organic solvent or oil as the bulk fluid with small amounts of surfactant and water. In this case the surfactant and water self assemble to form a thermodynamically stable reverse micelle. The reverse micelle consists of a small water pool encased in a surfactant monolayer where the hydrophilic head group preferentially orients itself at the water surface and the surfactant tails protrude into the bulk organic fluid, as seen in Figure 1-1b. The size and number of reverse micelles which are dispersed in the bulk organic fluid largely depends on the concentrations of water and surfactant, as well as their molar ratio. The ratio of water molecules to surfactant molecules is used to describe the water content of the reverse micelles and is commonly termed a W value, $W = [\text{H}_2\text{O}] / [\text{Surfactant}]$. The water content, W, is directly related to the size of the AOT reverse micelle water core by a simple relation, $R(\text{nm}) = 0.18 W$, where R is the hydrodynamic radius of the AOT reverse micelle⁶⁵. An AOT reverse micelle system typically exists with a W in the range of 0 to ~100 (depending on the bulk solvent, temperature, etc.) resulting in a water pool varied from 0 to 30 nanometers in diameter⁶⁶.

The concentration of surfactant required to form spherical reverse micelles is determined by the critical micelle concentration, CMC, which is the minimum surfactant concentration necessary to form micelles. The CMC is affected by various properties of the reverse micelle system, such as the solvent interactions between the surfactant tails and bulk organic solvent, the geometry of the surfactant, the addition of cosolvents or

salts, and temperature. Above the CMC, the surfactant aggregates exist as reverse micelles until the surfactant concentration is increased to a point where the reverse micelles begin to aggregate into larger structures and flocculation begins. The CMC and flocculation are dependant on the physical and thermodynamic properties of the reverse micellar system. The same properties largely influence the microemulsion stability as well as the controlling factors of nanoparticle synthesis within the reverse micelle cores.

The reverse micelle core acts as a nanoreactor for aqueous phase reactions dispersed within an organic bulk phase. AOT has been used extensively in the formation of reverse micellar systems, mainly due to the fact that the inverted cone geometry of the surfactant allows for the formation of evenly dispersed, thermodynamically stable, spherical reverse micelles¹. Due to the popularity of this system, an extraordinary amount of research has been and continues to be conducted in order to gain a complete understanding of each governing entity. Investigations of the water core have revealed the presence of two water environments seen in Figure 1-1b. Bound water exists in the vicinity of the AOT head groups where the ionic environment influences the water by restricting the mobility of the water molecules. Free water exists in the center of the reverse micelle and has properties closely resembling those of bulk water. Reaction studies have shown that the water environment plays an important role in micelle kinetics thus influencing nanoparticle formation within the reverse micelle cores^{50-52,67-73}. There have been several mechanisms proposed that govern micelle kinetics and thus influence reactions in reverse micelle systems.

The most widely accepted mechanism, seen in Figure 1-4 , involves an intermicellar exchange of the aqueous micelle core and the dissolved contents which occurs through random micelle collisions resulting from micelle diffusion through the bulk fluid and Brownian motion^{56,66,74,75}. The intermicellar exchange process has been studied by a variety of methods including laser flash photolysis, spectrophotometry, NMR and electrochemistry^{66,74,76-80}. Robinson and co-workers performed one of the first in depth studies of micelle kinetics on the water/alkane/AOT system using laser flash photolysis and a stopped flow technique where two micelle solutions containing reactants were mixed and product evolution was measured to determine the intermicellar exchange rate constant, k_{ex} ⁶⁶. The study included three different reactions and variation in the bulk liquid alkane fluid, water content, AOT concentration, and temperature. The results from their study reveal that k_{ex} decreases with increasing water content for W = 10, 15, 20, and 30; k_{ex} is independent of AOT and reactant concentration; k_{ex} increases with an increase in temperature; and k_{ex} increases slightly with carbon number for pentane through dodecane in addition to a significant decrease in k_{ex} for the corresponding cyclic compounds, particularly cyclohexane. The dependency of k_{ex} on the bulk solvent can be explained by the solvent interactions with the AOT tails where a more favorable interaction will allow for the solvent to insert itself within the surfactant tails thus creating a more rigid micelle and resulting in a slower exchange rate^{66,81}. Thermodynamic and physical properties other than k_{ex} , such as critical micelle concentration, phase separation, diffusions, microemulsion stability, interaction forces, and solvent effects also play an important in reverse micelle synthesis. Additional studies on the water/alkane/AOT system have been performed using a variety of methods and

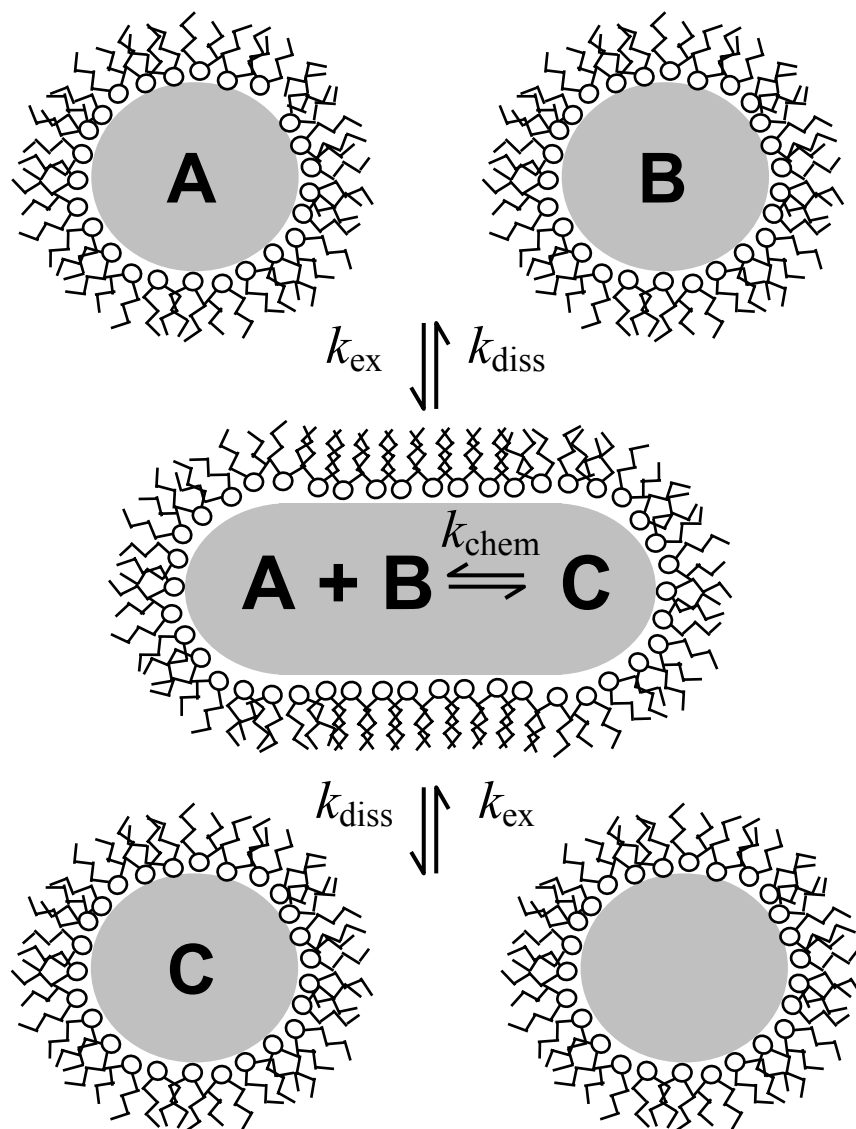


Figure 1-4. Mechanism for intermicellar exchange of the water cores within the AOT reverse micelles which mediates the chemical reaction between water soluble reactants A and B to form reactant C.

techniques and will be discussed throughout the dissertation in order to support the current research.

1-3. METALLIC NANOPARTICLE PRODUCTION

Control of metallic nanoparticle synthesis within the reverse micelle system requires an understanding of the reaction mechanism and controlling thermodynamic and physical properties. Use of the reverse micellar system for nanomaterial synthesis began in the early 1990's by a few prominent and influential research groups. These materials consist of purely metallic particles (Cu, Ag, Co, Al), metal sulfides (CdS, ZnS), oxides (TiO₂, SiO₂), and various nano-composite materials^{50-52,67,71,73}.

Synthesis of metallic nanoparticles within the AOT reverse micelle system consists of an initial reduction of metal ions within the reverse micelle cores to produce ground state metal atoms followed by particle growth facilitated by agglomeration and the intermicellar exchange of the reverse micelle cores. The pioneering work by Pileni and co-workers demonstrated the ability to produce copper and silver nanoparticles using the water/AOT/liquid alkane reverse micelle system^{43,82-84}. The work of Pileni played an influential role in the development of the current research in this dissertation, providing means for metallic nanoparticle production. A schematic of an example reaction mechanism is shown in Figure 1-5. Metal ion starting materials are introduced into the system either as a metal salt dissolved in the aqueous micelle core or by functionalization of the AOT surfactant head group where the sodium counter ion is exchanged with the desired metal ion. The purpose of the second method is to eliminate the presence of the salt anion from the core of the reverse micelle. The use of salts and the presence of

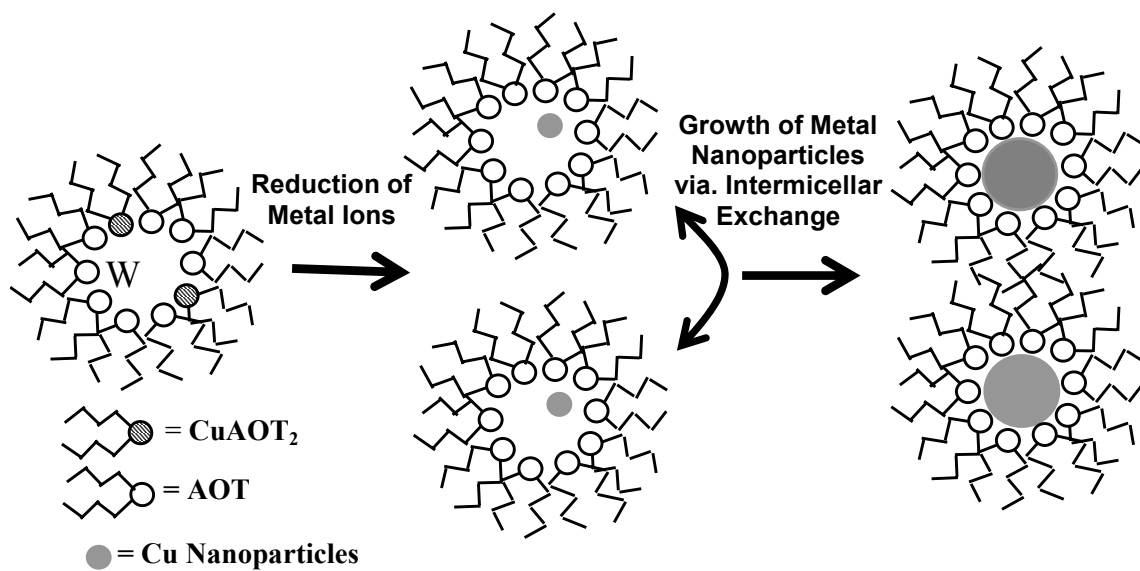


Figure 1-5. Reaction mechanism for the synthesis of copper nanoparticles via chemical reduction of the copper functionalized AOT surfactant followed by particle growth through the dynamic intermicellar exchange of the micelle contents.

anions within reverse micelles have been shown to alter the physical properties of the water environment and surfactant layer resulting in variations in the size and shape of the reverse micelles and metallic particles synthesized⁸⁵⁻⁸⁸.

Reduction of the metal ion is achieved by either thermochemical methods, photochemical methods or the introduction of a chemical reducing agent either directly or through a second reverse micellar system. Typical reducing agents include hydrazines or borohydride derivatives. The initial reduction of the metal ions can generally be observed by a distinct color change in the solution and is then followed by the particle growth mechanism facilitated by the intermicellar exchange process. Particle growth continues until an ultimate particle size is achieved. The intricate particle synthesis mechanism has several factors which contribute to the reaction kinetics and properties of the resulting particles such as particle size and morphology. Investigation of the influence of reacting species and their concentrations, bulk solvent type, water content, anion presence, pH, and temperature have been studied by various research groups on multiple systems^{14,19,50-53,67,69-73,86-93}. Each study contributes to our understanding of particle synthesis within the reverse micelle system furthering our ability to control nanoparticle synthesis.

The most common and easily adjusted parameters of the AOT reverse micelle system are the bulk solvent type and the water content, W . As mentioned before, the bulk solvent type has an effect on the micelle stability and the intermicellar exchange rate, k_{ex} , while W is directly related to the size of the reverse micelle, also effecting k_{ex} . In the first papers by Pileni dealing with metallic nanoparticle production, it was

demonstrated that both the bulk solvent and W value have an effect on the synthesis of copper and silver nanoparticles within the AOT reverse micelle system^{68,69,94}. Analysis of the copper and silver nanoparticle synthesis was performed using UV-Vis absorbance spectroscopy and transmission electron microscopy, TEM, at a specific reaction time. From the TEM analysis, micrographs of the particles can be used to size individual particles and obtain an average particle size, as well as a particle size distribution. The UV-Vis absorption measurements take advantage of the unique optical properties of the copper and silver nanoparticles where characteristic absorption bands appear at wavelengths of 566 nm and 400 nm respectively⁹⁵. These characteristic peaks are due to surface plasmon resonance of the metallic particles can be seen in Figure 1-6. It has been shown that the relative intensity and shape of the peaks can be correlated to the average particle size within the microemulsion. The work by Pileni demonstrated that for copper nanoparticles, the relative intensity of the absorbance peak measured as a ratio of the absorbance at 566 nm to the absorbance at 500 nm, $AR = \epsilon_{566}/\epsilon_{500}$, can be correlated to the average copper particle diameter⁶⁹. The relationship between the particle diameter and AR reported by Pileni was estimated by a second order fit of the particle size as a function of the AR, equation 1-1. This relationship is based purely on average particle sizes measured experimentally and is purely approximate. For silver particles it has been shown that the average particle diameter is inversely related the full width at half max, FWHM, of the characteristic peak centered at 400 nm⁹⁶.

$$\text{Copper Particle Diameter (nm)} = 80.0 \times AR^2 - 98.7 \times AR + 31.2 \quad (1-1)$$

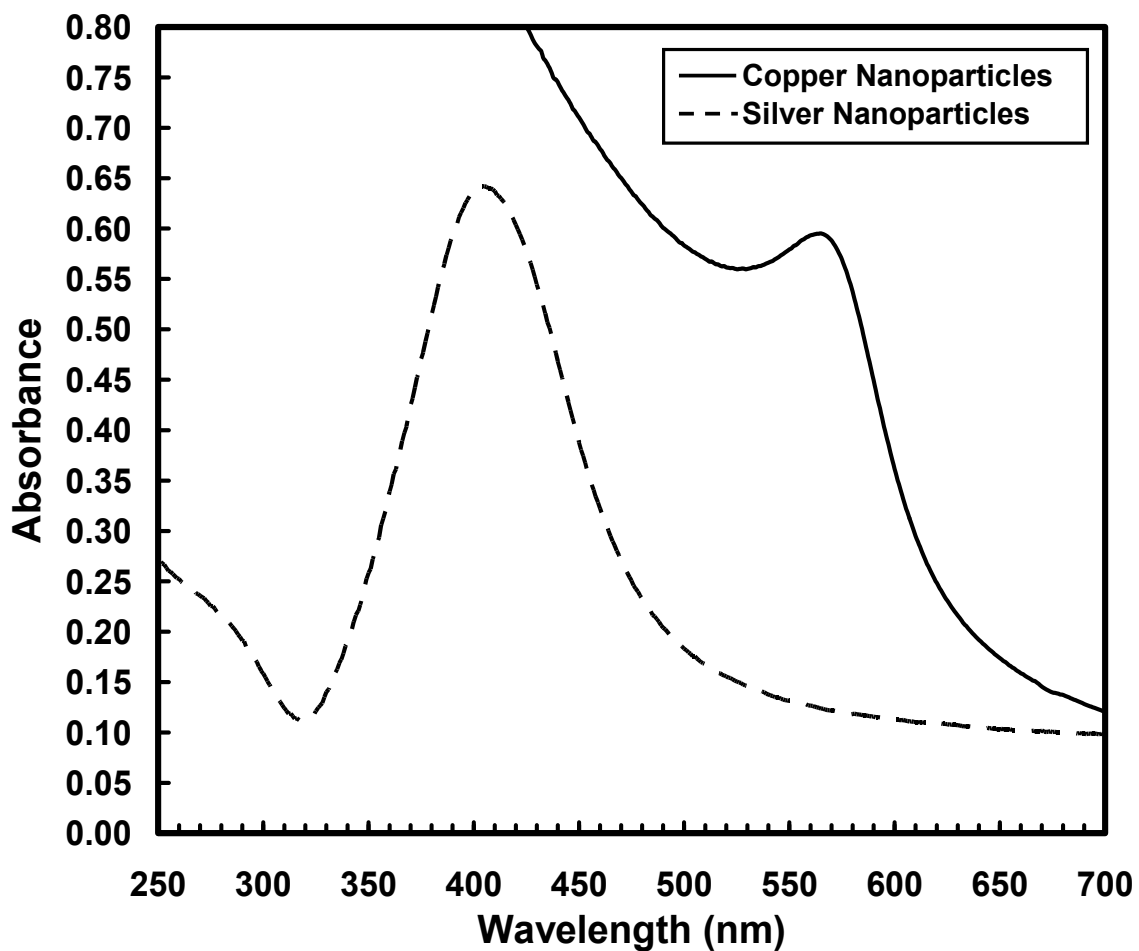


Figure 1-6. Characteristic UV-Vis absorbance bands for Copper and Silver nanoparticles in solution.

The static measurements presented by Pileni for the copper system demonstrated that at a particular reaction time, the copper particle diameter measured by TEM and UV-Vis absorption is related to the W value where an increase in W or the size of the reverse micelle corresponds to an increase in the copper particle diameter. Further investigations by Cason et al. took advantage of the ability to relate the absorbance measurements to the particle size in order to perform in-situ time resolved absorbance measurements and thus study the reaction kinetics governing copper particle formation⁷³. The time resolved studies revealed that given adequate reaction time for W values ranging from 3 to 15 in a particular bulk solvent, the average particle sizes obtained were consistent. This demonstrates that the W value does not have an effect on the ultimate particle size, but rather has a profound effect on the particle growth rate.

This observation is of particular interest in understanding the underlying properties that govern nanoparticle formation within the AOT reverse micelle system. There have been a variety of studies that have described the reverse micelle system as a template for particle synthesis where the size and shape of the reverse micelles will determine the size and shape of the resulting nanoparticle^{48,89,97-99}. Studies of the ultimate copper particle size as a function of W or the size of the reverse micelle itself have shown that the particle sizes obtained are independent of the initial reverse micelle size and in fact, the copper particles obtained are up to four times larger in diameter than the original reverse micelle^{69,73}. This occurrence does not apply to the production of all nanomaterials however; it clearly demonstrates that the ultimate size of Cu metallic nanoparticles synthesized is not the result of micelle templating. This leads to an

alternate explanation where the ultimate metallic particle size obtained within the AOT reverse micelle system is largely a result of steric stabilization of the metallic particles by the AOT surfactant. In this case the surfactant acts as a stabilizing ligand where the head group interacts with the particle surface and the surfactant tails support the particle in solution through solvent interactions with the bulk fluid. Other studies have shown the effects of conventional stabilizing ligands, such as thiols, on the stabilization and dispersion of metallic nanoparticles through the solvent interactions between the ligands and the bulk fluid¹⁰⁰⁻¹⁰⁴. It is quite possible that steric stabilization plays a significant role in particle synthesis in microemulsion systems by methods similar to those responsible for particle stabilization and dispersion. Debate over steric stabilization versus templating effects remains an area of interest. Investigation of steric stabilization as a governing factor over the synthesis of metallic nanoparticles is a large focus of the research presented in this dissertation and will be examined by experimental and theoretical techniques.

Previous time resolved absorption studies on the kinetics of Cu, Ag, AgCl, Co, CdS and ZnS^{50,51,67,70-72} particle synthesis within the AOT reverse micelle have also been investigated in order to determine the effects of bulk solvent type, surfactant concentrations, reactant concentrations, anion presence, pH, and temperature. The influence of the liquid bulk solvent on the particle growth rate and ultimate particle size in the AOT reverse micelle system has also been investigated for Cu, Ag, Co, CdS and ZnS nanoparticles. These studies have demonstrated the solvent effects on the particle growth rates corresponding to the trends seen with the measurements of k_{ex} for the

water/AOT/alkane system, discussed earlier. Thus the thermodynamic properties that govern the micelle dynamics and the intermicellar exchange process also play a significant role in particle kinetics. The solvent effects on the particle growth rates are the result of the solvent interactions with the micelle surfactant shell which acts to create a stable colloidal dispersion, necessary for particle synthesis. The observed trends suggest that a more favorable solvent interaction with the surfactant tails will result in a more stable microemulsion as well as a more rigid reverse micelle thus affecting k_{ex} and particle growth rates. The stability of the microemulsion can also influence the growth and dispersion of various sized metallic particles within the AOT reverse micelles.

Variations in the surfactant concentration, reactant concentrations, temperature and adjustments on the water core properties through the addition of salts and pH adjustments also influence particle growth and morphology and will be discussed throughout the dissertation^{14,18,19,23,25,87,103,105,106}. Manipulation of the components of the reverse micelle system can be used to tailor particle synthesis for desired applications however a more precise understanding of the underlying thermodynamics and kinetics of the reverse micelle system is required.

1-4. SUPERCRITICAL FLUIDS

It has been shown that the thermodynamic properties of the reverse micelle bulk solvent influences the intermicellar exchange process as well as nanoparticle growth kinetics and particle morphology. Thus the use of a thermodynamically tunable solvent as the bulk fluid, will allow particle synthesis to become more robust and controllable. Supercritical fluids afford the opportunity to adjust their thermodynamic properties by

simple adjustments in the temperature and pressure of the system. A supercritical fluid exists in a thermodynamic state above the critical point which is achieved by heating above the critical temperature, T_c , and compression beyond the critical pressure, P_c . Transition of a fluid from the liquid – vapor state to the supercritical state can be observed experimentally by simultaneously heating and compressing a single component two phase system along the vapor – liquid equilibrium curve shown on the T – P phase diagram in Figure 1-7. As the system approaches the critical point, the thermodynamic properties of the two phases become more alike until the critical point is reached. At this point the liquid and vapor phases have the same thermodynamic properties and thus the phase separation line vanishes and a single supercritical phase exists. Supercritical fluids, SCFs, have received attention as solvents for various separation and synthesis procedures due to their unique properties. SCFs are compressible fluids that have liquid-like densities and gas-like mass transfer properties which can be manipulated by small changes in the temperature and pressure of the system in the vicinity of the critical point¹⁰⁷⁻¹¹⁰. This allows for tunable density dependant properties such as diffusion, solubility parameter, and dielectric constant which happen to be influential in micelle dynamics as well as nanoparticle synthesis¹¹¹.

SCFs also afford unique opportunities for particle collection methods and applications. Techniques such as rapid expansion of supercritical solvents (RESS), have been developed as particle collection methods where upon depressurization of the system, suspended nanoparticles will precipitate out of solution^{37,111}. The pressurized system also provides means for particle spray coating applications to obtain thin films of

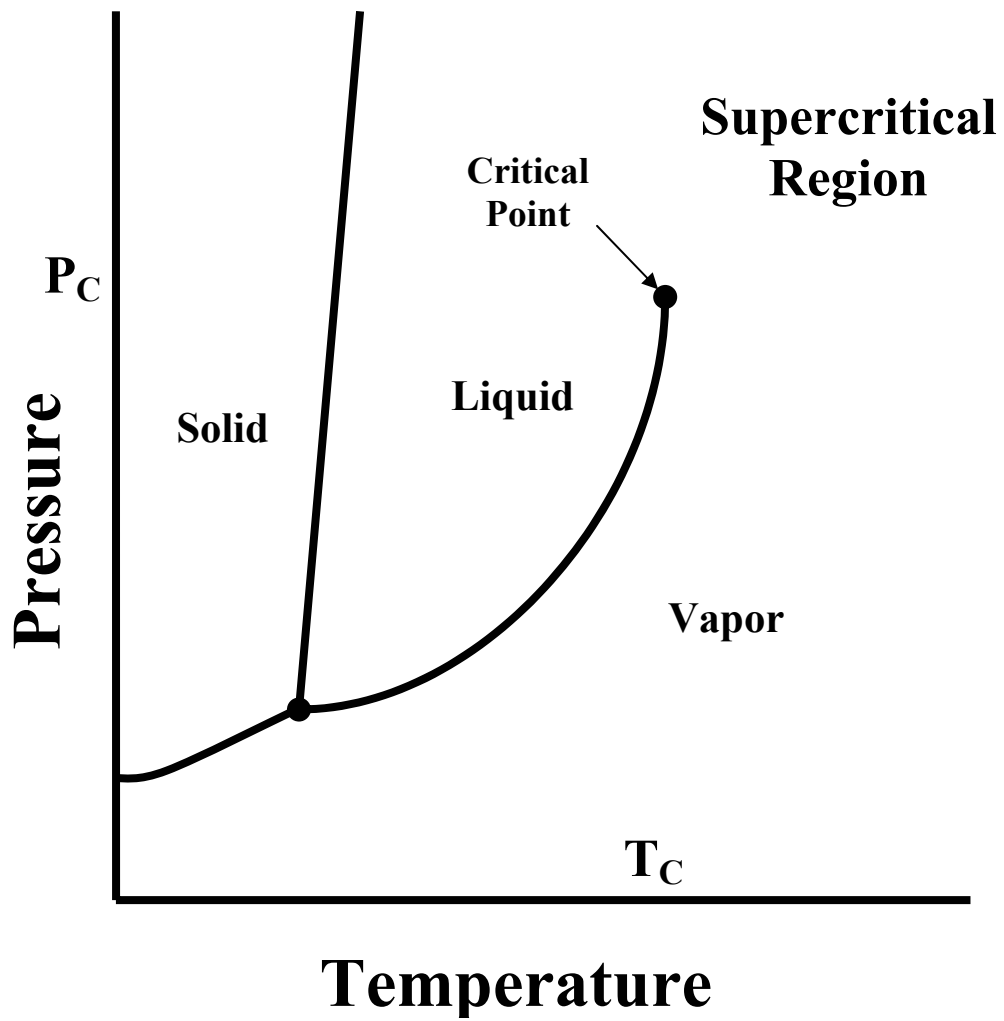


Figure 1-7. Pressure - Temperature phase diagram demonstrating the supercritical fluid region at the culmination of the vapor – liquid equilibrium curve.

nanoparticles. Other properties such as increased diffusion of SCFs have been shown to be effective for depositing thin metallic films within narrow channels by chemical fluid deposition, CFD¹¹²⁻¹¹⁵.

Fulton and coworkers were the first to demonstrate the formation of thermodynamically stable AOT reverse micelles in compressed and supercritical alkane solvents, specifically SCF ethane and compressed propane^{116,117}. Additional studies have been performed to determine the phase behavior of the SCF alkane – AOT reverse micelle system in order to gain a better understanding of the physical nature of these systems^{118,119}. Since then Cason et al. has shown that copper particles can be formed in compressed propane AOT reverse micelle system as well as in SCF ethane reverse micelle system with the addition of an alkane cosolvent^{120,121}. Other researchers have demonstrated the ability to form nanomaterials using AOT reverse micelles within a compressible alkane bulk solvent as well as in SCF carbon dioxide^{37,60,108,122-125}. SCF CO₂ has the advantages of being nonflammable, inert, inexpensive, environmentally benign, and has a modest critical temperature and pressure, however, the solubility of many conventional surfactants and ability to create a stable emulsion is extremely poor, thus inhibiting nanoparticle synthesis. Nanoparticle synthesis has been achieved using perfluorinated surfactants, however the fluorinated surfactants are not considered environmentally friendly, hence a quest for non-fluorinated, CO₂ soluble surfactants, suitable for nanoparticle synthesis is a current goal in the field of SCF nanoparticle synthesis.

Cason et al. demonstrated the ability for particle synthesis in a near critical and supercritical phase, however the influences of temperature and pressure on the particle kinetics and morphology was not investigated. Johnston and coworkers have recently demonstrated that silver and gold nanocrystals, sterically stabilized by dodecanethiol ligands and dispersed in supercritical ethane, can be selectively separated according to size by adjusting the temperature and pressure of the system¹⁰⁰. Therefore, the solvent strength of the supercritical phase can be adjusted to support various sized particles by adjusting the operating conditions of the system. In the same respect, variation in the solvent strength by temperature and pressure variations influences the solvent properties thus allowing for control over metallic nanoparticle synthesis and stabilization.

1-5. CHAPTER OVERVIEW

The general research objectives of this work are to investigate controlling mechanisms which govern metallic nanoparticle formation within reverse micellar microemulsion systems. Chapter 2 demonstrates the synthesis of copper nanoparticles synthesized within the liquid phase AOT reverse micelle microemulsion. Time resolved UV-vis absorbance measurements and TEM analysis were used to investigate the kinetics of copper nanoparticle synthesis and the ultimate average particle size synthesized. The study demonstrates primarily the effects of the bulk liquid solvent and the water content on the particle growth rate and ultimate particle size. Other components of particle synthesis investigated include the use of copper salts as the metallic precursor, temperature, reducing agent, surfactant concentration, and cosolvent addition. Chapter 3 implements a total interaction energy model; developed to study the interactions of

spherical metallic nanoparticles encased in a monolayer of surfactant / stabilizing agent and dispersed in the bulk organic solvent. The model is used to investigate the thermophysical properties of the bulk solvent and the solvent - surfactant tail interactions to effectively predict the ultimate particle size synthesized within the microemulsion system. The model is applied to particle synthesis within the liquid alkane, compressed propane, supercritical ethane, and ethane plus cosolvent systems by calculating the interaction energies of spherical metallic nanoparticles coated with a monolayer of a stabilizing agent (eg. AOT) dispersed within a bulk fluid. Chapter 4 investigates nanoparticle synthesis using compressible fluids as the bulk solvent, where temperature, pressure, and cosolvent can be utilized to alter the properties of the bulk alkane solvent and thus control the particle size synthesized. The results from Chapters 2 – 4 support our proposal that the AOT surfactant acts as a dispersing ligand and sterically stabilizes the metallic nanoparticles in solution where the thermophysical interactions of the bulk fluid with the surfactant tails are deterministic of the particle growth kinetics and maximum particle size synthesized.

Chapter 5 presents the neutron scattering work performed at the NIST Center for Neutron Research (NCNR) in Gaithersburg, MD which consisted of two accepted proposals for beam time on the NG5 Neutron Spin Echo (NSE) spectrometer (3 days for liquids, 8 days for compressed fluids) and one request for beam time on the NG1 8m Small Angle Neutron Scattering (SANS) instrument (2 days). NSE and SANS were used to determine the elastic properties of the AOT surfactant monolayers within the reverse micelles as a function of the bulk solvent properties and water content. The conditions

investigated include hexane with $W = 10$; cyclohexane with $W = 5, 10, \text{ and } 18$; and compressed propane with $W = 8$. The values of the bending elasticity determined for each of the conditions investigated demonstrate the same trends observed for micelle rigidity observed for micelle dynamics and our studies of nanoparticle kinetics.

Chapter 6 demonstrates the effects of chloride ion on the synthesis of copper nanoparticles within the AOT reverse micelle system utilizing both liquid isooctane and compressed propane as the bulk solvent. Copper nanoparticle synthesis can be achieved in the presence of HCl in the micelle core taking advantage of the buffering action of the AOT surfactant. The concentration of chloride ion influences the particle growth rate and dispersion in liquid isooctane. The presence of chloride ions during particle synthesis in compressed propane has a significant effect on the geometry and structure of the copper nanomaterials produced. As a result of chloride ion addition to the compressed propane / $\text{Cu(AOT)}_2 - \text{AOT} / \text{water}$ reverse micelle system at 20°C and 310 bar, the formation of diamond-shaped copper nanoparticle assemblies is observed. The copper nanoparticle assemblies exhibit unique structure and retain this structure through repeated solvent processing which is advantageous for methods to selectively separate and assemble the diamond-shaped copper nanoparticle structures for potential applications.

Chapter 7 discusses the future work for metallic nanoparticle synthesis within microemulsion systems which utilizes our improved understanding of nanoparticle synthesis for potential applications. These new areas of research include particle separation and deposition techniques for directed assembly of uniform arrays of nanoparticles with desired orientation for potential applications. The use of ionic species

for directing the synthesis of nanoparticles and nano-assemblies into specific geometries will be investigated further in attempt to synthesize novel yet practical nanomaterials.

1-6. REFERENCES

- (1) Hiemenz, P. C.; Rajagopalan, R. *Principles of colloid and surface chemistry*; 3rd , rev. and expanded / ed.; Marcel Dekker: New York, 1997.
- (2) Zhang, J. Z. *Self-assembled nanostructures*; Kluwer Academic/Plenum Publishers: New York, 2003.
- (3) Nalwa, H. S. *Nanostructured materials and nanotechnology*; Concise ed.; Academic Press: San Diego, Calif. London, 2002.
- (4) Nalwa, H. S. *Handbook of nanostructured materials and nanotechnology*; Academic Press: San Diego, 2000.
- (5) Shalaev, V. M.; Moskovits, M.; American Chemical Society. Division of Physical Chemistry.; American Chemical Society. Meeting *Nanostructured materials : clusters, composites, and thin films*; American Chemical Society: Washington, DC, 1997.
- (6) Koch, C. C. *Nanostructured materials : processing, properties, and potential applications*; Noyes Publications/William Andrew Pub.: Norwich, N.Y., 2002.
- (7) Timp, G. L. *Nanotechnology*; Springer: New York, 1999.
- (8) Drexler, K. E.; Peterson, C.; Pergamit, G. *Unbounding the future : The Nanotechnology Revolution*; Morrow: New York, 1991.
- (9) National Research Council (U.S.) *Implications of emerging micro- and nanotechnologies*; National Academies Press: Washington, D.C., 2002.
- (10) Drexler, K. E. *Engines of creation*; 1st ed.; Anchor Press/Doubleday: Garden City, N.Y., 1986.
- (11) Newton, D. E. *Recent advances and issues in molecular nanotechnology*; Greenwood Press: Westport, Conn., 2002.
- (12) Drexler, K. E. *Nanosystems : molecular machinery, manufacturing, and computation*; Wiley: New York, 1992.
- (13) Adair, J. H.; Li, T.; Kido, T.; Havey, K.; Moon, J.; Mecholsky, J.; Morrone, A.; Talham, D. R.; Ludwig, M. H.; Wang, L. *Materials Science & Engineering R-Reports* 1998, 23, 139-242.
- (14) Adair, J. H.; Suvaci, E. *Current Opinion in Colloid & Interface Science* 2000, 5, 160-167.
- (15) Kruis, F. E.; Fissan, H.; Peled, A. *Journal of Aerosol Science* 1998, 29, 511-535.
- (16) Moriarty, P. *Reports on Progress in Physics* 2001, 64, 297-381.
- (17) Toshima, N.; Yonezawa, T. *New Journal of Chemistry* 1998, 22, 1179-1201.
- (18) Yacaman, M. J.; Ascencio, J. A.; Liu, H. B.; Gardea-Torresdey, J. *Journal of Vacuum Science & Technology B-an International Journal Devoted to Microelectronics and Nanometer Structures- Processing Measurement and Phenomena* 2001, 19, 1091-1103.

- (19) Dixit, S. G.; Mahadeshwar, A. R.; Haram, S. K. *Colloids and Surfaces a-Physicochemical and Engineering Aspects* 1998, *133*, 69-75.
- (20) Murphy, C. J. *Science* 2002, *298*, 2139-+.
- (21) Rao, C. N. R.; Govindaraj, A.; Sen, R.; Satishkumar, B. C. *Materials Research Innovations* 1998, *2*, 128-141.
- (22) Service, R. F. *Science* 2002, *298*, 2322-2323.
- (23) Sun, Y. G.; Mayers, B.; Xia, Y. N. *Advanced Materials* 2003, *15*, 641-646.
- (24) Sun, Y. G.; Mayers, B.; Xia, Y. N. *Nano Letters* 2003, *3*, 675-679.
- (25) Sun, Y. A.; Xia, Y. N. *Advanced Materials* 2003, *15*, 695-699.
- (26) Pileni, M. P. *Abstracts of Papers of the American Chemical Society* 2002, *224*, 091-PHYS.
- (27) Maillard, M.; Giorgio, S.; Pileni, M. P. *Advanced Materials* 2002, *14*, 1084-+.
- (28) Pinna, N.; Weiss, K.; Sack-Kongehl, H.; Vogel, W.; Urban, J.; Pileni, M. P. *Langmuir* 2001, *17*, 7982-7987.
- (29) Maillard, M.; Motte, L.; Pileni, M. P. *Advanced Materials* 2001, *13*, 200-204.
- (30) Legrand, J.; Ngo, A. T.; Petit, C.; Pileni, M. P. *Advanced Materials* 2001, *13*, 58-+.
- (31) Lisiecki, I.; Sack-Kongehl, H.; Weiss, K.; Urban, J.; Pileni, M. P. *Langmuir* 2000, *16*, 8807-8808.
- (32) Lisiecki, I.; Sack-Kongehl, H.; Weiss, K.; Urban, J.; Pileni, M. P. *Langmuir* 2000, *16*, 8802-8806.
- (33) Lisiecki, I.; Billoudet, F.; Pileni, M. P. *Journal of Physical Chemistry* 1996, *100*, 4160-4166.
- (34) Holmes, J. D.; Johnston, K. P.; Doty, R. C.; Korgel, B. A. *Science* 2000, *287*, 1471-1473.
- (35) Lu, X. M.; Hanrath, T.; Johnston, K. P.; Korgel, B. A. *Nano Letters* 2003, *3*, 93-99.
- (36) Adschiri, T.; Hakuta, Y.; Sue, K.; Arai, K. *Journal of Nanoparticle Research* 2001, *3*, 227-235.
- (37) Holmes, J. D.; Lyons, D. M.; Ziegler, K. J. *Chemistry-a European Journal* 2003, *9*, 2144-2150.
- (38) Roucoux, A.; Schulz, J.; Patin, H. *Chemical Reviews* 2002, *102*, 3757-3778.
- (39) Holmes, J. D.; Bhargava, P. A.; Korgel, B. A.; Johnston, K. P. *Langmuir* 1999, *15*, 6613-6615.
- (40) Lim, K. T.; Hwang, H. S.; Lee, M. S.; Lee, G. D.; Hong, S. S.; Johnston, K. P. *Chemical Communications* 2002, 1528-1529.
- (41) Petit, C.; Lixon, P.; Pileni, M. P. *Langmuir* 1991, *7*, 2620-2625.
- (42) Pileni, M. P.; Motte, L.; Petit, C. *Chemistry of Materials* 1992, *4*, 338-345.
- (43) Lisiecki, I.; Pileni, M. P. *Journal of the American Chemical Society* 1993, *115*, 3887-3896.

- (44) Moumen, N.; Veillet, P.; Pileni, M. P. *Journal of Magnetism and Magnetic Materials* 1995, *149*, 67-71.
- (45) Feltin, N.; Pileni, M. P. *Langmuir* 1997, *13*, 3927-3933.
- (46) Petit, C.; Pileni, M. P. *Journal of Magnetism and Magnetic Materials* 1997, *166*, 82-90.
- (47) Pileni, M. P.; Motte, L.; Billoudet, F.; Mahrt, J.; Willig, F. *Materials Letters* 1997, *31*, 255-260.
- (48) Ingert, D.; Feltin, N.; Levy, L.; Gouzerh, P.; Pileni, M. P. *Advanced Materials* 1999, *11*, 220-+.
- (49) Alivisatos, A. P. *Science* 1996, *271*, 933-937.
- (50) Hirai, T.; Sato, H.; Komasaawa, I. *Industrial & Engineering Chemistry Research* 1994, *33*, 3262-3266.
- (51) Hirai, T.; Tsubaki, Y.; Sato, H.; Komasaawa, I. *Journal of Chemical Engineering of Japan* 1995, *28*, 468-473.
- (52) Sato, H.; Hirai, T.; Komasaawa, I. *Industrial & Engineering Chemistry Research* 1995, *34*, 2493-2498.
- (53) Wu, M. L.; Chen, D. H.; Huang, T. C. *Langmuir* 2001, *17*, 3877-3883.
- (54) Eastoe, J.; Cox, A. R. *Colloids and Surfaces A: Physicochemical and Engineering Aspects* 1995, *101*, 63-76.
- (55) Davis, S. A.; Breulmann, M.; Rhodes, K. H.; Zhang, B.; Mann, S. *Chemistry of Materials* 2001, *13*, 3218-3226.
- (56) Eastoe, J.; Warne, B. *Current Opinion in Colloid & Interface Science* 1996, *1*, 800-805.
- (57) Shipway, A. N.; Katz, E.; Willner, I. *Chemphyschem* 2000, *1*, 18-52.
- (58) Berchmans, S.; Thomas, P. J.; Rao, C. N. R. *Journal of Physical Chemistry B* 2002, *106*, 4647-4651.
- (59) Chaiyasit, W.; Silvestre, M. P. C.; McClements, D. J.; Decker, E. A. *Journal of Agricultural and Food Chemistry* 2000, *48*, 3077-3080.
- (60) Crooks, R. M.; Zhao, M. Q.; Sun, L.; Chechik, V.; Yeung, L. K. *Accounts of Chemical Research* 2001, *34*, 181-190.
- (61) Gelbart, W.; Ben-Shaul, A.; Roux, D. *Micelles, membranes, microemulsions, and monolayers*; Springer-Verlag: New York, 1994.
- (62) Chen, S.-H.; Rajagopalan, R. *Micellar solutions and microemulsions : structure, dynamics, and statistical thermodynamics*; Springer-Verlag: New York, 1990.
- (63) Mittal, K. L.; Kumar, P.; NetLibrary Inc.; QEMK NetLibrary; HTTP *Handbook of microemulsion science and technology*; Marcel Dekker: New York, 1999.
- (64) Israelachvili, J. N.; Mitchell, D. J.; Ninham, B. W. *Biochimica et Biophysica Acta (BBA) - Biomembranes* 1977, *470*, 185-201.
- (65) Eastoe, J.; Fragneto, G.; Robinson, B. H.; Towey, T. F.; Heenan, R. K.; Leng, F. J. *J. Chem. Soc.-Faraday Trans.* 1992, *88*, 461-471.
- (66) Fletcher, P. D. I.; Howe, A. M.; Robinson, B. H. *Journal of the Chemical Society-Faraday Transactions I* 1987, *83*, 985-1006.
- (67) Towey, T. F.; Khanlodhi, A.; Robinson, B. H. *Journal of the Chemical Society-Faraday Transactions* 1990, *86*, 3757-3762.
- (68) Pileni, M. P. *Langmuir* 1997, *13*, 3266-3276.

- (69) Lisiecki, I.; Pileni, M. P. *Journal of Physical Chemistry* 1995, *99*, 5077-5082.
- (70) Petit, C.; Lixon, P.; Pileni, M. P. *Journal of Physical Chemistry* 1990, *94*, 1598-1603.
- (71) Bagwe, R. P.; Khilar, K. C. *Langmuir* 2000, *16*, 905-910.
- (72) Bagwe, R. P.; Khilar, K. C. *Langmuir* 1997, *13*, 6432-6438.
- (73) Cason, J. P.; Miller, M. E.; Thompson, J. B.; Roberts, C. B. *Journal of Physical Chemistry B* 2001, *105*, 2297-2302.
- (74) Eicke, H. F.; Shepherd, J. C. W.; Steinemann, A. *Journal of Colloid and Interface Science* 1976, *56*, 168-176.
- (75) Howe, A. M.; McDonald, J. A.; Robinson, B. H. *Journal of the Chemical Society-Faraday Transactions I* 1987, *83*, 1007-1027.
- (76) Charlton, I. D.; Doherty, A. P. *Electrochemistry Communications* 1999, *1*, 176-179.
- (77) Charlton, I. D.; Doherty, A. P. *Journal of Physical Chemistry B* 2000, *104*, 8061-8067.
- (78) Blitz, J. P.; Fulton, J. L.; Smith, R. D. *Journal of Physical Chemistry* 1988, *92*, 2707-2710.
- (79) Eastoe, J.; Young, W. K.; Robinson, B. H.; Steytler, D. C. *Journal of the Chemical Society-Faraday Transactions* 1990, *86*, 2883-2889.
- (80) Atik, S. S.; Thomas, J. K. *Journal of the American Chemical Society* 1981, *103*, 3543-3550.
- (81) Binks, B. P.; Kellay, H.; Meunier, J. *Europhysics Letters* 1991, *16*, 53-58.
- (82) Petit, C.; Lixon, P.; Pileni, M. P. *Journal of Physical Chemistry* 1993, *97*, 12974-12983.
- (83) Pileni, M. P.; Lisiecki, I. *Colloids and Surfaces A: Physicochemical and Engineering Aspects* 1993, *80*, 63-68.
- (84) Pileni, M. P. *Journal of Physical Chemistry* 1993, *97*, 6961-6973.
- (85) Hassan, P. A.; Raghavan, S. R.; Kaler, E. W. *Langmuir* 2002, *18*, 2543-2548.
- (86) Pileni, M. P.; Gulik-Krzywicki, T.; Tanori, J.; Filankembo, A.; Dedieu, J. C. *Langmuir* 1998, *14*, 7359-7363.
- (87) Filankembo, A.; Pileni, M. P. *Applied Surface Science* 2000, *164*, 260-267.
- (88) Lisiecki, I.; Filankembo, A.; Sack-Kongehl, H.; Weiss, K.; Pileni, M. P.; Urban, J. *Physical Review B* 2000, *61*, 4968-4974.
- (89) Pileni, M. P. *Nature Materials* 2003, *2*, 145-150.
- (90) Cheng, G. X.; Shen, F.; Yang, L. F.; Ma, L. R.; Tang, Y.; Yao, K. D.; Sun, P. C. *Materials Chemistry and Physics* 1998, *56*, 97-101.
- (91) Quintillan, S.; Tojo, C.; Blanco, M. C.; Lopez-Quintela, M. A. *Langmuir* 2001, *17*, 7251-7254.
- (92) Natarajan, U.; Handique, K.; Mehra, A.; Bellare, J. R.; Khilar, K. C. *Langmuir* 1996, *12*, 2670-2678.
- (93) Sato, H.; Hirai, T.; Komasa, I. *Journal of Chemical Engineering of Japan* 1996, *29*, 501-507.

- (94) Petit, C.; Lixon, P.; Pileni, M. P. *Journal of Physical Chemistry* 1993, *97*, 12974-12983.
- (95) Creighton, J. A.; Eadon, D. G. *Journal of the Chemical Society-Faraday Transactions* 1991, *87*, 3881-3891.
- (96) Andrews, M. P.; Ozin, G. A. *Journal of Physical Chemistry* 1986, *90*, 2929-2938.
- (97) Pileni, M. P.; Ninham, B. W.; Gulik-Krzywicki, T.; Tanori, J.; Lisiecki, I.; Filankembo, A. *Advanced Materials* 1999, *11*, 1358-1362.
- (98) Filankembo, A.; Pileni, M. P. *Journal of Physical Chemistry B* 2000, *104*, 5865-5868.
- (99) Pileni, M. P. *Berichte Der Bunsen-Gesellschaft-Physical Chemistry Chemical Physics* 1997, *101*, 1578-1587.
- (100) Shah, P. S.; Holmes, J. D.; Johnston, K. P.; Korgel, B. A. *Journal of Physical Chemistry B* 2002, *106*, 2545-2551.
- (101) Vincent, B.; Edwards, J.; Emmett, S.; Jones, A. *Colloids and Surfaces* 1986, *18*, 261-281.
- (102) Motte, L.; Pileni, M. P. *Applied Surface Science* 2000, *164*, 60-67.
- (103) Urban, J.; Sack-Kongehl, H.; Weiss, K.; Lisiecki, I.; Pileni, M. P. *Crystal Research and Technology* 2000, *35*, 731-743.
- (104) Korgel, B. A.; Fullam, S.; Connolly, S.; Fitzmaurice, D. *Journal of Physical Chemistry B* 1998, *102*, 8379-8388.
- (105) Sun, Y. G.; Xia, Y. N. *Science* 2002, *298*, 2176-2179.
- (106) Pileni, M. P. *Journal of Physical Chemistry B* 2001, *105*, 3358-3371.
- (107) Clifford, T. *Fundamentals of supercritical fluids*; Oxford University Press: Oxford ; New York, 1999.
- (108) Hutchenson, K. W.; Foster, N. R.; American Institute of Chemical Engineers. Meeting *Innovations in supercritical fluids : science and technology*; American Chemical Society: Washington, DC, 1995.
- (109) McHugh, M. A.; Krukonis, V. J. *Supercritical fluid extraction : principles and practice*; 2nd ed.; Butterworth-Heinemann: Boston, 1994.
- (110) Technical Insights Inc. *Supercritical fluids processing : emerging opportunities*; Technical Insights: Fort Lee, N.J., 1985.
- (111) Bartscherer, K. A.; Minier, M.; Renon, H. *Fluid Phase Equilibria* 1995, *107*, 93-150.
- (112) Cabanas, A.; Blackburn, J. M.; Watkins, J. J. *Microelectronic Engineering* 2002, *64*, 53-61.
- (113) Blackburn, J. M.; Long, D. P.; Cabanas, A.; Watkins, J. J. *Science* 2001, *294*, 141-145.
- (114) Long, D. P.; Blackburn, J. M.; Watkins, J. J. *Advanced Materials* 2000, *12*, 913-915.
- (115) Watkins, J. J.; Blackburn, J. M.; McCarthy, T. J. *Chemistry of Materials* 1999, *11*, 213-215.
- (116) Smith, R. D.; Fulton, J. L.; Blitz, J. P.; Tingey, J. M. *Journal of Physical Chemistry* 1990, *94*, 781-787.

- (117) Fulton, J. L.; Smith, R. D. *Journal of Physical Chemistry* 1988, *92*, 2903-2907.
- (118) McFann, G. J.; Johnston, K. P. *Journal of Physical Chemistry* 1991, *95*, 4889-4896.
- (119) Roberts, C. B.; Thompson, J. B. *Journal of Physical Chemistry B* 1998, *102*, 9074-9080.
- (120) Cason, J. P.; Khambaswadkar, K.; Roberts, C. B. *Industrial & Engineering Chemistry Research* 2000, *39*, 4749-4755.
- (121) Cason, J. P.; Roberts, C. B. *Journal of Physical Chemistry B* 2000, *104*, 1217-1221.
- (122) Ji, M.; Chen, X. Y.; Wai, C. M.; Fulton, J. L. *Journal of the American Chemical Society* 1999, *121*, 2631-2632.
- (123) McLeod, M. C.; McHenry, R. S.; Beckman, E. J.; Roberts, C. B. *Journal of Physical Chemistry B* 2003, *107*, 2693-2700.
- (124) Ohde, H.; Hunt, F.; Wai, C. M. *Chemistry of Materials* 2001, *13*, 4130-4135.
- (125) Shah, P. S.; Husain, S.; Johnston, K. P.; Korgel, B. A. *Journal of Physical Chemistry B* 2002, *106*, 12178-12185.

CHAPTER 2

2. SOLVENT EFFECTS ON THE GROWTH AND STERIC STABILIZATION OF COPPER METALLIC NANOPARTICLES IN AOT REVERSE MICELLE SYSTEMS

2-1. INTRODUCTION

Reactions within the aqueous cores of water-in-oil AOT reverse micelle system are proven to be a viable method for the production of nanomaterials of controllable composition and geometry while maintaining narrow size distributions. Synthesis of nanomaterials within the AOT reverse micelle system is a strong function of the intermicellar exchange process and other governing features of the reverse micelle system mentioned previously. Considerable research has been done to better understand the governing features which comprise the AOT reverse micellar system, particularly microemulsion stability and the intermicellar exchange of the contents within the aqueous micelle cores. The intermicellar exchange rate is affected by the bulk solvent type, the contents dissolved within the core, and the size of the reverse micelle or the water content, referred to as the W value where W is the ratio of the water to AOT surfactant concentrations. Conflicting opinions on some aspects of the AOT system remain despite the numerous studies performed in order to improve the fundamental understanding of the AOT reverse micelle system¹⁻⁹. In particular, the underlining factors controlling the synthesis of nanomaterials via aqueous phase reduction reactions within the AOT reverse

micelle cores are not fully understood. Previous work done with the alkane / AOT surfactant / water system has shown that the bulk solvent and water content, $W = [\text{H}_2\text{O}] / [\text{AOT}]$, have a significant effect on the intermicellar exchange of the water cores and the kinetics of nanoparticle formation^{7,10-18}. This study examines the effects of varying the bulk liquid solvent, the source of copper ions and the W value on the growth rate and ultimate particle size of copper nanoparticles produced via reduction of Cu^{2+} ions within the micelle core. Particle growth is measured in-situ using time resolved UV-Vis absorbance spectroscopy and the particle size is determined by both absorbance measurements and Transmission Electron Microscopy, TEM, analysis.

Studies of the water-in-oil microemulsion system have presented a mechanism of intermicellar exchange of the water core contents²⁻⁵ as a rate determining step in particle formation^{6,7}. Robinson and coworkers⁴ presented a comprehensive study on the alkane / AOT / water system where the intermicellar exchange rate constant k_{ex} was measured as a function of the water content W , the AOT concentration, temperature, and the bulk solvent type. The results from their study reveal that k_{ex} decreases with increasing water content for $W = 10, 15, 20, \text{ and } 30$; k_{ex} is independent of AOT and reactant concentration; k_{ex} increases with an increase in temperature; and k_{ex} increases slightly with carbon number of the bulk solvent for pentane through dodecane in addition to a significant decrease in k_{ex} for the corresponding cyclic compounds, particularly cyclohexane. The dependency of k_{ex} on the bulk solvent can be explained by the solvent interactions with the AOT tails where a more favorable interaction will allow for the solvent to insert itself within the surfactant tails thus creating a more rigid micelle. Binks et al.⁹ discuss the

extent of oil penetration into the surfactant chain region, showing an increase in micelle rigidity with decreasing solvent chain length from C_{14} to C_7 . Studies on particle formation have shown that underlying properties of the AOT reverse micelle system resulting from the water content, dissolved salt, and interactions between the bulk solvent and AOT surfactant tails significantly effect the particle growth rate and the particle sizes obtained^{7,13-17}. The thermophysical properties which determine the overall stability of the reverse micelle have been determined by a variety of techniques including phase behavior and conductivity measurements to determine the CMC, maximum W value, and percolation threshold. These values can be used to determine the relative microemulsion stability and rigidity of the reverse micelles with respect to the adjustments in the bulk fluid, water content, temperature, surfactant and salt concentration. The microemulsion stability and reverse micelle rigidity have been used to explain the results observed from metallic nanoparticle growth studies within the AOT reverse micelle system and the general consensus is that a more stable microemulsion and a more rigid reverse micelle, results in the formation of larger nanoparticles at slower reaction rates^{7,10,14-16,18,19}.

Pioneering work by Lisiecki and Pileni¹² on the production of copper nanoparticles in the AOT reverse micelle system established synthesis methods via reduction of Cu^{2+} ions within the micelle cores. Two methods were used to introduce the Cu^{2+} ions into the reverse micelles; 1) Replacing the Na^+ ion of AOT to form $Cu(AOT)_2$ thereby functionalizing the AOT surfactant and 2) dissolving a copper salt (eg. Copper nitrate) within the aqueous micelle core. In Lisiecki and Pileni's work, it was noted that the bulk solvent and W value have a significant effect on metallic nanoparticle

production. In addition, a direct relationship between the size of copper nanoparticles in solution and the UV-Vis absorption spectra was used to indirectly determine the copper nanoparticles diameter. Spherical copper nanoparticle dispersions have a characteristic absorption band centered at 566 nm. The ratio of the absorbance at 566 nm and the absorbance off the peak at 500 nm (Abs_{566}/Abs_{500}) was correlated directly to the average particle diameter measured by TEM imaging techniques using the relation mentioned previously. This proves to be invaluable for the in-situ measurement of the copper nanoparticle diameter and thus allows time resolved absorption measurements to be used to study the growth of the copper particles over time. From this absorption ratio we are able to perform a kinetic analysis on the particle synthesis and obtain the particle growth rates as well as the ultimate particle size obtained. Related in-situ time resolved absorption studies have been done to study the kinetics of nanoparticle synthesis within AOT reverse micelle systems including Ag, Co, CdS and ZnS particles^{7,10,11,14-16,20,21}. In this chapter, investigations of particle growth rates and the ultimate particle size obtained will reveal the effects of solvent properties, water content, and the presence of dissolved salt within the aqueous core on the synthesis of copper nanoparticles in the AOT reverse micellar system.

2-2. EXPERIMENTAL

2-2a. Materials

Sodium bis(2-ethylhexyl) sulfosuccinate (AOT) and DIUF Water were obtained from Fisher Scientific and used without further purification. Anhydrous Hydrazine 98%, Isooctane, and other alkane solvents were purchased from Sigma Aldrich. The alkane

solvents were stored over molecular sieves to remove any dissolved water. Copper AOT (CuAOT_2) was synthesized by two separate methods published previously^{12,19} where the sodium ion of the AOT head group was replaced by a Cu^{2+} ion to create the functionalized surfactant. The synthesis details are discussed in appendix A, where two different synthesis approaches are taken into consideration. The first method was originally used by Pileni and coworkers where ion exchange resins were implemented to replace the sodium ion with the desired metal ion starting material such as Cu^{2+} or Ag^+ . This method was also implemented by Cason et al. in the work from the Roberts lab that preceded this research. The second method was used by Eastoe et al. where the natural ion selectivity affords the displacement of the sodium ion with other metal ions. Comparison of the two methods are discussed in appendix A revealing the Eastoe method as the better synthesis technique due to ease of synthesis and improved Na conversion.

2-2b. Particle Synthesis

The methods for the synthesis of copper nanoparticles via $\text{Cu}(\text{AOT})_2$ and $\text{Cu}(\text{NO}_3)_2$ reduction using hydrazine within a liquid phase AOT reverse micelle system is discussed in detail in appendix A. For synthesis using CuAOT_2 , the bulk liquid alkane solvents investigated included pentane, hexane, heptane, octane, decane, dodecane, isooctane, and cyclohexane. AOT and $\text{Cu}(\text{AOT})_2$ were added in a 10 to 1 ratio at concentrations of 1.1×10^{-1} M and 1.1×10^{-2} M, respectively. W values ($[\text{H}_2\text{O}]/[\text{AOT}]$) ranging from 3 to 15 were examined with isooctane as the bulk solvent and W values of 5 and 10 were examined in the other solvents. Solutions were sonicated and purged with

nitrogen to remove oxygen from the system in order to prevent the formation of copper oxide. The solutions were then allowed to equilibrate after which the hydrazine reducing agent was injected through a rubber septum at a concentration three times the copper concentration. Upon reduction the solutions would go through a distinct color change from a light blue to a dark blue and then to a brownish color due to the reduction of Cu^{2+} to Cu^0 . This initial reduction is followed by a progressive color change to a deep red wine color resulting from the growth of copper nanoparticles through the intermicellar exchange process over the course of a few hours. This final color transition is monitored using the time resolved UV-Vis absorbance measurements.

Copper nanoparticle synthesis using $\text{Cu}(\text{NO}_3)_2$ as the metal ion source was achieved in a method similar to the use of $\text{Cu}(\text{AOT})_2$ mentioned previously. The desired concentration of AOT was dissolved in the bulk alkane followed by the addition of 1.0 M $\text{Cu}(\text{NO}_3)_2$ aqueous solution and additional water to achieve the desired copper concentration and W value. The bulk alkane solvents used include hexane, isooctane, decane and cyclohexane with concentrations of 0.011 M $\text{Cu}(\text{NO}_3)_2$ and 0.133 M AOT and with W values of 5 and 10. For cyclohexane as a bulk solvent the previous concentrations would not form a single phase microemulsion due to the effects of the salt, thus concentrations of 5.5×10^{-3} M $\text{Cu}(\text{NO}_3)_2$ and 0.265 M AOT were used with W values of 5 and 10.

A Varian, Cary 300 UV-Vis spectrophotometer was used to record the time resolved absorbance measurements as the reaction proceeded. The Cary spectrophotometer was set up to take time incremented scans over the wavelength range

from 800 nm to 200 nm throughout the extent of the experiment. The data file obtained from the Cary spectrophotometer was then processed to extract the absorbance values at 566 nm and 500 nm and plot the ratio of the two absorbance values. The absorbance ratio can then be related to the copper particle size in solution by the relation discussed earlier. Processing the data obtained from the Cary proved to be a redundant, time intensive task and thus an Excel VBA program was written to automatically process the data (Program is available upon request and detailed in the preliminary dissertation). The spectra obtained from the Cary is accurate and precise, however there is a minimum time increment of approximately 2 minutes with the desired accuracy due to a progressive scan of the wavelength spectrum. In order to obtain absorbance measurements on a much faster time scale a different spectrometer must be used. This second spectrometer is an Ocean Optics UV-Vis fiber optic dual spectrometer, capable of recording UV-Vis absorbance measurements in the range of 785 nm to 176 nm with 0.2 nm resolution on a millisecond time scale. This is done with the use of a diode array and diffraction gratings where the entire spectrum is recorded at once rather than performing a scan of the wavelength spectra. One disadvantage is that for time resolved measurements, the software package saves each spectrum in a separate file. To alleviate this problem, an Excel VBA program was written to compile and reduce the data into a single file as well as extract the absorbance ratio necessary to track the in situ copper particle growth. Details on the spectrometer can be found in appendix C and the program code is available upon request and detailed in the preliminary dissertation. The use of the dual spectrometer which acts to divide the spectrum in half, affords increased accuracy

approaching that of the Cary. The millisecond time scale and fiber optic design affords a versatile instrument capable of diverse applications, especially for high pressure supercritical research. For this portion of the research, the Ocean Optics spectrometer was used for some of the particle synthesis reactions and shown to be just as capable as the Cary instrument.

Particle images were obtained using a Zeiss EM 10 Transmission Electron microscope (TEM). The particles were collected by placing a droplet of the solution on a nickel TEM grid. An alternate particle collection technique was also implemented where the liquid sample was sprayed onto the TEM grid using a Pelco all-glass nebulizer obtained from Ted Pella Inc. This method proved effective in providing more even surface coverage and the absence of excess surfactant and any potential wetting effects. The presence of excess AOT surfactant severely inhibited TEM analysis and thus several attempts were made to develop a method to extract the AOT surfactant. The most effective method involved the introduction of a particle stabilizing agent such as dodecylamine followed by a liquid – liquid extraction of the AOT with a 20 to 50 percent ethanol / water solution. This method is discussed in further detail in Chapters 6 and 7.

2-3. RESULTS AND DISCUSSION

The formation of copper nanoparticles within the AOT reverse micelle system was monitored in-situ using time resolved UV-Vis absorption measurements. The relative growth rates and maximum particle sizes are obtained from these absorbance measurements using relationships established for the absorbance ratio (Ab_{S566}/Ab_{S500}) versus particle size developed by Lisiecki and Pileni¹². This chapter presents an

investigation of the effects of bulk solvent type and water content, W , on the particle growth rate and maximum particle size in conventional liquids. The relative growth rate is determined from the initial 3 to 4 hours of particle growth obtained from a plot of Abs_{566}/Abs_{500} as a function of time, shown in Figure 2-1 through 2-3. Quantitative representation of the relative particle growth rates based on the absorption measurements are listed in Table 2-1 and Table 2-2. The relative growth rates are determined by the slope of the particle size vs. time plots, where the particle sizes are obtained from the Abs_{566}/Abs_{500} by the relation mentioned previously. The slope was determined by a linear regression analysis of multiple experimental growth curves for each of the bulk solvents and W values. How well the regression analysis fits the particle growth curves is represented by an R^2 value. The error in the particle growth rate represented by the slope is determined from a 95% confidence interval calculated by twice the standard error obtained from the regression analysis. Details of the regression analysis are located in appendix B. The maximum particle size is obtained from the maximum absorbance ratio (Abs_{566}/Abs_{500}) observed throughout each experiment.

2-3a. Solvent Effects on Copper Nanoparticle Synthesis

Figure 2-1 is a plot of the absorbance ratio (Abs_{566}/Abs_{500}) measured as a function of time where each curve represents an average of 2 to 10 particle growth measurements in each solvent for synthesis via $Cu(AOT)_2$ reduction within the reverse micelle system with $W = 5$ (only the results from the even carbon number solvents are shown for clarity). In analyzing the particle growth curves in each liquid solvent, the particle growth in

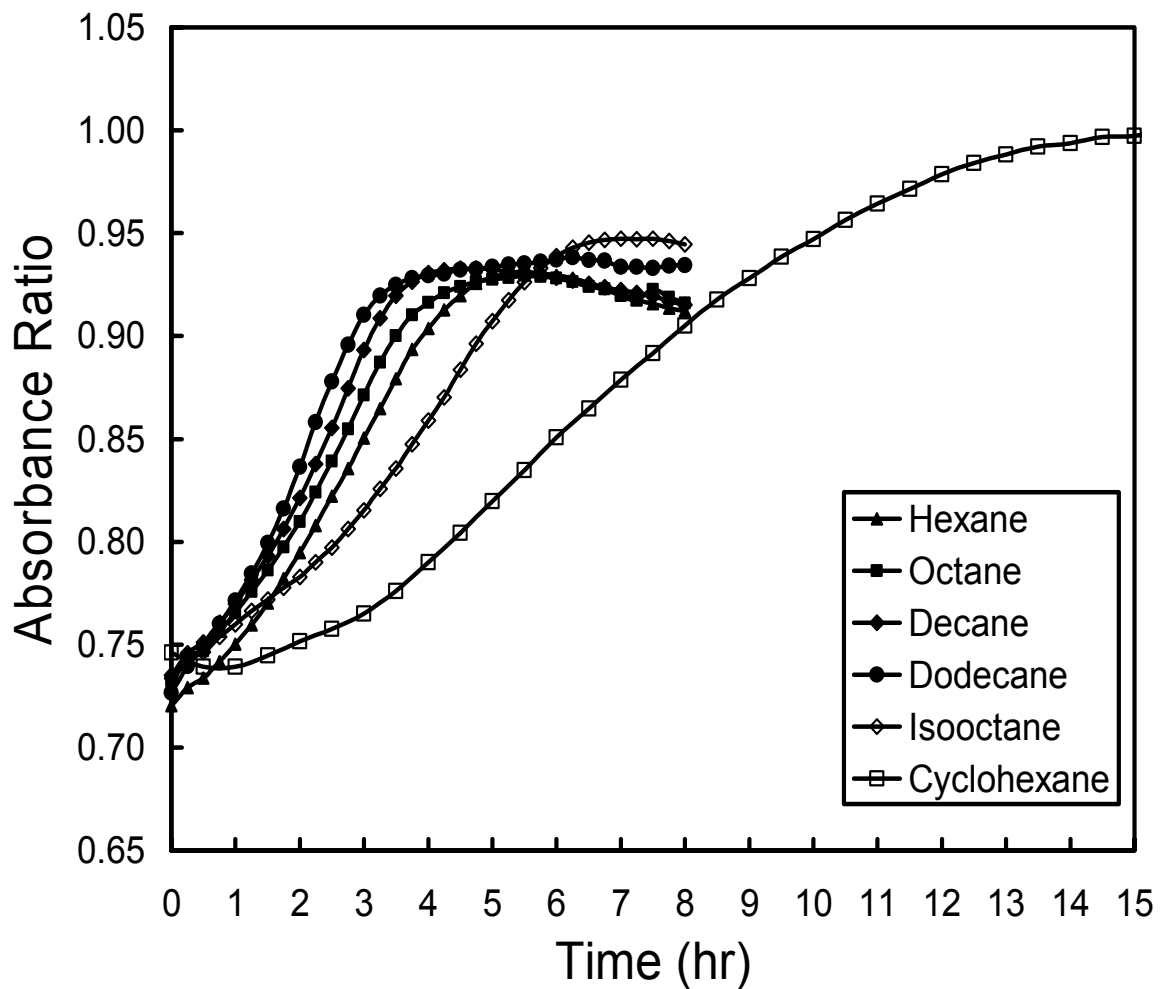


Figure 2-1. Copper nanoparticle growth curves measured in-situ by plotting the UV-vis absorbance ratio (Abs_{500}/Abs_{566}) as a function of time using various alkane bulk solvents with $W = 5$, $[AOT] = 0.1106$ M, $[CuAOT_2] = 0.01106$ M, $N_2H_4 = 3 \times [Cu]$. The even carbon number alkanes are shown for clarity.

Table 2-1. Experimental results of the relative particle growth rates and ultimate particle sizes obtained for Copper nanoparticles synthesized in various alkane bulk solvents with $[\text{CuAOT}_2] = 0.01106 \text{ M}$, $[\text{AOT}] = 0.1106 \text{ M}$ and $W = 5$ and 10 .

Solvent	W = 5			W = 10		
	Size (nm)	Slope \pm 95%	R ² (%)	Size (nm)	Slope \pm 95%	R ² (%)
Pentane	8.3	1.74 \pm 0.14	93.4	8.6	1.16 \pm 0.08	90.5
Hexane	8.6	1.62 \pm 0.17	81.4	8.9	1.87 \pm 0.20	91.4
Heptane	8.6	1.36 \pm 0.13	72.4	8.6	1.44 \pm 0.08	96.7
Octane	8.5	1.96 \pm 0.15	92.0	8.4	1.39 \pm 0.10	93.3
Decane	9.1	1.77 \pm 0.17	84.5	8.9	1.85 \pm 0.12	94.0
Dodecane	9.0	2.00 \pm 0.19	87.6	9.7	2.31 \pm 0.49	36.4
Isooctane	9.4	1.25 \pm 0.10	86.5	9.6	2.11 \pm 0.18	97.8
Cyclohexane	12.6	1.09 \pm 0.27	59.6	12.6	1.55 \pm 0.38	76.1

Table 2-2. Experimental results of the relative particle growth rates and ultimate particle sizes obtained for Copper nanoparticles synthesized in an isooctane reverse micelle system with $[\text{CuAOT}_2] = 0.01106 \text{ M}$ and $[\text{AOT}] = 0.1106 \text{ M}$ for W values ranging from 3 to 15.

Isooctane	Diameter (nm)	Slope \pm 95%	R² (%)
W = 3	10.5	0.14 ± 0.03	79.9
W = 5	9.4	1.25 ± 0.10	86.4
W = 6.5	9.1	1.91 ± 0.24	88.8
W = 8	9.7	2.23 ± 0.18	93.5
W = 10	9.6	2.11 ± 0.18	94.9
W = 12	10.7	2.35 ± 0.18	96.0
W = 15	10.8	1.64 ± 0.17	92.7

isooctane and cyclohexane is slower than all of the straight chain hydrocarbons at a water content of 5. Figure 2-1 illustrates that for the n- alkane solvents there is only a very slight increasing trend in the growth rate with an increase in carbon number. Similar results are observed for the maximum particle sizes obtained in each solvent as shown in Table 2-1. The maximum particle size shows a general increase in particle size as the carbon chain increases in length with a maximum size of 8.3 nm in pentane and a maximum size of 9.0 nm in dodecane. Larger particle sizes were obtained in both isooctane (9.4 nm) and cyclohexane (12.6 nm) solvents compared to all of the n-alkane solvents. This suggests that growth rate and particle size are inversely related where a decrease in growth rate corresponds to a larger maximum particle size at a specific W value. Increased interaction between the solvent and the surfactant tails results in a more stable micelle system and an enhanced ability to stabilize larger particles while reducing the intermicellar exchange.

Previous investigations by other researchers on the effects of the bulk alkane solvent on the AOT reverse micelle system have produced results that support these findings^{2,4,9,16}. Considerable work has been done to gain a better understanding of CdS nanocrystal growth where Towey states that particle formation is controlled to an extent by the nature of the continuous phase, where the growth rate increases from cyclohexane to n-heptane to n-decane⁷. Bagwe demonstrated with the production of silver and silver chloride particles that an increased intermicellar exchange rate has the effect to increase the growth rate and more importantly decrease the final particle size^{16,17}. These results are explained by the solvent-tail interactions or more generally, a decrease in the rigidity

of the micelle. Additional supporting evidence may be available on the bulk solvent effect on the AOT reverse micelle CMC, maximum water uptake and the percolation limit to support the trends observed for microemulsion stability and micelle rigidity.

2-3b. Water Content Effect on Copper Nanoparticle Synthesis

Also of interest is the influence of W on the particle growth rate and maximum particle size for particles synthesized via $\text{Cu}(\text{AOT})_2$ reduction. Figure 2-2 represents the particle growth curves for the same alkane solvents as in Figure 2-1 with an increased $W = 10$. An interesting observation from this figure is that there is essentially no influence of the solvent on the particle growth rate within the experimental error at the increased water content value of 10. Previous studies¹⁸ of copper particle growth as a function of bulk solvent type have demonstrated that the particle growth rate increases with increasing W from 5 to 10 in both isooctane and cyclohexane solvents. Additionally, Figure 2-2 and Table 2-1 show that the influence of W on the final particle size obtained is negligible. This shows that even though W influences the intermicellar exchange it is not the controlling factor for the maximum particle size obtained given sufficient reaction time. The solvent and its interaction with the surfactant tails, however, is a contributing factor for the stabilization of particles in solution and the maximum particle size obtainable. These results suggest a lesser effect of solvent chain length on the growth rate and the ultimate particle size for n-alkane solvents when compared to isooctane or cyclohexane. For the cyclohexane and isooctane solvents, it has been suggested that the solvent molecules will pack within the surfactant tails creating a more rigid micelle and

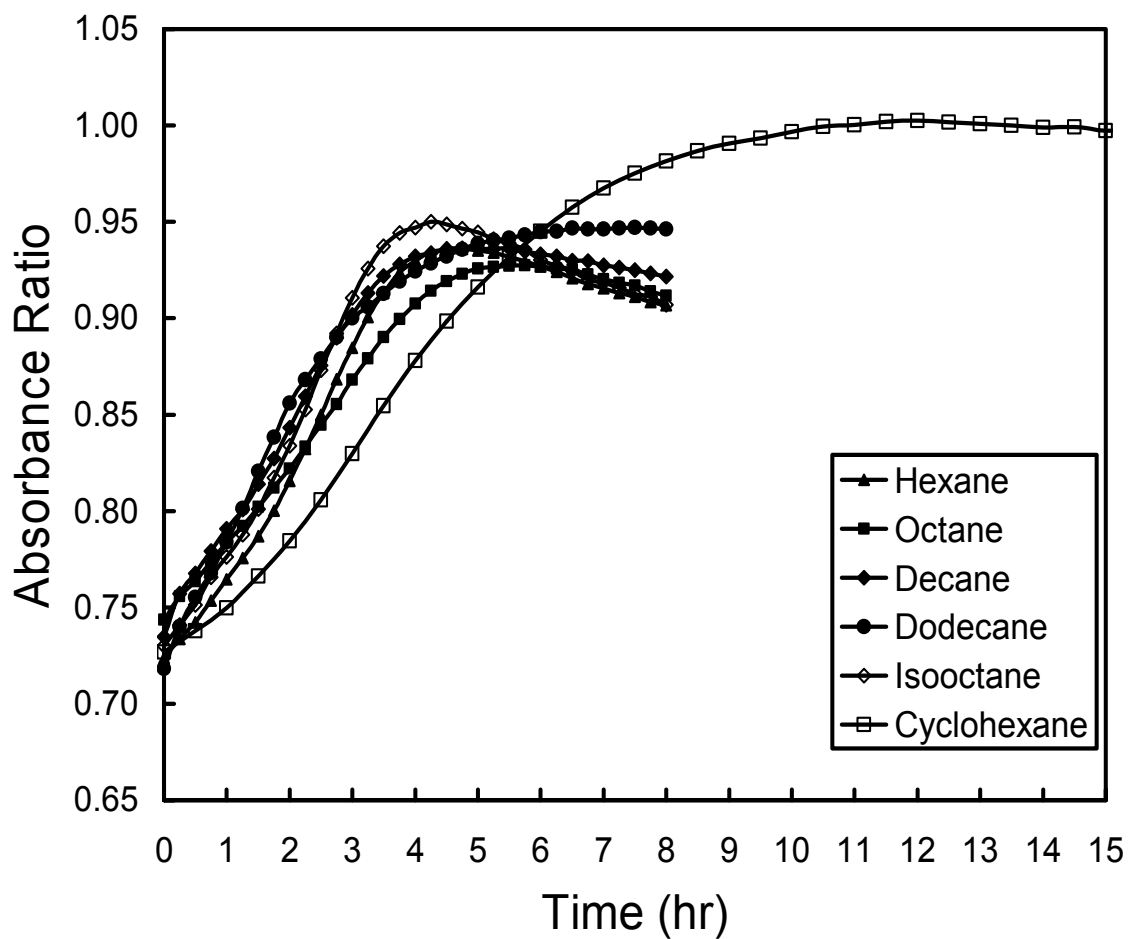


Figure 2-2. Cu nanoparticle growth curves measured in-situ by (Abs_{500}/Abs_{566}) as a function of time using various alkane bulk solvents with $W = 10$, $[AOT] = 0.1106$ M, $[CuAOT_2] = 0.01106$ M, $N_2H_4 = 3 \times [Cu]$. The even carbon number alkanes are shown for clarity.

thus retarding the intermicellar exchange¹⁷.

Further investigation of W on copper nanoparticle synthesis is shown in Figure 2-3 in the range of $W = 3$ to 15 for the isooctane/water/AOT system. Table 2-2 demonstrates that the particle growth rate goes through a maximum at approximately $W = 12$. The role of the water content in particle growth is of particular interest in the intermicellar exchange process and has been studied in several systems^{6,7,10,15,17,18}. A similar maximum was presented by Atik and Thomas² where for low W values (for $W = 5.5$ to 11), an increase in water content leads to a decrease in the rigidity of the water region which in turn leads to a more rapid reaction rate. Continued increase of the water content, above $W = 11$, leads to a decrease in the reaction rate which was explained by Atik and Thomas through a decrease in local concentration of the reactants in the larger water cores. These trends observed for the reaction rate lead to a maximum in the intermicellar exchange rate as a function of the W value which corresponds to the particle growth rates observed in this study, a maximum at $W = 12$.

At low W values the water has been shown to hydrate the polar head group of the surfactants and is considered bound water. This provides a rigid water environment², and differs significantly from a bulk water environment. Experimental instances where an increase in particle growth rate with increasing water content at low W values has been presented for AgCl ¹⁷, CdS and ZnS ¹⁵ nanoparticle formation which is attributed to the dynamics of the water environment and the intermicellar exchange rate of the reverse micelles. With an increase in W , ~ 10 , the water core becomes free from the binding

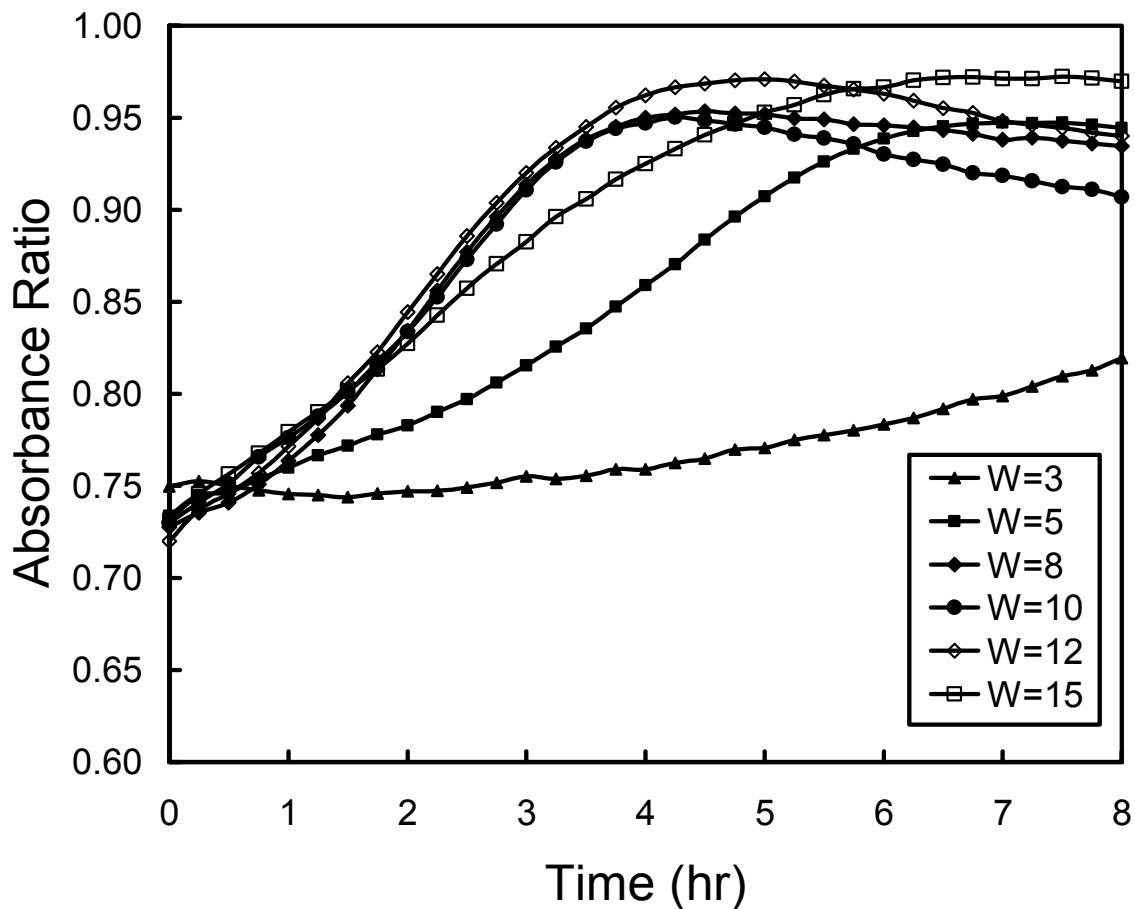


Figure 2-3. Cu nanoparticle growth curves measured in-situ by (Abs_{500}/Abs_{566}) as a function of time using an isooctane bulk solvent and adjusting the W value with $[AOT] = 0.1106 \text{ M}$, $[CuAOT_2] = 0.01106 \text{ M}$, $N_2H_4 = 3 \times [Cu]$.

head groups but still differs from bulk water and is considered to be intermediate water. As a result, the rigidity of the water decreases and an increase in reaction rate is observed. For larger W , ~ 20 , a bulk water environment appears and a decrease in intermicellar exchange is observed with increasing water content although, not as dramatic effect as for lower W values. The decrease in intermicellar exchange rate at larger W values has been observed in a variety of systems^{2,4,5} including the work previously mentioned by Atik and Thomas². Several explanations for decrease in intermicellar exchange at larger W values have been presented. In particular, Fletcher et al.⁴ explained the decreasing exchange rate for W values greater than 10 by an increase in the apparent activation energies for micelle exchange. This is associated with instances of structural states with interfacial regions of unfavorable surfactant film curvature in the range of W from 10 to 30. More recently, investigations by Goto and coworkers have examined the isooctane / AOT / water reverse micellar system and have found that at low W (~ 2), the mobility of the water is significantly suppressed. It was also observed that at $W > 10$ there is an onset of the formation of loose aggregates of reverse micelles which is termed flocculation. The flocculation was shown to precede the onset of percolation which has been observed at higher AOT and water concentrations having the effect of forming more rigid and larger network structure of reverse micellar solutions.

While the growth rate of copper nanoparticles is influenced by the water content, there is no noticeable effect of W on the ultimate particle size obtained in a given solvent. In fact, 10 nm diameter particles are obtained from 3 – 4 nm diameter reverse micelles for a $W = 10$ (reverse micelle radius $r(\text{\AA}) = 1.8 W$) suggesting that the ultimate particle

size is not controlled simply by a micelle core templating effect. This supports a theory that the surfactant has multiple functionalities in the particle growth and stabilization process. Initially the surfactant provides an initiation site, the micelle core, for the reduction of the metal followed by particle growth through intermicellar exchange, and at the latter end of the particle growth the surfactant acts as a stabilizing ligand with a weak interaction energy between the metal particle and the surfactant head group. The results from the isooctane system, shown in Table 2-2 and Figure 2-3, display that given enough reaction time, W has negligible effect on the maximum particle size. This suggests that the surfactant and bulk solvent, rather than W, influence the ultimate copper nanoparticle size obtained. These results will be explained below in terms of steric stabilization of the particles in a given solvent/surfactant system. This approach may provide insight as to whether the micelle core truly provides a template for particle growth or if steric stabilization controls the maximum particle size.

2-3c. Salt Effect on Copper Nanoparticle Synthesis

The presence of various salts within microemulsion phases for metallic nanoparticle synthesis has shown to influence the formation of interesting geometries including nanocubes, nanorods, and nanoplates with defined lattice structures²²⁻³⁰. The effects of salts and ionic species addition to a reverse micelle microemulsion formed with an ionic surfactant can be profound. For the anionic AOT surfactant, the presence of the additional ionic species in the micelle core can have a screening effect, reducing the electrostatic repulsion between head groups thus reducing the effective head group area

and increasing the critical packing parameter. For reverse micelles, this increase will increase the monolayer curvature thus forming a smaller micelle. Similarly, salts in reverse micelles have been termed dewatering agents where an exponential decrease in reverse micelle diameter is observed with the addition of salt with no effect on the micelle rigidity³¹. Additional studies by Liu et al. on the AOT reverse micelle system with the addition of NaCl have shown that with the addition of small amounts of salt, the maximum amount of water that can be supported decreases dramatically³². It was also shown that the percolation temperature decreases with the addition of NaCl, demonstrating a less stable microemulsion. The addition of ionic salt species to the anionic AOT surfactant reverse micelle would be expected to influence microemulsion properties due to local interactions with surfactant headgroups. Furthermore, with the addition of metallic nanoparticles which have surfaces inductive to ionic interactions, the effect of various ionic species on nanoparticle synthesis and micelle dynamics becomes interesting. Chapter 6 discusses in greater detail the addition of Cl⁻ to copper nanoparticle synthesis.

From the research published it is evident that the presence of salts in the reverse micelle cores can dramatically affect the thermophysical properties and the extent is dependant on the type of ions and the concentrations. In general terms, the salt cation influences the micelle water uptake as well as the micelle geometry. Due to ion selectivity, certain cations in solution will exchange with the head group cation. In the case of an AOT reverse micelle system with copper nitrate dissolved in the aqueous core, the Cu²⁺ ion will preferentially replace the Na⁺ ion of the AOT surfactant while in

solution. The salt anions play an important role in influencing the size and shape of nanoparticles synthesized where the most dramatic effects are seen with the chloride ion, discussed in Chapter 6.

The experimental results plotted in Figure 2-4a. demonstrate copper particle synthesis in AOT reverse micelle solutions with hexane and isooctane as the bulk solutions and W values of 5 and 10. The copper precursor used here is copper nitrate salt, $[\text{Cu}(\text{NO}_3)_2] = 0.011 \text{ M}$, which is dissolved within the water core and the AOT concentration of 0.133 M used is comparable to the previous result where $\text{Cu}(\text{AOT})_2$ was used. The growth curves from Figure 2-4 and the relative growth rates in Table 2-3, it can be determined that the particle growth rate is increased by at least a factor of 2 when compared to the $\text{Cu}(\text{AOT})_2$ results. The particle sizes obtained from the $\text{Cu}(\text{NO}_3)_2$ reduction are also smaller compared to the results from $\text{Cu}(\text{AOT})_2$ reduction, however similar trends in the particle size are observed with respect to the bulk solvent type with a larger particle size resulting from synthesis in the isooctane bulk phase. Another significant observation that parallels the previous results is the lack of significant influence of the W value on the copper particle sizes. These results lead to the conclusion that the mechanism for copper particle synthesis via $\text{Cu}(\text{NO}_3)_2$ reduction is similar to the mechanism of synthesis via $\text{Cu}(\text{AOT})_2$ reduction with the exception that the presence of the salt leads to faster growth rates and smaller particles. Thus it can be inferred that the presence of the salt decreases the stability of the microemulsion. Further evidence of the decreased stability lies in the attempt to synthesize copper particles with the same AOT and copper salt concentrations using cyclohexane and decane as the bulk

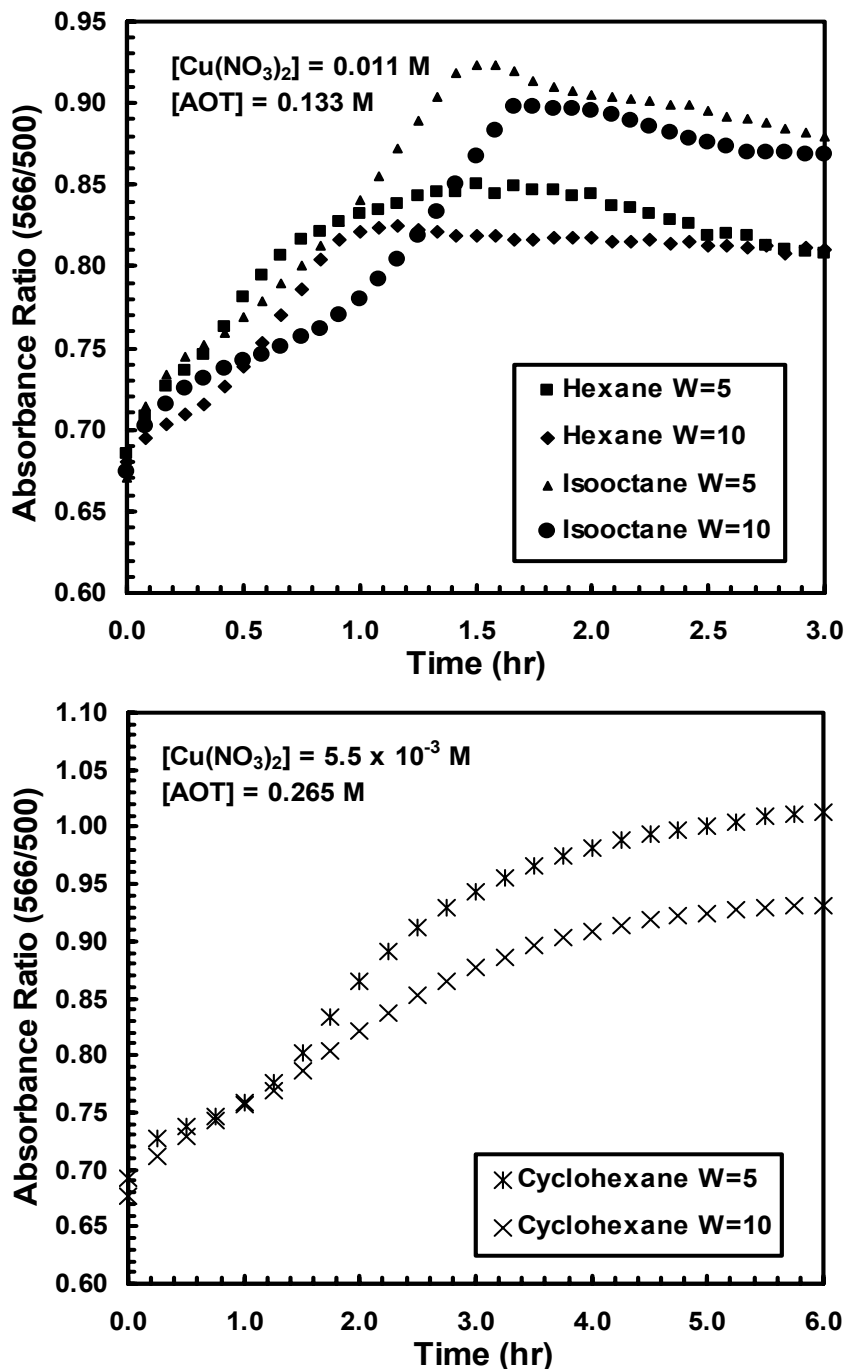


Figure 2-4. Cu nanoparticle growth curves measured in-situ by (Abs_{566}/Abs_{500}) as a function of time through the reduction of $Cu(NO_3)_2$ dissolved in AOT reverse micelle cores with W values of 5 and 10. a) Hexane and isooctane as the bulk alkane solvent and concentrations of AOT = 0.133 M, $Cu(NO_3)_2$ = 0.011 M, and $N_2H_4 = 3 \times [Cu]$. b) Cyclohexane as the bulk alkane solvent and concentrations of AOT = 0.265 M, $Cu(NO_3)_2 = 5.5 \times 10^{-3}$ M, and $N_2H_4 = 3 \times [Cu]$.

Table 2-3. Experimental results of the relative particle growth rates, maximum absorbance ratio and ultimate particle size obtained for copper nanoparticles synthesized in AOT reverse micelles by the reduction of $\text{Cu}(\text{NO}_3)_2$ salt.

Solvent	W = 5				W = 10			
	Growth ± Error	R ² (%)	Max Ratio	Max Size	Growth ± Error	R ² (%)	Max Ratio	Max Size
Hexane	3.6 ± 0.5	86.4	0.85	5.07	3.1 ± 0.3	93.2	0.83	4.19
Decane	--				--			
Isooctane	4.7 ± 0.3	93.3	0.92	8.21	2.6 ± 0.4	86.0	0.90	7.00
Cyclohexane*	1.3 ± 0.3	82.1	1.03	14.17	1.3 ± 0.2	92.3	0.94	8.86

*Max Ratio and Size may be influenced the formation of a larger network of particles and surfactant

phase. For the case of decane as the bulk solvent and the concentrations from above, a stable microemulsion was achieved, however upon reduction the characteristic color change was observed followed by extensive copper plating and precipitation. The experimental growth curves and particle size was unattainable. For the case of cyclohexane as the bulk solvent with the $\text{Cu}(\text{NO}_3)_2$ concentration of 0.011 M the AOT concentration of 0.133 M at W values of 5 and 10, a stable microemulsion was never achieved. In order to form a stable microemulsion the concentrations of $\text{Cu}(\text{NO}_3)_2$ and AOT were adjusted to 5.5×10^{-3} M and 0.265 M respectively. Figure 2-4b. displays the particle growth curves obtained using this system. Analyzing the results, typical absorbance measurements were observed for the initial portion of the synthesis reaction but after the first 1.5 hours, the characteristic copper peak centered at 566 nm began to shift gradually towards a wavelength of 600 nm and also the absorbance value increased dramatically in comparison to the previous cyclohexane results from the $\text{Cu}(\text{AOT})_2$ reduction. This absorbance and wavelength shift has been observed in the formation of copper rods and large interconnected networks of copper particles³³. The in situ UV-Vis absorbance measurements of the copper particle growths for the reduction of $\text{Cu}(\text{AOT})_2$ and $\text{Cu}(\text{NO}_3)_2$ are shown in Figure 2-5. Figure 2-6 is a TEM image of the interconnected network of copper particles synthesized by this method with $W = 5$. A nearly identical network of copper particles was obtained by Pileni through the reduction of copper dodecyl sulfate by NaBH_4 in a o/w microemulsion at concentrations above the CMC, and in this case changes in optical properties with size and shape of copper particle was also observed^{11,34}. The changes in optical properties create some error in the relationship of

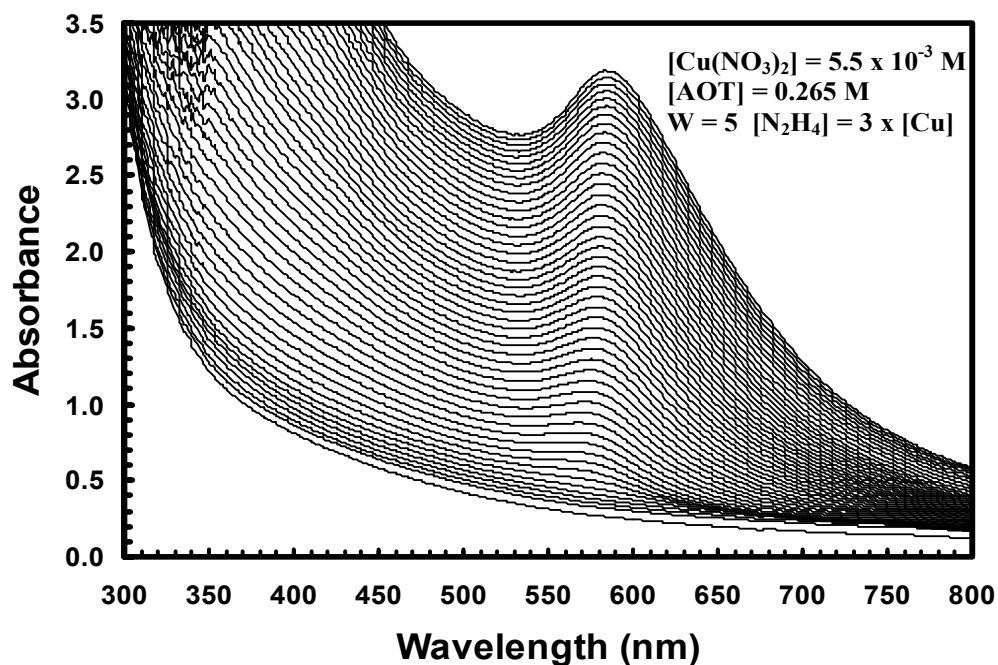
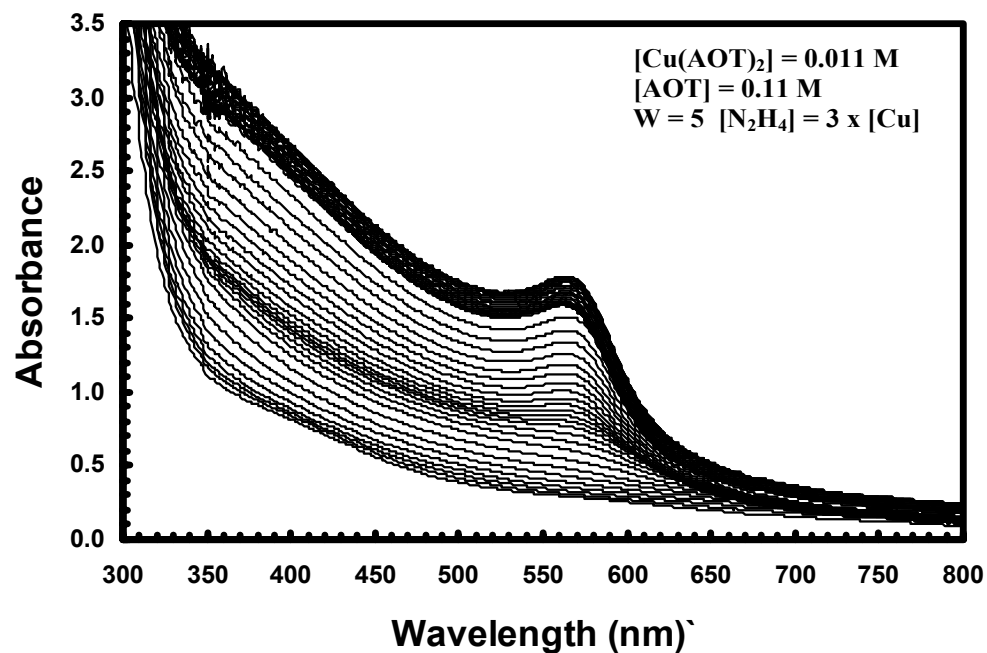


Figure 2-5. In Situ UV-Vis absorption measurements of copper nanoparticle growth in AOT/Cyclohexane reverse micelle system with $W = 5$. a) Particle synthesis via $\text{Cu}(\text{AOT})_2$ reduction with $[\text{AOT}] = 0.11 \text{ M}$, $[\text{Cu}(\text{AOT})_2] = 0.011 \text{ M}$ with each scan at 30 minute intervals. b) Particle synthesis via $\text{Cu}(\text{NO}_3)_2$ reduction with $[\text{AOT}] = 0.265 \text{ M}$, $[\text{Cu}(\text{NO}_3)_2] = 5.5 \times 10^{-3} \text{ M}$ with each scan at 15 minute intervals. The characteristic peak at 566 nm continues to grow and shifts slightly toward 600 nm with the formation of copper particle network.

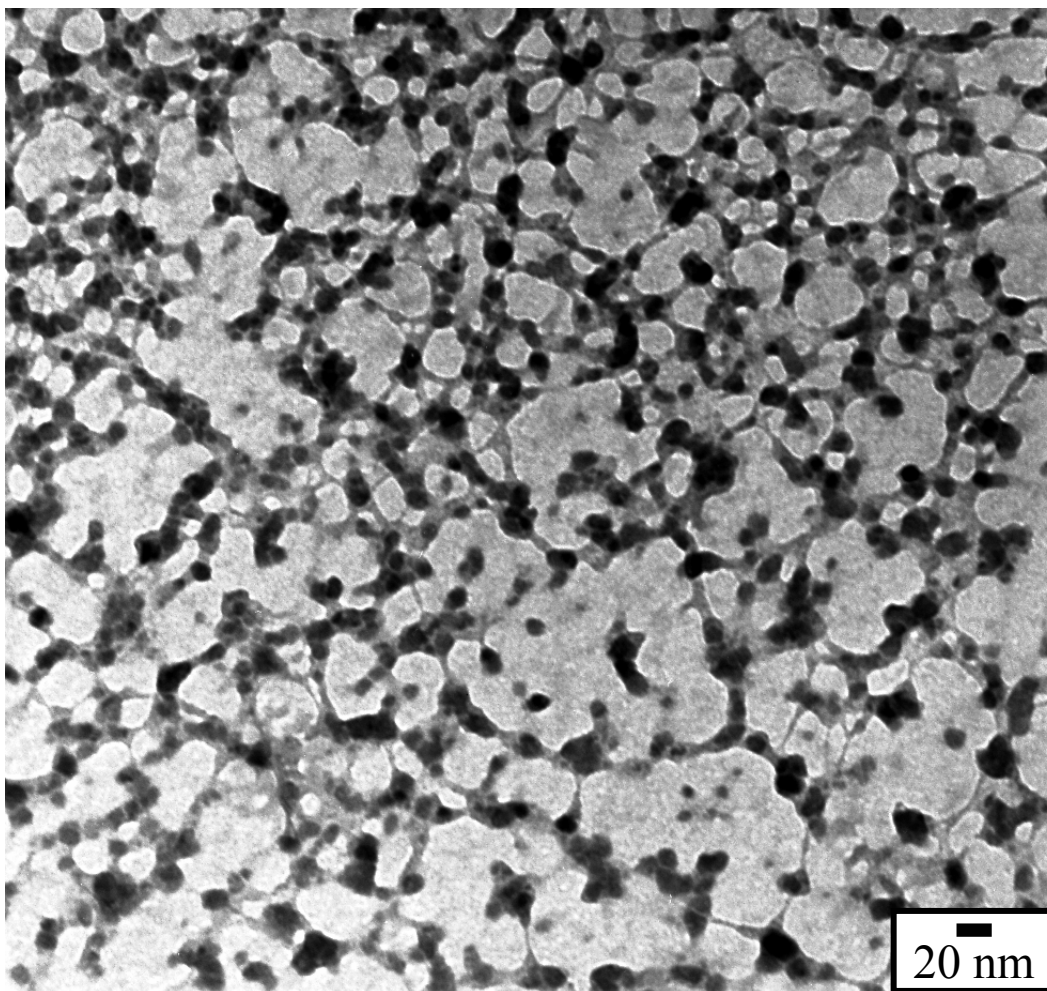


Figure 2-6. TEM image of copper nanoparticle network synthesized in an AOT reverse micelle system with cyclohexane as the bulk solvent, $[AOT] = 0.265 \text{ M}$ and $W = 5$. Copper particles were synthesized by reduction of $\text{Cu}(\text{NO}_3)_2$, $5.5 \times 10^{-3} \text{ M}$, using hydrazine, $[\text{N}_2\text{H}_4] = 3 \times [\text{Cu}]$.

the absorbance ratio and particle size and the error can be observed in the particle growth curves in Figure 2-4b and the values listed for cyclohexane in Table 2-3.

2-3d. Temperature Effect on Copper Nanoparticle Synthesis

The effect of temperature on copper nanoparticles synthesized within AOT reverse micelles is an interesting phenomenon, particularly in relation to microemulsion stability. Kinetic studies have shown that k_{ex} increases with increasing temperature which is consistent with most rate constants⁴. Factors contributing to the increased k_{ex} include typical effects such as increased diffusion and reaction rate, but more importantly is the effect on the physical properties of the reverse micelles. Temperature changes have the effect of altering the density and viscosity and adjusting the solvent strength which will affect the solvation of the surfactant tails within the bulk phase. Conductivity measurements have also demonstrated the increased presence of free water at higher temperatures³⁵. The overall result of increasing the temperature is the formation of a less rigid micelle and a decrease in the free energy barrier for the intermicellar process. Additional temperature effects include the increase in thermal fluctuations determined by the bending modulus of the surfactant monolayer resulting in deviations from the ideal spherical geometry. An increase in the ease of micelle deformation does not affect the micelle rigidity but would influence the intermicellar exchange process and thus k_{ex} .

Phase behavior studies have also shown that as the temperature increases, the amount of water that can be supported in the microemulsion, the maximum W value, decreases⁴. Other properties affected by temperature include aggregation, agglomeration

and the CMC, where the CMC increases with increasing temperature³⁶. Conductivity measurements have shown that barriers exist for the onset of flocculation and percolation where the transition from reverse micelles to a bicontinuous type network of spherical aggregates is approached as temperature increases^{35,36}. These transitions are determined by the thermodynamics of the system, particularly the bulk solvent properties and the interactions with the surfactant molecules and each supports a decrease in the microemulsion stability with an increase in temperature. These same interactions are responsible for the stability of the reverse micelle system which influences nanoparticle synthesis within the reverse micelle core. The effects of temperature on nanoparticle synthesis within the reverse micelle system mainly consist of faster reaction rates due to the reaction kinetics of the system. For the ultimate particle size obtained at higher temperatures a smaller average particle size would be expected due to the UCST and the decrease in the microemulsion stability. On the other hand, increased tail solvation and solvent penetration into the tail region and could also lead to the formation of a more rigid micelle allowing for larger particles. Increased agglomeration may also effect the particle sizes where a larger particle size distribution would be expected as well as the presence of larger particle aggregates. Overall, no noticeable effects of temperature on the particle size were observed and this will be discussed further in Chapters 3 and 4.

2-3e. Reducing Agent Effect on Copper Nanoparticle Synthesis

For the synthesis of copper nanoparticles in this research, hydrazine was used exclusively and it is assumed that an initial complete reduction occurs prior to particle

growth, which is observed by the solution color change mentioned earlier. Hydrazine has the advantages of effectively reducing metal ions and existing in the liquid phase for ease of introduction into the reverse micelle system. However it must be mentioned that the presence of water is required for the reduction reaction to proceed and thus the water concentration may influence the reduction reaction. Borohydride compounds have also been used as effective metal ion reducing agents, although they are solid compounds and must be suspended in a liquid phase. For the case of copper particles, sodium borohydride dispersed in water have proven to be concentration sensitive as well as disruptive to the microemulsion causing excessive metal plating and precipitation. Various borohydride derivatives and complexes dispersed in water and other polar solvents were investigated with minimal success. For copper nanoparticle synthesis within AOT reverse micelles, hydrazine was found to be the most effective reducing agent and it is thought that the hydrazine has little effect on particle synthesis and stabilization given enough water within the micelle core to promote the reduction reaction. For copper nanoparticle synthesis by alternate means, such as aqueous based synthesis and two phase methods, the borohydride reducing agents were effective.

2-3f. Effects of Surfactant / Cosurfactant Concentration

As discussed in Chapter 1, the concentration of surfactant within the microemulsion influences the morphology of the surfactant aggregates affording various geometries. The concentration envelope for the formation of reverse micelles exists above the CMC and below an upper critical solution concentration (UCSC). As the

surfactant concentration approaches the UCSC the formation of interesting networks of surfactant and nanoparticles as can be seen in Figure 2-6. Continued increase of the surfactant concentration can lead to the formation of cylindrical micelles as well as cylindrical nanorods²³. Variation in the surfactant concentration allows for interesting media for nanomaterial production. These conditions fall outside of the reverse micelle region on the ternary phase diagram and exceed the scope of this research.

The addition of cosolvents and cosurfactants has been shown to affect the stability of the reverse micelle system as well as the surfactant aggregate geometry. Cason et al. demonstrated the addition of octanol and benzyl alcohol cosurfactants and the effects on the growth rate of copper nanoparticles in AOT reverse micelles. Alterations in the growth rates were explained by the microemulsion stability and interactions at the micelle interface. Other researchers have demonstrated that with the addition of cosurfactants with molecular geometries of different critical packing parameters can adjust the geometry of the self assembled surfactant aggregates. This preferred geometry of the reverse micelle can then be transposed to the formation of nanoparticles of the same shape. For the case of pure $\text{Cu}(\text{AOT})_2$, Eastoe et al.³⁷ demonstrated that cylindrical micelles are the preferred geometry and in another study, Pileni et al. showed evidence of the formation of cylindrical copper nanorods with the addition of Cl^- ^{38,39}. Again the use of various cosolvents, cosurfactants, and other ionic directing species allows for the formation of interesting nanomaterials. For the application to this research the sole purpose is to demonstrate that the thermodynamic and physical properties of the reverse micelle system has a controlling effect over the

“bottom up“ synthesis of nanomaterials. The use of cosurfactants to create a more stable microemulsion for nanoparticle synthesis will be discussed in Chapter 4 with applications to compressed alkanes and supercritical fluid synthesis. Chapter 6 demonstrates the use of ionic species for the synthesis of directed particle geometries and assemblies.

2-4. STERIC STABILIZATION OF PARTICLES BY SURFACTANT

Various spectroscopy, scattering, and imaging techniques have been utilized to determine the geometry and structure of the micelles with a variety of surfactant systems. The surfactants act to stabilize the water core creating a minimum energy environment forming a most desirable geometry. In the same respect, particles formed in these systems are built from smaller particles down to the atomic level and the surfactants act to sterically stabilize the growing particle, conforming to a similar geometry. Depending on the strength of the solvent/tail interactions, the particles will continue to grow until they are no longer sterically stabilized thus allowing for particle sizes to exceed the size of the original micelle.

In some specific cases, researchers have found the sizes of particles synthesized in AOT reverse micelles can in fact correlate with the size of the reverse micelle core (core size is proportional to W). Examples include CdS, ZnS, AgCl and CdTe^{10,13,15,17,40,41}. However, in each of these cases, the particle sizes obtained rarely exceeded the size of the micelle core. The particles examined in these cases are not pure metals and it is possible that a weaker interaction between the particle surface and the ionic head group of the surfactant exists, thus inhibiting the steric stabilization of particles larger than the

micelle core. Sato et al.⁴⁰ demonstrated that the deposition of a Cd layer on the surfaces CdS particles synthesized within AOT reverse micelles was required in order to attach a thiol ligand for particle separation and imaging. Further evidence of interactions between the metallic nanoparticles and the ionic surfactant head groups will be explored throughout this dissertation, demonstrating the role of the AOT surfactant in the synthesis of metallic nanoparticles.

2-5. CONCLUSIONS

This chapter demonstrates the synthesis of copper nanoparticles via $\text{Cu}(\text{AOT})_2$ reduction within the AOT reverse micelle system. The bulk organic phase influences both the particle growth rate and ultimate particle size obtained. The size of the micelle, determined by W , significantly effects the particle growth rate, which goes through a maximum at $W = 12$, but given adequate reaction time, W does not have an effect on the ultimate particle size obtained. This leads to the conclusion that surfactant templating is not the particle size determining factor, but rather steric stabilization of the particles by the AOT surfactant is responsible for the particle size and geometry synthesized. Similar results with respect to the water content were observed for copper particle synthesis via $\text{Cu}(\text{NO}_3)_2$ reduction within the AOT reverse micelle system where there was no significant effect of the W value on the particle size. The same trends in bulk solvent effects were also seen for both copper reduction reactions where the hexane reaction was faster and yielded a smaller particle size. In the same respect, the copper particles synthesized via the copper salt reduction have a faster reaction rate and smaller particle sizes which is a result of the decreased stability of the microemulsion from the addition

of the salt ionic species. The results presented here effectively demonstrate that thermodynamic, kinetic and physical properties of the AOT reverse micelle system and the influence of each of its components has an influential effect on the synthesis of copper nanoparticles. Through a better understanding of these properties, future applications for the production of tailored particles with desired shape and size will be possible in reverse micellar microemulsion systems.

2-6. REFERENCES

- (1) Nave, S.; Eastoe, J.; Heenan, R. K.; Steytler, D.; Grillo, I. *Langmuir* 2000, 16, 8741-8748.
- (2) Atik, S. S.; Thomas, J. K. *Journal of the American Chemical Society* 1981, 103, 3543-3550.
- (3) Eicke, H. F.; Shepherd, J. C. W.; Steinemann, A. *Journal of Colloid and Interface Science* 1976, 56, 168-176.
- (4) Fletcher, P. D. I.; Howe, A. M.; Robinson, B. H. *Journal of the Chemical Society-Faraday Transactions I* 1987, 83, 985-1006.
- (5) Howe, A. M.; McDonald, J. A.; Robinson, B. H. *Journal of the Chemical Society-Faraday Transactions I* 1987, 83, 1007-1027.
- (6) Natarajan, U.; Handique, K.; Mehra, A.; Bellare, J. R.; Khilar, K. C. *Langmuir* 1996, 12, 2670-2678.
- (7) Towey, T. F.; Khanlodhi, A.; Robinson, B. H. *Journal of the Chemical Society-Faraday Transactions* 1990, 86, 3757-3762.
- (8) Tojo, C.; Blanco, M. C.; Rivadulla, F.; Lopez-Quintela, M. A. *Langmuir* 1997, 13, 1970-1977.
- (9) Binks, B. P.; Kellay, H.; Meunier, J. *Europhysics Letters* 1991, 16, 53-58.
- (10) Sato, H.; Hirai, T.; Komasaawa, I. *Industrial & Engineering Chemistry Research* 1995, 34, 2493-2498.
- (11) Pileni, M. P. *Langmuir* 1997, 13, 3266-3276.
- (12) Lisiecki, I.; Pileni, M. P. *Journal of Physical Chemistry* 1995, 99, 5077-5082.
- (13) Petit, C.; Lixon, P.; Pileni, M. P. *Journal of Physical Chemistry* 1990, 94, 1598-1603.
- (14) Hirai, T.; Tsubaki, Y.; Sato, H.; Komasaawa, I. *Journal of Chemical Engineering of Japan* 1995, 28, 468-473.
- (15) Hirai, T.; Sato, H.; Komasaawa, I. *Industrial & Engineering Chemistry Research* 1994, 33, 3262-3266.
- (16) Bagwe, R. P.; Khilar, K. C. *Langmuir* 2000, 16, 905-910.
- (17) Bagwe, R. P.; Khilar, K. C. *Langmuir* 1997, 13, 6432-6438.
- (18) Cason, J. P.; Miller, M. E.; Thompson, J. B.; Roberts, C. B. *Journal of Physical Chemistry B* 2001, 105, 2297-2302.
- (19) Eastoe, J.; Fragneto, G.; Robinson, B. H.; Towey, T. F.; Heenan, R. K.; Leng, F. J. *Journal of the Chemical Society-Faraday Transactions* 1992, 88, 461-471.
- (20) Cason, J. P.; Khambaswadkar, K.; Roberts, C. B. *Industrial & Engineering Chemistry Research* 2000, 39, 4749-4755.
- (21) Pileni, M. P.; Moumen, N.; Hochepped, J. F.; Bonville, P.; Veillet, P.

- Journal De Physique Iv* 1997, 7, 505-508.
- (22) Tanori, J.; Pileni, M. P. *Langmuir* 1997, 13, 639-646.
- (23) Pileni, M. P.; Gulik-Krzywicki, T.; Tanori, J.; Filankembo, A.; Dedieu, J. *C. Langmuir* 1998, 14, 7359-7363.
- (24) Filankembo, A.; Pileni, M. P. *Applied Surface Science* 2000, 164, 260-267.
- (25) Maillard, M.; Motte, L.; Pileni, M. P. *Advanced Materials* 2001, 13, 200-204.
- (26) Maillard, M.; Giorgio, S.; Pileni, M. P. *Journal of Physical Chemistry B* 2003, 107, 2466-2470.
- (27) Maillard, M.; Giorgio, S.; Pileni, M. P. *Advanced Materials* 2002, 14, 1084+.
- (28) Pinna, N.; Weiss, K.; Sack-Kongehl, H.; Vogel, W.; Urban, J.; Pileni, M. *P. Langmuir* 2001, 17, 7982-7987.
- (29) Sun, Y. G.; Xia, Y. N. *Science* 2002, 298, 2176-2179.
- (30) Sun, Y. A.; Xia, Y. N. *Advanced Materials* 2003, 15, 695-699.
- (31) Kellay, H.; Meunier, J.; Binks, B. P. *Physical Review Letters* 1993, 70, 1485-1488.
- (32) Liu, D. J.; Ma, J. M.; Cheng, H. M.; Zhao, Z. G. *Colloids and Surfaces a-Physicochemical and Engineering Aspects* 1998, 143, 59-68.
- (33) Creighton, J. A.; Eadon, D. G. *Journal of the Chemical Society-Faraday Transactions* 1991, 87, 3881-3891.
- (34) Lisiecki, I.; Billoudet, F.; Pileni, M. P. *Journal of Physical Chemistry* 1996, 100, 4160-4166.
- (35) Cheng, G. X.; Shen, F.; Yang, L. F.; Ma, L. R.; Tang, Y.; Yao, K. D.; Sun, P. C. *Materials Chemistry and Physics* 1998, 56, 97-101.
- (36) Moroi, Y. *Micelles : theoretical and applied aspects*; Plenum Press: New York, 1992.
- (37) Eastoe, J.; Towey, T. F.; Robinson, B. H.; Williams, J.; Heenan, R. K. *Journal of Physical Chemistry* 1993, 97, 1459-1463.
- (38) Pileni, M. P.; Ninham, B. W.; Gulik-Krzywicki, T.; Tanori, J.; Lisiecki, I.; Filankembo, A. *Advanced Materials* 1999, 11, 1358-1362.
- (39) Lisiecki, I.; Sack-Kongehl, H.; Weiss, K.; Urban, J.; Pileni, M. P. *Langmuir* 2000, 16, 8802-8806.
- (40) Sato, H.; Asaji, N.; Komasaawa, I. *Industrial & Engineering Chemistry Research* 2000, 39, 328-334.
- (41) Feltin, N.; Levy, L.; Ingert, D.; Pileni, M. P. *Journal of Physical Chemistry B* 1999, 103, 4-10.

CHAPTER 3

3. INTERACTION ENERGY MODEL FOR STERICALLY STABILIZED METALLIC NANOPARTICLES

3-1. INTRODUCTION

The thermophysical properties controlling the ultimate size and shape of particles synthesized within the reverse micelles remains an area of significant interest. One opinion that the reverse micelles act as a template for the production of particles has been suggested for nanoparticle synthesis in various geometries such as spheres and rods^{1,2}. For materials such as CdS, ZnS³, and AgCl⁴ it has been observed that the particle size corresponds to the size of the micelle. Time resolved studies on the formation of Cu nanoparticles by Cason et al.⁵, as well as the work presented in Chapter 2, has shown that given adequate reaction time, the ultimate particle size obtained in the AOT/Alkane reverse micelle system is independent of W, although the particle growth rate is a function of W and the bulk solvent type. This leads to a theory that the particle sizes obtained are largely controlled by solvent stabilization of the particles where the surfactant acts as a stabilizing ligand.

In order to control and tailor nanoparticle synthesis within microemulsion systems, one must first understand the microemulsion system. Over the past two

decades, developments in small-angle neutron scattering (SANS) and small-angle X-ray scattering (SAXS) have provided insight into the micro and nanostructure of microemulsion systems as discussed in detail in Chapter 5. With the addition of studies including CMC determination, phase behavior, flocculation, percolation, rheology and water uptake an accurate description of the microemulsion structure and stability is achieved and can be further supported by modeling techniques⁶⁻¹⁰. A variety of modeling theories exist for various microemulsion systems, however they all stem from the same underlying theory, modeling the interaction energies of the micro and nano-scale colloidal assemblies within the bulk phase. One of the most widely known models is the classical Derjaguin-Landau-Verwey-Overbeek (DLVO) theory of colloidal stability^{6,8,10,11}. The DLVO potentials model the interactions between two colloidal aggregates in solution consisting of two contributions. The first is an attractive component arising from the van der Waals interactions of the aggregate constituents. The magnitude of the attractive vdW forces are determined by the particle size and composition determined from the Hamaker interaction with a Hamaker constant, A , which is dependant on the colloidal aggregate composition. The second is an electrostatic double-layer repulsion term arising from the overlapping of the colloidal aggregates. While the DLVO theory has proven effective in many areas of colloid science, it has not been very successful in dealing with properties of some colloidal aggregates including surfactants and thin films.

Vincent et al. have developed a “soft sphere” theory to model depletion flocculation of colloidal dispersions through the interactions of sterically stabilized particles within a bulk phase¹². The theory acts to model the colloidal dispersion by

determining the net interaction free energy between two particles with an adsorbed polymer layer at a given separation distance. The terminology for the model of Vincent refers to any type of colloidal aggregate with specific geometry, not to be confused with metallic nanoparticles. The model is composed of attractive depletion interactions between the particles and repulsion forces due to steric interactions. The steric repulsion forces account for the interactions of the adsorbed colloid layers with themselves and the bulk solvent, resulting from solvation and mixing effects. For the modeling of particles as soft spheres the steric repulsion is comprised of an osmotic or mixing term and an elastic term. A summation of the attractive and repulsion contributions is the total interaction energy determined as a function of the center to center separation distance of two particles. The steric repulsion forces for soft spheres have been used to model the dispersion forces of a variety of colloidal aggregates including surfactants^{13,14}.

Johnston and coworkers have recently demonstrated that silver and gold nanocrystals, sterically stabilized by dodecanethiol ligands and dispersed in supercritical ethane, can be selectively separated according to size by adjusting the temperature and pressure of the system¹³. Therefore, the solvent strength of the supercritical phase can be adjusted to support various sized particles by adjusting the operating conditions of the system. As such, particle dispersibility is a function of the solvent strength where an increase in pressure or a decrease in temperature, raises the solvent density and ability to support larger particles. These results were supported through the development of a total interaction energy model which incorporated the van der Waals attractive forces between the metallic nanoparticles and the osmotic and elastic steric repulsion forces developed by Vincent to model the adsorbed dodecane thiol ligand.

In this Chapter, a similar theoretical approach is used to examine solvent effects on the ultimate particle size that can be synthesized and stabilized in the AOT reverse micelle system. We have experimentally observed that adjusting the properties of the bulk solvent can induce a change in the growth rate and the ultimate particle size obtained which will be explained through the solvation interactions between the surfactant tails and the bulk phase. The total interaction energy model is implemented to represent the attractive van der Waals forces, acting between the metallic particles, and the repulsive osmotic and elastic forces, resulting from the surfactant tail – tail and solvent – tail interactions responsible for the steric stabilization of the metallic particles within the microemulsion. The model is able to predict the ultimate particle sizes obtained experimentally in the previous chapter for copper nanoparticles synthesized using a variety of bulk liquid solvents including isooctane, cyclohexane and n-alkanes ranging from pentane to dodecane. The model was also used to investigate the effects of solubility parameters and surfactant coverage as well as investigations of nanoparticle synthesis in compressed propane and SCF ethane including temperature, pressure, and cosolvent effects. The model was similarly employed for the synthesis of silver particles in hexane / AOT / water reverse micelles to demonstrate the range of application.

3-2. MODELING

A soft sphere approach was employed to model spherical metallic nanoparticles surrounded by an AOT monolayer with the alkyl tails interacting with the bulk solvent. The AOT encased metallic particle excludes the presence of the water in the model for simplification as well as the fact that typical synthesis begins with ~2 nm diameter

reverse micelles and results in ~10 nm diameter particles. It is assumed that the amount of water present in the particle/surfactant system modeled is minimal and limited to the smallest amount necessary to hydrate the surfactant head groups for particle stabilization. The total interaction energy is achieved by a simple summation of attractive and repulsive forces demonstrated by equation 3-1 and Figure 3-1. The repulsive energy

$$\Phi_{\text{total}} = \Phi_{\text{vdW}} + \Phi_{\text{osm}} + \Phi_{\text{elas}} \quad (3-1)$$

$$\Phi_{\text{vdW}} = -\frac{A_{131}}{6} \left[\frac{2R^2}{d^2 - 4R^2} + \frac{2R^2}{d^2} + \ln \left(\frac{d^2 - 4R^2}{d^2} \right) \right] \quad (3-2)$$

$$A_{131} \approx \left(\sqrt{A_{11}} - \sqrt{A_{33}} \right)^2 \quad (3-3)$$

$$A_{33} = \frac{3}{4} k_B T \left(\frac{\varepsilon_3 - \varepsilon_{\text{vacuum}}}{\varepsilon_3 + \varepsilon_{\text{vacuum}}} \right)^2 + \frac{3h\nu_e}{16\sqrt{2}} \frac{\left(n_3^2 - n_{\text{vacuum}}^2 \right)^2}{\left(n_3^2 + n_{\text{vacuum}}^2 \right)^{3/2}} \quad (3-4)$$

contribution consists of an osmotic term, Φ_{osm} , and an elastic term, Φ_{elas} , which will be discussed later. The van der Waals attractive force, Φ_{vdW} , between two nanoparticles is a function of the particle radius R , the center to center separation d , and the Hamaker constant A . The Hamaker constant A_{131} is a proportionality factor that accounts for two nanoparticles of the same material (component 1) interacting through a solvent (component 3) and is determined from pure component values by equation 3-3. The Hamaker constant for the metal nanoparticles are constant with $A_{11} = 1.723$ eV for copper and $A_{11} = 2.440$ eV for silver¹⁵. For the bulk fluid A_{33} is calculated on the basis of Lifshitz theory by equation 3-4¹⁶. Where ε is the dielectric constant, n is the refractive index, k_B is Boltzmann's constant, T is temperature, h is Planck's constant, and ν_e is the main electronic UV absorption frequency, typically assumed to be $3 \times 10^{15} \text{ s}^{-1}$. Values for $\varepsilon_{\text{vacuum}}$ and n_{vacuum} are assumed to be 1 while the ε and n for bulk liquids at 20°C were

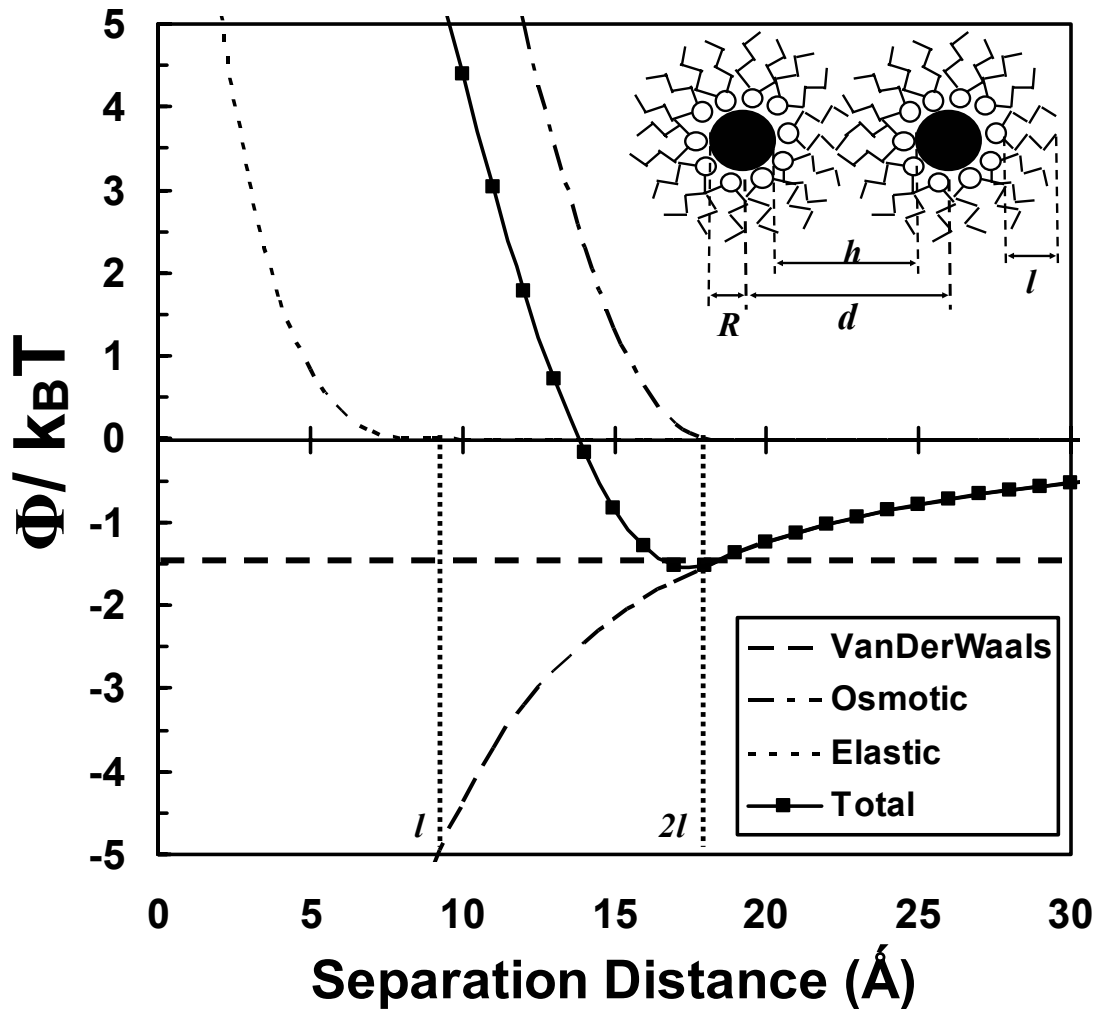


Figure 3-1 Contributions to the Total Interaction Energy Model for 8 nm diameter copper nanoparticles coated with AOT dispersed in hexane at 25°C and 1 bar.

obtained from the literature¹⁷ and for liquids at elevated temperatures ranging from 25°C to 65°C, ε and n are determined from the solubility parameter, δ , by equations 3-5 and 3-6 when not available in the literature.

$$n = \frac{0.48872 \times \delta + 5.55}{9.55} \quad (3-5)$$

$$\varepsilon = n^2 \quad (3-6)$$

Values of ε and n for compressed propane (eq. 3-6 and 3-7) and SCF ethane (eq. 3-8 and 3-9) were estimated using a Clausius-Mossotti relation and equations of state reported by Younglove and Ely as a function of the density, reduced density, reduced temperature and pressure¹⁸. Determination of ε and n for mixtures of SCF ethane and liquid alkane cosolvent are determined from the pure component values using the Lorentz-Lorenz mixing rule, equation 3-10, where n can be substituted with $\sqrt{\varepsilon}$ ¹⁹.

$$\frac{\varepsilon - 1}{\varepsilon + 2} = \rho \left(0.0156 + 7.72 \times 10^{-5} \rho - 4.04 \times 10^{-6} \rho^2 + 5.11 \times 10^{-4} \ln \left(1 + \frac{T_c}{T} \right) - 4.51 \times 10^{-7} P \right) \quad (3-7)$$

$$\frac{n^2 - 1}{n^2 + 2} = 0.07741 \rho_r + 1.097 \times 10^{-3} \rho_r^2 - 5.427 \times 10^{-4} \rho_r^3 \quad (3-8)$$

$$\frac{\varepsilon - 1}{\varepsilon + 2} = \left[0.077 + 4.33 \times 10^{-4} \ln \left(1 + \frac{T_c}{T} \right) \right] \rho_r + 9.78 \times 10^{-4} \rho_r^2 - 4.42 \times 10^{-4} \rho_r^3 - 1.46 \times 10^{-6} P \quad (3-9)$$

$$\frac{(n_{mix} - 1)^2}{(n_{mix} + 2)^2} = \sum \phi_i \frac{(n_i - 1)^2}{(n_i + 2)^2} \quad (3-10)$$

Figure 3-2 demonstrates the attractive forces due to the van der Waals interactions

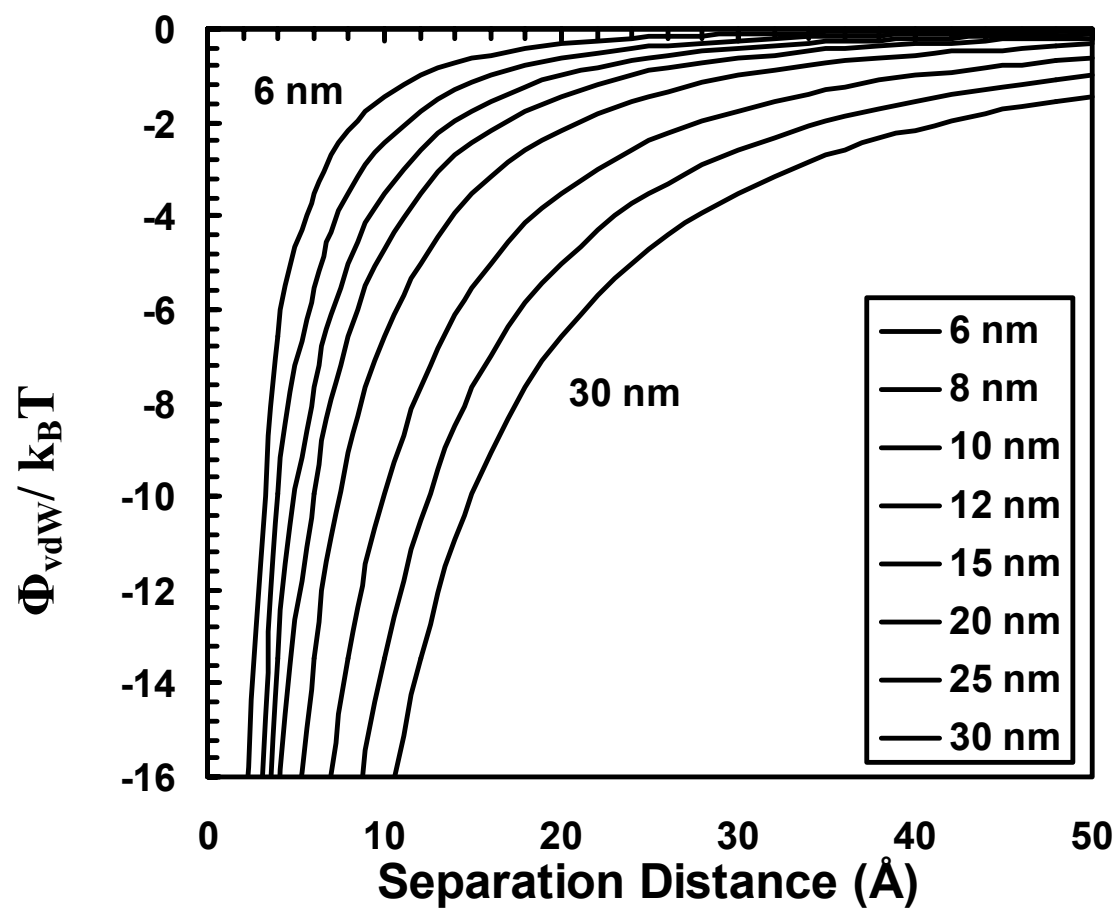


Figure 3-2 Attractive van der Waals contribution to the total interaction energy calculated for spherical copper nanoparticles coated with AOT surfactant and dispersed in hexane at 20°C for various particle diameters as a function of the separation distance.

between copper nanoparticles coated with AOT surfactant and dispersed in hexane at 25°C plotted as a function of separation distance and particle diameter. The negative trend of the interaction energy, $\Phi_{\text{vdW}}/k_{\text{B}}T$, with increasing particle size is representative of increasing van der Waals attractive forces between spherical copper particles interacting through the hexane bulk phase.

The repulsive contribution to the total interaction energy originates from the “soft sphere” theory developed by Vincent et al.¹² and implemented by Shah et al.¹³ where the following relations are proposed for the osmotic and elastic interaction terms.

$$\Phi_{\text{osm}} = \frac{4\pi R k_{\text{B}} T}{v_{\text{solv}}} \phi^2 \left(\frac{1}{2} - \chi \right) \left(l - \frac{h}{2} \right)^2 \quad l < h < 2l \quad (3-11)$$

$$\Phi_{\text{osm}} = \frac{4\pi R k_{\text{B}} T}{v_{\text{solv}}} \phi^2 \left(\frac{1}{2} - \chi \right) \left[l^2 \left(\frac{h}{2l} - \frac{1}{4} - \ln \left(\frac{h}{l} \right) \right) \right] \quad h < l \quad (3-12)$$

$$\Phi_{\text{elas}} = \frac{2\pi R k_{\text{B}} T l^2 \phi \rho}{\text{MW}_2} \left\{ \frac{h}{l} \ln \left[\frac{h}{l} \left(\frac{3-h/l}{2} \right)^2 \right] - 6 \ln \left(\frac{3-h/l}{2} \right) + 3 \left(1 - \frac{h}{l} \right) \right\} \quad h < l \quad (3-13)$$

$$h = d - 2R \quad (3-14)$$

Here again R is the particle radius and d is the center-to-center separation and from equation 3-14, h is the separation distance from the particle surfaces. As will be seen from the interaction energy diagrams, this separation distance at a minimum energy will determine the dispersibility of the particles. It must also be noted that the repulsive forces are independent of the particle material and do not contribute to the total interaction energy until the separation distance is less than twice the ligand length l . To obtain the ligand volume fraction, ϕ , the AOT was modeled as a cylindrical structure extending from the particle surface with a head group cross-sectional area of 75 Å² and a

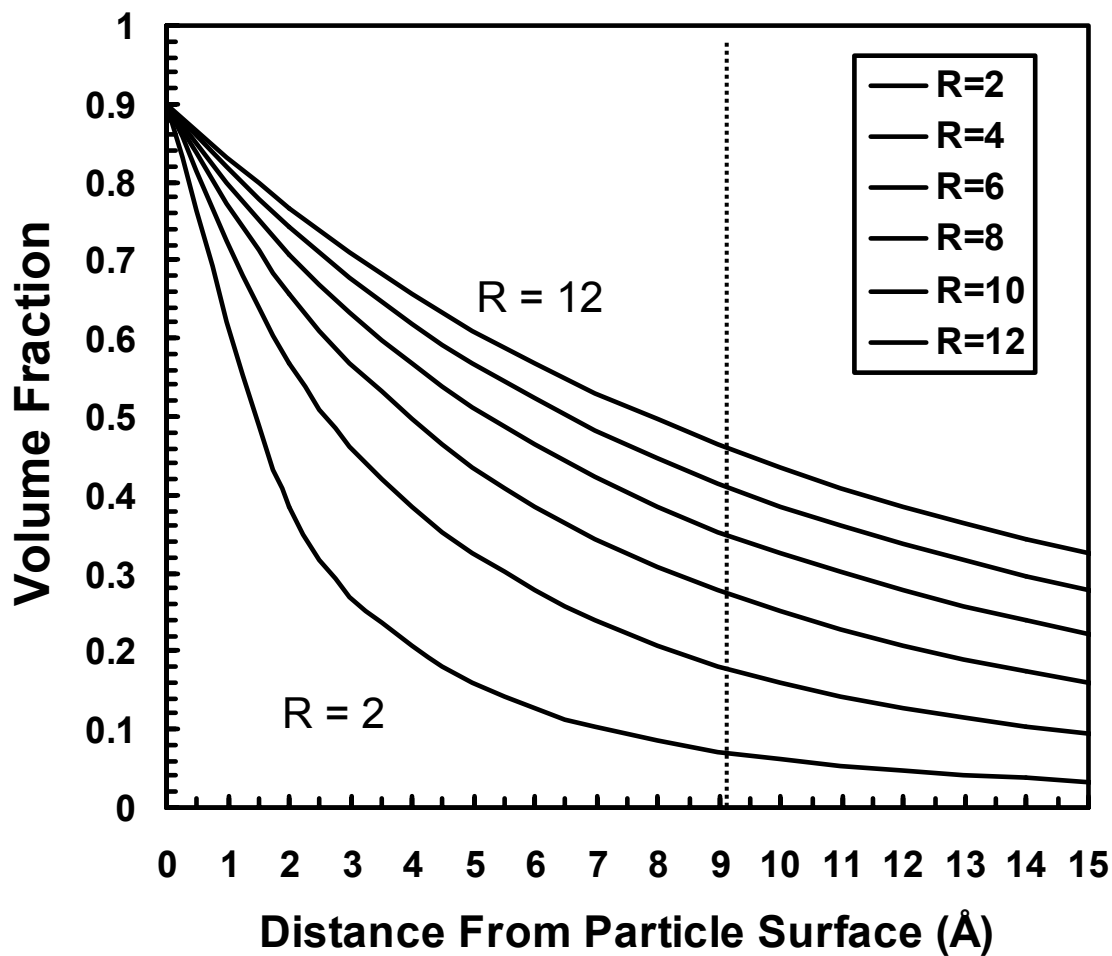


Figure 3-3 Plot of the ligand volume fraction as a function of the distance from the particle surface for various sized particles. At a distance of 9.1 Å corresponds to the length of the AOT surfactant.

$$\phi = 0.90 \left(\frac{3R^2l}{(R+l)^3 - R^3} \right) \quad (3-15)$$

length of 9.1 \AA^{20} with a 90% surface coverage determined by equation 3-15. Figure 3-3 is a plot of the ligand volume fraction for particles ranging in diameter from 2 nm to 12 nm. As the particle size increases, the curvature of the particle and surfactant layer decreases causing the surfactant tails to pack together resulting in an increase in the AOT volume fraction at distances from the particle surface. This is a rough approximation due to the neglect of factors such as the actual surface coverage, the known cone shaped structure of AOT, and the overlap of the surfactant tails especially in the region of $h < 2l$ where repulsive forces come into play.

The molecular volume of the solvent, v_{solv} , is required in the osmotic repulsion term. The Flory-Huggins interaction parameter, χ , also referred to as the Chi interaction parameter is function of the Hildebrand solubility parameters δ_i . The Chi interaction parameter can be determined by equation 3-16 where R is the ideal gas constant and \bar{v}_3 is the molar volume of the solvent. The solubility parameter for the solvent is related to the cohesive energy density, E_3^{coh} , and can be calculated by equation 3-17²¹ where ΔH_3^v is the enthalpy of vaporization for the liquid solvents as obtained from the literature^{17,22}.

$$\chi = \frac{\bar{v}_3}{RT} (\delta_3 - \delta_2)^2 \quad (3-16)$$

$$\delta_3 = \sqrt{E_3^{\text{coh}}} = \sqrt{\frac{\Delta H_3^v - RT}{\bar{v}_3}} \quad (3-17)$$

$$\Delta H_{20^\circ\text{C}} = \Delta H_{bp} \left(\frac{T_C - T}{T_C - T_{bp}} \right)^{0.38} \quad (3-18)$$

The values obtained correspond either to the desired temperature or at the boiling point of the liquid. In order to account for any temperature effects, the solubility parameter at the desired temperature was determined using Watson's correlation for latent heat, eq. 3-18²³.

For a SCF a liquid-vapor phase transition does not exist and an approximation of the enthalpy of vaporization must be used to calculate the solubility parameter. In eq 3-19, $H_{3,ig}$ is the ideal gas enthalpy, H_3 is the actual enthalpy, and P is the pressure²⁴. The solubility parameter for SCF ethane + liquid cosolvent was obtained using a volume fraction weighted average of the pure component values, equation 3-20. The solubility parameter for AOT must be estimated using a group contribution method typically implemented for polymer solutions where a molar attraction constant is assigned for each chemical group in the surfactant tail. There are three group contribution methods available²¹ provided by Small, Hoy, and van Krevelen resulting in values of 517.52, 510.81 and 578.42 MPa^{1/2} respectively. The Hoy method was implemented for the liquid solvent model. For the compressed and SCF solvents an average of the three methods was used to obtain $\delta_2 = 535.32$ MPa^{1/2}.

$$\delta_3 = \sqrt{E_3^{\text{coh}}} = \sqrt{\frac{\Delta H_{3,ig} - RT - H_3 + P\bar{v}_3}{\bar{v}_3}} \quad (3-19)$$

$$\delta_3 = \sum \phi_i \delta_i \quad (3-20)$$

The osmotic repulsion term deals solely with the interactions of the surfactant tails with themselves and the bulk solvent, calculated by equation 3-11 for $l < h < 2l$ and equation 3-12 for $h < l$. The key terms which determine the intensity of the osmotic repulsive energy are ϕ , v_{solv} and in particular χ . These terms are significant in determining the repulsive forces due to the surfactant tail – tail and tail – solvent interactions which

are responsible for particle stabilization and preventing agglomeration. The Chi interaction parameter is an indicator of the solvent interaction between the AOT tails and the bulk solvent where solvation occurs when $\chi < 0.5$ and the solvent strength increases as χ decreases²¹. The elastic repulsion term contributes to the interaction energy in the range $h < l$ and represents the energy requirement for compression of the surfactant tails. The contribution can be calculated from equation 3-13 where ρ and MW_2 represent the surfactant density and molecular weight. The elastic term represents the surfactant tail – tail repulsion that occurs on compression of the tails and is largely a function of the surfactant density and volume fraction.

The contribution of each of the forces to the total interaction energy can be seen in Figure 3-1 as a function of the separation distance of the particles. The elastic term does not contribute greatly and it is the osmotic forces that more strongly influences the particle dispersion by countering the attractive van der Waals forces. Along the total interaction energy curve a minimum value exists that corresponds to an optimum position of the particles with respect to each other. A threshold energy of $-3/2 k_B T$ or greater is required to disperse the particles within the bulk solvent by overcoming the average translational energy of colloidal particles undergoing Brownian motion¹⁰. Particle growth occurs through random exchange of micelle contents and will continue to grow until this threshold energy limit is reached. If particle growth occurs beyond an optimum size, the total interaction energy will drop below this threshold energy limit of $-3/2 k_B T$ and the particles will agglomerate and precipitate out of solution. In this case, the repulsive terms are insufficient to balance the attractive van der Waals forces thereby resulting in an inability to disperse the particles. The total interaction energy can be

calculated as a function of the separation distance for various particle sizes, solvents, temperatures and pressures in order to determine the optimum operating conditions for particle growth.

3-3. EXPERIMENTAL

Synthesis of copper nanoparticles was described in the previous chapter and the experimental results will be compared to the modeling results in this chapter. Silver particles were produced in a similar manor to the copper particles with concentrations of $\text{AgAOT} = 1.0 \times 10^{-3} \text{ M}$, $\text{AOT} = 9.9 \times 10^{-2} \text{ M}$, $W = 10$ and reduction using hydrazine at ten times excess of silver²⁵. AgAOT surfactant was synthesized by an ion exchange process similar to the synthesis of CuAOT_2 by the Eastoe method discussed in Appendix A. The Total Interaction Energy Model calculations were accomplished with a spreadsheet using Microsoft Excel XP.

3-4. MODELING RESULTS

3-4a. Liquid Phase Results

The previous discussion reveals the bulk solvent effects on the stabilization of various particle sizes which can be described by the solvent-surfactant tail interactions. The proposed interaction energy model provides an explanation for the maximum particle sizes obtained in various solvents by balancing the attraction and repulsion forces between AOT covered particles interacting in a bulk solvent. Figure 3-4 exhibits the results of the total interaction energy calculations for copper nanoparticles coated with AOT surfactant as a function of the separation distance and particle size at 20 °C and 1

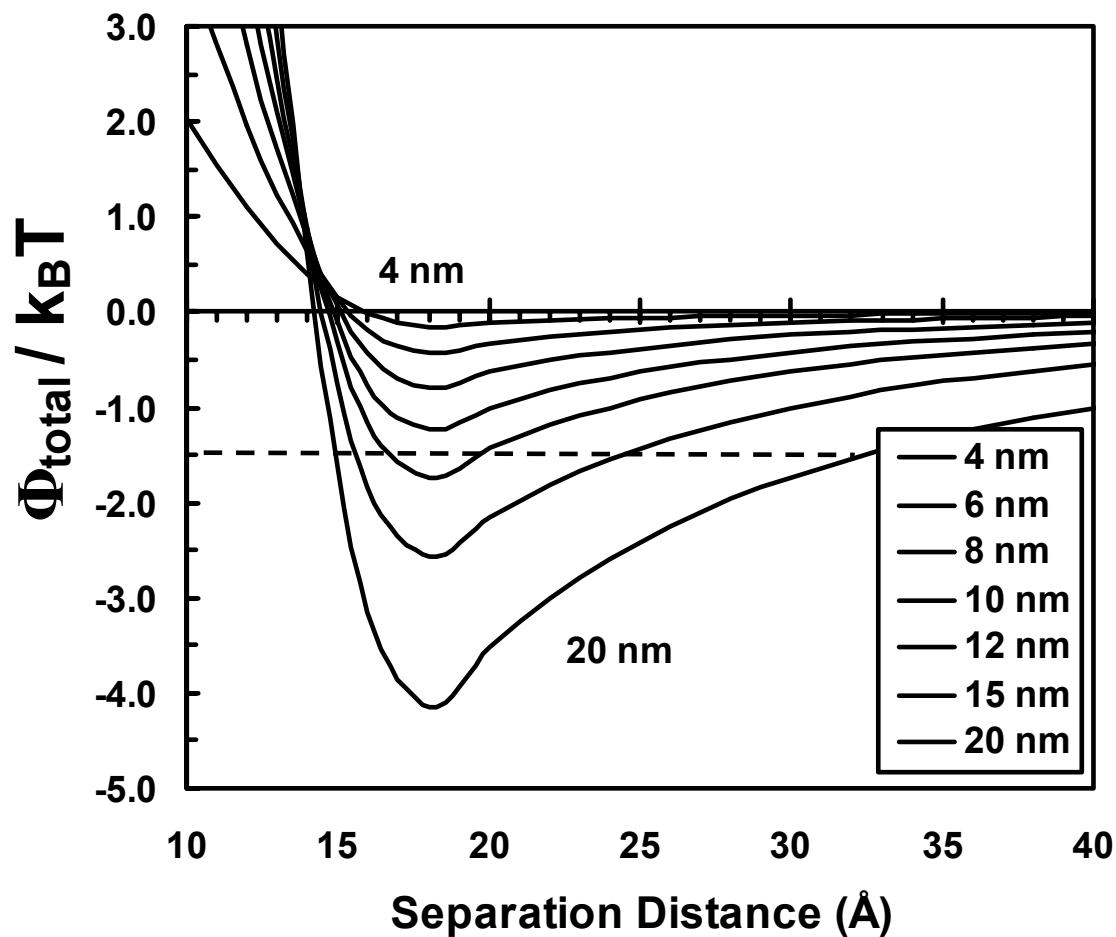


Figure 3-4 . Plot of the Total Interaction Energy, $\Phi_{total}/k_B T$, curves calculated for 4nm to 20nm diameter Cu nanoparticles coated with AOT and dispersed in hexane at 20°C and 1 bar. The model predicts an ultimate particle size of ~9 nm in diameter for hexane.

bar in hexane. From Table 3-1, the model predicts maximum particle diameters in each of the solvents ranging from a diameter of 10.6 nm in pentane through a diameter of 12.8 nm in cyclohexane. The calculated maximum particle diameters correspond well with the experimental results at W values of 5 and 10 in Table 3-1. Comparison of the experimental particle sizes and the model predictions shows good agreement for the solvent cyclohexane with a maximum particle size of 12.6 nm. The model predicts increasing particle size from 10.6 nm to 12.6 nm with increasing carbon number for the *n*-alkane solvents with a further increase in particle size with cyclohexane. For the case of cyclohexane, both the modeling and experimental results suggest that larger copper particles can be synthesized using cyclohexane as the bulk solvent compared to the other solvents investigated. Table 3-1 lists the thermophysical properties which influence the steric stabilization of the copper particles particularly the Hamaker constant, A , and the Chi interaction parameter, χ , which contribute to the attractive and repulsive forces respectively. Table 3-1 displays the bulk solvent and temperature effects on A and χ . The trends observed demonstrate that an increase in temperature results in an increase in A and a decrease in χ and thus an increase in the van der Waals attractive forces and a decrease in the solubility of the AOT tails. This would suggest that temperature has a dramatic effect on the stabilization of copper particles within the AOT reverse micelle system and that synthesis at elevated temperatures is not feasible, as seen in Figure 3-5. Solvent effects on A and χ demonstrate that χ decreases with decreasing molar density with the exception of cyclohexane and isooctane. The properties of cyclohexane result in a low value for χ and A for which it would be expected a larger particle would be sterically stabilized. Isooctane proves to be an interesting case where an increased value

Table 3-1. Experimental results of the relative particle growth rates and ultimate particle sizes obtained for Copper nanoparticles synthesized in various alkane bulk solvents with $[\text{CuAOT}_2] = 0.01106 \text{ M}$, $[\text{AOT}] = 0.1106 \text{ M}$ and $W = 5$ and 10 . The calculation results obtained from the total interaction energy model show excellent agreement with the ultimate particle sizes obtained experimentally.

Solvent	W = 5 Size (nm)	W = 10 Size (nm)	Calculations Size (nm)
Pentane	8.3	8.6	10.6
Hexane	8.6	8.9	11.1
Heptane	8.6	8.6	11.5
Octane	8.5	8.4	11.8
Decane	9.1	8.9	12.2
Dodecane	9.0	9.7	12.6
Isooctane	9.4	9.6	11.3
Cyclohexane	12.6	12.6	12.8

Table 3-2 Table of thermophysical properties of the copper nanoparticle – liquid alkane – AOT system for various bulk alkane solvents.

Solvent	T (°C)	P (bar)	ρ (mol/L)	ε	n	A_{131} (eV)	h (kJ/mol)	δ (J/ml)^{1/2}	χ
Hexane	20	1.0	7.60	1.89	1.37	0.358	31.9	15.0	0.107
Hexane	40	1.0	7.45	1.74	1.32	0.649	30.6	14.4	0.194
Hexane	60	1.0	7.22	1.67	1.29	0.726	29.4	13.9	0.312
Pentane	20	1.0	8.68	1.84	1.36	0.552	26.7	14.5	0.163
Heptane	20	1.0	6.82	1.92	1.39	0.480	36.8	15.3	0.067
Octane	20	1.0	6.12	1.95	1.40	0.458	41.3	15.4	0.060
Decane	20	1.0	5.13	1.99	1.41	0.430	49.6	15.5	0.053
Dodecane	20	1.0	4.40	2.01	1.42	0.405	59.7	15.9	0.024
Isooctane	20	1.0	6.02	1.94	1.39	0.471	35.6	14.1	0.342
Cyclohexane	20	1.0	9.25	2.02	1.43	0.394	33.2	16.9	0.011

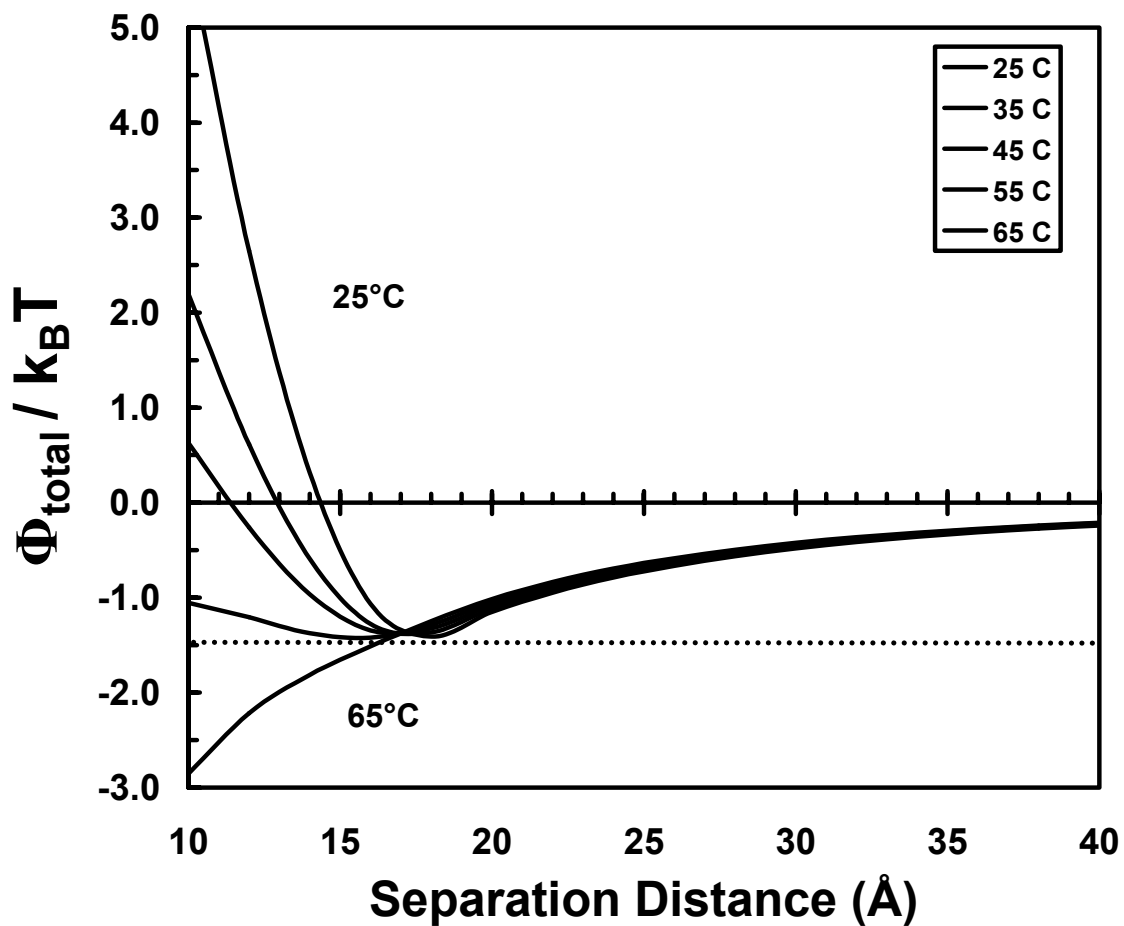


Figure 3-5 Plot of the $\Phi_{\text{total}}/k_B T$ curves calculated for 10 nm diameter Cu nanoparticles coated with AOT and dispersed in hexane at 1 bar and temperatures ranging from 25°C to 65°C. The model predicts that 10 nm diameter Cu particles would be sterically stabilized in hexane at 25°C, however as the temperature is increased to 65°C the particles would agglomerate and precipitate out of solution.

for χ and A exists however particle stabilization is still possible which may exist due to a balancing of the attractive and repulsive forces. A minimum value of A exists for hexane when compared to the other solvents studied. Interestingly this minimum corresponds to a maximum water uptake value for 0.1 M AOT in hexane reverse micellar solution²⁶. Further comparison of the A for spherical water / AOT reverse micelles and χ for various bulk solvents with measurements of the CMC, maximum water uptake, percolation threshold and phase behavior provides interesting correlation and insight into the interaction forces within the AOT reverse micelle system.

The model predicts slightly larger particles in each alkane solvent compared to the particle sized observed experimentally in chapter 2. The experimental results show particle sizes ranging from 8.3 nm to 9.7 nm from pentane to dodecane, however the maximum particle size trend predicted by the model is not as significant. From the calculations it would be expected that larger particles would be obtained for the larger alkanes although additional properties not accounted for by the model may contribute to instability in the micellar system resulting in the smaller sizes observed in the experimental results. Fletcher et al.²⁷ discuss that for the decane and dodecane systems, the experimental conditions explored in this study approach an upper phase transition where it has been shown that clustering of AOT stabilized droplets in dodecane occurs around 25°C and above. A SANS structure-factor analysis in the vicinity of this region reveals a sharp increase in additional short range attractive interactions. If this attractive interaction were accounted for by the model then it would have the effect of lowering the total interaction energy curve in the region $h < 2l$ resulting in a particle size smaller than what is predicted by the model, thereby more closely relating to the experimental data.

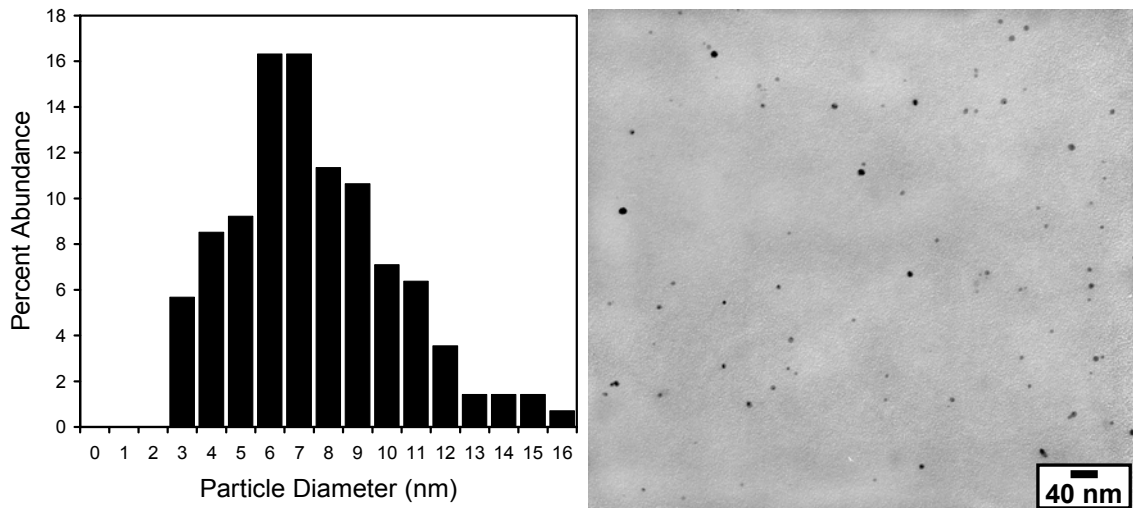
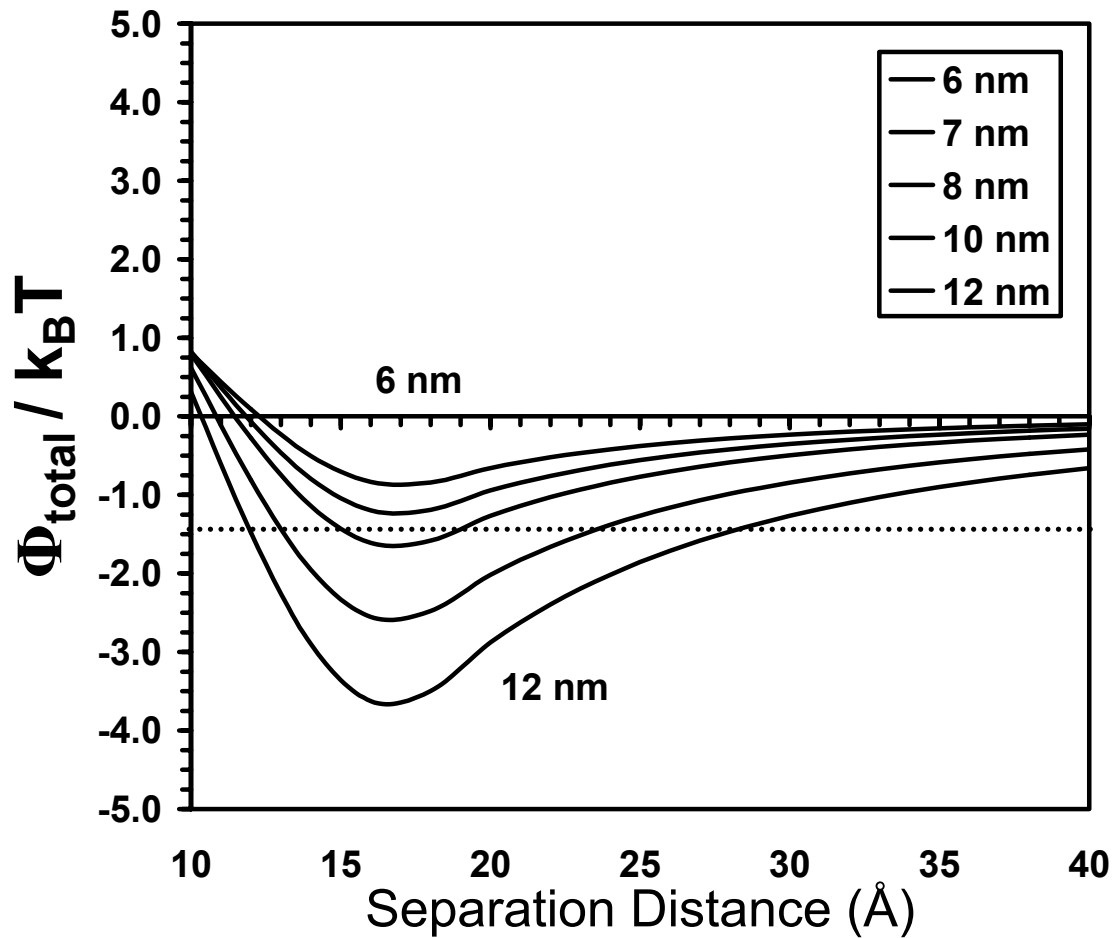


Figure 3-6 a) Plot of the $\Phi_{\text{total}}/k_B T$ curves calculated for 6nm to 12nm diameter Ag nanoparticles coated with AOT and dispersed in hexane at 25°C and 1 bar. b,c) TEM image and size distribution for Ag particles synthesized in liquid hexane–AOT– water reverse micelle system with 1.0×10^{-3} M AgAOT, 9.9×10^{-2} M AOT, and $W = 10$.

Figure 3-6a demonstrates that this model is also applicable to the synthesis of silver particles in hexane / AOT reverse micelle systems which predicts a maximum particle size of ~ 7.5 would be synthesized. Figure 3-6b,c is a TEM image and particle size distribution of silver nanoparticles synthesized in a hexane solution with $[\text{AgAOT}] = 0.001\text{M}$, $[\text{AOT}] = 0.099\text{M}$, and $W = 10$ where the majority of the silver nanoparticles are 6 to 7 nm in diameter, corresponding directly to the predictions of the model.

Other properties of the system that the model takes into account which affect the predicted ultimate particle size include temperature and percentage of particle surface coverage by the surfactant. Figure 3-5 shows the effect of temperature on 10 nm copper particles in hexane where the ability to sterically stabilize the particles becomes increasingly difficult as the temperature increases to 65°C where the particles would no longer be supported. By increasing the temperature, an increase in van der Waals attraction and a decrease in the AOT tail solubility is observed according to the modeling results thus decreasing the ability to sterically stabilize particles at elevated temperatures. The same effect of temperature was observed by Shah et al.¹³ where an increase in temperature requires an increase in pressure of the SCF ethane to obtain an adequate solvent interaction parameter in order to selectively separate silver nanoparticles. Figure 3-7 shows the effect of decreasing particle surface coverage from 90% to 30% which largely influences the surfactant volume fraction calculated in equation 3-15. As the surfactant surface coverage decreases below 50% for silver particles in hexane, the particles would no longer be sterically stabilized by the surfactant. The effect of surface coverage has bearing on the previously mentioned case for particles consisting of multiple atomic species^{3,4,28-32}. The inability of the ionic head group to interact with the

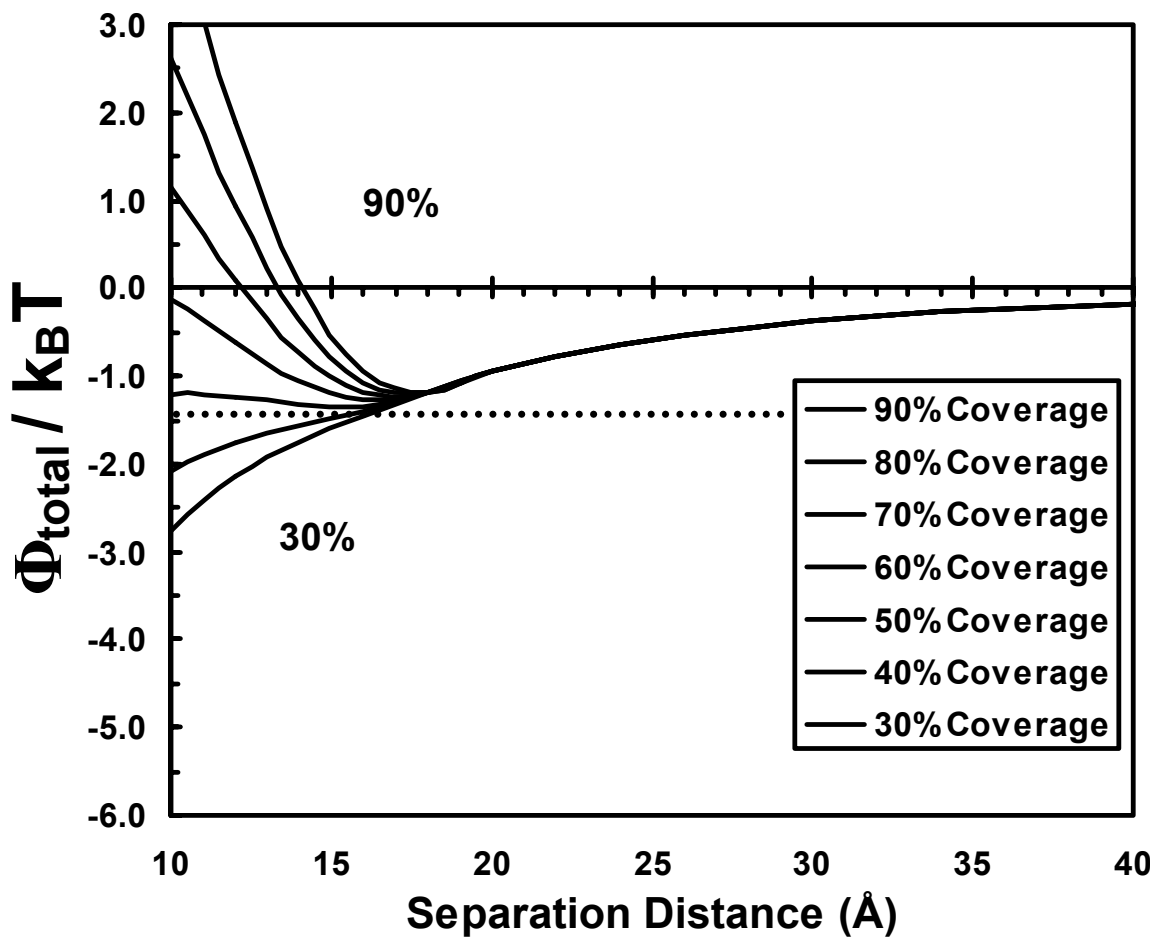


Figure 3-7 Plot of the $\Phi_{\text{total}}/k_B T$ curves calculated for 8 nm diameter Ag nanoparticles coated with AOT and dispersed in hexane at 20°C and 1 bar with decreasing surface coverage of AOT on the Ag particles. The model predicts that as the percent surface coverage decreases, the ability to stabilize particles in solution also decreases.

particle surface directly would effectively lower the particle surface coverage and thus restrict particle growth beyond the size of the micelle. This may explain the occurrence of purely metallic particles exceeding the size of the original micelle where the AOT surfactant acts to sterically stabilize the particles in solution allowing for growth beyond the size of the water core. Further investigation of the interaction forces between the particle surface and the ionic surfactant head group will provide a better understanding of the mechanism of steric stabilization of metallic nanoparticles in the AOT reverse micelle system.

3-4b. Compressed Propane Results

Replacing the liquid solvents with compressible and SCF solvents allows for variation of the thermophysical properties of the bulk phase, particularly the solvent strength of the bulk phase, with adjustments to the temperature and pressure of the system. By adjusting the conditions of the compressible bulk phase, the density and solubility parameter are altered, thus varying the solvent interactions with the surfactant tails. It has been observed that more favorable solvent interactions with the surfactant tails results in slower reaction rates and the synthesis of larger particle sizes with the liquid solvents³³. Thus, the ability to adjust the solvent strength of compressible fluids using temperature and pressure provides control over the ultimate particle size and growth rate. Johnston and co-workers demonstrated the size selective dispersion of sterically stabilized silver and gold nanocrystals using SCF ethane by adjusting the temperature and pressure of the system¹³. Thus, increasing the pressure and decreasing

the temperature of the compressed and supercritical fluid microemulsion systems should result in the synthesis of larger metallic nanoparticles based on this principle.

The total interaction energy model is used to investigate the stabilization of copper nanoparticles synthesized in the compressed propane – AOT reverse micelle system. The model examines the effects of temperature and pressure on the particle size stabilized in this system and is compared to the particles synthesized experimentally. The effects of temperature and pressure on the predicted ultimate particle size that would be obtained experimentally were investigated. Figure 3-8 demonstrates that χ decreases with decreasing temperature and increasing pressure thus providing more favorable solvent conditions. Figure 3-9 demonstrates that A_{131} also decreases with decreasing temperature and increasing pressure although a lesser effect than for χ . The increased solvent strength (χ) and decreased attractive forces (A_{131}) would suggest that larger copper particles would be sterically stabilized at lower temperatures and higher pressures. Table 3-3 also illustrates that χ and A_{131} decrease with decreasing temperature and increasing pressure as well as the effects interchanging the bulk solvent, thus providing more favorable solvent conditions and a decrease in the attractive force between particles. The increased solvent strength and decreased attractive forces suggest that larger copper particles would be sterically stabilized at lower temperatures and higher pressures. The effect of the particle size on $\Phi_{\text{total}}/k_{\text{B}}T$ from the total interaction energy model is presented in Figure 3-10a where the minima in the interaction energy curve decreases and crosses the $-3/2 k_{\text{B}}T$ stabilization threshold as the particle size is increased from 6 nm to 15 nm in diameter. The conditions at which the interaction energy curve crosses this threshold corresponds to the predicted ultimate particle size synthesized. In compressed propane at 25°C and 310

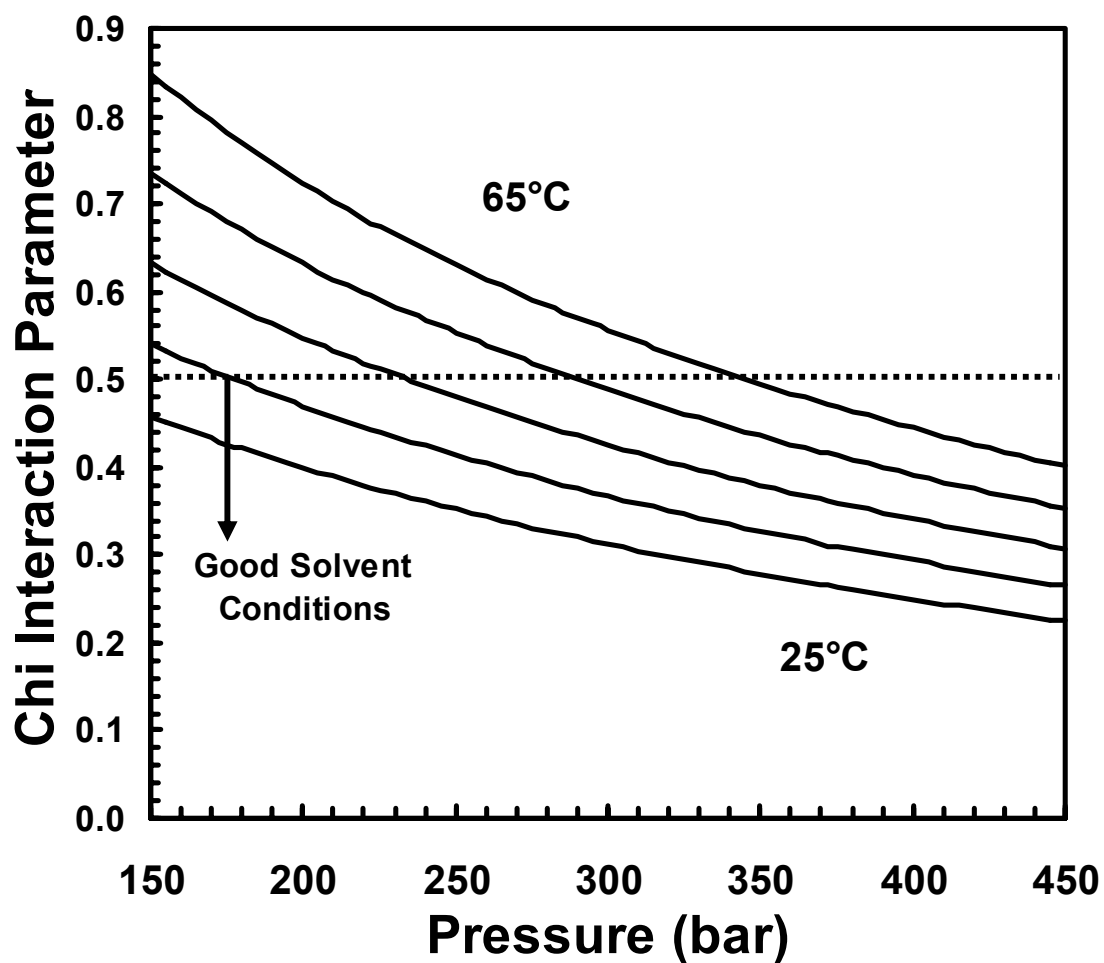


Figure 3-8 Chi interaction parameter, χ , for AOT in compressed propane as a function of temperature and pressure. Typically values of χ less than 0.5 are characteristic of good solvent conditions.

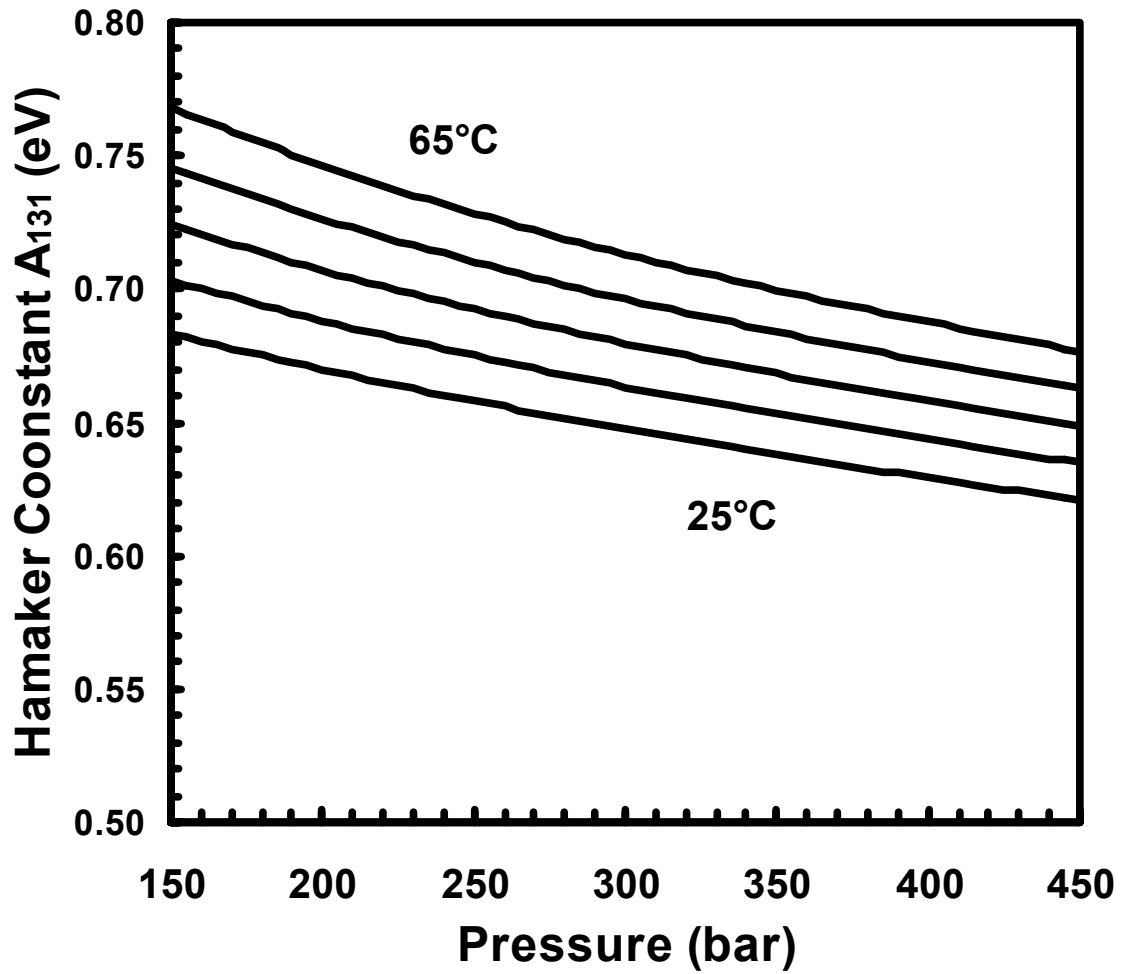


Figure 3-9 Hamaker constant A_{131} for copper nanoparticles interacting through compressed propane as a function of temperature and pressure.

Table 3-3 Table of thermophysical properties of the copper nanoparticle – alkane – AOT system for various compressed, SCF, and compressed + cosolvent alkane solvents.

Solvent	T (°C)	P (bar)	ρ (mol/L)	ε	n	A_{131} (eV)	H_v (kJ/mol)	δ (J/ml) ^{1/2}	χ	Dia. (nm)
Propane	25	150	11.90	1.71	1.31	0.68	16.0	13.3	0.46	-
Propane	25	350	12.54	1.75	1.32	0.64	15.3	14.0	0.28	9.96
Propane	45	150	11.35	1.67	1.29	0.72	15.2	12.6	0.63	-
Propane	45	350	12.13	1.72	1.31	0.67	14.6	13.4	0.38	9.82
Ethane	20	150	13.84	1.56	1.25	0.85	10.9	11.5	0.88	-
Ethane	20	500	16.03	1.66	1.29	0.73	10.3	13.3	0.34	9.16
SCF Ethane	35	350	14.80	1.60	1.27	0.79	10.3	12.2	0.59	-
SCF Ethane	35	500	15.57	1.64	1.28	0.75	9.9	12.8	0.42	8.98
Eth.+ 7.9% Cyclo	20	150	13.29	1.62	1.28	0.77	-	12.1	0.57	-
Eth.+ 7.9% Cyclo	20	350	14.60	1.68	1.30	0.71	-	13.2	0.29	9.38
Eth.+ 7.9% Cyclo	20	500	15.21	1.71	1.31	0.68	-	13.7	0.20	9.60
Eth.+ 7.9% Cyclo	45	350	13.78	1.63	1.28	0.76	-	12.4	0.44	-
Eth.+ 5.8% Cyclo	20	350	14.78	1.67	1.29	0.72	-	13.0	0.31	9.28
Eth.+ 10.0% Cyclo	20	350	14.42	1.70	1.30	0.69	-	13.3	0.27	9.48
Eth.+ 7.9% Iso	20	350	13.72	1.64	1.28	0.76	-	12.9	0.36	8.88
Eth.+ 7.9% Hexane	20	350	14.23	1.65	1.29	0.74	-	13.0	0.33	9.04

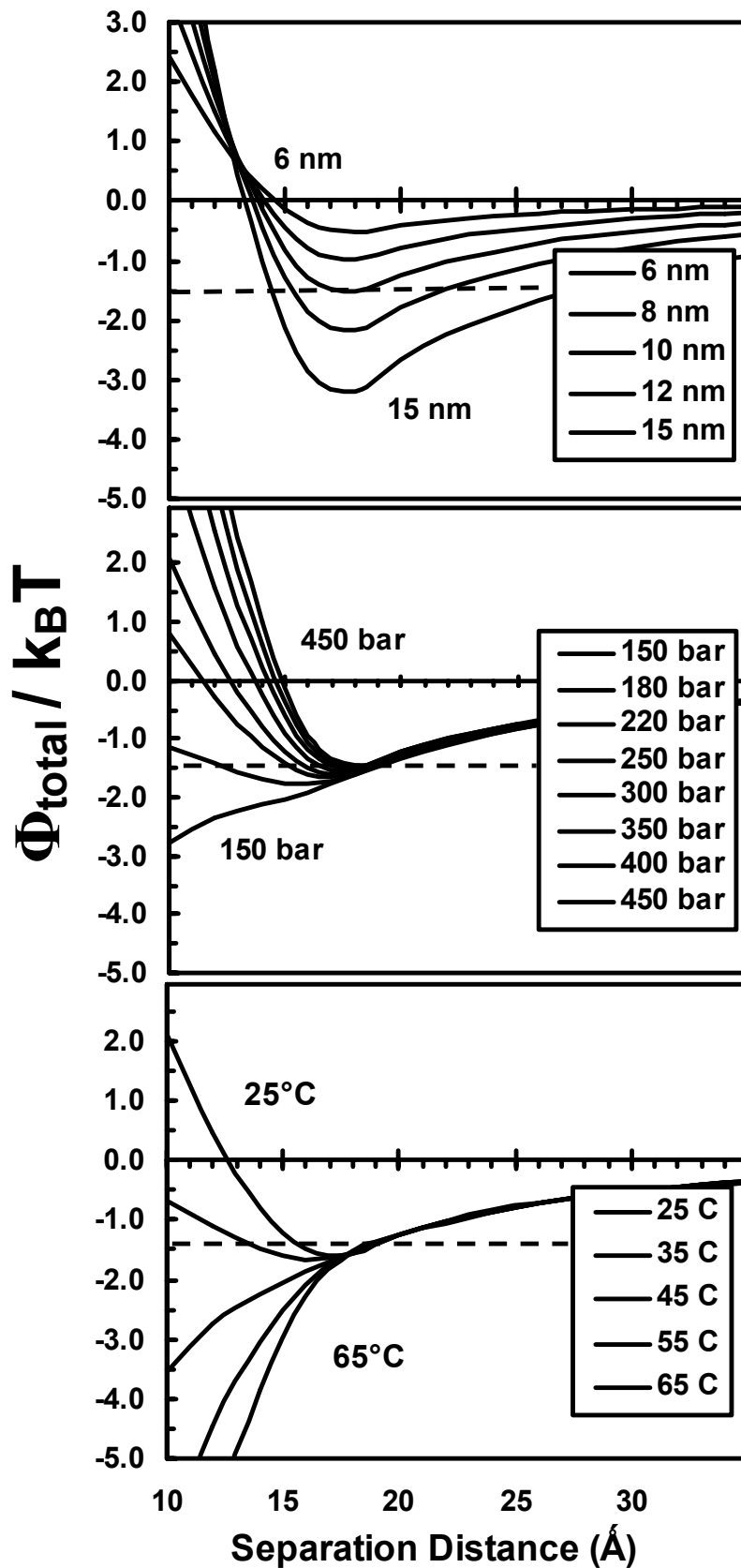


Figure 3-10. Plot of the $\Phi_{\text{total}}/k_B T$ curves for Cu nanoparticles coated with AOT and dispersed in compressed propane. 3a) Shows the effect of particle diameter from 6nm to 15 nm at 310 bar and 25°C. 3b) shows the effects of pressure on 10nm diameter Cu particles at 25°C and in the range of 150 to 450 bar. 3c) Shows the effect of temperature on a 10nm diameter Cu particle at 310 bar and pressures ranging from 25°C to 65°C.

bar the model predicts the stabilization of a 9 nm diameter particle where as a 10 nm diameter particle would not be supported since the increase in particle size results in the interaction energy curve crossing the stabilization threshold. Figure 3-10b illustrates the effects of pressure on the stabilization of 10 nm copper particles in compressed propane at 25°C, predicting that the ability to sterically stabilize a particle of a given size increases with an increase in pressure. The $-3/2 k_B T$ energy limit corresponds to a minimum pressure required for particle stabilization and thus a minimum pressure required for synthesis of a particular particle size as well as a tunable pressure effect on the ultimate particle size. In the same respect that a minimum pressure is required to stabilize a specific particle size, as the particle size is increased the minimum pressure required for particle stabilization also increases. Application of this model to particle synthesis suggests that as the pressure of the compressed propane system is increased, the maximum particle size that can be synthesized and stabilized increases. Figure 3-10c presents the effect of temperature on $\Phi_{\text{total}}/k_B T$ where the model predicts a decreasing ability to synthesize a particle of a given diameter with an increase in temperature. The model suggests that a maximum temperature limit exists for particle stabilization of a given size at a particular pressure. The ability to stabilize a specific particle size at elevated temperatures must be countered with an increase in pressure to obtain the solvent conditions necessary for particle stabilization. Similarly, as the temperature is increased at a constant pressure, the maximum particle size that would be stabilized by the system decreases and thus as the temperature is increased, a decrease in the maximum particle size synthesized is predicted by the model. The effects of temperature and pressure on the maximum particle size synthesized and stabilized as predicted by the

model correspond to microemulsion stability measurements where an increase in pressure and a decrease in temperature results in a more stable microemulsion and the ability to stabilize an increased water content³⁴.

3-4c. Compressed and SCF Ethane Results

Interactions between ethane as the bulk solvent and the AOT surfactant tails are decreased as compared to those of the propane solvent system and thus the model suggests that elevated pressures are required for particle synthesis in ethane as demonstrated in Figure 3-11 and Table 3-4. Figure 3-12 displays the interaction energy curves calculated by the model demonstrating the effect of particle size and pressure at 25°C. The modeling results suggest that copper nanoparticle synthesis in compressed ethane at 20°C may be achieved at pressures of 400 bar and above. As the temperature of the ethane system is increased to 35°C, above the critical temperature of pure ethane (32.15°C), a decrease in the ability to stabilize particles is observed where pressures of 500 bar and above are required for synthesis as demonstrated in Figure 3-11. A continued increase in the minimum pressure required for synthesis at 550 bar is also observed as the temperature is increased to 45°C. Additionally, a decrease in the predicted particle size with increasing temperature at a fixed pressure is shown in Table 3-4. The prediction of the ability to synthesize copper nanoparticles in compressed and SCF ethane is also extremely significant due to the reported inability to synthesize copper particles in ethane without the use of a liquid cosolvent by Cason^{35,36}, however the pressures investigated were below those predicted by the model. Thus copper nanoparticle synthesis in SCF ethane may be possible at pressures above 500 bar.

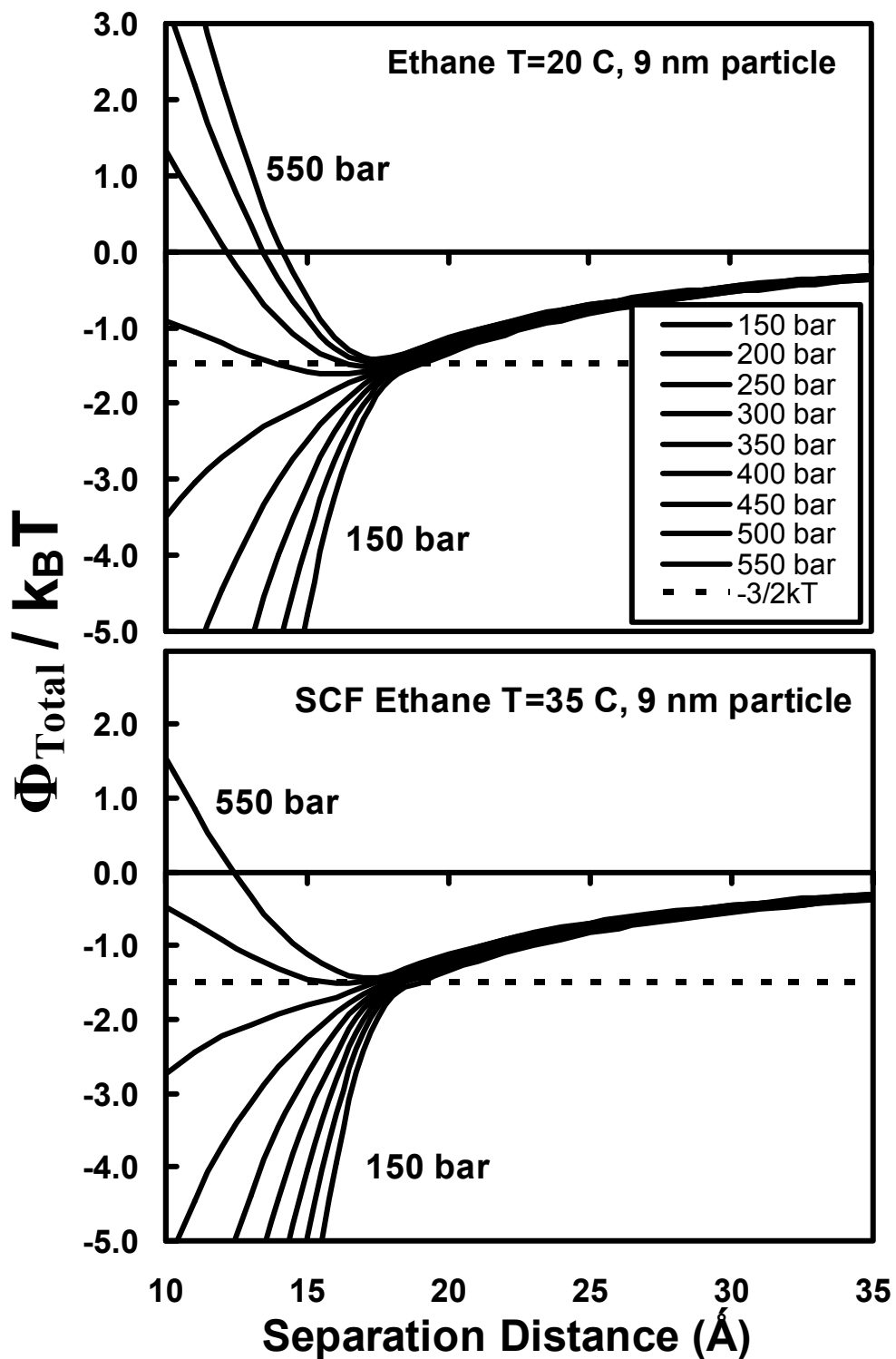


Figure 3-11 Plot of the $\Phi_{\text{total}}/k_B T$ curves for 9 nm diameter Cu nanoparticles coated with AOT and dispersed in SCF ethane at 35°C as a function of separation distance and pressure.

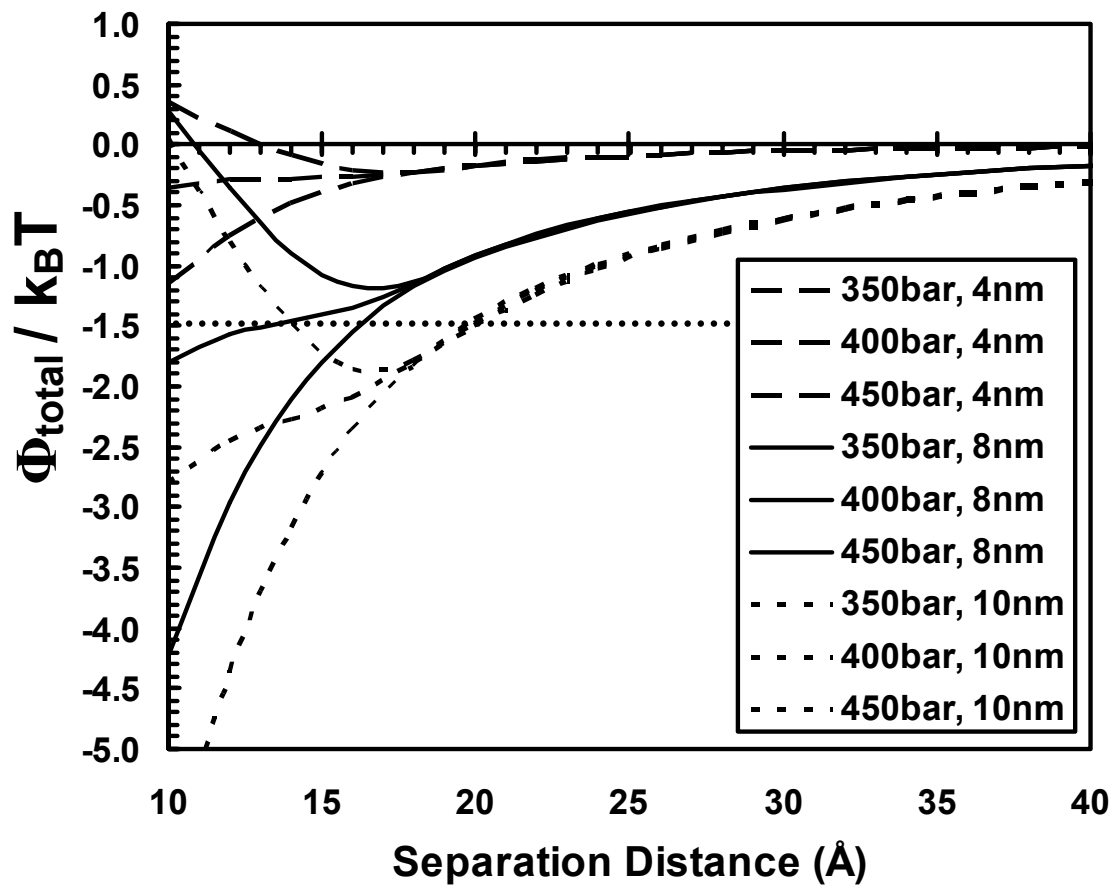


Figure 3-12 Plot of the $\Phi_{\text{total}}/k_B T$ curves for Cu nanoparticles coated with AOT and dispersed in compressed ethane at 25°C for various particle diameters and pressures.

The temperature and pressure effects in ethane parallel the modeling results observed for the propane system with the exception that significantly higher pressures are required to achieve the desired solvent conditions for particle synthesis. Table 3-3 lists the thermophysical properties used in the model for each of the solvent systems investigated as a function of temperature and pressure. For each of the solvents investigated, an increase in pressure and a decrease in temperature result in a decrease in A_{131} and χ . A decrease in A_{131} represents a decrease in the attractive van der Waals forces between particles. A decrease in χ demonstrates a more favorable interaction between the solvent and AOT tails, thus an increase in the repulsive osmotic dispersion forces. The decrease in attractive forces and increase in repulsive forces between the particles interacting in the bulk solvent, as determined by the model, would result in an increased ability to stabilize larger particles and thus demonstrates the effects of temperature and pressure on the ability to sterically stabilize particles as well as provide control over the particle sizes synthesized.

3-4d. Compressed Ethane + Cosolvent Results

The solvent strength necessary for particle synthesis in the ethane system can be achieved at lower pressures with the addition of liquid alkane cosolvents which will change the solvent properties of the bulk phase allowing conditions more favorable for particle synthesis at lower pressures. The thermophysical properties in Table 3-3 demonstrate the influence of added liquid alkane cosolvent on the ethane – AOT reverse micelle system. The stability of the ethane – AOT reverse micelle system is affected by the addition of the liquid alkane cosolvents with increasing stability determined by

Table 3-4. Maximum copper nanoparticle diameters predicted by the total interaction energy model for various ethane – AOT systems as a function of pressure, temperature and the addition of hexane, isooctane and cyclohexane cosolvents at different mol fractions. The predicted particle sizes demonstrate the effects of the bulk solvent properties on particle synthesis. The – indicates a prediction of the inability to synthesize particles of any size.

Cosolvent	Hexane			Cyclohexane			Isooctane		
	20°C	35°C	45°C	5.8%	7.9%	10.0%	7.9%	7.9%	7.9%
mol% Cosol.	20°C	35°C	45°C	20°C	20°C	20°C	45°C	20°C	20°C
200 bar	-	-	-	-	-	-	-	-	-
250 bar	-	-	-	8.80	8.98	9.14	-	-	-
300 bar	-	-	-	9.08	9.24	9.38	-	8.82	-
350 bar	-	-	-	9.28	9.38	9.48	9.22	9.04	8.88
400 bar	8.68	-	-	9.36	9.46	9.54	9.46	9.18	9.08
450 bar	8.98	-	-	9.44	9.52	9.62	9.56	9.26	9.16
500 bar	9.16	8.98	-	9.50	9.60	9.68	9.64	9.32	9.24
550 bar	9.30	9.20	9.00	9.56	9.66	9.74	9.70	9.38	9.30

decreasing values of χ (from 0.76 to 0.71 eV) and A_{131} (from 0.36 to 0.29) for isooctane, hexane and cyclohexane cosolvents, respectively. The results reflect a decrease in the minimum pressure required for particle synthesis as the cosolvent is switched from isooctane to hexane and to cyclohexane, corresponding to an increase in solvent – tail interactions. This correlates with phase behavior measurements that indicate an increase in microemulsion phase stability with this solvent change. The model predicts the synthesis of 9.46 nm diameter particles in the ethane system with 7.9 mol percent cyclohexane at 20°C and 400 bar with decreasing particle sizes as the cosolvent is interchanged to hexane and isooctane, as shown in Table 3-4. Overall, the modeling results indicate that particle synthesis can be achieved in the ethane – cosolvent systems at 20°C with pressures much lower than would be required for synthesis in ethane at 20°C.

When the temperature is increased from 20°C to 45°C in the ethane + 7.9 mol percent cyclohexane system, there is an increase in the minimum pressure required for ~9 nm diameter particle synthesis from 200 bar to 400 bar. Moreover, the predicted particle size at a fixed pressure of 400 bar decreases with the temperature increase. This corresponds well with the previous results where a decrease in the stability of the microemulsion and particle size is predicted with increasing pressure. Interestingly, as the pressure is increased the trend is reversed and the model predicts slightly larger particle sizes at the higher temperatures despite a lower density and higher values of χ and A_{131} . This emphasizes the role of temperature in determining whether particle synthesis is feasible and determining a minimum pressure required for synthesis rather than providing control over the particle sizes obtained.

The modeling results also predict a slight increase in the particle size with an increase in the cyclohexane mol fraction from 5.8 to 10.0 mol percent. In discussing the modeling results for varying the cosolvent concentration in the ethane system it must be noted that the model does not account for the preferential insertion of the cosolvent into the surfactant tail region. Roberts et al.³⁷ performed a solvatochromatic investigation on the effects of adding small amounts of benzene cosolvent to the ethane – AOT reverse micelle system and found that with the addition of 2.5 mole percent benzene, a solvatochromic probe in the AOT tail region sensed an enhanced benzene environment approaching near saturation³⁷. The model accounts for the ethane and cosolvent as a well mixed solvent and does not account for preferential solvation of the AOT tail groups by the cosolvent which would have the effect of a much larger volume fraction of cosolvent in the tail region and a lower volume fraction in the bulk phase. In comparing the modeling results with the experimental system, a much higher cosolvent concentration in the vicinity of the AOT tail region may be observed experimentally compared to the uniform cosolvent fraction assumed by the model. However, the presence of the cosolvent has the effect of promoting micelle stabilization and particle synthesis as predicted by the model and demonstrated experimentally, as will be discussed below.

For each of the bulk solvent systems investigated, the temperature and pressure effects on the thermophysical properties of the system impacted the predicted particle size as well as the ability to synthesize particles. It can be concluded that the ability to sterically stabilize particles in solution, and thus synthesize them, is largely influenced by the solvent interactions with the AOT tails. This is confirmed with values of χ greater than 0.43 that resulted in the inability to synthesize particles and with χ less than 0.43,

particle synthesis was predicted. The solvent interactions, coupled with A_{131} and the attractive forces between particles also impart control over the particle size. Overall the predicted trends of synthesized particle sizes generally parallel with microemulsion stability where a more stable microemulsion results in the synthesis of larger particles. A comparison with experimental results will confirm the accuracy of the model.

3-5. CONCLUSIONS

The total interaction energy model takes a simplistic approach to modeling the metallic particles coated with AOT surfactant as soft spheres. The model calculates the attractive van der Waals forces acting between the metallic particles and the repulsive osmotic and elastic forces which result from the tail – tail and solvent – tail interactions responsible for the steric stabilization of the metallic particles. The model accurately predicts the ultimate copper and silver particle sizes obtained experimentally in the various liquid alkane solvents. The model is also used to predict the bulk solvent effects on copper nanoparticle growth using a compressible fluid as the bulk phase where the thermophysical properties can be fine tuned using temperature and pressure for tailored nanoparticle synthesis. The ability of the model to accurately predict the size of metallic nanoparticles further supports the steric stabilization theory for control over the morphology of particles synthesized within the reverse micelle system. Chapter 4 presents the experimental results for the synthesis of copper nanoparticles in compressible alkane – AOT reverse micelle system in addition to comparison of the results with the modeling work previously discussed.

3-6. REFERENCES

- (1) Pileni, M. P. *Langmuir* 1997, 13, 3266-3276.
- (2) Eastoe, J.; Warne, B. *Current Opinion in Colloid & Interface Science* 1996, 1, 800-805.
- (3) Hirai, T.; Sato, H.; Komasaawa, I. *Industrial & Engineering Chemistry Research* 1994, 33, 3262-3266.
- (4) Bagwe, R. P.; Khilar, K. C. *Langmuir* 1997, 13, 6432-6438.
- (5) Cason, J. P.; Miller, M. E.; Thompson, J. B.; Roberts, C. B. *Journal of Physical Chemistry B* 2001, 105, 2297-2302.
- (6) Morrison, I. D.; Ross, S. *Colloidal dispersions : suspensions, emulsions, and foams*; Wiley-Interscience: New York, 2002.
- (7) Hiemenz, P. C.; Rajagopalan, R. *Principles of colloid and surface chemistry*; 3rd, rev. and expanded / ed.; Marcel Dekker: New York, 1997.
- (8) Chen, S.-H.; Rajagopalan, R. *Micellar solutions and microemulsions : structure, dynamics, and statistical thermodynamics*; Springer-Verlag: New York, 1990.
- (9) Sjöblom, J. *Emulsions and emulsion stability*; Marcel Dekker: New York, 1996.
- (10) Everett, D. H. *Basic principles of colloid science*; Royal Society of Chemistry: London, 1988.
- (11) Derjaguin, B. V. *Theory of stability of colloids and thin films*; Consultants Bureau: New York, 1989.
- (12) Vincent, B.; Edwards, J.; Emmett, S.; Jones, A. *Colloids and Surfaces* 1986, 18, 261-281.
- (13) Shah, P. S.; Holmes, J. D.; Johnston, K. P.; Korgel, B. A. *Journal of Physical Chemistry B* 2002, 106, 2545-2551.
- (14) Romero-Cano, M. S.; Puertas, A. M.; de las Nieves, F. J. *Journal of Chemical Physics* 2000, 112, 8654-8659.
- (15) Eichenlaub, S.; Chan, C.; Beaudoin, S. P. *Journal of Colloid and Interface Science* 2002, 248, 389-397.
- (16) Israelachvili, J. N. *Intermolecular and surface forces : with applications to colloidal and biological systems*; Academic Press: London ; Orlando, [Fla]. 1985.
- (17) Lide, D. R. *Handbook of organic solvents*; Crc: Boca Raton, 1995.
- (18) Younglove, B. A.; Ely, J. F. *Journal of Physical and Chemical Reference Data* 1987, 16, 577-798.
- (19) Hadrich, J. *Applied Physics* 1975, 7, 209-213.
- (20) Nave, S.; Eastoe, J.; Heenan, R. K.; Steytler, D.; Grillo, I. *Langmuir* 2000, 16, 8741-8748.
- (21) Fried, J. R. *Polymer Science and Technology*; Prentice Hall: Englewood Cliff, NJ, 1995.

- (22) Smith, B. D.; Srivastava, R. *Thermodynamic data for pure compounds*; Elsevier ;Distributors for the U.S. and Canada Elsevier Science Pub. Co.: Amsterdam ; New York, New York, N.Y., U.S.A., 1986.
- (23) Smith, J. M.; Van Ness, H. C.; Abbott, M. M. *Introduction to chemical engineering thermodynamics*; 5th ed.; McGraw-Hill: New York, 1996.
- (24) Lee, C. T.; Psathas, P. A.; Johnston, K. P.; deGrazia, J.; Randolph, T. W. *Langmuir* 1999, *15*, 6781-6791.
- (25) Petit, C.; Lixon, P.; Pileni, M. P. *Journal of Physical Chemistry* 1993, *97*, 12974-12983.
- (26) Liu, D. J.; Ma, J. M.; Cheng, H. M.; Zhao, Z. G. *Colloids and Surfaces a-Physicochemical and Engineering Aspects* 1998, *143*, 59-68.
- (27) Fletcher, P. D. I.; Howe, A. M.; Robinson, B. H. *Journal of the Chemical Society-Faraday Transactions I* 1987, *83*, 985-1006.
- (28) Hirai, T.; Tsubaki, Y.; Sato, H.; Komasaawa, I. *Journal of Chemical Engineering of Japan* 1995, *28*, 468-473.
- (29) Petit, C.; Lixon, P.; Pileni, M. P. *Journal of Physical Chemistry* 1990, *94*, 1598-1603.
- (30) Towey, T. F.; Khanlodhi, A.; Robinson, B. H. *Journal of the Chemical Society-Faraday Transactions* 1990, *86*, 3757-3762.
- (31) Feltin, N.; Levy, L.; Inger, D.; Pileni, M. P. *Journal of Physical Chemistry B* 1999, *103*, 4-10.
- (32) Sato, H.; Asaji, N.; Komasaawa, I. *Industrial & Engineering Chemistry Research* 2000, *39*, 328-334.
- (33) Kitchens, C. L.; McLeod, M. C.; Roberts, C. B. *J. Phys. Chem. B.* 2003, *107*, 11331-11338.
- (34) McFann, G. J. In *Chemical Engineering*; University of Texas at Austin, 1993, p 395.
- (35) Cason, J. P.; Roberts, C. B. *J. Phys. Chem. B* 2000, *104*, 1217-1221.
- (36) Cason, J. P.; Khambaswadkar, K.; Roberts, C. B. *Ind. Eng. Chem. Res.* 2000, *39*, 4749-4755.
- (37) Roberts, C. B.; Thompson, J. B. *Journal of Physical Chemistry B* 1998, *102*, 9074-9080.

CHAPTER 4

4. COPPER NANOPARTICLE SYNTHESIS IN COMPRESSED AND SCF PHASE REVERSE MICELLE SYSTEMS

4-1. INTRODUCTION

Investigations of metallic nanoparticle synthesis within liquid phase, water in oil AOT reverse micelle systems have demonstrated the influence of the bulk fluid solvent properties on the particle growth rate and ultimate particle size¹⁻⁴ as demonstrated in Chapters 2 and 3. Synthesis of nanoparticles within compressed and SCF reverse micelles systems began with the initial work by Fulton and coworkers who discovered the ability to form AOT reversed micelles in compressed propane and SCF ethane^{5,6}. Microemulsions in compressible fluids have been studied by various techniques to gain an understanding of the fundamental properties which can be applied to numerous applications⁵⁻¹⁵, including metallic nanoparticle synthesis in reverse micelle self-assemblies^{16,17}. Cason et al. first demonstrated copper nanoparticle synthesis in AOT reverse micelle systems with compressed propane and SCF ethane + liquid isooctane cosolvent as the bulk fluids¹⁸. The ability to synthesize metallic nanoparticles in these systems is closely related to the requirements for microemulsion stabilization where specific solvent conditions are necessary to support particles in solution via surfactant stabilization. The work of Johnston and co-workers demonstrated the ability to size

selectively disperse dodecanethiol capped particles in supercritical ethane through adjustments in temperature and pressure¹⁹. As such, particle dispersibility is a function of the solvent strength where an increase in pressure or a decrease in temperature provides the ability to support larger particles.

In this chapter, copper nanoparticle synthesis within AOT reverse micelles was achieved, implementing compressed liquid and supercritical fluid alkanes as the bulk solvent of the microemulsion system. These results further demonstrate the role of the anionic surfactant AOT in reverse micelle based nanoparticle synthesis. Initially, the AOT creates a thermodynamically stable microemulsion system consisting of water and metal ions encased within an AOT surfactant reverse micelle and dispersed within a bulk oil phase. The AOT surfactant also acts as a stabilizing ligand where the surfactant tails sterically stabilize the synthesized copper particles in solution. The experimental and modeling results in Chapters 2 and 3 have shown that the strength of the solvent interactions between the bulk liquid organic solvent and the surfactant tails affect the particle growth rate and mean copper nanoparticle size synthesized within the microemulsion system. The thermophysical properties of compressed liquids and supercritical fluids (SCF) can be tuned through adjustments in temperature and pressure. This affords the unique ability to control particle synthesis within the reverse micelle systems by adjusting the strength of interaction between the surfactant tails and the bulk solvent. Our results demonstrate that an increase in pressure or decrease in temperature results in the ability to synthesize slightly larger particles. In compressed propane, the median particle diameter synthesized can be shifted from 5.4 nm to 9.0 nm with an

increase in pressure from 241 bar to 345 bar. Synthesis in compressed and SCF ethane is achieved at a pressure of 517 bar and can be slightly adjusted with temperature and even more so with the addition of a liquid alkane cosolvent.

This experimental results presented in this chapter demonstrate the influence of the adjustable thermophysical properties on copper nanoparticle synthesis, particularly the feasibility of particle growth and particle size control. The solvents investigated include compressed propane, compressed and SCF ethane, and ethane + cosolvent mixtures which include cyclohexane, hexane and isooctane cosolvents. Implementing compressed and supercritical microemulsion systems for the production of nanomaterials yields the ability to harness the adjustable thermophysical properties of the solvent that governs particle synthesis. This method of metallic nanoparticle synthesis has proven to be an effective method for the production of nanoparticles with relatively narrow size distributions and mean particle diameters ranging from 6.4 to 11.3 nm under moderate conditions. Synthesis in compressed and SCF ethane is achieved at a pressure of 517 bar and can be slightly adjusted with temperature and even more so with the addition of a liquid alkane cosolvent.

The compressed solvent systems allow for thermodynamic control over particle synthesis and also offer unique particle collection techniques and spray coating methods. Additional advantages over conventional liquid systems include the ease of solvent removal by simply depressurizing the system, novel transport and deposition properties, and reduction in surface tension and wetting effects during solvent removal²⁰.

4-2. EXPERIMENTAL

4-2a. Materials

Sodium bis(2-ethylhexyl) sulfosuccinate (AOT) and DIUF Water were obtained from Fisher Scientific and used without further purification. Ethane and propane gases were purchased from BOC Gases and were passed through a High Pressure Gas Drier moisture trap and a High Pressure Oxy-Trap oxygen trap, both purchased from Alltech. Anhydrous hydrazine 98%, isooctane, and other alkane solvents were purchased from Sigma Aldrich. Copper AOT (CuAOT₂) was synthesized by replacing the sodium ion of the AOT head group with a Cu²⁺ ion to create the functionalized surfactant²¹. The AOT and CuAOT₂ surfactants were dried in a vacuum oven until no noticeable change in mass was observed and any hydration of the surfactants or solvents was not taken into account.

4-2b. Phase Behavior Measurements

Phase behavior measurements were used to determine the demixing pressure for the ethane + cosolvent / AOT / water reverse micelle system at various temperatures, W values and cosolvent concentrations in order to determine the relative stabilities of the microemulsion with the addition of the hexane, isooctane, and cyclohexane cosolvents into the ethane bulk phase. The demixing pressure for a specific temperature is the point at which the stable microemulsion is broken and a phase separation occurs as the pressure of the system is slowly decreased. This phase separation can be observed visually by the transition from a clear solution to a cloudy solution and the percent transmittance drops from 100% to below 80 %. These measurements were performed using the variable volume view cell equipped with a piston displacement hand pump in conjunction with

percent transmittance measurements using the Ocean Optics fiber optic UV-Vis spectrophotometer as seen in Figure 4-1 and detailed in the appendices. A quartz window in the face allows the entire contents of the vessel to be observed. The sides of the vessel are equipped with opposing windows which allow for UV-Vis absorption measurements necessary to monitor in-situ nanoparticle growth as well as phase behavior measurements. The vessel is also equipped with inlet and outlet valves, an RTD temperature controller and a flush mount pressure transducer. The vessel has the ability to be used as a constant volume reaction vessel by replacing the modified displacement pump with a back plate resulting in a vessel volume of 30ml. This vessel design has proven very useful in the measurement of solubility demixing pressures in addition to nanoparticle synthesis in compressed and supercritical fluids where the temperature and pressure of the system can be controlled. A Logitech QuickCam Pro 4000 web camera and ring light have also been adapted to allow for digital monitoring of the reaction vessel.

4-2c. Particle Synthesis

Particle synthesis in compressed propane, SCF ethane and SCF ethane + liquid cosolvent was achieved in the 30 ml fixed volume stainless steel reactor fitted with two opposing quartz windows for in-situ, UV-vis absorption measurements. AOT and CuAOT₂ were added to the reactor in a 10 to 1 molar ratio and the vessel was then sealed, purged with nitrogen gas and evacuated by a vacuum pump to ensure an oxygen free environment to prevent the formation of copper oxide. The reactor was filled with the bulk compressed fluid using an ISCO 260D high pressure syringe pump and

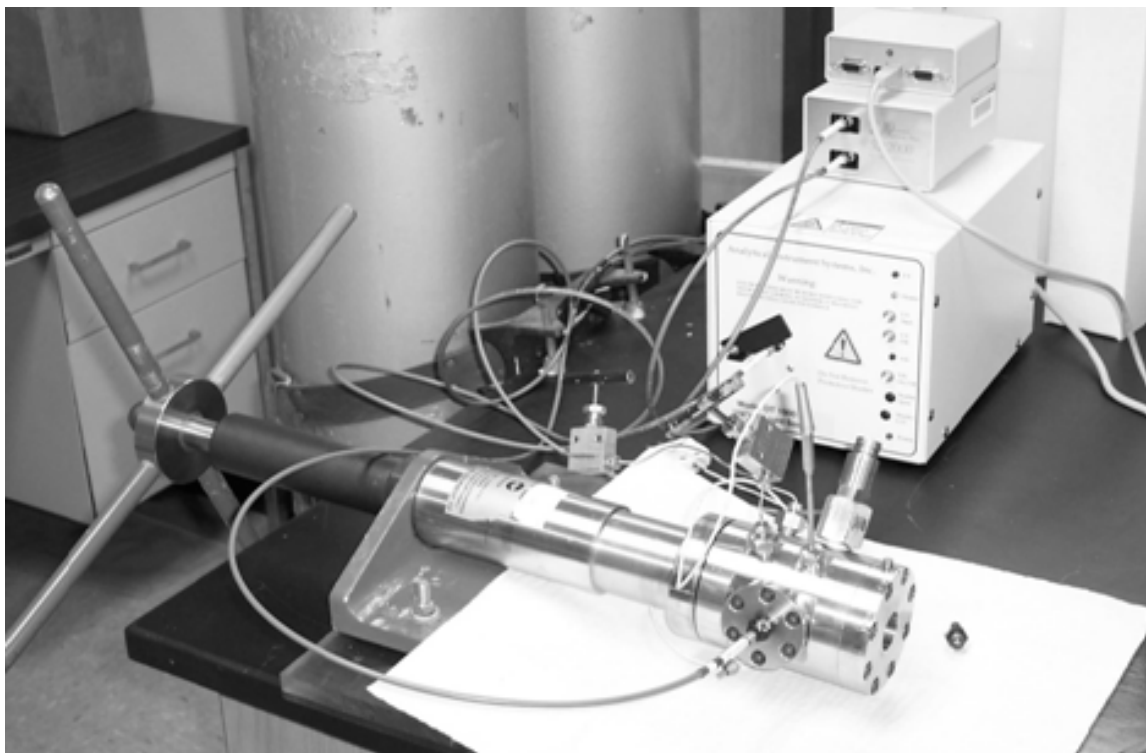


Figure 4-1. High pressure reaction vessel equipped with a modified piston displacement hand pump, opposing windows for in-situ UV-Vis measurements, a face plate window, RTD temperature control, and flush mount pressure transducer.

simultaneously a Valco Instruments six port injection loop was used to introduce the desired amount of water for a $W = 5$ or less ($W = [\text{H}_2\text{O}]/[\text{AOT}]$). The W value was determined by the amount of water added to the system neglecting any surfactant hydration water. An RTD and temperature control device was used with heating and insulating tape wrapped around the stainless steel vessel to achieve effective temperature control. The reactor pressure was brought to a pressure necessary to form a thermodynamically stable microemulsion at the desired temperature for the reaction. Hydrazine reducing agent was then added at $10 \times [\text{CuAOT}_2]$, by the injection loop, with stirring and the system was brought to the desired reaction pressure. A Varian Cary 300 UV-Vis spectrophotometer was used to monitor copper nanoparticle synthesis using time resolved absorbance measurements as the reaction proceeded through the intermicellar exchange process in the absence of stirring. Copper nanoparticles dispersed in solution exhibit a characteristic absorption band centered at a wavelength of 566 nm. The intensity of the absorbance band is representative of the mean particle diameter in solution and allows for monitoring of the copper particle growth rate and the mean particle size synthesized²².

Particle images were obtained using a Zeiss EM 10 Transmission Electron microscope (TEM). The particles were collected by various methods. A spray coating method was implemented by expanding the compressed particle solution through a 0.10 mm capillary tube, 5 cm in length, onto a nickel TEM grid. A second method involved the use of a stabilizing ligand (dodecanethiol and lauric acid) in order to prevent agglomeration. Particles were collected by redispersion in an isoctane solution with 0.01 M stabilizing ligand and placing a droplet of the solution on the TEM grid. The

stabilizing ligand was also introduced directly into the particle solution using the injection loop and particles collected by the spray technique. The TEM images obtained were analyzed using Scion Image software for windows²³ to obtain particle size distributions.

4-3. PARTICLE SYNTHESIS RESULTS

4-3a. Compressed Propane / AOT Reverse Micelle System

Copper nanoparticle synthesis was achieved experimentally in compressed propane at 21°C and TEM images were used to obtain a particle size distribution for synthesis at various pressures. Figure 4-2 displays a histogram of the particle size distribution obtained from TEM analysis as a function of pressure and it can be seen that as the operating pressure is increased the particle size distribution shifts slightly towards a larger particle diameter. The experimental data supports the modeling results where an increase in the ultimate particle size obtained increases slightly with increasing pressure. The modeling predictions and the experimental results represented by the median particle size listed in Table 4-1 show the same trends with some differences in the predicted particle diameters. The model predicts a slightly larger particle size than what was observed experimentally, however a more significant effect of pressure on the median particle size is observed experimentally.

Table 4-1 displays the descriptive statistics of the particle distributions for the experimental conditions investigated where the particle sizes were measured by TEM analysis and N is the number of particles measured. From the particle size distribution histogram in Figure 4-2 it is evident that the particle sizes represent a skewed right

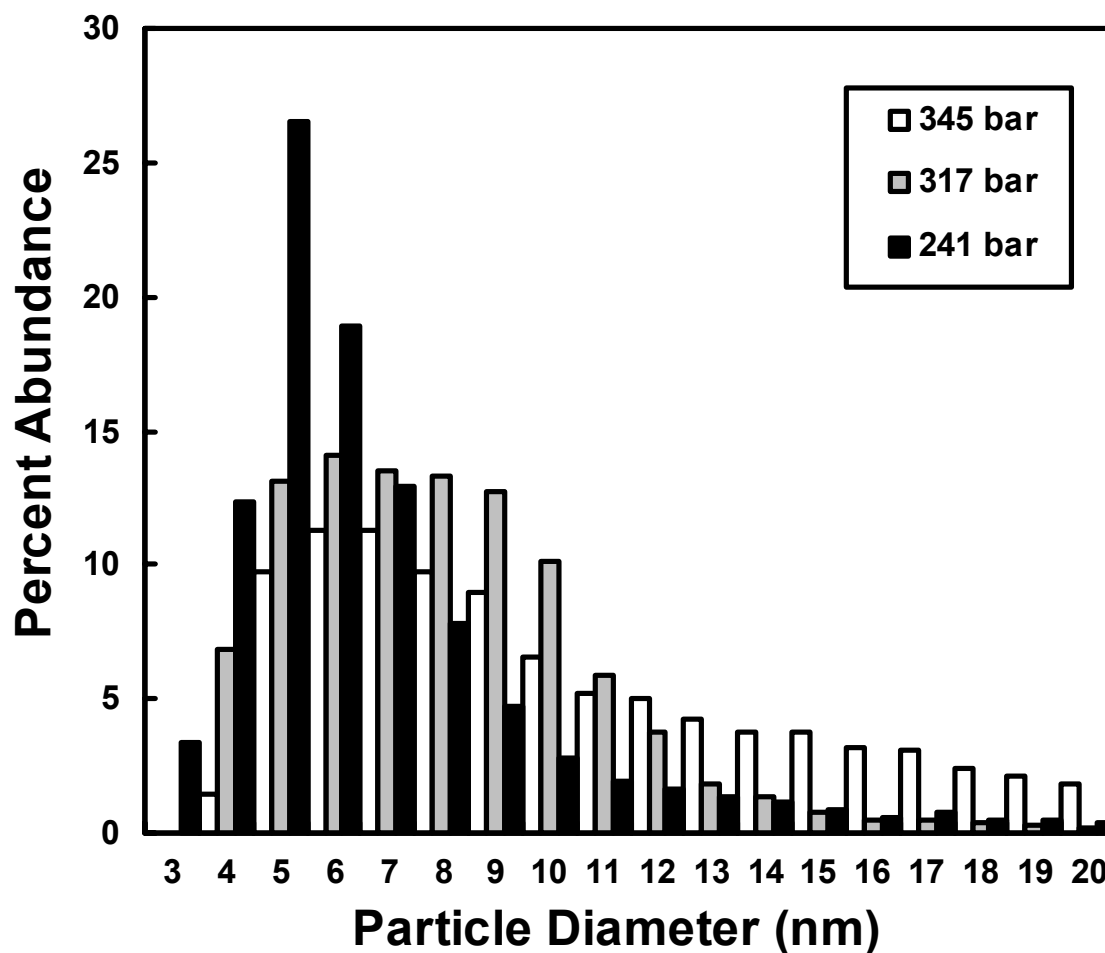


Figure 4-2. Copper nanoparticle size distribution for synthesis in compressed propane with $[AOT] = 5.5 \times 10^{-2} \text{ M}$, $[CuAOT_2] = 5.5 \times 10^{-3} \text{ M}$ and $W = 1.5$ at 21°C and pressures of 241, 276, and 317 bar.

Table 4-1. Descriptive statistics of experimental particle size distributions obtained from TEM analysis for copper nanoparticles synthesized in compressed propane, ethane + cosolvent, and SCF ethane at various temperatures, pressures, cosolvent mol fractions and water contents. The predicted particle sizes by the total interaction energy model are listed for comparison.

Compressed Propane									
Cosolvent	W	Temp.	Pressure	N	Mean	StDev	Median	IQR	Model
-	1.5	21°C	241 bar	11282	6.4 nm	3.5	5.4 nm	2.8 nm	9.82 nm
-	1.5	21°C	276 bar	607	7.8 nm	3.2	7.1 nm	3.9 nm	9.88 nm
-	1.5	21°C	317 bar	4098	7.7 nm	3.4	7.2 nm	3.7 nm	9.94 nm
-	1.5	21°C	345 bar	8061	11.3 nm	6.6	9.0 nm	8.2 nm	10.00 nm
Ethane + Cyclohexane Cosolvent									
Cosolvent	W	Temp.	Pressure	N	Mean	StDev	Median	IQR	Model
5.8 mol%	1.5	20°C	290 bar	3636	6.5 nm	3.9	5.7 nm	3.9 nm	9.00 nm
5.8 mol%	3	20°C	379 bar	493	9.7 nm	5.5	8.4 nm	7.0 nm	9.30 nm
7.9 mol%	1.5	20°C	345 bar	1624	8.1 nm	6.1	6.1 nm	5.4 nm	9.34 nm
7.9 mol%	3	20°C	345 bar	449	8.1 nm	4.8	6.5 nm	5.9 nm	9.34 nm
7.9 mol%	1.5	35°C	345 bar	168	10.6 nm	6.3	9.3 nm	8.7 nm	9.16 nm
10 mol%	1.5	40°C	228 bar	1062	8.1 nm	7.5	5.1 nm	4.3 nm	-
Supercritical Ethane									
Cosolvent	W	Temp.	Pressure	N	Mean	StDev	Median	IQR	Model
-	1.5	35°C	517 bar	11468	6.5 nm	3.4	5.5 nm	3.0 nm	9.06 nm

frequency distribution due to the presence of larger particles most likely formed through agglomeration during particle collection. The larger particles were included in the particle size measurements in order to obtain a true measure of the particles synthesized experimentally. Due to the presence of the large particle aggregate outliers, which produce a skewed right distribution, a measure of the particle size synthesized can be more accurately obtained from the median particle size, as opposed to the mean particle size which can be distorted by outliers. The median provides an un-weighted, centrally located particle size with 50% of the particles above and 50 percent below. The range of the particle distributions can be identified by the standard deviation which relates to the mean or by the interquartile range, IQR. The IQR measures the range of particle diameters that makes up the middle 50% of the particles measured and discards the high and low 25%. The IQR allows for the treatment of outliers and is descriptive of the mono-dispersity of the particle size distribution where a lower IQR, represents a more mono-dispersed particle size distribution. From the results listed in Table 4-1 for copper particle synthesis in compressed propane at a constant pressure and W value, an increase in the median particle size is observed with an increase in the reaction pressure. The results listed for pressures of 241 bar, 276 bar and 317 bar correspond to the particle size distributions in Figure 4-2. With an increase in particle median diameter there is also an increase in the IQR and thus the range of particle sizes synthesized. This is also evident in Figure 4-2 where a broader and flatter distribution is obtained at higher pressures and can be attributed to the ability to synthesize larger particles as well as the smaller particles.

The increase in particle size with the increase in pressure of the compressed propane / AOT reverse micelle system is the result of the formation of a more stable microemulsion and the ability to sterically stabilize the particles in solution. Experimental results have shown that the water content also plays a role in the formation of copper nanoparticles. With a W value of 10, particle synthesis was not achieved and with a W value of 5, particle synthesis was not consistently reproducible in propane. For the cases of the higher water content, the microemulsion would break upon reduction and precipitation would occur. At W values less than 1.5, particle growth was not achieved due to the inability to get a complete reduction with hydrazine. It was found that in order to synthesize copper particles reproducibly, a W value of 1.5 to 3 is necessary in order to maintain a stable single phase system and achieve an effective chemical reduction of the copper ions. It must also be noted that the particle growth rate in propane (2-3 hrs) is observed to be much faster than for synthesis in liquid isooctane at similar W values (12-14 hrs) indicating less favorable solvent conditions and a less stable microemulsion⁴.

Figure 4-3 displays a TEM image of copper nanoparticles synthesized in propane / AOT / W=1.5 reverse micelle system at 241 bar T=21°C, $[CuAOT_2] = 5.53 \times 10^{-3} M$, $[AOT] = 5.53 \times 10^{-2} M$. The particle collection technique involved spray through 0.10 mm capillary tubing onto a TEM grid. Dodecanethiol stabilizing ligands were also implemented in particle collection with no noticeable effect on the particle sizes however the thiol capping may affect the surface properties of the particles. Additional TEM images are shown in Figure 4-4 for copper particles synthesized in propane at the pressures investigated.

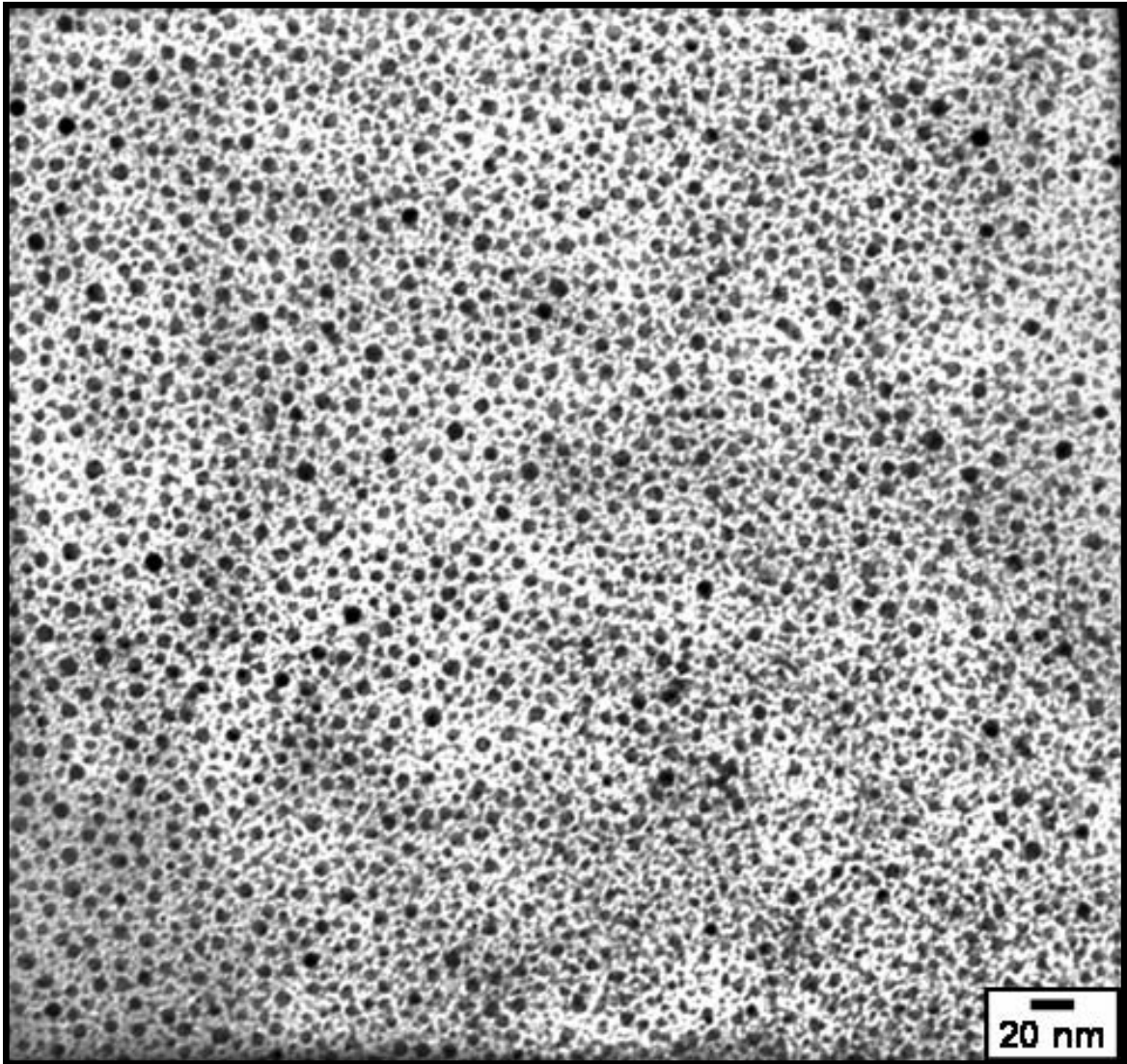


Figure 4-3. TEM image of copper nanoparticles synthesized in propane / AOT / W=1.5 reverse micelle system at 241bar T=21°C, $[\text{CuAOT}_2] = 5.53 \times 10^{-3} \text{M}$, $[\text{AOT}] = 5.53 \times 10^{-2} \text{M}$. Particles collected by spray techniques through capillary tubing.

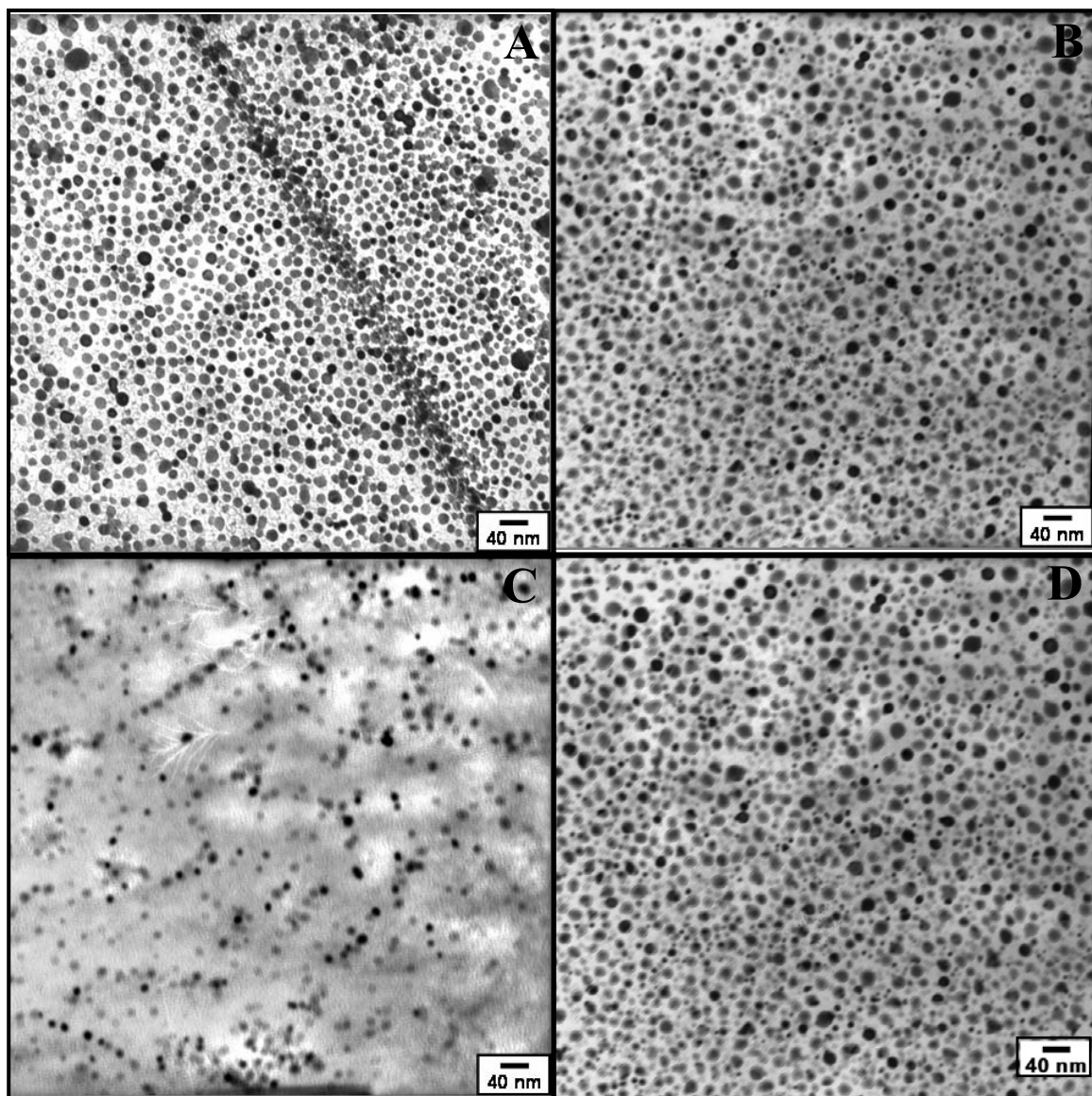


Figure 4-4 TEM images of copper nanoparticles synthesized in propane / AOT / W=2 reverse micelle system at bar T=21°C, $[CuAOT_2] = 5.53 \times 10^{-3} M$, $[AOT] = 5.53 \times 10^{-2} M$. Images A and B were synthesized at P=275 bar, Image C at 241 bar and Image D at P=345 bar.

4-3b. Compressed and SCF Ethane / AOT Reverse Micelle System

Synthesis in ethane without the use of a cosolvent requires a minimum pressure and was not achieved by Cason et. al.¹⁸ because adequate pressures were not implemented for particle synthesis. The modeling results discussed previously suggest that particle synthesis in compressed ethane at 20°C and in SCF ethane at 35°C require a minimum pressure of 400 bar and 500 bar respectively. In this study, copper nanoparticle synthesis was achieved in compressed and SCF ethane at a reaction pressure of 517 bar and temperatures of 20°C and 35°C with $[CuAOT_2] = 5.5 \times 10^{-3}$ M, $[AOT] = 5.5 \times 10^{-2}$ M and $W=1.5$. Figure 4-5 displays the particle growth curves for synthesis in compressed and SCF ethane which were measured by time resolved in-situ UV-Vis absorbance techniques⁴ where the average particle diameter dispersed in solution is plotted as a function of time. From the growth curves a particle growth rate can be obtained from the initial increase in particle diameter and an ultimate particle size can be obtained from the leveling off of the curve at later times. The particle growth curves suggest that particle synthesis in compressed ethane at 20°C results in a slightly larger particle size than in SCF ethane at 35°C and the same pressure with particle diameters of 5 nm and 4 nm respectively, thus corresponding to the modeling trends. The ultimate particle size obtained from the UV-Vis absorbance measurements at 35°C is smaller than the median particle diameter in Table 4-1 which may be due to the presence of particle aggregates from the particle collection. It is also evident that particle synthesis at elevated temperatures results in a significantly faster particle growth rate due to the increased kinetics of the intermicellar exchange mechanism responsible for particle synthesis. The increase in particle growth rate and decrease in particle size synthesized with an increase

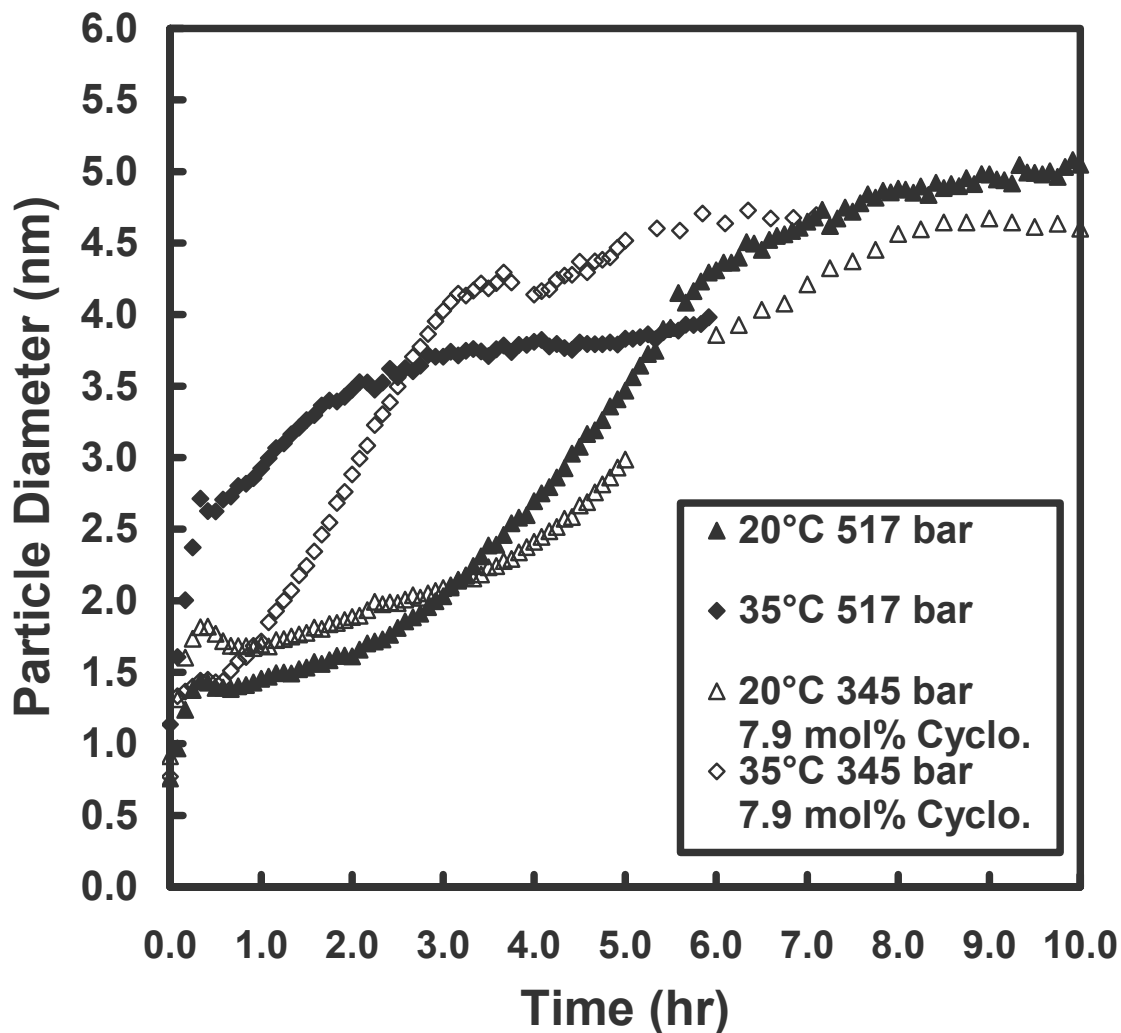


Figure 4-5. Copper particle growth curves plotted as the average particle diameter in solution as a function of time, measured by in-situ UV-Vis absorption techniques. The particle growth curves demonstrate the effects of temperature and cosolvent presence on particle synthesis in the AOT – ethane reverse micelle system.

in temperature may also be the result of a decrease in the stability of the microemulsion where decreased solvent interactions with the surfactant tails would result in the formation of a less rigid micelle and a decrease in the ability to synthesize larger diameter particles.

Figure 4-6 is a TEM image of copper nanoparticles synthesized in the SCF ethane / AOT reverse micelle system at 35°C and 517 bar with $W = 1.5$. The TEM image appears to exhibit a bi-modal distribution of the particle diameters consisting of smaller particles and slightly larger spherical aggregates which may have formed during the rapid depressurization of the spray process in particle collection. However, all particles observed were accounted for in the statistical analysis of the particle sizes listed in Table 4-1. The larger particle agglomerates observed lead to a skewed right distribution with the presence of larger outliers. The median particle diameter for synthesis in SCF ethane listed in Table 4-1 of 5.5 nm is slightly larger than the 4 nm particle diameter obtained from the particle growth curve in Figure 4-5 and smaller than the particle diameter predicted by the model. In this case the modeling results predicted the synthesis of larger particles and do not reflect the extent of particle size control through manipulations in temperature and pressure. However, the modeling results did prove extremely significant in the prediction of particle synthesis at elevated pressures of 400 bar at 20°C and 500 bar at 35°C which were not achieved previously.

Particle synthesis was also attempted at 45°C and 517 bar and upon reduction the characteristic color change of the system from blue to brown, indicating a successful reduction of the copper ions. The reduction was followed by progressive copper plating on the sapphire windows at this higher temperature, prohibiting in-situ UV-Vis analysis.

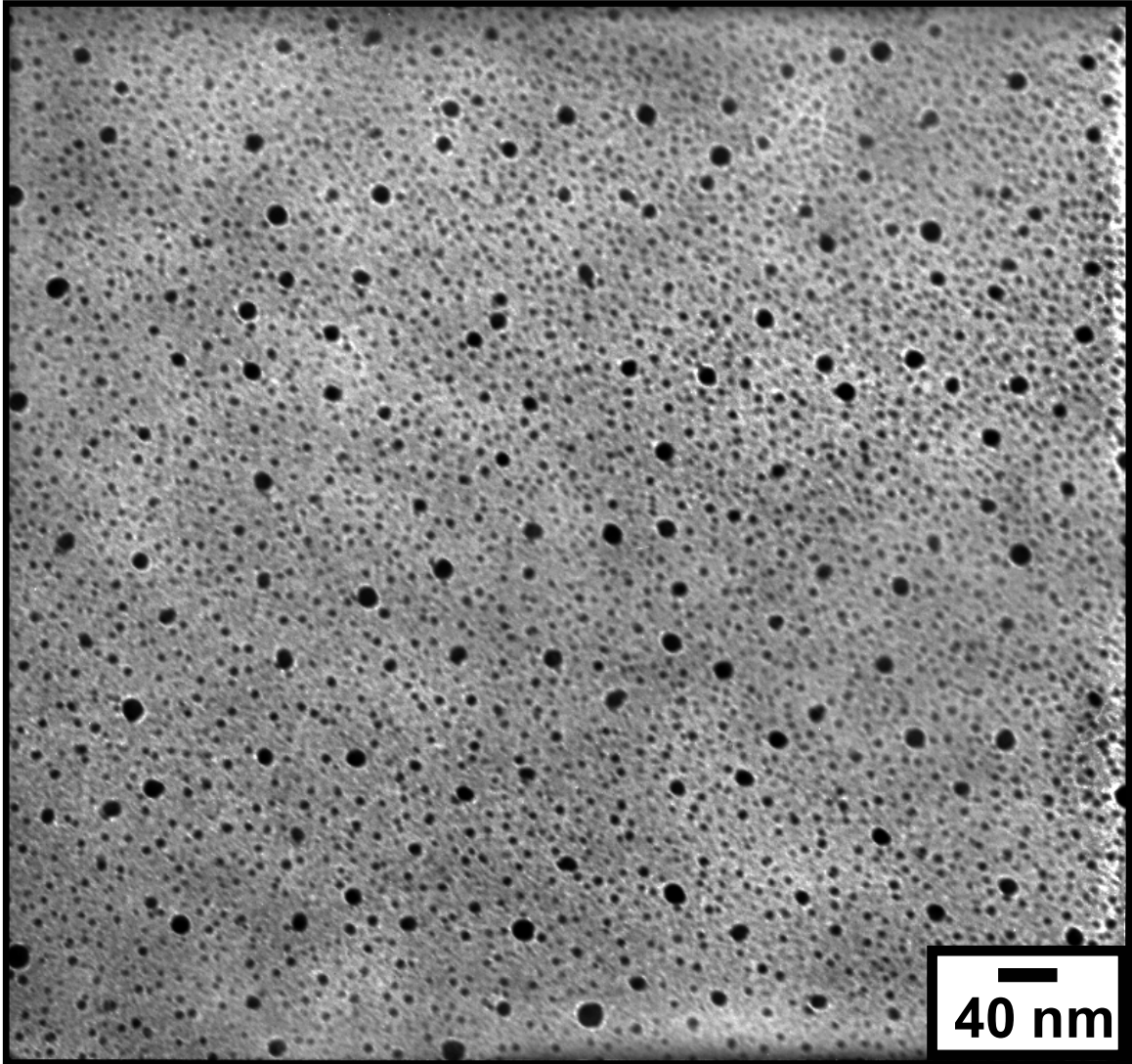


Figure 4-6. TEM image of copper nanoparticles synthesized in SCF ethane – AOT reverse micelle system with $[\text{CuAOT}_2]=5.5 \times 10^{-3}$, $[\text{AOT}]=5.5 \times 10^{-2}$ and $W=1.5$ at 35°C and 517 bar. Particles were collected by spray deposition through 0.1 micron capillary tubing.

Attempts to analyze the particles by TEM methods resulted in the observation of large agglomerations in the range of 100 nm to 1 μm . The modeling results predict particle synthesis would be achieved at 45°C and 550 bar however it is also possible that at the elevated temperatures, the AOT surfactant no longer acts as an effective stabilizing ligand and no longer has the ability to effectively sterically stabilize the synthesized particles in solution resulting in significant agglomeration and deposition.

4-3c. Ethane + Alkane Cosolvent / AOT Reverse Micelle System

The addition of liquid alkane cosolvents to the SCF ethane / AOT reverse micelle system creates a stable microemulsion necessary for copper nanoparticle synthesis and stabilization. Cason et al. demonstrated the ability to synthesize copper nanoparticles in SCF ethane with the addition of 14 volume percent isooctane¹⁸. The model predicts a significant decrease in pressure required for particle synthesis with the addition of a liquid alkane cosolvent to the ethane system, particularly cyclohexane. Thus cyclohexane would be the cosolvent of choice to promote particle synthesis. As proposed throughout this paper, the synthesis of copper nanoparticles parallels the trends of microemulsion stability and thus the trends observed for the addition of cosolvents to the ethane system for particle synthesis should mimic the effects on the microemulsion stability determined by phase behavior demixing measurements. Demixing pressures were measured for the ethane + cosolvent / AOT: CuAOT₂ / water microemulsion system at temperatures ranging from 20°C to 65°C and surfactant concentrations of [CuAOT₂] = 6.0x10⁻³ M and [AOT] = 6.0x10⁻² M. Figure 4-7 displays the demixing pressure measurements for the ethane system as a function of the W value, mol percent cosolvent

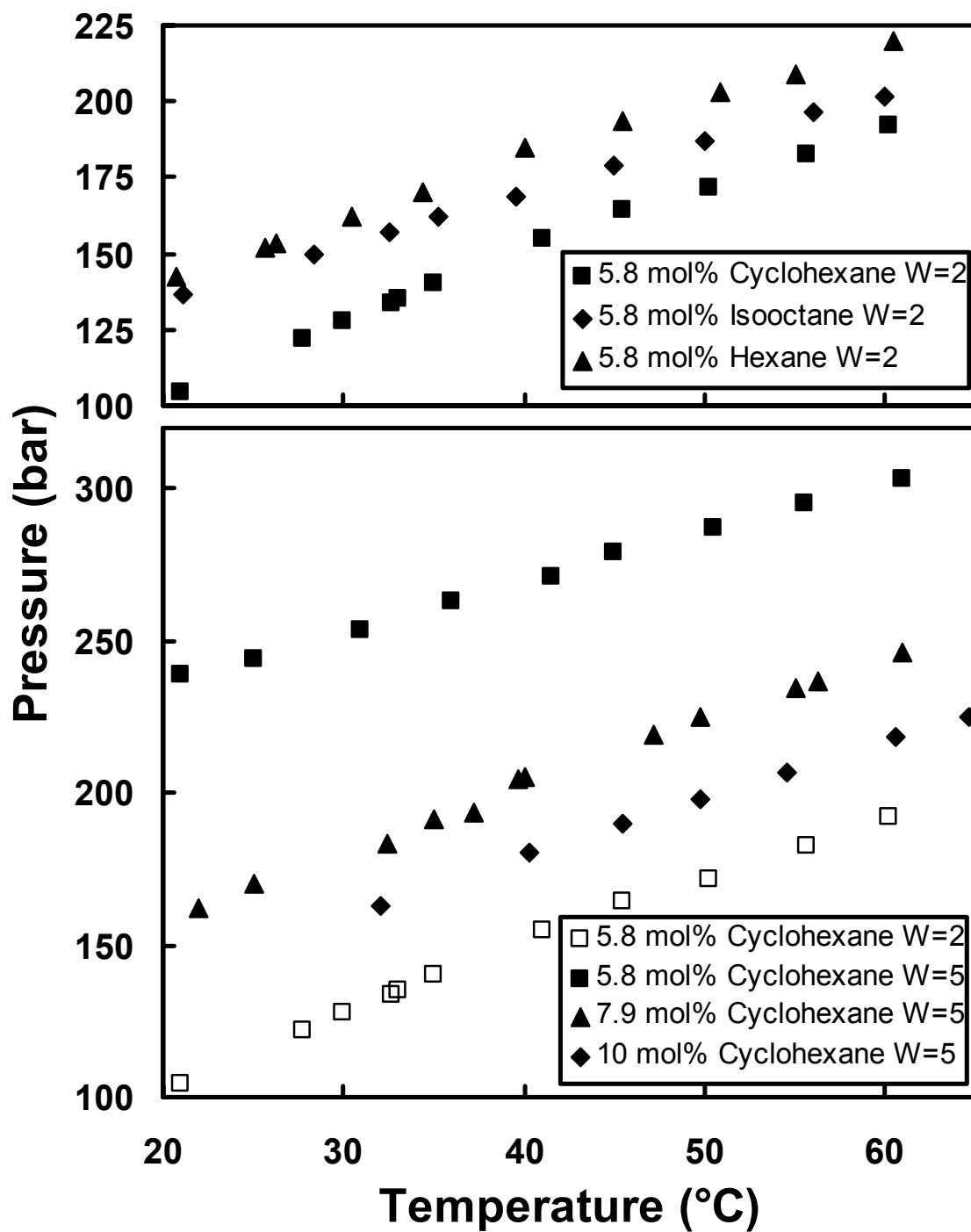


Figure 4-7. Demixing pressures for the ethane – cosolvent microemulsion system as a function of temperature, cosolvent mol fraction and water content with $[CuAOT_2] = 6.0 \times 10^{-3} \text{ M}$ and $[AOT] = 6.0 \times 10^{-2} \text{ M}$.

and cosolvent type. As the cosolvent is varied, the use of cyclohexane as the cosolvent results in a decrease in the demixing pressure and thus the formation of a more stable microemulsion. It is well known that the water content of a reverse micellar system can dramatically affect the demixing pressures and as the W value is increased from 2 to 5 a significant increase in the demixing pressure is observed in ethane with 5.8 mol percent cyclohexane. As the cyclohexane cosolvent is increased from 5.8 to 7.9 to 10.0 mol percent cyclohexane with $W = 5$, a decrease in the demixing pressure is observed. The phase behavior measurements display a consistent increase in the demixing pressure with increasing temperature, increasing W value and decreasing cosolvent mol fraction. The demixing pressure is a measure of the stability of the ethane + cosolvent / AOT: CuAOT_2 / water reverse micelle system, which is increased with the addition of liquid alkane cosolvent, particularly cyclohexane. Stability is also increased with an increase in the cosolvent volume fraction, a decrease in water content and at lower temperatures. Similarly, the trends toward microemulsion stability parallel the particle stabilization requirements for copper nanoparticle synthesis as well as particle size control.

Copper nanoparticle synthesis in the ethane – AOT reverse micellar system with cyclohexane as the cosolvent was achieved at the conditions listed in Table 4-1 with surfactant concentrations of $[\text{Cu}(\text{AOT})_2] = 5.5 \times 10^{-3} \text{ M}$ and $[\text{AOT}] = 5.5 \times 10^{-2} \text{ M}$. Particle synthesis was also achieved in ethane with 7.9 mol percent hexane and isooctane at 20°C ; however results for copper nanoparticle synthesis in the cyclohexane cosolvent system are presented here. Figure 4-5 displays the particle growth curves for particle synthesis with 7.9 mol percent cyclohexane with $[\text{CuAOT}_2] = 5.5 \times 10^{-3} \text{ M}$, $[\text{AOT}] = 5.5 \times 10^{-2} \text{ M}$ and $W = 1.5$ at 345 bar and temperatures of 20°C and 35°C . The particle

growth curves suggest that an average particle diameter of 4.5 nm are synthesized at both temperatures with an increased particle growth rate at 35°C and particle diameters similar to those obtained with a pure ethane bulk solvent at significantly higher pressures. Compared to the particle diameters listed in Table 4-1, a slightly larger median particle diameter was obtained from the TEM analysis at 20°C and a significant increase was observed at 35°C. The larger particle diameters obtained from TEM analysis can be attributed to particle agglomeration, especially at the increased temperature where the microemulsion stability is decreased. For many of the reaction systems, difficulties arose with the UV-Vis absorbance techniques due to copper plating on the windows and the decreased intensity of the absorbance peak as the particle synthesis reaction approached completion, preventing the measurement of the particle growth curves.

For synthesis with 5.8 mol percent cyclohexane, the characteristic color change of particle synthesis was observed but the characteristic 566nm absorbance peak was not pronounced. TEM samples were collected revealing the presence of very small particles with a particle diameter of 5.7 nm and a significant number of particles synthesized with $W = 1.5$ at 290 bar and 20°C. As the water content is increased to $W = 3$, a significant increase in the median particle size is observed as well as a decrease in the number of particles. This can be attributed to an increase in particle agglomeration resulting from a decrease in microemulsion stability due to the increase in water content despite the pressure increase. The decrease in microemulsion stability does not result in the inability to synthesize particles but rather decreases the ability of the AOT surfactant to sterically stabilize the particles and prevent agglomeration. An increase in the microemulsion stability is achieved with an increase to 7.9 mol percent cyclohexane where 6.1 nm and

6.5 nm median particle diameters are obtained for $W = 1.5$ and 3.0 respectively. This demonstrates that given a stable microemulsion system, the water content does not effect the particle size synthesized, which was also demonstrated in previous studies in liquid alkane systems^{2,4}.

Particle synthesis was achieved in ethane with 10.0 mol percent cyclohexane at 40°C and 228 bar where a median particle diameter of 5.1 nm was obtained despite the model predicting the inability to synthesize particles. For synthesis under these conditions, significant copper plating on the vessel windows was observed as well as the absence of the characteristic 566 nm absorbance band. The presence of significant outliers in the particle distribution observed from TEM analysis is evident from the difference in the median and mean particle diameter obtained from the statistical analysis. Simultaneously, a majority of the particles collected by the spray technique were on the order of 4 nm in diameter, the smallest obtained from each of the conditions investigated which resulted in particle synthesis. The occurrence of particle plating and agglomeration are indicators of microemulsion instability and a decreased strength of solvent interactions with the AOT stabilizing surfactant which essentially allows for the formation of smaller particles, as compared to synthesis in the analogous, conventional liquid systems.

Further work with metallic nanoparticle synthesis in compressed and SCF based reverse micelle system will include a study of particle aggregation and the use of stabilizing ligands such as alkane thiols to prevent agglomeration. Methods of particle deposition and post synthesis particle separation to remove agglomerations will be investigated for future applications of microemulsion based particle synthesis.

4-4. CONCLUSIONS

Copper nanoparticle synthesis in the compressed propane reverse micelle system has demonstrated that variations in the pressure have a direct effect on the ultimate particle size synthesized. By increasing the pressure of the microemulsion system, the solvent properties of the bulk propane phase are adjusted allowing for increased solvent interaction with the AOT surfactant tails and thus allowing for the synthesis and stabilization of larger particles in solution. Copper nanoparticle synthesis was also achieved in the ethane and ethane + cosolvent reverse micelle system under compressed and supercritical conditions. The ability to synthesize particles in reverse micellar systems hinges directly from the role of the AOT surfactant which acts to create a thermodynamically stable microemulsion and function as a particle stabilizing ligand.

The experimental results correspond with the trends and particle size predictions obtained from the total interaction energy model showing further evidence that copper nanoparticle synthesis within compressed and SCF reverse micelle systems is dependent on the thermophysical properties of the system. Overall this research has demonstrated that control over particle synthesis can be achieved by tailoring the thermophysical properties of the reverse micellar system, specifically the temperature and pressure of the compressed and supercritical solvents. This control provides the ability to synthesize particles with a median particle size ranging from 5.1 to 9.0 nm in diameter, providing smaller particle diameters and a wider envelope of particle sizes as compared to analogous conventional liquid systems. The use of compressed and supercritical fluids as the bulk phase also provides significant advantage through novel spray coating applications, as well as, effective solvent removal for particle collection by simply

depressurizing the system. The multifunctional role of the AOT surfactant is influential in particle synthesis, acting as a stabilizing ligand, size selectively dispersing synthesized particles in solution through steric interactions between the AOT tails and the bulk fluid.

4-5. REFERENCES

- (1) Bagwe, R. P.; Khilar, K. C. *Langmuir* 2000, *16*, 905-910.
- (2) Cason, J. P.; Miller, M. E.; Thompson, J. B.; Roberts, C. B. *Journal of Physical Chemistry B* 2001, *105*, 2297-2302.
- (3) Towey, T. F.; Khanlodhi, A.; Robinson, B. H. *Journal of the Chemical Society-Faraday Transactions* 1990, *86*, 3757-3762.
- (4) Kitchens, C. L.; McLeod, M. C.; Roberts, C. B. *J. Phys. Chem. B.* 2003, *107*, 11331-11338.
- (5) Fulton, J. L.; Smith, R. D. *Journal of Physical Chemistry* 1988, *92*, 2903-2907.
- (6) Gale, R. W.; Fulton, J. L.; Smith, R. D. *Journal of the American Chemical Society* 1987, *109*, 920-921.
- (7) McFann, G. J. In *Chemical Engineering*; University of Texas at Austin, 1993, p 395.
- (8) Tingey, J. M.; Fulton, J. L.; Smith, R. D. *Journal of Physical Chemistry* 1990, *94*, 1997-2004.
- (9) Smith, R. D.; Fulton, J. L.; Blitz, J. P.; Tingey, J. M. *Journal of Physical Chemistry* 1990, *94*, 781-787.
- (10) Eastoe, J.; Steytler, D. C.; Robinson, B. H.; Heenan, R. K. *Journal of the Chemical Society-Faraday Transactions* 1994, *90*, 3121-3127.
- (11) Eastoe, J.; Young, W. K.; Robinson, B. H.; Steytler, D. C. *Journal of the Chemical Society-Faraday Transactions* 1990, *86*, 2883-2889.
- (12) Kaler, E. W.; Billman, J. F.; Fulton, J. L.; Smith, R. D. *Journal of Physical Chemistry* 1991, *95*, 458-462.
- (13) Eastoe, J.; Robinson, B. H.; Steytler, D. C. *Journal of the Chemical Society-Faraday Transactions* 1990, *86*, 511-517.
- (14) Eastoe, J.; Robinson, B. H.; Visser, A.; Steytler, D. C. *Journal of the Chemical Society-Faraday Transactions* 1991, *87*, 1899-1903.
- (15) McFann, G. J.; Johnston, K. P. *Journal of Physical Chemistry* 1991, *95*, 4889-4896.
- (16) Bartscherer, K. A.; Minier, M.; Renon, H. *Fluid Phase Equilibria* 1995, *107*, 93-150.
- (17) Holmes, J. D.; Lyons, D. M.; Ziegler, K. J. *Chemistry-a European Journal* 2003, *9*, 2144-2150.
- (18) Cason, J. P.; Roberts, C. B. *Journal of Physical Chemistry B* 2000, *104*, 1217-1221.

- (19) Shah, P. S.; Holmes, J. D.; Johnston, K. P.; Korgel, B. A. *Journal of Physical Chemistry B* 2002, 106, 2545-2551.
- (20) Shah, P. S.; Novick, B. J.; Hwang, H. S.; Lim, K. T.; Carbonell, R. G.; Johnston, K. P.; Korgel, B. A. *Nano Letters* 2004, 3, 1671-1675.
- (21) Eastoe, J.; Fragneto, G.; Robinson, B. H.; Towey, T. F.; Heenan, R. K.; Leng, F. J. *Journal of the Chemical Society-Faraday Transactions* 1992, 88, 461-471.
- (22) Cason, J. P.; Khambaswadkar, K.; Roberts, C. B. *Industrial & Engineering Chemistry Research* 2000, 39, 4749-4755.
- (23) www.scioncorp.com; Beta 4.0.2 ed.; Scion Corporation.

CHAPTER 5

5. SOLVENT EFFECTS ON AOT REVERSE MICELLES IN LIQUID AND COMPRESSED ALKANES INVESTIGATED BY NEUTRON SPIN-ECHO SPECTROSCOPY

5-1. INTRODUCTION

Neutron Spin Echo (NSE) spectroscopy has been employed to study the interfacial properties of reverse micelles formed with AOT surfactant. NSE spectroscopy is a relatively new technique which provides means to measure small changes in energy on the nanosecond time scale and has been implemented in the study of various colloidal systems. NSE offers the unique ability to perform dynamic measurements of thermally induced shape fluctuation in the AOT surfactant monolayer. This study investigates the effects of the bulk solvent properties, water content, and the addition of octanol co-surfactant on the bending elasticity of AOT reverse micelles and the influences on reverse micelle dynamics. By altering these properties, specific trends in the bending elasticity constant, k , are observed where increasing k corresponds to an increase in micelle rigidity. We have also investigated the use of compressed propane as an adjustable bulk solvent where variations in temperature and pressure are used to tune the properties of the bulk phase. A decrease in the bending elasticity is observed for the d-propane / AOT / W = 8 reverse micelle system by simultaneously increasing the temperature and pressure to achieve a constant density and viscosity while maintaining a constant translational diffusion of the reverse micelles through the bulk phase.

AOT reverse micelles are thermodynamically stable dispersions of spherical water droplets within a bulk oil phase where the surfactant provides structure and stability. Simultaneously, the reverse micelles are very dynamic in nature consisting of translational diffusion, shape deformations and intermicellar exchange of the aqueous cores¹. Gale et. al.² first demonstrated the ability to synthesize AOT reverse micelles in compressed propane and supercritical ethane. Since then AOT reverse micelles dispersed within compressed and supercritical alkanes have been studied by a wide variety of techniques including: phase behavior and conductivity measurements to determine water uptake, phase transitions and stability; dynamic light scattering (DLS), small angle x-ray scattering (SAXS) and small angle neutron scattering (SANS) to determine structure and size; and fluorescence and solvatochromic spectroscopic methods to characterize local environments. In this study, the method of Neutron Spin Echo Spectroscopy (NSE) is used to determine the effects of water content and bulk solvent properties on AOT reverse micelle dynamics in hexane, cyclohexane, and compressed propane solvents with variations in temperature and pressure.

Neutron spectroscopy provides unique instrumentation for the study of colloidal systems based on the premise that neutrons possess a neutral charge and interact solely with the atomic nuclei and hydrogen in particular, thus making non-hydrogenated species virtually transparent to neutrons. Using contrast variation methods and forming AOT reverse micelle microemulsions with deuterated water, deuterated bulk solvent and hydrogenated AOT surfactant, the motions of the AOT surfactant monolayer can be isolated. Neutron Spin Echo is complementary to the more common Small Angle

Neutron Scattering (SANS) technique, however NSE allows for dynamic measurements of the scattering system while SANS only relates a static picture. SANS has been widely used in studying microemulsion systems in order to determine the size and shape of surfactant aggregates by measuring elastic neutron scattering. NSE is a quasielastic method which can be used to measure excitations in the range of 0.01 to 200 nanoseconds, bridging the gap in time scale between conventional inelastic neutron spectroscopy and dynamic light scattering (DLS). The ability to measure shape fluctuations in thin films and micellar diffusion with NSE affords a powerful technique for studying reverse micelle dynamics³⁻⁹.

5-2. REVERSE MICELLE MICROEMULSION BACKGROUND

Properties of surfactant films include interfacial tension, rigidity, spontaneous curvature, saddle-splay elasticity and bending elasticity, each of which are dependant on the surfactant structure, additives, ionic strength, solvent properties and temperature¹⁰⁻¹². The Helfrich stabilization model, equation 1, has proven to be able to successfully relate the bending energy of a spherical microemulsion droplet to the bending elasticity k , saddle-splay elasticity \bar{k} , and the spontaneous curvature¹¹. The Helfrich expression includes two radii of curvature R_1 and R_2 and the spontaneous radius of curvature R_s .

$$E_{bend} = \frac{k}{2} \int dS \left(\frac{1}{R_1} + \frac{1}{R_2} - \frac{2}{R_s} \right)^2 + \bar{k} \int dS \frac{1}{R_1 R_2} \quad (1)$$

The surfactant film properties largely control micelle dynamics and play an important role in micelle kinetics with applications to reactions and nanomaterial synthesis. In a previous study, we demonstrated that the interactions of the bulk alkane

solvent with the AOT surfactant tails affect the growth rate of copper nanoparticles within the AOT reverse micelle system. In particular, the growth rate in cyclohexane was shown to be considerably lower than in other n-alkane liquid solvents¹³. The growth rate of metallic nanoparticles within AOT reverse micelles is related to an intermicellar exchange process by which the contents of the aqueous cores of two reverse micelles are exchanged resulting in the combination of the metallic species within the cores and the growth of metallic nanoparticles. Similar results were observed by Towey et. al. where an increase in the growth rate of quantum sized cadmium sulfide particles within the AOT reverse micelles was observed as the solvent was altered from cyclohexane to heptane to decane¹⁴. Investigations of other reaction systems have demonstrated similar trends for the effects of the bulk solvent properties on the intermicellar exchange rate^{15,16}. In particular, Fletcher et. al. performed an in depth study of the solvent effects on the kinetics of the AOT intermicellar exchange rate. They observed an increase in the intermicellar exchange rate with increasing chain length of n-alkane solvents as well as a significantly slower exchange rate with cyclohexane as the bulk solvent¹.

The water content of the AOT reverse micelle system, where $W = [\text{H}_2\text{O}] / [\text{AOT}]$, is related to the radius of the reverse micelle water core by the following relation¹⁷: $R(\text{nm}) = 0.18 W$. Fletcher et. al. demonstrated a decrease in the intermicellar exchange rate with increasing water content when $W > 10$. Additional studies on intermicellar exchange rates and reverse micelle mediated reactions, including our study on copper nanoparticle synthesis^{1,13,14,16,18}, have demonstrated that a decrease in the intermicellar exchange or particle growth rate occurs as the water content is increased for higher water contents with $W > 10$. Additionally, these studies have also demonstrated a decrease in

the exchange and growth rates as the water content is decreased with $W < 10$. Comprehensive review of these results suggest a maximum in the exchange and growth rates in the vicinity of $W = 10$ ^{1,14,18-23}.

Many of the discussions concerning intermicellar exchange rates and nanoparticle growth rates within AOT reverse micelles suggest that the physical properties of the AOT monolayer govern micelle dynamics and particle synthesis within the media. The property most commonly referred to is the micelle rigidity, however the physical properties of surfactant monolayers also includes lateral elasticity, bending elasticities, interfacial forces and spontaneous curvature. Helfrich's model accounts for each of these contributions to the interfacial elasticity of surfactant monolayers. Values for the parameters have been determined by a variety of macroscopic and microscopic techniques with somewhat inconsistent results. Binks et. al. determined the bending elasticity constant for AOT aggregates in brine systems using macroscopic interfacial tension and ellipsometry measurements and found that the bending elasticity, k , decreased with increasing chain length from n-heptane to n-tetradecane with values ranging from 1.1 to 0.6 $k_B T$ respectively²⁴. Other methods, including DLS and SANS have been used to probe the properties of the AOT surfactant monolayer allowing determination of the micelle size, shape and polydispersity by scattering techniques. Both light and neutron scattering methods are based on Bragg's law as a function of the momentum transfer function, Q where $Q = 4\pi\sin(\theta)/\lambda$, 2θ is the scattering angle and λ is the wavelength of incident light or neutrons²⁵. The polydispersity values obtained for AOT reverse micelles, as well as other colloidal systems, have been indirectly used to determine values for the bending elasticity of surfactant layers, both independently and in

conjunction with other methods. The various methods used to determine the bending elasticities for the liquid phase AOT system have resulted in inconsistencies in the values reported throughout the literature. NSE has been demonstrated to be an effective method for determination of the bending elasticities of surfactant monolayers based on the abilities to accurately measure small changes in energy on the order of 10^{-5} to 10^{-2} meV and time scales of 0.01 to 100 ns³.

The spontaneous curvature, saddle splay elasticity and bending elasticity can be determined from shape fluctuations in the reverse micelles which are measured by NSE. This study examines the effect of the bulk solvent and water content on the properties of the AOT reverse micelles. The liquid alkane solvents investigated include d-hexane, d-cyclohexane, and d-decane, which are similar in composition but vary in structure, viscosity, and solvent strength. The influence of the W value on micelle dynamics is also of interest due to the demonstrated effects on the intermicellar exchange rate. Compressible fluids used to form microemulsions afford the ability to adjust the properties of the microemulsion by taking advantage of the tunable solvent properties. Previous temperature and pressure studies on AOT reverse micelles involving NSE employed d-decane as a fairly incompressible bulk solvent that exhibits a critical phase transition in the vicinity of the operating conditions. The compressed propane microemulsion is a thermodynamically stable system over a wide range of temperatures and pressures allowing for significant adjustments in the density and thermophysical properties of the bulk solvent. In this study, the effects of varying bulk compressed propane solvent properties on the dynamics of microemulsions through changes in temperature and pressure are investigated using neutron scattering techniques

5-3. NEUTRON SCATTERING BACKGROUND

The most widely used method of neutron scattering for the study of microemulsion systems is SANS, which is effective in determining the size and shape of surfactant aggregates. SANS techniques have been used extensively in studying microemulsions as they exist in single and multiple phases in order to understand the thermodynamics and interaction energetics associated with phase transitions at various positions on the oil / water / surfactant ternary phase diagram²⁶⁻³¹. The studies of AOT microemulsions in compressed propane and ethane³²⁻³⁶ using SANS were influential in determining the ability to form a stable microemulsion as well as temperature and pressure effects on the phase behavior and reverse micellar interactions. As mentioned previously, reverse micelles are very dynamic systems and describing their structure using SANS requires the use of a polydispersity term which accounts for the range of micelle diameters observed by the “static picture” of the entire microemulsion system. The polydispersity is related to spherical reverse micelles by equation 2 where R_0 is the mean radius, R_s is the radius of spontaneous curvature and $f(\phi)$ is the mixing entropy per droplet as a function of the volume fraction ϕ ^{6,37,38}.

$$p^2 = \frac{k_B T}{4\pi} \left[6(2k + \bar{k}) - 8k \frac{R_0}{R_s} - \frac{3k_B T}{2\pi} f(\phi) \right]^{-1} \quad (2)$$

The polydispersity equation also demonstrates the contribution of the bending elasticity k and saddle-splay elasticity \bar{k} and in several studies values of the elastic terms have been determined from SANS measurements^{9,39}. Comparison of the bending elasticity terms obtained from SANS with other methods of determination reveal significant inconsistencies which have been discussed in the literature^{8,40-43}. Typical values of k are

on the order of $k_B T$ or smaller, however the values obtained from SANS measurements are generally higher^{39,44} which may be a result of the dynamic fluctuations not being measured directly as is achieved with NSE^{40,45}.

The principals of NSE are based on neutrons which possess spin and magnetic moment. Neutrons undergo precession in magnetic field with the Larmor frequency which depends on the strength of the magnetic field. The neutron precession can be used as an internal clock for each neutron which allows for the measurement of very small velocity changes in the neutron beam due to quasi-elastic scattering by measuring the phase difference in the precession. From the phase difference, an inelasticity term can be separated and related to a change in wavelength allowing for the measurement of very small changes in energy on the order of 10^{-5} to 10^{-2} meV. From the measurements taken, an intermediate scattering function, $I(Q,t) / I(Q,0)$ is obtained which can be related to the effective diffusion coefficient, D_{eff} by equation 3 where t is the decay time.

$$\frac{I(Q,t)}{I(Q,0)} = \exp[-D_{\text{eff}}(Q)Q^2t] \quad (3)$$

The Q -dependant effective diffusion is comprised of a translational diffusion coefficient, D_{tr} , and a deformation diffusion coefficient, $D_{\text{def}}(Q)$ representative of the droplet shape deformations (equation 4). The energy associated with droplet deformations resulting from thermal fluctuations in the surfactant monolayer can be used to determine the spontaneous curvature of the AOT film, the saddle-splay modulus, polydispersity of the micelles and in particular the bending modulus of elasticity of the AOT monolayer⁴⁵⁻⁴⁷.

$$D_{eff}(Q) = D_{tr} + D_{def}(Q) \quad (4)$$

$$D_{def}(Q) = \frac{5\lambda_2 f_2(QR_0) \langle |a_2|^2 \rangle}{Q^2 [4\pi [j_0(QR_0)]^2 + 5f_2(QR_0) \langle |a_2|^2 \rangle]} \quad (5)$$

$$\text{with } f_2(QR_0) = [4j_2(QR_0) - QR_0 j_3(QR_0)]^2$$

From the Q-dependant $D_{def}(Q)$ term, equation 5 is used to determine values for the damping frequency of the droplet deformation λ_2 and the mean square displacement of the 2nd mode spherical harmonics $\langle |a_2|^2 \rangle$ where $j_n(x)$ is the n^{th} spherical Bessel function and R_0 is the mean droplet radius³⁷. The λ_2 and $\langle |a_2|^2 \rangle$ terms are obtained by fitting $D_{def}(Q)$ with equation 5 as a function of Q . λ_2 is related to the elastic properties of the reverse micelle by equation 6 where η is the bulk solvent viscosity and η' is the D₂O core viscosity. Using the methods of Kawabata et. al.^{37,48} based on the theory of Milner and Safran,⁶ k is determined by equation 7 from combining equations 2 and 6.

$$\lambda_2 = \frac{k}{\eta R_0^3} \left[4 \frac{R_0}{R_s} - 3 \frac{\bar{k}}{k} - \frac{3k_B T}{4\pi k} f(\phi) \right] \frac{24\eta}{23\eta' + 32\eta} \quad (6)$$

$$k = \frac{1}{48} \left[\frac{k_B T}{\pi p^2} + \lambda_2 \eta R_0^3 \frac{23\eta' + 32\eta}{3\eta} \right] \quad (7)$$

Previous neutron spectroscopy studies on AOT and other surfactant systems have concentrated mainly on microemulsion phase transitions, as well as, micelle structure, dynamics, and shape fluctuations. Huang and co-workers have performed several studies on the AOT reverse micelle system with decane as the bulk phase including the effects of water content for $W = 8$ to 40 ⁴⁹, as well as, the effects of pressure and the addition of butanol cosurfactant²⁶. The bending elasticity and diffusion constant were found to be

unaffected by the variations in W although a majority of the W values investigated were rather large compared to those studied for many applications, including nanoparticle synthesis. At lower W values, the surfactant head groups have a greater influence on the water environment and can limit the mobility of the water¹. The addition of butanol co-surfactant to the AOT – decane system was found to result in a decrease in the bending modulus^{26,50}. Takeda and co-workers^{4,5} have also used NSE to study the temperature and pressure effects on AOT reverse micelles dispersed in decane⁵¹⁻⁵³. It was found that an increase in temperature and decrease in pressure result in a decrease in k for both the two phase system⁵¹ and with $W = 18.4$ (conditions similar to the current study)³⁷. An increase in pressure was found to increase the rigidity of the AOT membrane while the membrane becomes more flexible with temperature increases. In a later study it was concluded that size fluctuations and droplet diffusion are enhanced by increasing the temperature as well as decreasing the pressure⁵³. These results were observed with decane, a relatively incompressible fluid as the bulk solvent, which leads to an interesting question concerning the effects of temperature and pressure on the reverse micelle shape fluctuations dispersed in a compressible fluid such as propane or ethane.

The goal of this study is to investigate the role of the bulk solvent and water content on the elasticity properties of the AOT reverse micelle system. The deuterated bulk solvents studied include cyclohexane, hexane, decane, and compressed propane. Each of the solvents form single phase, stable reverse micelle microemulsions at the conditions investigated and regions of phase transitions were avoided. The liquid solvents, cyclohexane and hexane, were implemented as alkane solvents with the same carbon number with differences in molecular structure, density, viscosity, and strength of

interaction with the AOT surfactant tails. The cyclohexane and hexane results were compared with decane results from the work of Kawabata and co-workers^{37,53} and measurements performed at the 2003 NIST Center for Neutron Research (NCNR) Summer School on Methods and Applications of Neutron Spectroscopy. Decane is a straight chain solvent with density and viscosity more comparable to cyclohexane than hexane. Compressed propane was also investigated as the bulk solvent where adjustments in temperature and pressure result in variation of the bulk solvent properties. The influence of water content in the cyclohexane system was investigated for W values of 5, 10, and 18. The addition of octanol co-surfactant to the cyclohexane, W = 10, microemulsion was also studied. Investigation of these aspects of the AOT reverse micelle system by neutron spectroscopy will provide further insight into the system and the governing properties of micelle dynamics with applications to the kinetics of nanoparticle formation.

5-4. EXPERIMENTAL

The liquid phase microemulsions consisted of d_{12} -cyclohexane (99.5% D from Norell Inc.) or d_{14} -hexane (99% D from Sigma-Aldrich) as the bulk organic solvent, 0.137 M AOT Surfactant (Sigma-Aldrich) and the necessary amount of D_2O (Norell Inc.) for the desired water content. The addition of 1-octanol (Sigma-Aldrich) at 1.0 vol. % was simply added to the stable microemulsion. The resulting microemulsions were single phase, stable, clear and colorless solutions. The solutions investigated included W values of 5, 10 and 18 in d-cyclohexane bulk solvent, W = 10 with d-hexane bulk solvent, and W=10 in d-cyclohexane with 1.0 volume % 1-octanol. Typically W is referred to as

the molar ratio of H₂O to surfactant, however for the contrast matching neutron scattering measurements it is necessary to use D₂O and for simplicity W will be used interchangeably for both cases.

The AOT reverse micelle microemulsion in compressed alkanes consisted of d₈-propane (98% D from Cambridge Isotope Labs) with 0.06 M AOT. The microemulsion was formed within a custom built 316 stainless steel high-pressure vessel, specifically designed and built for high-pressure NSE measurements at Auburn University. Details on the design of the high pressure vessel and the heating block assembly can be found in Appendix D. The vessel design consists of two circular sapphire windows (12.5 mm thick, 44.45 mm diameter) sealed with Viton o-rings and three 1/8" HiP fittings for inlet/outlet, RTD temperature control, 10,000 psi relief valve and a Heise digital pressure gauge. The capacity of the vessel is approximately 8ml with a path length of 6.2mm which was reduced to 3.0mm with the addition of quartz spacer windows. The accessible sample area for the neutron beam was 38.1 mm in diameter to obtain the maximum signal from the 35mm diameter neutron beam. An aluminum heating block was also constructed for temperature control using a silicone oil temperature bath and RTD temperature control device. The vessel was pressure tested to 500 bar for 48 hours without rupture.

5-4a. SANS Measurements

The SANS measurements were performed at the NIST Center for Neutron Research on the NG1 8m SANS with a distance of 3.6m from the sample to the 2-D detector. The liquid phase microemulsions were loaded in 1.0mm path length SANS

liquid sample holders. The wavelength of incident neutrons was 10\AA with a momentum transfer (Q) range from 0.006\AA^{-1} to 0.1\AA^{-1} . The compressed propane SANS measurements were performed using the high pressure vessel with a path length of 3.0mm. The wavelength of incident neutrons was 6\AA with q from 0.01\AA^{-1} to 0.17\AA^{-1} . Data reduction and fitting was done with Igor Pro 5.01 software.

5-4b. NSE Measurements

The NSE measurements were performed at the NIST Center for Neutron Research on the NG5 Neutron Spin Echo Spectrometer with 6\AA wavelength neutrons and $\Delta\lambda/\lambda = 17.5\%$. Measurements included the samples, backgrounds (vessel + solvent at each condition) and CarboPac (completely inelastic scattering sample to measure instrument resolution) at each of the Q values, and the percent transmission of the neutron beam for each sample. For each sample the detector was positioned at four different scattering angles to encompass the desired Q ranges, the Fourier times were determined by the decay rate of the intermediate scattering function and the collection times were determined by the intensity of the scattered neutrons.

5-5. RESULTS AND DISCUSSION

5-5a. SANS Measurements

The liquid alkane phase AOT reverse micelle microemulsion was investigated using SANS with hexane as the bulk solvent and $W=10$, as well as, in cyclohexane with $W = 5, 10, \text{ and } 18$. The addition of 1.0 volume % 1-octanol co-surfactant to cyclohexane with $W=10$ was also investigated. Figure 5-1 displays the SANS results, plotting

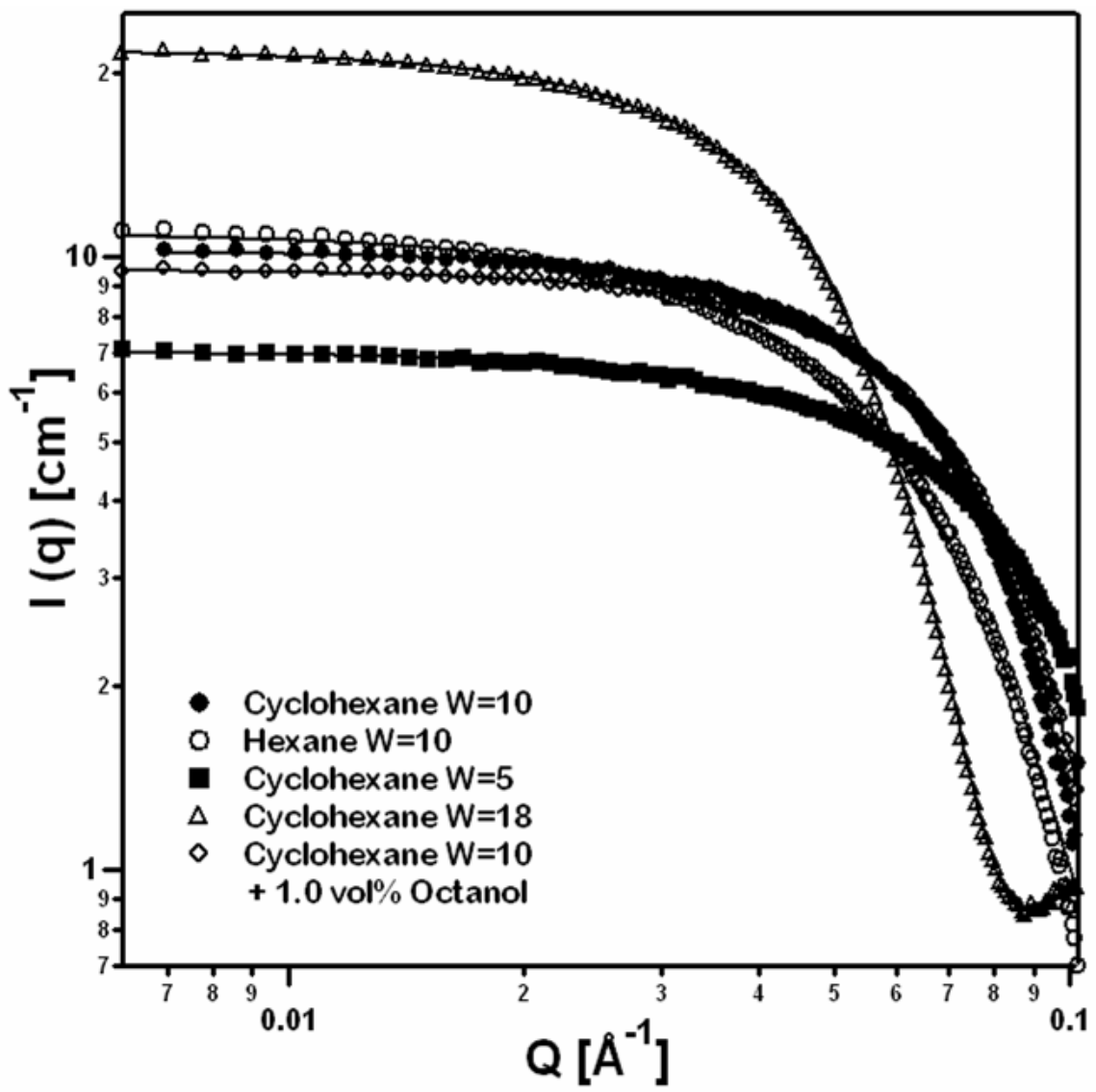


Figure 5-1. SANS results for liquid phase AOT reverse micelle microemulsion with $[\text{AOT}] = 0.137 \text{ M}$ and varying bulk solvent, W value and octanol additive. The solid lines represent the PCF-HS modeling fit of the data points.

the scattered intensity ($I(Q)$) as a function of Q on a log – log scale. The information obtained from SANS is a static measurement which takes an overall picture of the system and has been widely used on emulsion systems to determine size and geometry of surfactant aggregates. The reverse micelle system studied consists of a bulk solvent and water core have been contrast matched in order to isolate the surfactant shell. The reverse micelles are modeled with a poly core form factor $P(Q)$ which, describes monodisperse spherical particles with a core shell structure, and a hard sphere structure factor $S(Q)$ which accounts for hard sphere interparticle interaction.

$$I(Q) = nP(Q)S(Q) \quad (8)$$

The variables taken into account by the poly core form – hard sphere (PCF-HS) model include the micelle volume fraction, average core radius (\AA), polydispersity, shell thickness (\AA), scattering length density (SLD) of the core (\AA^{-2}), shell SLD (\AA^{-2}), solvent SLD (\AA^{-2}) and the background (cm^{-1}). The terms held constant during the fitting of the SANS data include the micelle volume fraction determined from the experimental conditions, the shell SLD for AOT at $6.42 \times 10^{-7} \text{\AA}^{-2}$ as obtained from the literature,⁵⁴ and the solvent SLD at values of $6.7 \times 10^{-6} \text{\AA}^{-2}$ and $6.14 \times 10^{-6} \text{\AA}^{-2}$ for d-cyclohexane and d-hexane respectively as determined by equation 9 by the atomic contribution of the bound coherent scattering length for n atoms in the solvent molecule⁵⁵.

$$\text{SLD} = \frac{\sum_{i=1}^n b_{c_i}}{v_m} \quad (9)$$

The background values were measured by the scattering of the pure solvents over the Q

range and were fixed at 0.08 cm^{-1} for d-cyclohexane and 0.1 cm^{-1} for d-hexane. The average core radius, polydispersity, shell thickness and core SLD were determined from the model fitting. For the case of the d-hexane $W=10$ system, it was necessary to fix the shell thickness in order to obtain acceptable results from the model and a shell thickness of 10 \AA was assumed based on the cyclohexane results and previously reported values⁵⁶. The D_2O core SLD was allowed to vary during the curve fitting and an initial value of $6.37 \times 10^{-6} \text{ \AA}^{-2}$ was used. The results obtained from the data fitting confirm the core-shell structure and are listed in Table 5-1 and the reverse micelle radius is obtained from the sum of the core radius and the shell thickness. The results demonstrate the expected decrease in core radius with decreasing W as well as a decrease in the scattering length density of the core which maybe the result of an increased influence of the surfactant head group or the presence of hydrogenated water that was not removed during surfactant drying. The polydispersity is influenced by the bulk solvent as well as the water content at low W values. An increased polydispersity was observed with d-hexane as the bulk solvent, compared to d-cyclohexane. An increase in polydispersity is also observed in d-cyclohexane with $W = 5$ compared to $W = 10$ and 18 . Interestingly, the addition of 1.0 volume percent octanol, known to act as a co-surfactant, had negligible effect on the polydispersity and micelle size. In contrast, the addition of butanol co-surfactant to the AOT – decane reverse micelle system was reported to increase the polydispersity²⁶.

Figure 5-2 plots the measured SANS intensity as a function of Q for the AOT / d-propane / D_2O microemulsion with $W = 3$, $[\text{AOT}] = 0.06\text{M}$ and temperatures of 20°C and 35°C and pressures of 138, 241 and 345 bar with solvent densities ranging from 11.57 to 12.63 mol/L. The SANS data reveal very little change with temperature and pressure

Table 5-1. Results obtained from the PCF-HS model fit of the SANS data for the liquid phase AOT microemulsions.

	Hexane W=10	Cyclohexane W=5	Cyclohexane W=10	Cyclohexane W=18	Cyclohexane W=10 + 1.0 vol% Octanol
Volume Fraction	0.079	0.066	0.079	0.099	0.089
Avg. Core Rad. (Å)	17.9	12.4	18.1	31.7	18.0
Polydispersity	0.39	0.33	0.24	0.22	0.24
Shell Thickness (Å)	10.0	10.3	10.5	10.0	9.7
SLD core (Å⁻²)	4.09E-06	3.34E-06	5.68E-06	5.91E-06	5.48E-06

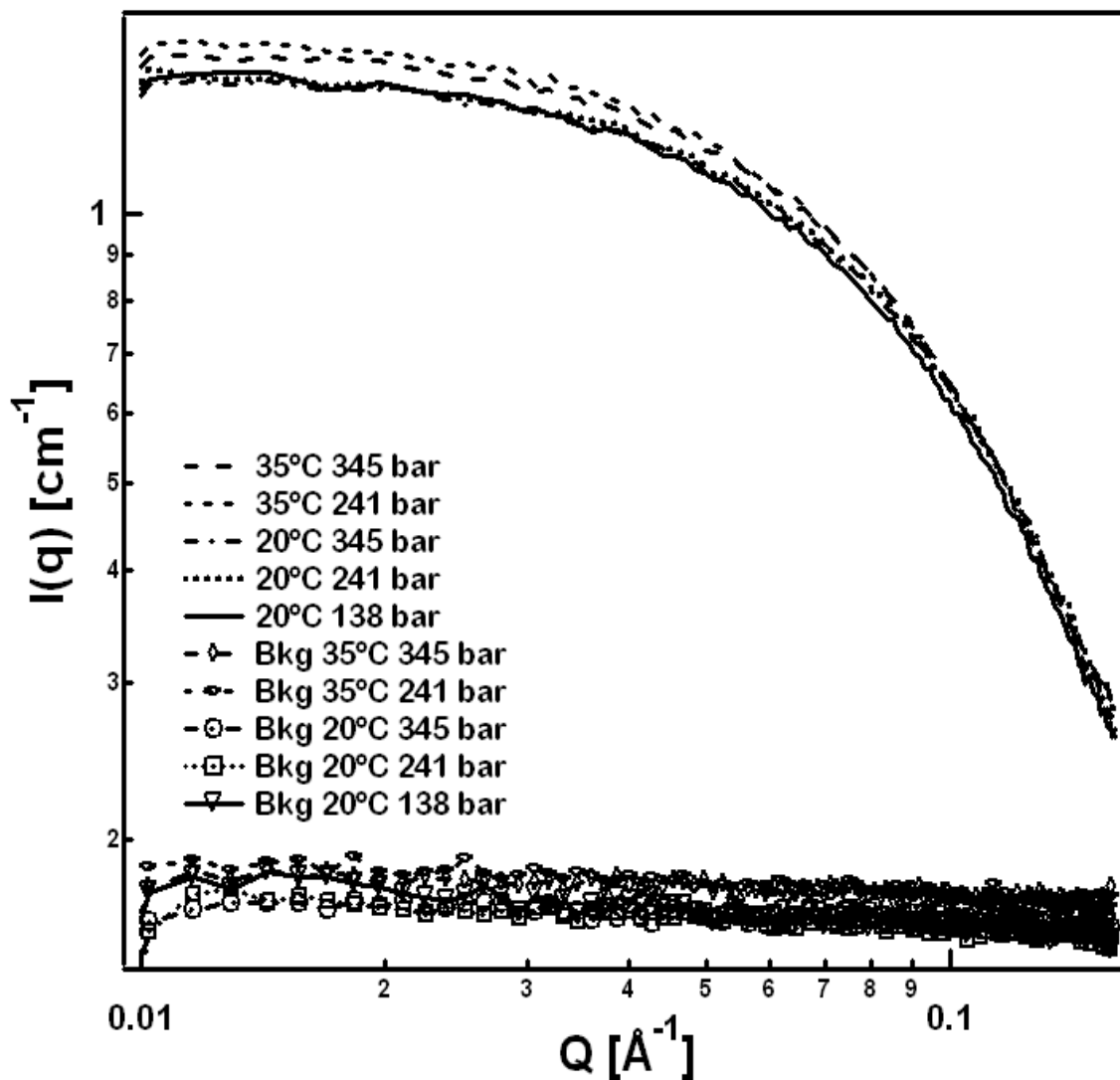


Figure 5-2. SANS results for the AOT reverse micelle microemulsion in compressed propane with $[\text{AOT}] = 0.6 \text{ M}$ at various temperatures and pressures. The lower curves are the measured backgrounds for the pure d-propane.

with a slight increase in scattering intensity at the higher temperature. The data was fit with the PCF-HS model, as well as a poly core form factor (PCF) model which neglects any interparticle interactions by setting $S(Q) = 1$. Both models fit the data well with a reverse micelle radius of $\sim 16 \text{ \AA}$ within $\pm .05 \text{ \AA}$, polydispersity of 0.62 within ± 0.04 and background values consistent with the measured values. Other model constraints included fixing the shell thickness at 10.0 \AA and volume fraction at 0.03, floating the background and consistently negative fitted values for the D_2O core SLD. The closeness of fit for the two models, demonstrates the relative weakness of interparticle interactions, confirming the observations of Eastoe et al. for the AOT / h-propane / D_2O system with $W = 20$ and polydispersity values for the D_2O core on the order of 0.20^{33} . The SANS results obtained for the d-propane / $W = 3$ microemulsion correspond well with the previous studies in compressed h-propane^{32,33,35}.

SANS is an excellent method for determining the size and shape of micellar aggregates in solution, as demonstrated by the presented data and comparison with literature results. The pertinent information for size and shape is obtained from the scattered neutron intensity at lower Q values ($Q < 0.1 \text{ \AA}^{-1}$) which are easily accessed. Detailed information pertaining to the polydispersity term is generally located in the vicinity of Q values equal to $\pi / R(\text{\AA})$ where a local minimum is located as seen in Figure 5-1 for $W=18$ with the largest micelle radius. Ideally, we would have liked to obtain the SANS measurements at higher Q values up to 0.22 \AA^{-1} , however beam time was limited to the 8 M SANS instrument with a configuration unable to access the wider Q range. Despite not making measurements at higher Q values, the modeling provided excellent fits of the measured data and acceptable values for the fitted parameters, although we are

not confident in determining elasticity properties from the SANS data beyond the polydispersity (eg. elasticity constants). The SANS measurements for the propane W=3 microemulsion implemented incident neutrons with a wavelength of 6 Å, accessing a slightly wider Q range. According to the $Q [D_{\text{eff}}(\text{Max})] = \pi / R(\text{Å})$ relation, 16 Å radius micelles would exhibit information pertaining to micelle dynamics in the Q range of 0.196 Å^{-1} and from the SANS curves in Figure 5-2, it may be perceived that in this Q range, the signal would be lost in the background. For this reason, the NSE study in compressed propane investigated a higher W value where information on the micelle dynamics would be more accessible. The results obtained from the SANS measurements which are implemented in the NSE study include the reverse micelle size and polydispersity for the liquid phase microemulsions.

5-5b. Liquid Phase NSE Measurements

Liquid phase AOT reverse micelle microemulsions corresponding to those studied by SANS, were investigated using NSE and Figure 5-3 displays the intermediate scattering function, $I(Q,t) / I(Q,0)$, decay curves for various Q values. A majority of the measured decay curves were eliminated for clarity of presentation. An indication of the micelle dynamics can be inferred from the decay rates where an increased decay is observed with a decrease in solvent viscosity from d-cyclohexane to d-hexane and with a decrease in micelle radius at lower W values. The increased decay rate is indicative of increased micellar effective diffusion where the $I(Q,t) / I(Q,0)$ data is fit by equation 3 resulting in the Q -dependant D_{eff} shown in Figure 5-4. The diffusion curves demonstrate a Q -independent translational diffusion term, D_{tr} , and a distinct Q -dependant peak which

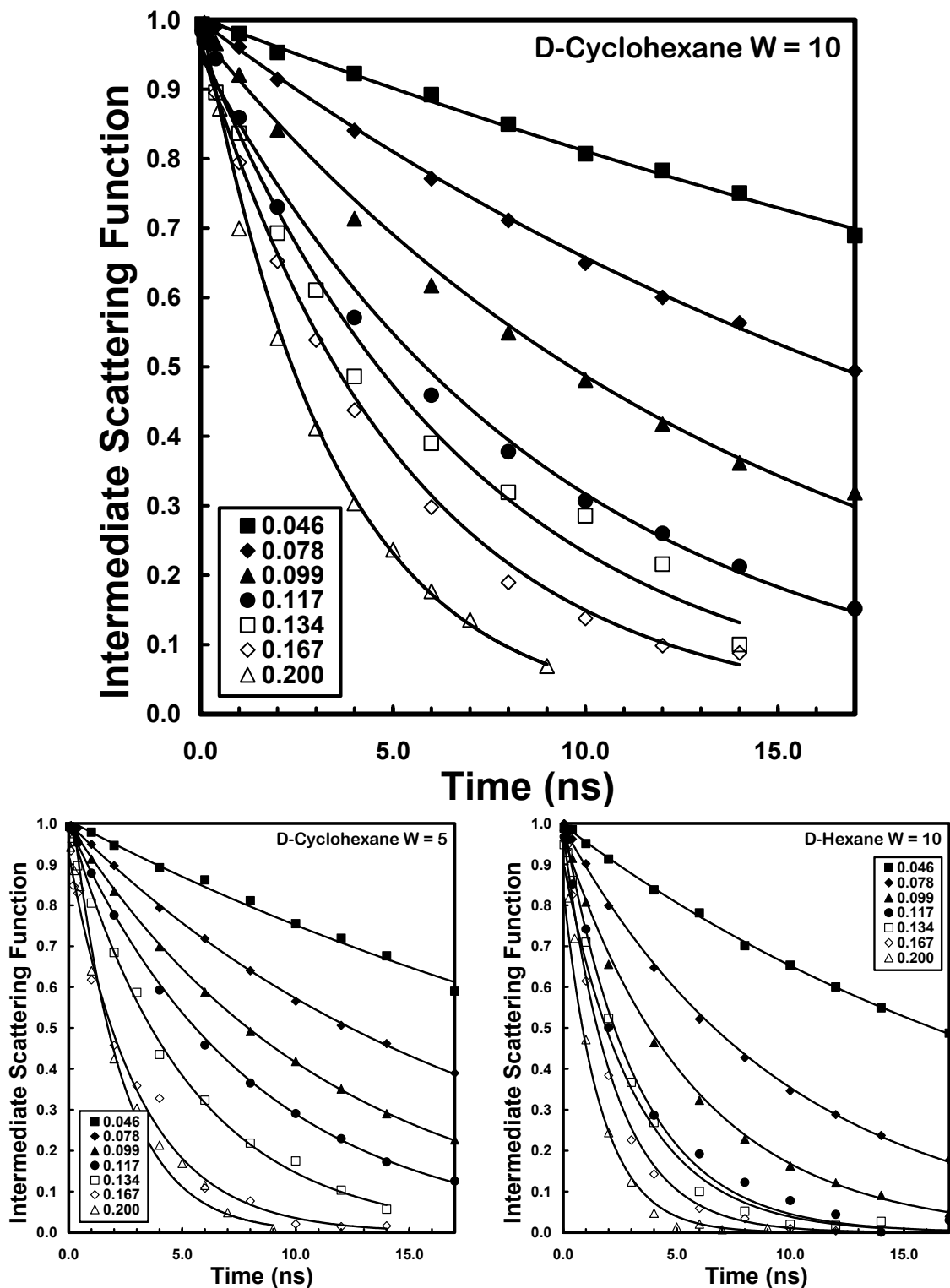


Figure 5-3. The Intermediate Scattering Function decay curves measured by NSE for the liquid phase AOT microemulsions for a) d-cyclohexane W = 10, b) d-cyclohexane W = 5 and c) d-hexane W = 10. The solid lines are to guide the eye.

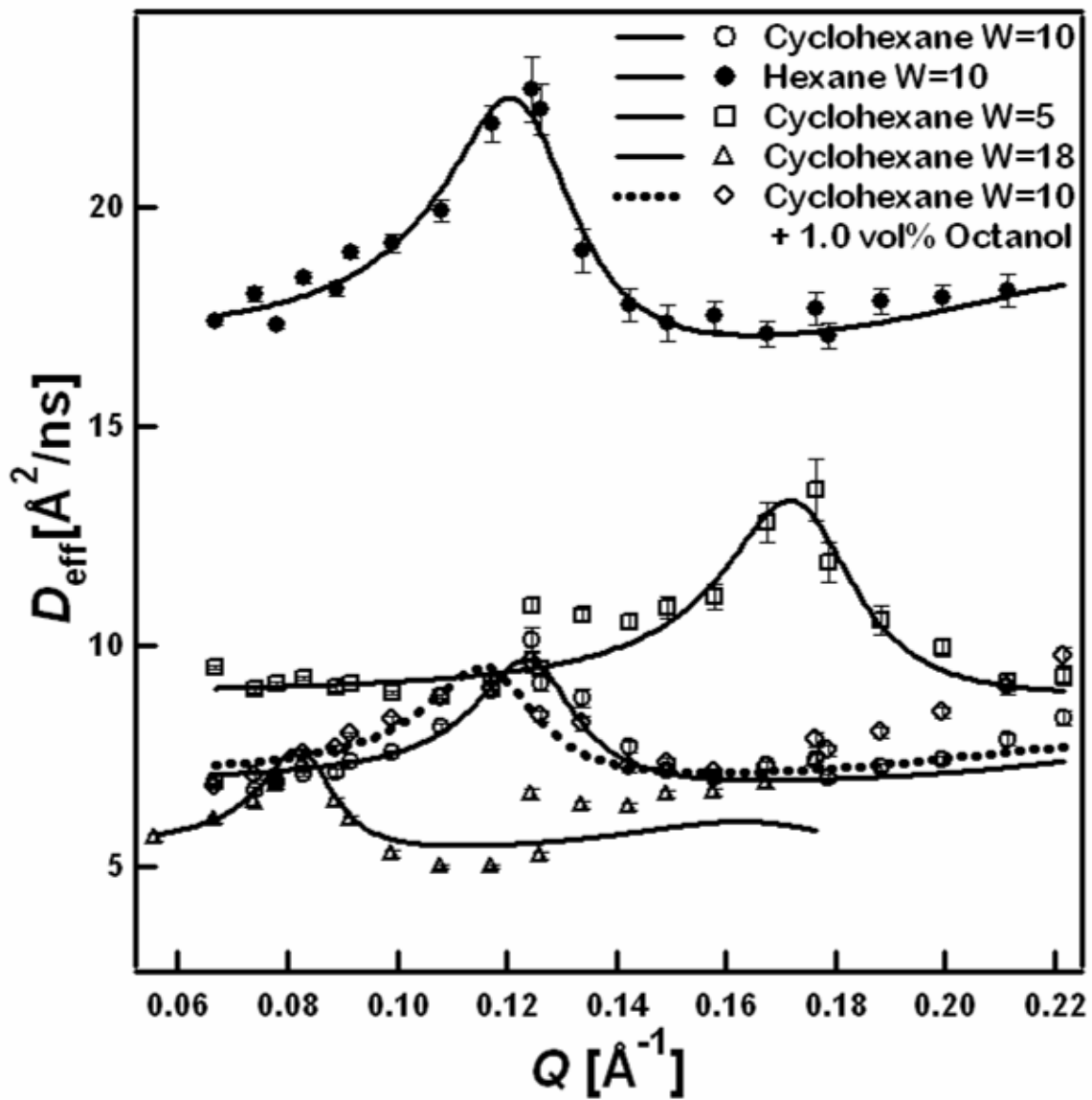


Figure 5-4. Q -dependant diffusion results obtained by NSE for the liquid phase AOT reverse micelle microemulsion. The solid lines represent the fitting of the data points with equations 4 and 5.

accounts for the deformation diffusion, D_{def} . The reverse micelle size and the viscosity of the bulk solvent impact the D_{tr} , which corresponds nicely with the Stokes-Einstein relation, given in equation 10:

$$D_{\text{tr}} = \frac{(1-\phi)k_B T}{6\pi\eta R_H} \quad (10)$$

where η is the bulk viscosity. The viscosity of the deuterated solvents was estimated from the hydrogenated solvent viscosity with density adjustments, assuming the force independent, kinematic viscosity is similar to that of the hydrogenated solvent. In the same respect, the Stokes-Einstein relation can be used to determine a correlation length, ξ_r , from the measured D_{tr} by equation 11.

$$\xi_r = \frac{(1-\phi)k_B T}{6\pi\eta D_{\text{tr}}} \quad (11)$$

ξ_r has been used to determine the degree of interparticle interactions between the reverse micelles in solution by differences in ξ_r and the micelle radius³⁴. With the correlation length, ξ_r , being greater than the micelle radius would suggest an increase in the interparticle interactions which are influential in micelle dynamics. Table 5-2 lists the results obtained from the NSE measurements as well as a comparison of the micelle radii determined by NSE, SANS and the correlation length. The micelle radius predicted by the SANS measurements are consistently higher than the NSE values but show very good agreement. Comparison of ξ_r and the micelle radii show excellent agreement for the reverse micelles in d-cyclohexane; however for d-hexane ξ_r suggests a slightly increased interparticle interaction, relative to d-cyclohexane. This increase may be explained by a decrease in the solvent interaction with the AOT tails as the bulk solvent is changed from d-cyclohexane to d-hexane. The solvent interaction can be characterized by the

Table 5-2. NSE results for the liquid phase microemulsions and comparison of the reverse micelle radius determined by SANS, NSE and the Correlation Length. The values for the bending elasticity modulus are determined by two different methods.

	Hexane W=10	Cyclohexane W=5	Cyclohexane W=10	Cyclohexane W=18	Cyclohexane W=10 + 1.0 vol% Octanol
Damping Freq.(Hz)	7.97E+07	1.29E+08	4.22E+07	1.48E+07	3.24E+07
Amplitude	1.32E-02	7.06E-03	7.78E-03	9.30E-03	1.06E-02
$Q D_{\text{eff}}(\text{Max}) (\text{\AA}^{-1})$	0.120	0.170	0.124	0.082	0.116
Pi / Radius	0.122	0.173	0.125	0.083	0.117
$D_{\text{tr}} (\text{\AA}^2/\text{ns})$	17.1	9.0	7.0	5.5	7.1
$D_{\text{eff}}(\text{Max}) / D_{\text{tr}}$	1.32	1.51	1.39	1.43	1.33
$R(\text{\AA})$ (NSE)	25.7	18.2	25.2	38.0	26.9
$R(\text{\AA})$ (SANS)	27.9	22.8	28.6	41.7	27.7
Corr. Length ξ (\AA)	32.2	20.1	25.6	32.0	24.8
$k/k_{\text{B}}T$ (Eq. 7)	0.16	0.23	0.22	0.25	0.19
$k/k_{\text{B}}T$ (Eq. 12)	1.11	1.77	1.38	1.50	1.17

Hildebrand Chi interaction parameter, χ , of 0.011 for cyclohexane – AOT and 0.11 for hexane – AOT where the AOT solubility parameter is calculated by the Hoy group contribution method^{13,57}. The greater χ for the hexane system would suggest enhanced self association of the AOT surfactant tails due to the decreased solvent – tail interactions.

The Q -dependant D_{def} contribution to the diffusion curves contains two distinct pieces of information, the position of the peak, $Q [D_{\text{eff}}(\text{Max})]$, and the relative intensity, $D_{\text{eff}}(\text{Max})/D_{\text{tr}}$. The peak position is significant because it is identical to the Q -dependant relation ($\pi/\text{micelle radius}$) as demonstrated in Table 5-2. In a similar NSE study by Hirai et. al. on AOT microemulsions in d-heptane with $W = 5, 10$ and 20 it was concluded that at low W , the predicted $Q [D_{\text{eff}}(\text{Max})] = \pi / R$ relation does not hold true⁴. In contrast, this study with d-hexane and d-cyclohexane as the bulk organic solvent demonstrates convincing evidence that the predicted relation does hold true and thus corresponds with neutron scattering theory^{6,39,49}. Analyzing the D_{def} peak it is observed that the intensity increases with increasing micellar dynamics, including D_{tr} . In previous studies, it has been suggested that the relative intensity of this peak is related to the dynamic properties of the surfactant monolayer^{6,49} as discussed below.

Implementing the methods of determining the AOT monolayer bending elasticity from equation 7 using the SANS polydispersity and the dampening frequency, λ , from the NSE measurements, the values of $k/k_{\text{B}}T$ listed in Table 5-2 are obtained. The dimensionless bending elasticity constants obtained are small in comparison to previously obtained values, however the values are acceptable in that they are positive and less than 1, corresponding more closely with accepted values^{40,44} and those obtained by Binks et.

al.²⁴ ($\sim 1.0 k_B T$ to $0.06 k_B T$), as opposed to the significantly larger values obtained by SANS methods both independently and in conjunction with DLS^{7,8,40,45,58}. Granted, the differences in $k/k_B T$ for the liquid phase systems are small, the relative trends observed correspond well with the predictions of micelle rigidity as seen by micelle dynamics studies. As the bulk solvent is changed from d-cyclohexane to d-hexane, $k/k_B T$ decreases from 0.22 to 0.19 and thus a decrease in the bending elasticity would correspond to a decrease in the micelle rigidity. The addition of 1.0 volume percent octanol co-surfactant to the d-cyclohexane $W = 10$ microemulsion also resulted in a decrease in $k/k_B T$, corresponding to a decrease in micelle rigidity. The addition of 5 volume % octanol to the d-cyclohexane, $W = 10$ microemulsion resulted in decreased stability of the microemulsion and a two phase system. These observations are consistent with a decrease in the bending modulus observed with the addition of butanol to the decane / AOT microemulsion by Farago^{26,50}. The effect of W on $k/k_B T$ is also small with a minimum observed for $W = 10$. This suggests an increase in micelle rigidity would exist at both lower and higher W values. Despite the small changes in $k/k_B T$, the observed trends correspond with previously observed solvent and water content effects on micelle dynamics measured by the intermicellar exchange rate where a decrease in micelle bending elasticity or rigidity would result in an increased intermicellar exchange rate^{1,18,59}.

The bending elasticity constants for the AOT surfactant monolayer have been determined by various techniques. The most commonly referenced study by Binks et al. used ellipsometry to determine k for AOT in the lamellar phase and reported values of $1 k_B T$ with heptane, octane, and decane as the oil phase at 20°C. As the oil phase increased

in carbon number to undecane, dodecane, and tetradecane, k decreased to 0.4, 0.16, and 0.06 respectively as a transition to a bicontinuous phase was observed^{24,44}. In another study, Nagao et al. used NSE and SANS to study the decane / AOT microemulsion in the dense droplet regime with equal volume fractions of D₂O and n-decane at 25°C and reported $k = 1.4 k_B T$ ⁵¹. The d-decane / AOT reverse micelle system has also been investigated with defined W values including the initial study by Huang et al. in 1987 who reported $k \sim 5 k_B T$ using NSE⁴⁹. The d-decane / AOT / D₂O microemulsion has since then been studied using NSE by Farago et al. [$k = 3.0 k_B T$ with $W = 24.5$]⁵⁰, [$k = 3.8 k_B T$ with $W = 24.4$]²⁶, and by Kawabata et al. with similar methods to this study [$k = 0.3 k_B T$ with $W = 18.4$]³⁷. A wide range of values for k have been determined from different research groups, instrumentation, and methods. The d-decane / AOT / $W = 18.4$, $T = 20^\circ\text{C}$, reverse micelle system was also studied on the NG5 NSE spectrometer at the NCNR during the 2003 NCNR Summer School on Methods and Applications of Neutron Spectroscopy. Results from this study yielded: $\lambda_2 = 1.77 \times 10^7$, $\langle |a_2|^2 \rangle = 8.64 \times 10^{-3}$, $D_{tr} = 4.5 \text{ \AA}^2/\text{ns}$, $R(\text{NSE}) = 39.2 \text{ \AA}$, $R(\text{SANS}) = 42.0 \text{ \AA}$, polydispersity = 0.25, $\zeta_r = 40.5$, and $k = 0.22 k_B T$. This k value is comparable to that obtained by Kawabata and again is low with respect to other values listed in the literature, but is very consistent with the values determined in this study. The k determined for d-decane / $W = 18.4$ is less than that for d-cyclohexane / $W = 18$, suggesting a less rigid micelle would be formed with decane as the bulk solvent, as compared to cyclohexane. The reverse micelle radii determined in the two systems by SANS and NSE show excellent agreement. The increased correlation length suggests some interparticle interaction which may be expected based on microemulsion stability and an accessible phase transition around 60°C ³⁷. The D_{tr} values

obtained for d-cyclohexane and d-decane also correspond nicely for micelles of comparable size and bulk solvents with similar viscosities.

$$\frac{k}{k_B T} = \left(\frac{\pi}{0.9} \right) \left[\frac{D_{eff}[Max]}{D_{trans}} - 1 \right] \quad (12)$$

The bending elasticity constant was also determined using equation 12, which was previously implemented by Huang et. al.⁴⁹ and based on the theory of Milner and Safran⁶. The Huang study, mentioned previously, investigated the d-decane / AOT / D₂O microemulsion with W ranging from 8.2 to 40.8 and found bending elastic constants of $\sim 5 k_B T$ and $D_{eff}(Max) / D_{tr} \sim 2.5$ for all cases. Equation 12 makes several assumptions, including the ratio of micelle radius to the spontaneous micelle radius is equal to 0.5, and is taken as a rough approximation, implemented for comparison. Table 5-2 lists the bending elasticity constants determined using equation 12 resulting in consistently higher values than those determined by equation 7. Interestingly, the values determined by equation 12 exhibit the same trends observed for the previous results with enhanced influence of the bulk solvent, water content and co-surfactant. A more significant decrease in k is observed as the bulk solvent is changed from cyclohexane to hexane for $W = 10$. The addition of octanol to the cyclohexane / $W = 10$ microemulsion also resulted in a decrease in k . A minimum in k is observed in cyclohexane at $W = 10$ compared to $W = 18$ and $W = 5$. The values obtained from equation 12 are significant because they are slightly higher than accepted values for typical microemulsion systems but not unreasonable, as the NSE techniques based on the theory of Milner and Safran have received some criticism as differing from other methods of determination by a factor of two or more^{40,45,60}.

The bending elasticity is not the only contribution to the properties of the surfactant monolayer that can be determined from NSE. As discussed in the theory section, the saddle-splay elasticity, spontaneous curvature, and interfacial tension also play a role in micelle dynamics. Despite the ability to determine the saddle-splay elasticity constants from the methods provided, this study has been limited to the determination of the bending elasticity.

5-5c. Compressed Propane Phase NSE Measurements

Figure 5-5 displays the Q -dependant D_{eff} results obtained by NSE for the d-propane / AOT / W = 8 reverse micelle microemulsion at three conditions of varying temperature and pressure. The results at 20°C, 180 bar and 35°C, 290 bar demonstrate the effects of increased temperature and pressure such that the density and viscosity are varied only slightly with values of 0.536 g/ml and 0.156 cP respectively. The NSE results at these conditions yielded excellent results with a distinct peak where Q [$D_{\text{eff}}(\text{Max})$] = π / R and nearly identical values for D_{tr} which would be expected for the same bulk solvent viscosity. The NSE results at 20°C and 345 bar are questionable where the expected peak in the D_{eff} curve was not observed. The results do indicate acceptable behavior in the low Q range with a decrease in D_{tr} observed, corresponding to an increased viscosity of 0.184 cP for the bulk solvent. The NSE results presented in Table 5-3 for measurements at 20°C, 180 bar and 35°C, 290 bar demonstrate a decrease in the damping frequency, λ_2 , an increase in $\langle |a_2|^2 \rangle$ with increased temperature and pressure, as well as, excellent agreement for the reverse micelle radius, D_{tr} , and the Q [$D_{\text{eff}}(\text{Max})$] = π / R relationship. The NSE temperature and pressure study on the

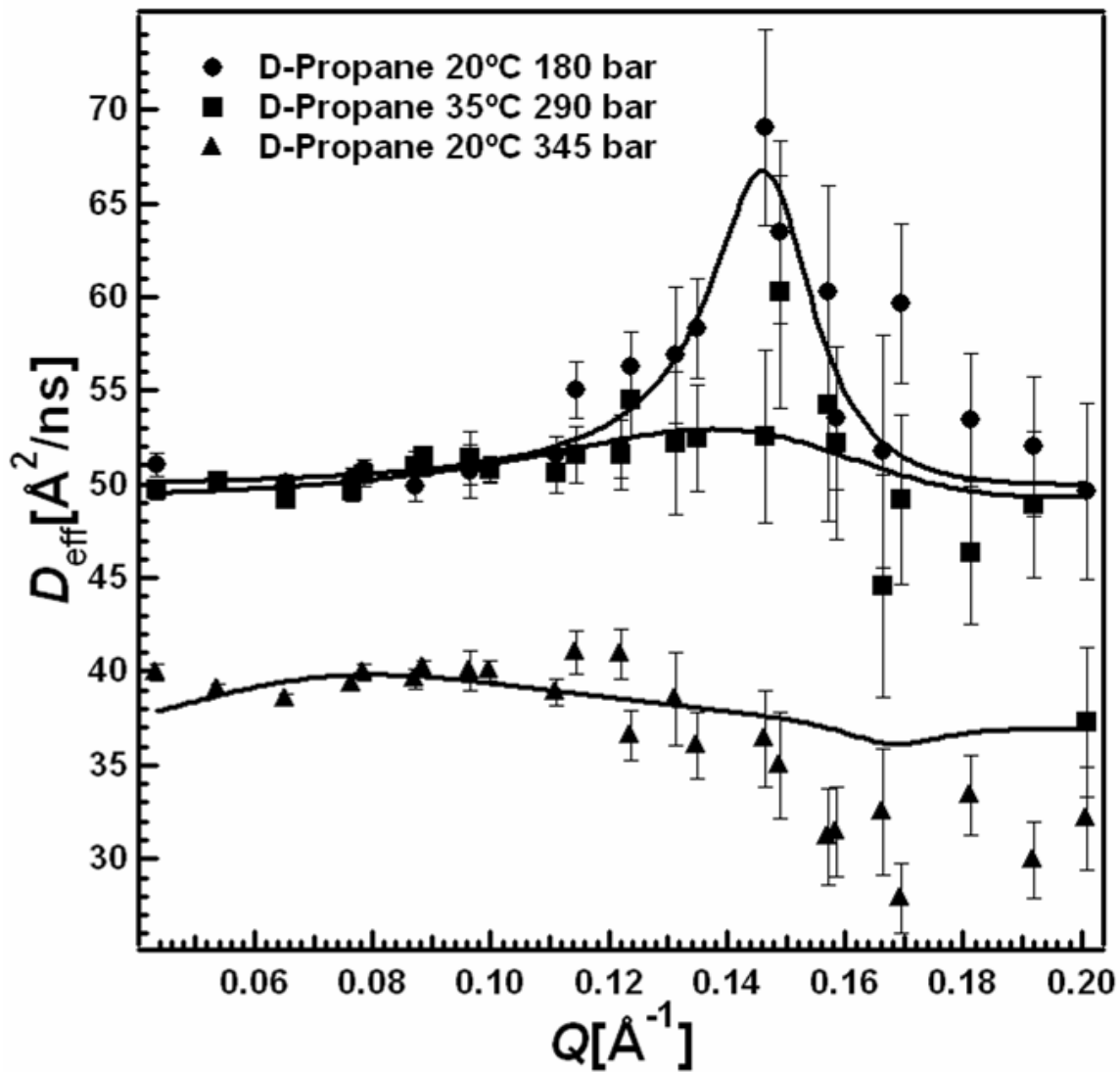


Figure 5-5. Q -dependant diffusion results obtained by NSE for the compressed d-propane / AOT / $W=8$ reverse micelle microemulsion.

Table 5-3. NSE results for the compressed d-propane / AOT / W=8 microemulsions as a function of temperature and pressure. The values for the bending elasticity modulus are determined by two different methods.

D-Propane / AOT / W=8	20°C 2600psi	35°C 4200psi	20°C 5000psi
Damping Freq.(Hz)	3.59E+08	7.26E+07	3.60E+07
Amplitude	5.40E-03	4.53E-02	4.34E-01
$Q [D_{\text{eff}}(\text{Max})] (\text{\AA}^{-1})$	0.146	0.140	NA
Pi / Radius	0.147	0.145	NA
$D_{\text{tr}} (\text{\AA}^2/\text{ns})$	50.0	49.3	36.1
$D_{\text{eff}}(\text{Max}) / D_{\text{tr}}$	1.34	1.07	NA
R(\AA) (NSE)	21.4	21.7	25.1
Corr. Length ξ (\AA)	26.8	28.4	31.4
$k/k_{\text{B}}T$ (Eq. 7)	0.37	0.19	0.20
$k/k_{\text{B}}T$ (Eq. 12)	1.17	0.26	NA

d-decane / AOT / W = 18.4 by Kawabata et al. showed that $\langle |a_2|^2 \rangle$ increased with temperature and decreased with pressure, indicating that the micelle shape fluctuations are enhanced with increasing temperature and suppressed with increasing pressure³⁷. This study demonstrates an increase in $\langle |a_2|^2 \rangle$ with increased temperature and pressure at a constant bulk solvent viscosity, suggesting a greater effect of temperature on shape fluctuations, which was also observed by Kawabata³⁷. Comparison of the calculated correlation length with the micelle radius show little deviation and thus any interparticle interaction is minimal which is expected for a stable microemulsion at conditions far from a phase transition^{33,34}.

Determination of the bending elasticity constant using equation 7 was achieved assuming a constant polydispersity of 0.20³³, yielding values of $0.43 k_B T$ at 20°C, 180 bar and $0.20 k_B T$ at 35°C, 290 bar. In the case that a polydispersity of 0.30 is used, slightly lower values of $0.34 k_B T$ and $0.11 k_B T$ are obtained which exhibit the same decreasing trend. Determination of the bending elasticity from the ratio $D_{\text{eff}}(\text{Max}) / D_{\text{tr}}$ by equation 12, again predicts slightly larger values but is consistent in predicting a significant decrease in k with increased temperature and pressure at a constant density. Previous NSE studies of temperature and pressure effects on the AOT microemulsion system include the Kawabata study and the previously mentioned Nagao study of n-decane in the dense droplet regime. Nagao et al. found that k decreased from $1.4 k_B T$ to $0.4 k_B T$ with an increase in temperature from 25°C to 40°C at 1 bar and increased to $2.6 k_B T$ with an increase in pressure from 1 bar to 600 bar at 25°C⁵¹. Kawabata et al. also reported a decrease in k with increasing temperature and an increase in k with increasing pressure³⁷, however the effect of temperature less than that of pressure, as well as the observations of

Nagao. For the d-propane system, a decrease in k with simultaneous increases in temperature and pressure, suggests that temperature may influence k more so than pressure despite the compressible nature of the bulk fluid.

5-6. CONCLUSIONS

This work has demonstrated the effects of the bulk solvent, water content and octanol co-surfactant on the AOT reverse micelle system by measuring shape fluctuations to determine the bending elasticity of the surfactant monolayer. The results revealed subtle differences in the bending elasticity for each of the liquid systems investigated, however the trends observed correspond very well with the results obtained by alternative methods of studying AOT reverse micelle dynamics, particularly microemulsion stability and intermicellar exchange rates. The bending elasticity constants are consistently low compared to previous values in the literature, but are convincing in that the observed increases in bending elasticity correspond to increases in micelle rigidity in the liquid phase AOT microemulsion. To our knowledge, this is the first NSE study of temperature and pressure effects on a microemulsion formed within a compressible solvent. The measurements performed on the compressed propane / AOT $W = 8$ reverse micelle system demonstrate the use of a tunable solvent to adjust the properties of the reverse micelle surfactant monolayer without changing the density or viscosity of the bulk fluid. This affords the ability to alter the micelle rigidity while maintaining constant translational diffusion through the bulk fluid, or vice versa.

5-7. REFERENCES

- (1) Fletcher, P. D. I.; Howe, A. M.; Robinson, B. H. *Journal of the Chemical Society-Faraday Transactions I* 1987, *83*, 985-1006.
- (2) Gale, R. W.; Fulton, J. L.; Smith, R. D. *Journal of the American Chemical Society* 1987, *109*, 920-921.
- (3) Rosov, N.; Rathgeber, S.; Monkenbusch, M. In *Scattering from Polymers*, 2000; Vol. 739, pp 103-116.
- (4) Hirai, M.; Hirai, R. K.; Iwase, H.; Arai, S.; Mitsuya, S.; Takeda, T.; Seto, H.; Nagao, M. *Journal of Physics and Chemistry of Solids* 1999, *60*, 1359-1361.
- (5) Komura, S.; Takeda, T.; Kawabata, Y.; Ghosh, S. K.; Seto, H.; Nagao, M. *Physical Review E* 2001, *6304*.
- (6) Milner, S. T.; Safran, S. A. *Physical Review A* 1987, *36*, 4371-4379.
- (7) Hellweg, T.; Langevin, D. *Physical Review E* 1998, *57*, 6825-6834.
- (8) Gradzielski, M.; Langevin, D.; Farago, B. *Physical Review E* 1996, *53*, 3900-3919.
- (9) Gradzielski, M.; Langevin, D. *Journal of Molecular Structure* 1996, *383*, 145-156.
- (10) Kellay, H.; Binks, B. P.; Hendriks, Y.; Lee, L. T.; Meunier, J. *Advances in Colloid and Interface Science* 1994, *49*, 85-112.
- (11) Helfrich, W. *Zeitschrift Fur Naturforschung Section a-a Journal of Physical Sciences* 1978, *33*, 305-315.
- (12) Hiemenz, P. C.; Rajagopalan, R. *Principles of colloid and surface chemistry*; 3rd, rev. and expanded / ed.; Marcel Dekker: New York, 1997.
- (13) Kitchens, C. L.; McLeod, M. C.; Roberts, C. B. *J. Phys. Chem. B.* 2003, *107*, 11331-11338.
- (14) Towey, T. F.; Khanlodhi, A.; Robinson, B. H. *Journal of the Chemical Society-Faraday Transactions* 1990, *86*, 3757-3762.
- (15) Bagwe, R. P.; Khilar, K. C. *Langmuir* 1997, *13*, 6432-6438.
- (16) Bagwe, R. P.; Khilar, K. C. *Langmuir* 2000, *16*, 905-910.
- (17) Eastoe, J.; Fragneto, G.; Robinson, B. H.; Towey, T. F.; Heenan, R. K.; Leng, F. J. *J. Chem. Soc.-Faraday Trans.* 1992, *88*, 461-471.
- (18) Atik, S. S.; Thomas, J. K. *Journal of the American Chemical Society* 1981, *103*, 3543-3550.
- (19) Sato, H.; Hirai, T.; Komasaawa, I. *Industrial & Engineering Chemistry Research* 1995, *34*, 2493-2498.
- (20) Hirai, T.; Sato, H.; Komasaawa, I. *Industrial & Engineering Chemistry Research* 1994, *33*, 3262-3266.

- (21) Hirai, T.; Tsubaki, Y.; Sato, H.; Komasaawa, I. *Journal of Chemical Engineering of Japan* 1995, 28, 468-473.
- (22) Cason, J. P.; Miller, M. E.; Thompson, J. B.; Roberts, C. B. *Journal of Physical Chemistry B* 2001, 105, 2297-2302.
- (23) Kitchens, C. L.; McLeod, M. C.; Roberts, C. B. *Currently in Review* 2003.
- (24) Binks, B. P.; Kellay, H.; Meunier, J. *Europhysics Letters* 1991, 16, 53-58.
- (25) Chu, B. *Laser light scattering : basic principles and practice*; 2nd ed.; Academic Press: Boston, 1991.
- (26) Farago, B.; Richter, D.; Huang, J. S.; Safran, S. A.; Milner, S. T. *Physical Review Letters* 1990, 65, 3348-3351.
- (27) Huang, J. S.; Safran, S. A.; Kim, M. W.; Grest, G. S.; Kotlarchyk, M.; Quirke, N. *Physical Review Letters* 1984, 53, 592-595.
- (28) Kotlarchyk, M.; Chen, S. H.; Huang, J. S.; Kim, M. W. *Physical Review Letters* 1984, 53, 941-944.
- (29) Kotlarchyk, M.; Chen, S. H.; Huang, J. S. *Physical Review A* 1983, 28, 508-511.
- (30) Safran, S. A.; Turkevich, L. A. *Physical Review Letters* 1983, 50, 1930-1933.
- (31) Huang, J. S.; Kim, M. W. *Physical Review Letters* 1981, 47, 1462-1465.
- (32) Eastoe, J.; Robinson, B. H.; Visser, A.; Steytler, D. C. *Journal of the Chemical Society-Faraday Transactions* 1991, 87, 1899-1903.
- (33) Eastoe, J.; Steytler, D. C.; Robinson, B. H.; Heenan, R. K. *Journal of the Chemical Society-Faraday Transactions* 1994, 90, 3121-3127.
- (34) Eastoe, J.; Young, W. K.; Robinson, B. H.; Steytler, D. C. *Journal of the Chemical Society, Faraday Transactions* 1990, 86, 2883-2889.
- (35) Kaler, E. W.; Billman, J. F.; Fulton, J. L.; Smith, R. D. *Journal of Physical Chemistry* 1991, 95, 458-462.
- (36) Peck, D. G.; Johnston, K. P. *Journal of Physical Chemistry* 1991, 95, 9549-9556.
- (37) Kawabata, Y.; Nagao, M.; Seto, H.; Komura, S.; Takeda, T.; Schwahn, D.; Yamada, N. L.; Nobutou, H. *Physical Review Letters* 2004, 92, 056103/056101-056103/056104.
- (38) Eastoe, J.; Sharpe, D. *Langmuir* 1997, 13, 3289-3294.
- (39) Arleth, L.; Pedersen, J. S. *Physical Review E* 2001, 6306.
- (40) Lisy, V.; Brutovsky, B. *Physical Review E* 2000, 61, 4045-4053.
- (41) Lisy, V. *Colloids and Surfaces A: Physicochemical and Engineering Aspects* 2003, 221, 255-256.
- (42) Hellweg, T.; Gradzielski, M.; Farago, B.; Langevin, D. *Colloids and Surfaces A: Physicochemical and Engineering Aspects* 2001, 183-185, 159-169.
- (43) Hellweg, T.; Gradzielski, M.; Farago, B.; Langevin, D.; Safran, S. *Colloids and Surfaces A: Physicochemical and Engineering Aspects* 2003, 221, 257-262.
- (44) Kellay, H.; Meunier, J. *Journal of Physics-Condensed Matter* 1996, 8, A49-A64.
- (45) Lisy, V.; Brutovsky, B.; Zatorovsky, A. V.; Zvelindovsky, A. V. *Journal of Molecular Liquids* 2001, 93, 113-118.

- (46) Farago, B.; Monkenbusch, M.; Goecking, K. D.; Richter, D.; Huang, J. S. *Physica B* 1995, *213*, 712-717.
- (47) Farago, B.; Richter, D.; Huang, J. S. *Physica B* 1989, *156*, 452-455.
- (48) Kawabata, Y.; Seto, H.; Nagao, M.; Takeda, T. *Journal of Neutron Research* 2002, *10*, 131-136.
- (49) Huang, J. S.; Milner, S. T.; Farago, B.; Richter, D. *Physical Review Letters* 1987, *59*, 2600-2603.
- (50) Farago, B.; Huang, J. S.; Richter, D.; Safran, S. A.; Milner, S. T. *Progr. Colloid Polym. Sci.* 1990, *81*, 60-63.
- (51) Nagao, M.; Seto, H.; Takeda, T.; Kawabata, Y. *Journal of Chemical Physics* 2001, *115*, 10036-10044.
- (52) Nagao, M.; Seto, H.; Kawabata, Y.; Takeda, T. *Journal of Applied Crystallography* 2000, *33*, 653-656.
- (53) Kawabata, Y.; Nagao, M.; Seto, H.; Komura, S.; Takeda, T.; Schwahn, D. *Applied Physics a-Materials Science & Processing* 2002, *74*, S534-S536.
- (54) Nagao, M.; Seto, H.; Shibayama, M.; Yamada, N. L. *Journal of Applied Crystallography* 2003, *36*, 602-606.
- (55) <http://www.ncnr.nist.gov/resources/sldcalc.html>; NIST Center for Neutron Research.
- (56) Nave, S.; Eastoe, J.; Heenan, R. K.; Steytler, D.; Grillo, I. *Langmuir* 2000, *16*, 8741-8748.
- (57) Fried, J. R. *Polymer Science and Technology*; Prentice Hall: Englewood Cliff, NJ, 1995.
- (58) Hellweg, T.; Langevin, D. *Physica A* 1999, *264*, 370-387.
- (59) Howe, A. M.; McDonald, J. A.; Robinson, B. H. *Journal of the Chemical Society-Faraday Transactions I* 1987, *83*, 1007-1027.
- (60) Lisy, V.; Brutovsky, B. *Czechoslovak Journal of Physics* 2000, *50*, 239-250.

CHAPTER 6

6. CHLORIDE ION EFFECTS ON SYNTHESIS AND DIRECTED ASSEMBLY OF COPPER NANOPARTICLES IN LIQUID AND COMPRESSED ALKANE MICROEMULSIONS

6-1. INTRODUCTION

The field of nanotechnology is rapidly progressing with the development of a vast variety of novel materials with length scales of less than 100nm. Particular interest in metallic and semi-conductor nanomaterials exists based on the unique properties that depend on the size and shape of the nanoparticles. Several methods of nanoparticle synthesis have been and continue to be developed which consist mainly of the “bottom up” method of particle synthesis from atomic species or “building blocks”¹. The methods of particle synthesis are evolving beyond the formation of spherical particles and focus has been placed in two main areas. The first is deposition techniques and the directed assembly of mono-dispersed particles into uniform, closely packed thin films and multilayers, implementing capping ligands with specific functionalities and methods of depositing particles on surfaces both uniformly and with desired packing order¹⁻⁵. Applications for highly ordered, uniform nanoparticle arrays include data storage, catalysts, electronics, optics, coatings, and sensors^{6,7}. The second is directed synthesis of nanomaterials with specific geometry and composition consisting of single and multi component materials in core-shell configurations with geometries of varying aspect ratios

resulting in spheres, rods and wires. Other particle geometries include nanodisks⁸, nanocubes⁹⁻¹¹, nanoboxes^{12,13}, nanotubes and 1-D nanoplates with triangular, diamond, pentagon and hexagon shapes¹⁴⁻²⁰. In most cases the synthesis of nanoparticles with specified geometries is achieved with the use of a colloidal mediator or stabilizing agent such as polypeptides, poly(vinyl pyrrolidone) (PVP)²¹, poly(vinyl alcohol) (PVA)²², poly(ethylene glycol) (PEG)^{10,23}, cetyltrimethylammonium (CTAB)^{9,16} and other surfactants. Nanocrystal seed mediated synthesis in the presence of colloidal agents has also been demonstrated as an effective method for the production of novel nanomaterials, particularly nanowires and nanowhiskers^{21,24-29}. The ability to reproducibly synthesize these materials is of significant interest for potential applications which require nanomaterials of uniform size, shape, and dispersion. A further understanding of the governing factors which direct the synthesis of these novel nanomaterials is necessary to fully harness the use of nanomaterials for future applications. For many of the nanomaterials previously investigated, different aspects of the synthesis conditions were studied to determine their effects on the resulting size, shape, crystallinity, structure and composition. The concentrations of stabilizing agent and metallic precursor have been demonstrated to influence the size and uniformity of synthesized materials, eg. silver nanocubes stabilized by PVP¹², cuprous oxide (Cu₂O) nanocubes stabilized by PEG or CTAB^{9,10}, and various alkanethiolate stabilized metallic particles. For the synthesis of Cu₂O nanocubes synthesized in the presence of CTAB, the concentration of CTAB is directly related to the nanocube size⁹. Similarly, the synthesis of copper nanocubes has been demonstrated with the use of CTAB surfactant, as well as within a multiple phase Cu(AOT)₂ – isooctane – water solution with the addition of NaBr salt^{16,19}. It has been

suggested that the presence of the Br^- ion in CTAB and NaBr is responsible for the formation of the nanocubes by selective anion absorption onto the (111) and (100) fcc faces³⁰. Chloride ions have been shown to enable the synthesis of copper nanorods where the aspect ratio varies with the Cl^- concentration. This has been demonstrated with the use of CTAC surfactant as well as the addition of NaCl to a $\text{Cu}(\text{AOT})_2$ – isooctane – water three phase emulsion and again is explained by anion absorption of specific crystal faces^{16,19,30}.

In this study, we will investigate the effects of chloride ion addition to the AOT reverse micelle system on copper nanoparticle synthesis utilizing liquid isooctane and compressed propane as the bulk organic solvent. Previous studies have demonstrated the synthesis of spherical copper nanoparticles in single phase AOT reverse micelles with varying water content ($W = [\text{H}_2\text{O}] / [\text{AOT}]$) and bulk organic solvent ranging from conventional liquid solvents to compressed and supercritical fluids³¹⁻³⁵. Compressed and supercritical fluids are emerging as a unique media for nanomaterial synthesis and processing due to their adjustable properties such as density, viscosity, diffusivity, and solvent strength³⁶⁻⁵⁰. Compressed and supercritical fluids have also been utilized as effective means of particle deposition, separation, and collection. This study demonstrates the novel synthesis of diamond-shaped copper nanoparticle assemblies which is unique to the compressed propane / $\text{Cu}(\text{AOT})_2$ – AOT / $W = 3$ reverse micelle system with small concentrations of HCl dissolved in the micelle core.

6-2. EXPERIMENTAL METHODS

All chemical reagents used in the copper nanoparticle synthesis were obtained from Sigma Aldrich Chemical, excluding nitrogen and propane gases that were obtained from BOC gasses. Similar methods of microemulsion based copper nanoparticle synthesis within sodium bis-2-ethylhexyl-sulfosuccinate (AOT) reverse micelles are detailed in previous literature^{32,35,51}. Liquid isooctane phase nanoparticle synthesis was performed with $[AOT] = 0.11 \text{ M}$ and $W = 10$ (where $W = [H_2O] / [AOT]$) in an oxygen free environment obtained by nitrogen purging. The copper precursor was introduced at 0.011 M concentration by two methods; first using $Cu(AOT)_2$ co-surfactant synthesized by an ion exchange method that replaces the sodium ion on the AOT head group with Cu^{2+} and secondly by dissolving $CuCl_2$ salt in the water core of the reverse micelles. Copper nanoparticle synthesis is achieved by reduction of the Cu^{2+} with anhydrous hydrazine at $[N_2H_4] = 3 \times [Cu^{2+}]$ that is added to the single phase reverse micelle microemulsion. Synthesis using $CuCl_2$ involves introduction of the Cl^- ion via the copper salt. In the case of $Cu(AOT)_2$ the Cl^- ion was added by using dilute HCl within the reverse micelle core at concentrations of 0.42 M , 0.042 M , and 0.0042 M to yield overall Cl^- concentrations of $1 \times 10^{-2} \text{ M}$, $1 \times 10^{-3} \text{ M}$, and $1 \times 10^{-4} \text{ M}$ respectively for $W = 10$. Particle synthesis was monitored in situ via UV-vis absorbance measurements, as detailed previously³², to obtain the particle growth rate and average particle size synthesized. The synthesized particles were also characterized using a Zeiss EM 10 transmission electron microscope (TEM) to determine particle sizes and a Jeol JEM 2010 for individual particle analysis including selected area electron diffraction (SAED) patterns and energy dispersive X-ray spectroscopy (EDS). The synthesized particles were

collected by evaporating a small droplet of the surfactant-particle solution on a TEM support. The TEM supports used were obtained from Ted Pella Inc. and included 200 mesh nickel grids and 400 mesh copper ultra thin grids. In many cases, the excess AOT surfactant resulted in poor TEM particle imaging and a liquid – liquid extraction technique was implemented to remove the excess surfactant. The extraction involved vigorous mixing of the surfactant / particle solution with an equal volume of a 50% ethanol – water solution followed by a phase separation and removal of the aqueous phase containing the excess surfactant. The addition of a 0.01 M dodecanethiol or dodecylamine particle stabilizing agent in isooctane solution prior to surfactant extraction was used to prevent particle agglomeration and precipitation. An alternate particle collection technique utilized a Pelco all-glass nebulizer obtained from Ted Pella Inc. to obtain a fine mist of the particle solution, providing uniform particle deposition on the TEM support.

Particle synthesis in the compressed propane reverse micelle system was achieved using methods detailed previously³¹ in a 30ml high pressure reaction vessel with $[\text{Cu}(\text{AOT})_2] = 5.5 \times 10^{-3} \text{ M}$, $[\text{AOT}] = 5.5 \times 10^{-2}$, $W = 3$, and $[\text{N}_2\text{H}_4] = 10 \times [\text{Cu}]$. To study the influence of Cl^- ions on particle synthesis, dilute HCl was added to the aqueous micelle core at the concentrations mentioned above, yielding overall Cl^- concentrations of $1.5 \times 10^{-3} \text{ M}$, $1.5 \times 10^{-4} \text{ M}$, and $1.5 \times 10^{-5} \text{ M}$ respectively with $W = 3$. Synthesis using CuCl_2 salt precursor was not achieved due to the inability to form a single phase microemulsion with the salt present in the core of the propane reverse micelle system. Particle collection methods from the propane system included a spray-coating technique where the particles dispersed in compressed propane were sprayed through 400 micron diameter capillary

tubing onto a TEM grid approximately 6 inches from the nozzle tip. In addition to this spray technique, particles were collected after depressurization of the vessel. Once completely depressurized, a surfactant – particle matrix was present in the bottom of the vessel, which was re-dispersed in 10 ml of isooctane solution containing 0.01 M stabilizing agent. The AOT surfactant was then removed with 10 ml of 50% ethanol solution as described above. Particle samples were collected from the isooctane phase both before and after the liquid – liquid extraction of the AOT surfactant by droplet evaporation as well as nebulizer spray. Furthermore, during the surfactant removal, a precipitate was observed at the aqueous – oil interface and after removal of the two liquid phases, this solid precipitate was re-dissolved in acetone and these samples were also collected.

6-3. RESULTS AND DISCUSSION

6-3a. Particle Synthesis in Liquid Phase AOT Reverse Micelles

Our previous investigations of copper nanoparticle synthesis in the AOT reverse micelle system demonstrated the effects of the bulk solvent and water content on particle synthesis and stabilization³². The anionic surfactant, AOT, acts to sterically stabilize the copper particles via ionic interaction with the particle surface which has been demonstrated as being influential in metallic nanoparticle synthesis. This study investigates the effects of chloride ion on copper nanoparticle synthesis by the addition of dilute HCl to the aqueous core of AOT reverse micelles with both isooctane and compressed propane as the bulk organic phases. Hasegawa reported the buffer-like action of AOT reverse micelles for the pH range from 2 to 11.5 within the aqueous core

for $W = 10$ in heptane⁵². The buffering of the micelle core allows for the addition of dilute HCl to the micelle core without creating an acidic environment which would prohibit the synthesis of copper nanoparticles. Copper nanoparticles are easily oxidized and must be synthesized in an oxygen free environment. Similarly, an acidic environment is not favorable for copper nanoparticle synthesis. The addition of 0.42 M HCl to the isooctane / Cu(AOT)₂ - AOT / $W = 10$ reverse micelle system resulted in the inability to synthesize copper particle upon reduction. Particle synthesis was achieved with the addition of 4.2×10^{-2} M HCl and 4.2×10^{-3} M HCl to the micelle core. Figure 6-1 displays the copper nanoparticle growth curves obtained from in situ UV-vis absorbance measurements. Spherical copper nanoparticles dispersed in solution exhibit a characteristic absorbance band consistently centered at a wavelength of 566 nm. Previous studies have demonstrated the relationship of the average particle diameter dispersed in solution to the relative absorbance intensity at 566 nm^{32,35,53}. The relative absorbance intensity is measured by the ratio of absorbance intensities located at 566nm and 500nm (a position off the main peak) where an increase in the absorbance ratio corresponds to an increase in the average copper particle diameter. As a reference point for comparison, a measured absorbance ratio equal to 1 corresponds to approximately 10 nm spherical particles dispersed in solution. The particle growth curves demonstrate that the presence of HCl does not significantly affect the maximum particle size synthesized but there is an influence on the particle growth rate as demonstrated by the initial rate of increase in the absorbance ratio. As the HCl concentration is decreased in the $W = 10$ reverse micelles from 4.2×10^{-2} M to 4.2×10^{-3} M to no HCl, a decrease in the particle growth rate is observed. Two separate experiments are displayed for 4.2×10^{-3} M HCl,

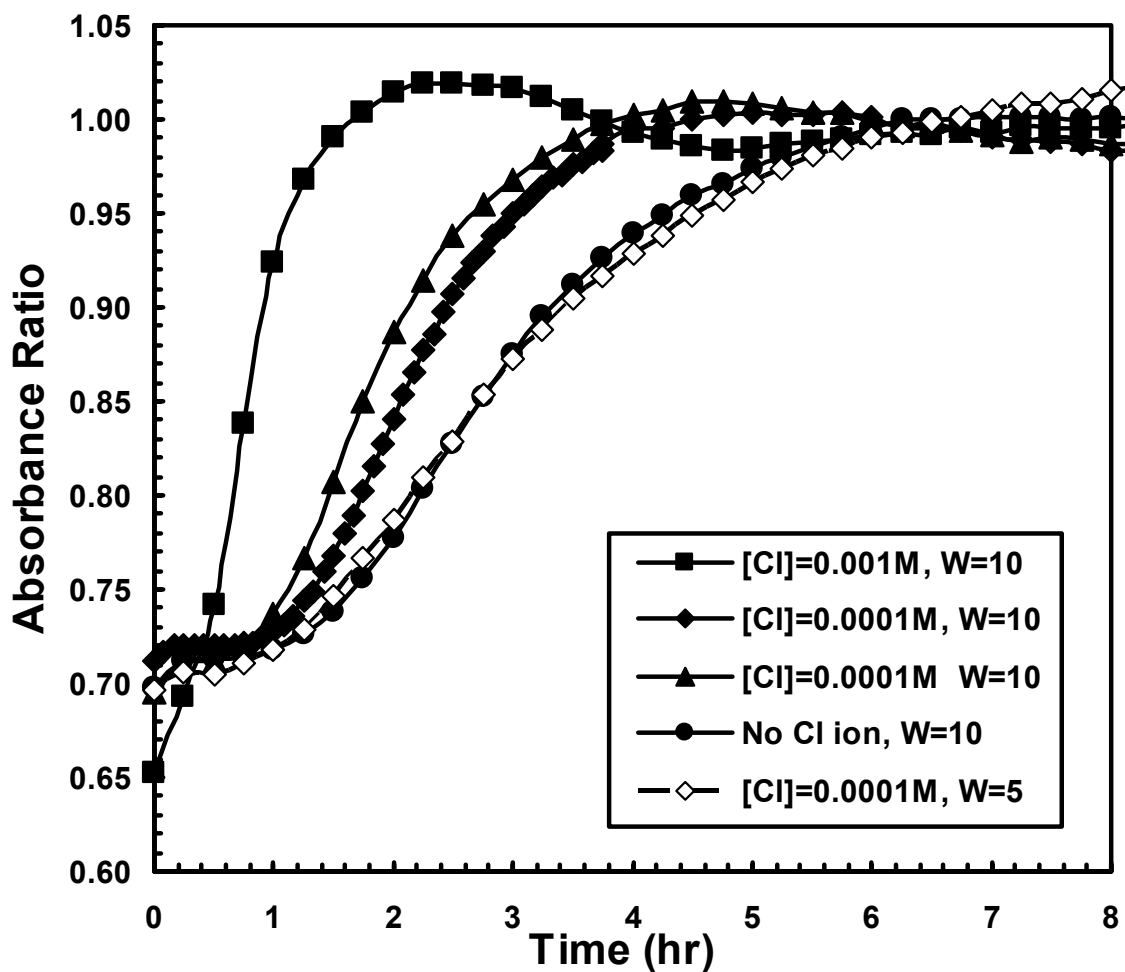


Figure 6-1. Copper nanoparticle growth curves measured in situ by the absorbance ratio of the intensity at $\lambda = 566$ nm relative to $\lambda = 500$ nm. The time resolved UV-vis absorbance measurements demonstrate the kinetics of spherical copper nanoparticle synthesis within the isooctane / AOT – $Cu(AOT)_2$ / H_2O reverse micelle microemulsion with varying W value and HCl concentration within the micelle core.

W = 10 to demonstrate the reproducibility of these growth curves. The particle growth curve for 4.2×10^{-3} M HCl, W = 5 is equivalent to W = 10 with no HCl illustrating the influence of W on the growth rate. This observation corresponds with our previous observations of a decreasing particle growth rate as the W value decreases from 10 to 5 with no Cl⁻ present.

The effect of Cl⁻ ion on the copper nanoparticle growth rate is of interest in determining the mechanism of particle synthesis. Previous studies have demonstrated that the properties of the reverse micelles, particularly the rigidity and intermicellar exchange rate, correlate with the nanoparticle growth rate within the reverse micelles where increases in rigidity and decreases in the intermicellar exchange rate result in decreased particle growth rates^{32,35,54-57}. The addition of NaCl to AOT microemulsions has been shown to induce phase separations, as well as, affect the elastic properties and spontaneous curvature of the surfactant film⁵⁸⁻⁶⁰. Studies of chloride addition to AOT reverse micelles have been performed in various alkane solvents, including isooctane and propane, demonstrating a significant decrease in water uptake of the microemulsions with the addition of small amounts of NaCl and other salts^{54,61-65}. The induced phase separation and decrease in water uptake are indicative of a decrease in micelle stability and thus a decrease in the intermicellar exchange potential and hence an increase in the nanoparticle growth rate would be expected.

TEM analysis of the particles synthesized in isooctane with W = 10 and varying HCl concentrations were with a Zeiss EM with 60 keV accelerating voltage and magnification up to 160,000X. The use of a particle stabilizing agent and removal of the surfactant by the liquid – liquid extraction technique significantly improved the ability to

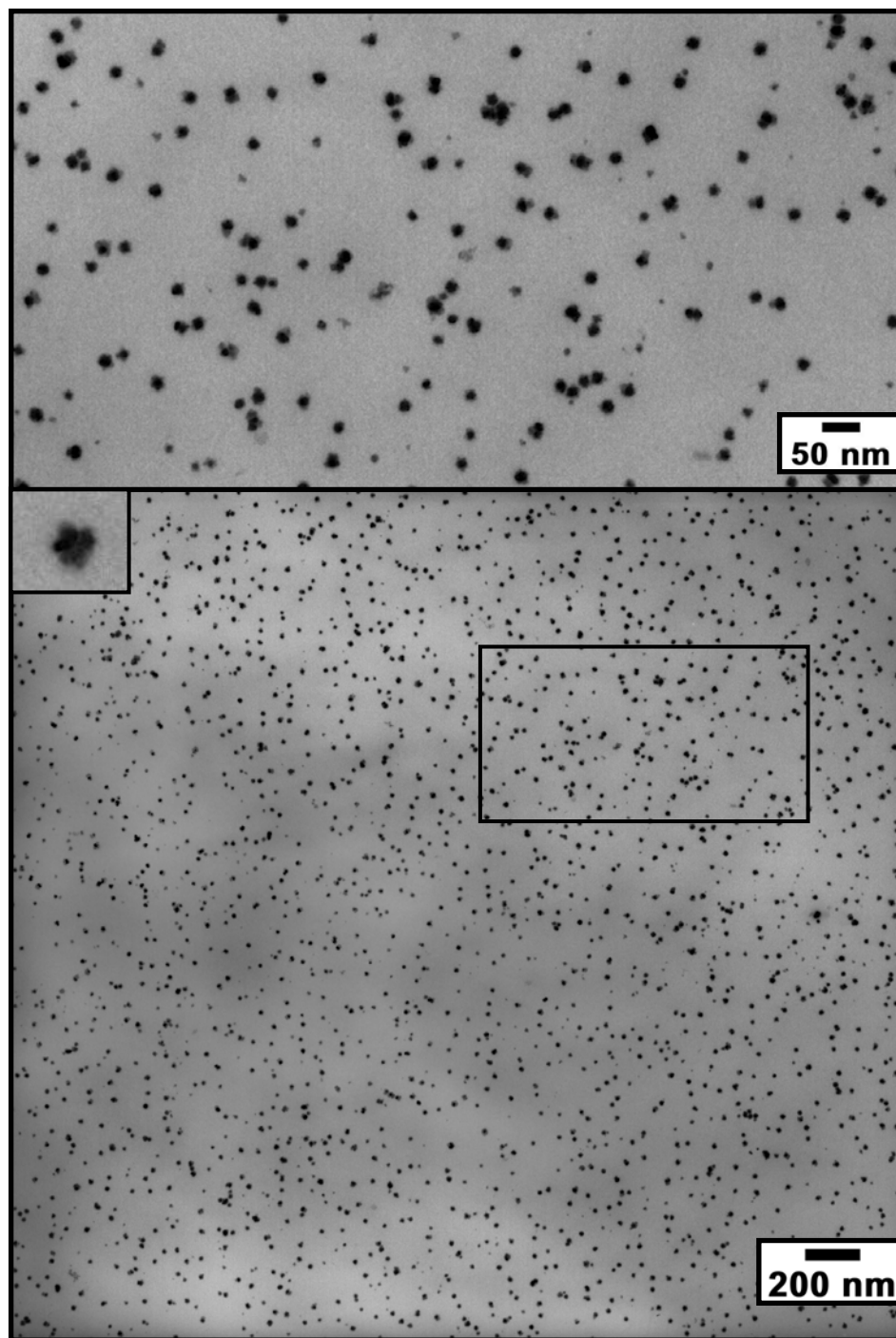


Figure 6-2. TEM image of copper nanoparticles synthesized in isooctane / AOT – $\text{Cu}(\text{AOT})_2$ / $W = 10$ reverse micelle microemulsion with $[\text{HCl}] = 4.2 \times 10^{-2}$ M within the micelle core. The copper particles are stabilized by dodecylamine, and the AOT surfactant was removed prior to particle collection. The image displays the uniformity of particle deposition and details of particle agglomerates with increasing magnification.

image the particles and obtain uniform particle dispersions, shown in Figure 6-2. Similar methods have been implemented for particle stabilization and the removal of surfactant from nanoparticles synthesized by emulsion techniques⁶⁶. Following the surfactant removal, particle concentration and size selective precipitation techniques can be used to obtain uniform, mono-dispersed particles, deposited in closely packed particle arrays, similar to those obtained by the phase transfer catalyst methods of particle synthesis and processing developed by Brust and others^{1,67,68}. The methods investigated in this study were limited to particle synthesis and the collection methods discussed previously, however the size selective precipitation and particle concentration techniques for obtaining particle arrays were not implemented. A variety of particle stabilizing agents including dodecylamine, lauric acid, and (3-Aminopropyl)trimethoxysilane were implemented with no noticeable effects on the particle size distributions. The commonly used particle stabilizer, dodecanethiol was also used but immediately following thiol addition, particle precipitation was observed and in some cases the formation of a gel like matrix of was formed. For this study, the analysis will concentrate on the use of dodecylamine as the stabilizing agent. The surfactant extraction technique following particle stabilization was found to be most effective using 50 % to 20 % ethanol / water solutions. Extraction with pure water resulted in minimal AOT removal and with pure ethanol, a phase separation was not observed. The effectiveness of AOT removal was judged by drying the extracted aqueous phase, as well as observing improved TEM imaging and EDS analysis. Qualitative atomic analysis using EDS was performed on a JEOL JEM 2010 TEM demonstrating a significant decrease in the intensity of peaks

corresponding to sodium, sulfur and oxygen when the AOT was extracted from the particle dispersion.

Figure 6-3 displays the particle size distributions obtained by TEM analysis, by plotting a histogram of particle diameters determined using ImageJ software. Figure 6-3a presents the particle size distribution for dodecylamine capped copper particles synthesized in the Isooctane / Cu(AOT)₂ - AOT / W = 10 reverse micelle system with no Cl⁻ present illustrating an 11.1 nm mean particle diameter and a standard deviation of 4.5. Figure 6-3b presents the particle size distribution for dodecylamine capped copper particles synthesized in the Isooctane / Cu(AOT)₂ - AOT / W = 10 reverse micelle system with [HCl] = 4.2 x 10⁻³M having a 10.0 nm mean particle diameter and a standard deviation of 3.6. Figure 6-3c displays the particle size distribution with for particle synthesis with [HCl] = 4.2 x 10⁻²M and interestingly, the particle diameters exhibit bimodal distribution with two peaks centered at 5 nm and 17 nm. The TEM image presented in Figure 6-2 displays the dodecylamine capped copper particles synthesized with [HCl] = 4.2 x 10⁻²M, collected after removal of the AOT. The deposited particles appear to be evenly distributed however, on analysis of individual particles at a higher magnification, it appears that the larger particles actually consist of aggregates of smaller particles which form a single particle. This observation corresponding to the increased [Cl⁻] concentration may be the result of the chloride ion interacting with the particle surface therefore competing with the capping agent. Upon the liquid – liquid extraction, the chloride ion is removed with the aqueous phase allowing for further particle agglomeration. In addition, this interaction between ionic species and the particle surfaces would result in stabilization of smaller particles during synthesis⁶⁹. This Cl⁻ ion

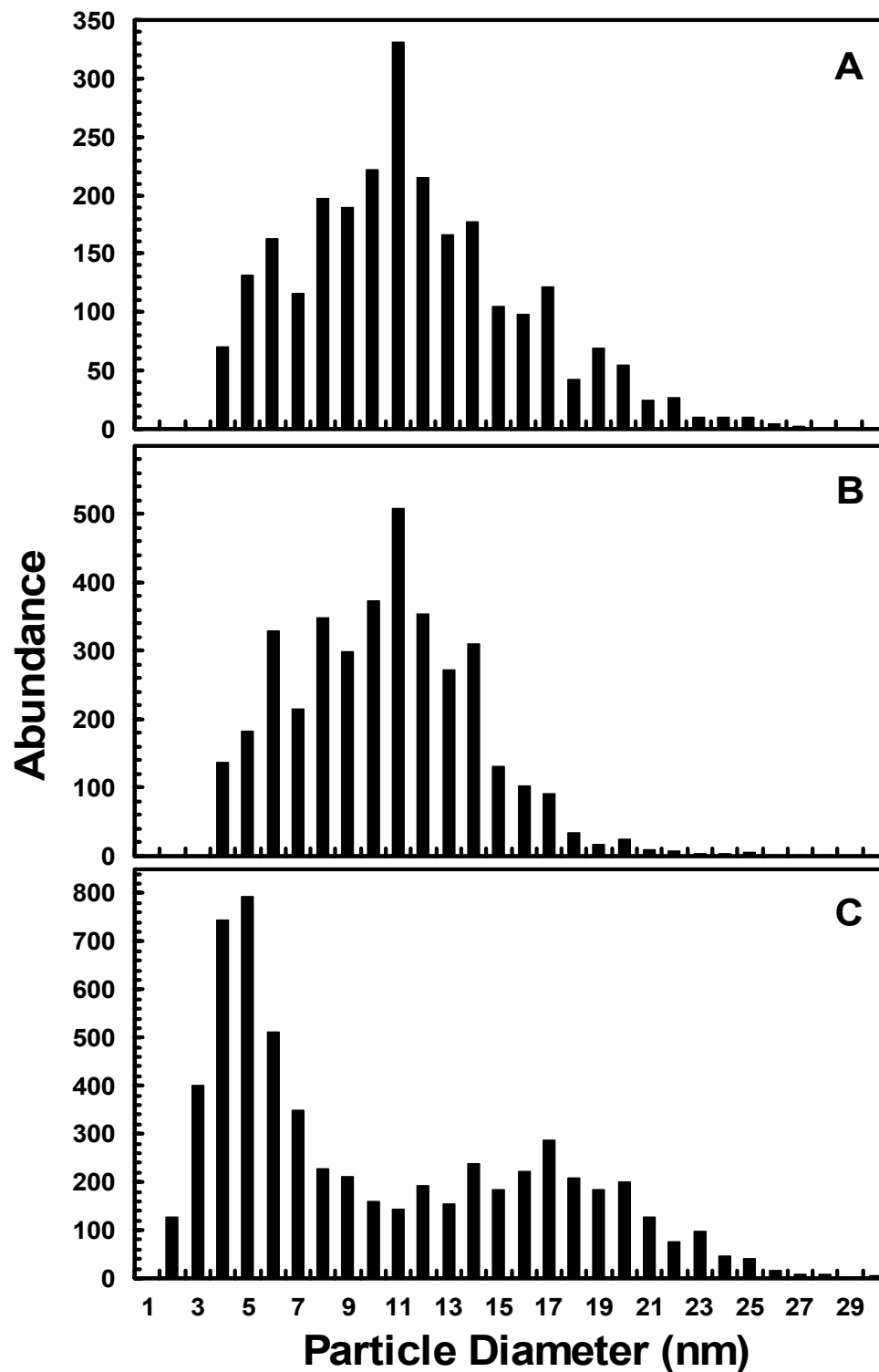


Figure 6-3. Particle size distributions obtained from TEM analysis of copper nanoparticles synthesized within isooctane / AOT – Cu(AOT)₂ / W = 10 reverse micelle microemulsion with HCl concentrations within the micelle core of a) 0.0 M, b) 4.2×10^{-3} M, c) 4.2×10^{-2} M.

surface interaction combined with aggregation upon extraction results in the bimodal distribution observed. To support this theory, an interaction energy model^{31,32,70} was implemented to predict the interaction energy between dodecylamine coated spherical copper nanoparticles dispersed in isooctane as a function of separation distance and particle size. Figure 6-4 displays the interaction energy curves where a decrease in the curve minimum is observed for increasing particle sizes from 12 nm to 22 nm. As particle size is increased, the curve minimum crosses the $-3/2 k_B T$ stabilization threshold (minimum energy required to disperse particles in solution) at approximately 19 nm and thus the model predicts that a maximum particle diameter of 19 nm would be stabilized in isooctane by the dodecylamine stabilizing agent. This corresponds well with the size distribution peak centered at 17 nm and it is viable that the van der Waals attractive forces between particles would promote the formation of larger particles during the stabilization, extraction and collection procedures.

The interaction of chloride ions with the nanoparticle surfaces has an effect on the particle synthesis of spherical copper nanoparticles as well as the stabilization methods. Previous studies of metallic nanoparticle synthesis in liquid solvents with chloride ions present (via NaCl), resulted in the formation of copper nanorods^{16,30}. In contrast, the particle geometries synthesized by the methods presented here consist solely of spherical nanoparticles and aggregates of spherical nanoparticles. However, synthesis of copper nanorods was achieved using the methods presented here with lower water contents in the isooctane / Cu(AOT)₂ – AOT / W = 3 reverse micelle system with [HCl] = 4.2 x 10⁻² M within the reverse micelle core. Overall, the copper nanomaterials synthesized in this manor consisted of a combination of spherical copper nanoparticles and randomly

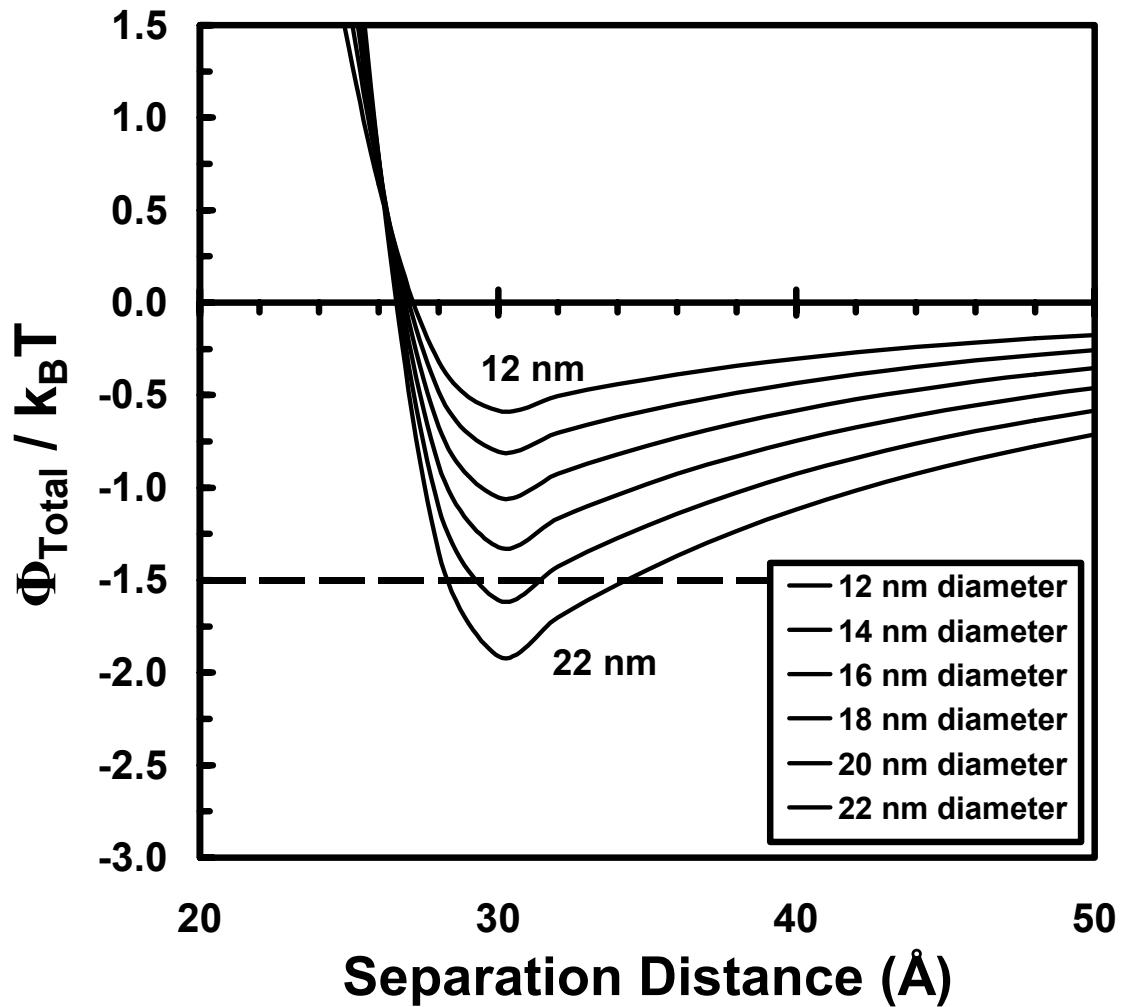


Figure 6-4. Total interaction energy of two spherical copper nanoparticles coated with dodecylamine and dispersed in isooctane as a function of the particle diameter and separation distance.

dispersed copper nanorods of inconsistent lengths and aspect ratios. Figure 6-5 presents an example of the copper nanorods synthesized.

Particle synthesis was also attempted using CuCl_2 as the copper precursor dissolved in the aqueous core of the AOT / Isooctane / $W = 10$ reverse micelle system; however microemulsion stability and reproducibility issues were experienced. Despite the ability to maintain a stable, single phase microemulsion during synthesis with CuCl_2 , copper nanoparticles were formed as well as larger aggregates ranging in size up to the 100 nm range and the presence of the occasional copper nanocube, as observed previously^{16,30}.

6-3b. Particle Synthesis in Compressed Propane – AOT Reverse Micelles

Synthesis of nanoparticles within compressed and supercritical fluids offer a several advantages over conventional fluid based synthesis methods including adjustable solvent properties, ease of solvent removal, and particle deposition techniques. We previously demonstrated copper nanoparticle synthesis within compressed propane / AOT reverse micelles including the effects of the adjustable bulk solvent properties on particle synthesis. This study investigates the effects of chloride addition on copper nanoparticle synthesis within compressed propane / $\text{Cu}(\text{AOT})_2$ – AOT / $W = 3$ reverse micelles at 20°C and 310 bar. Particle synthesis was monitored in situ by UV-vis absorbance measurements, however, difficulties arose due to copper plating on the vessel windows during the later stages of particle synthesis. Immediately following the introduction of the hydrazine reducing agent, copper nanoparticle synthesis in the compressed propane system in the absence of chloride ions results in an initial deep blue

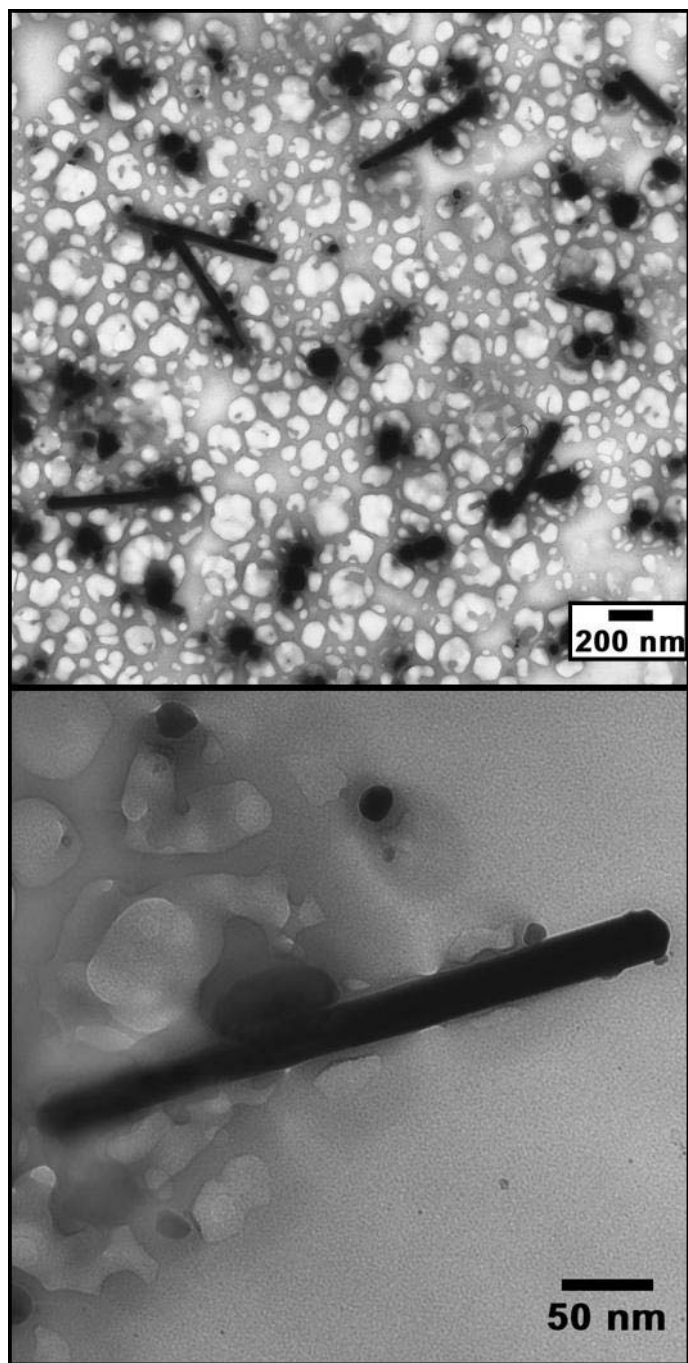


Figure 6-5. TEM image of copper nanorods synthesized in isooctane / AOT – Cu(AOT)₂ / W = 3 reverse micelle microemulsion with [HCl] = 4.2 x 10⁻² M.

solution color exhibiting a broad intense peak centered at 670 nm. The broad peak at 670 nm steadily decreases with a color change to light brown, followed by the appearance of the characteristic absorbance peak centered at 566 nm indicating spherical copper nanoparticle synthesis (similar to spectrum b in Figure 6-6). Unlike particle synthesis in the liquid isooctane reverse micelle system where the addition of HCl did not affect the UV-vis absorbance spectra during particle synthesis, the addition of HCl to the compressed propane reverse micelle system significantly affects the shape and position of the absorbance peak observed during particle synthesis. Spectra a and c in Figure 6-6 are the absorbance spectra measured 3 hours after the initial reduction for synthesis with Cl⁻ concentrations of 4.2×10^{-3} M and 4.2×10^{-2} M respectively. An increase in intensity and a shift to higher wavelengths for the absorbance spectra of copper nanoparticles in solution has previously been attributed to the formation of interconnected networks of copper nanoparticles^{71,72}. It has also been suggested that an increase in intensity and a shift to higher wavelengths for the copper absorbance band would be observed with an increase in the aspect ratio of copper nanoparticles, as predicted from Mie theory⁷³ and observed experimentally for copper nanorods²¹. The observed differences in the absorbance spectra prohibit the ability to monitor the particle growth rates, as demonstrated previously, however the changes do suggest alterations in the geometry or assembly of the copper nanoparticles during synthesis. TEM analysis of the copper nanoparticles synthesized in the compressed propane / Cu(AOT)₂ – AOT / W = 3 reverse micelle system at 20°C and 310 bar with the addition of HCl reveals the formation of diamond shaped aggregates of copper nanoparticles as shown in Figure 6-7 and Figure 6-8. To our knowledge, the formation of copper nanoparticle assemblies in this distinct

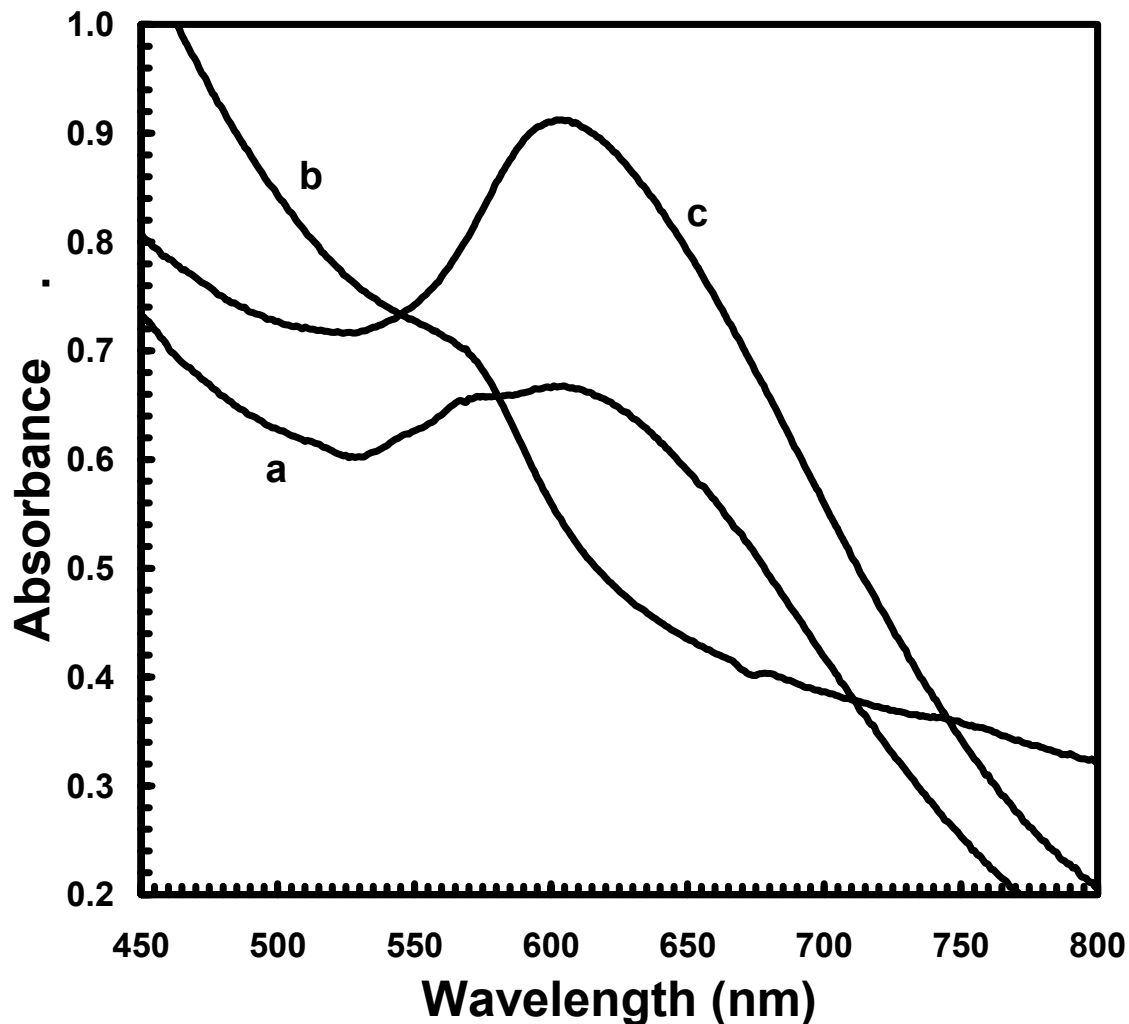


Figure 6-6. In situ UV-vis absorbance spectra of copper nanoparticles, synthesized in compressed propane / AOT – Cu(AOT)₂ / W = 3 reverse micelle microemulsion. Spectrum a was measured in situ, 3 hours after copper reduction with [HCl] = 4.2 × 10⁻³ M at 20°C and 310 bar. Spectrum b was measured from the organic isooctane phase after the liquid – liquid extraction step of the particle collection methods for the experiment corresponding to spectrum a. Spectrum c was measured in situ, 3 hours after copper reduction with [HCl] = 4.2 × 10⁻² M at 20°C and 310 bar.

diamond shaped geometry is unique to this compressed propane method of particle synthesis and has not been observed in any other method of nanomaterial production. TEM images of the diamond-shaped particle assemblies shown in Figure 6-7 were obtained from particle synthesis in the compressed propane / $\text{Cu}(\text{AOT})_2 - \text{AOT} / \text{W} = 3$ reverse micelle system with $[\text{HCl}] = 4.2 \times 10^{-2} \text{ M}$ at 20°C and 310 bar. The geometry and structure of the diamond-shaped assemblies are consistent with an apparent two dimensional, well defined parallelogram exterior geometry and a disordered array of small particles within the outer structure. The diamond-shaped assemblies vary widely in size and the number of smaller particles which fill the outer geometry. However, the assemblies are remarkably consistent in their shape and structure where $\theta_1 = 58^\circ \pm 2^\circ$ and $\theta_2 = 180^\circ - \theta_1$. Each of the assemblies has either a diamond-shaped outer structure or a closely related parallelogram structure with length scales of approximately 500 nm for the aggregate outer edges. A majority of the diamond-shaped assemblies also contain a distinct particle or dense agglomeration of particles in the center that is considerably larger than the surrounding particles within the outer structure. Variations were also observed in the large particles located in the center of the assembly, where in some cases, such as Figure 6-7a, it appears to be spherical and polycrystalline. For other cases, as observed in Figure 6-7b, the center particle appears to be crystalline with 5-fold geometry or in Figure 6-7c the center particle appears as a single crystal with hexagonal structure. High resolution TEM and SAED investigations confirm the varying degrees of crystallinity where the larger central particles are polycrystalline with fcc structure with twin boundaries. Overall the central particles appear to consist of a crystalline core particle with smaller fcc crystalline particles attached to the core particle with different

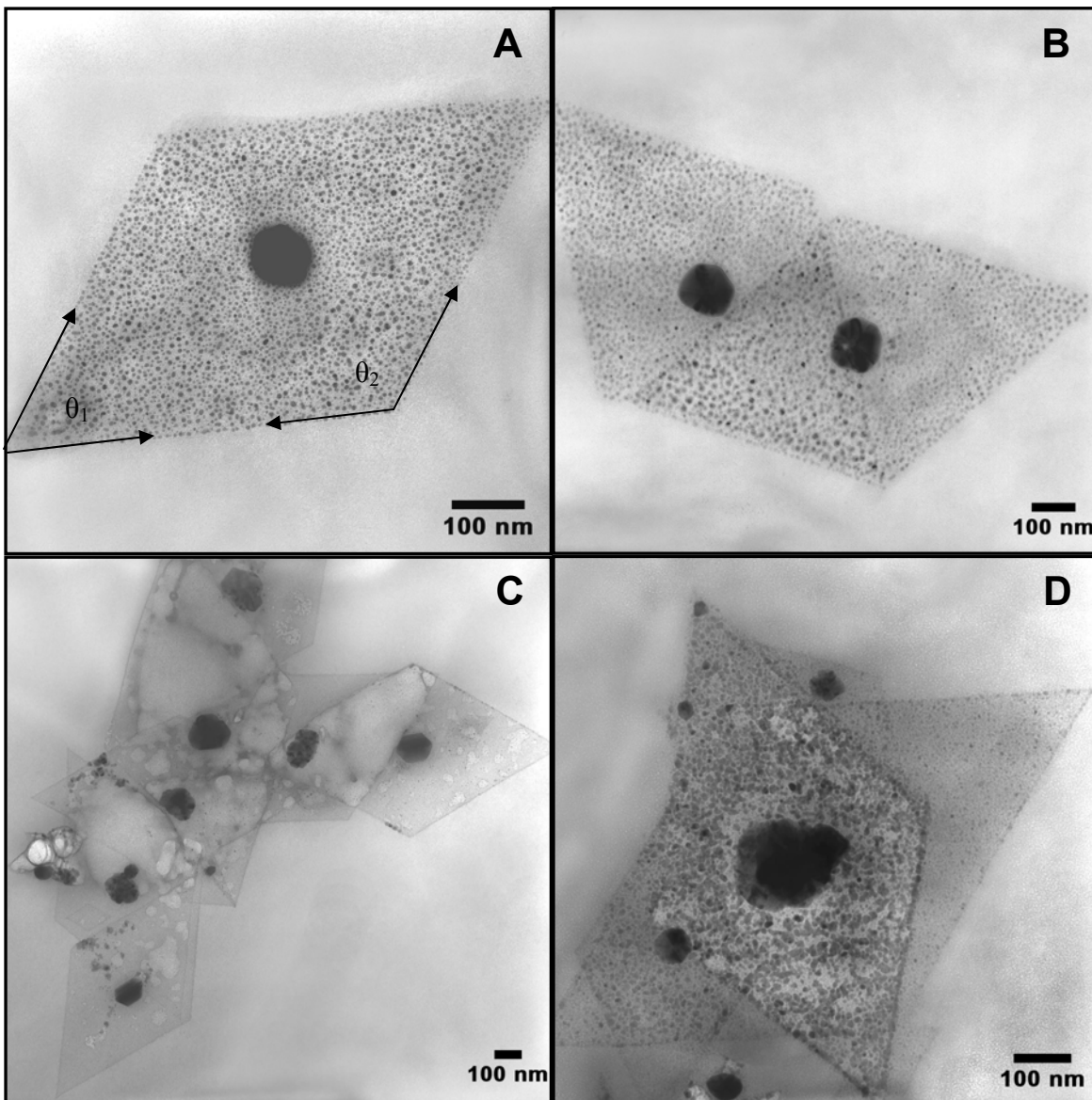


Figure 6-7. TEM Images of diamond shaped assemblies of copper nanoparticles synthesized in compressed propane / AOT – $\text{Cu}(\text{AOT})_2$ / $W = 3$ reverse micelles with $[\text{HCl}] = 4.2 \times 10^{-2}$ M within the micelle core. Particles were collected by a,b) spray process from the propane system and c,d) droplet method for particles re-dispersed in isoctane + 0.01 M dodecylamine.

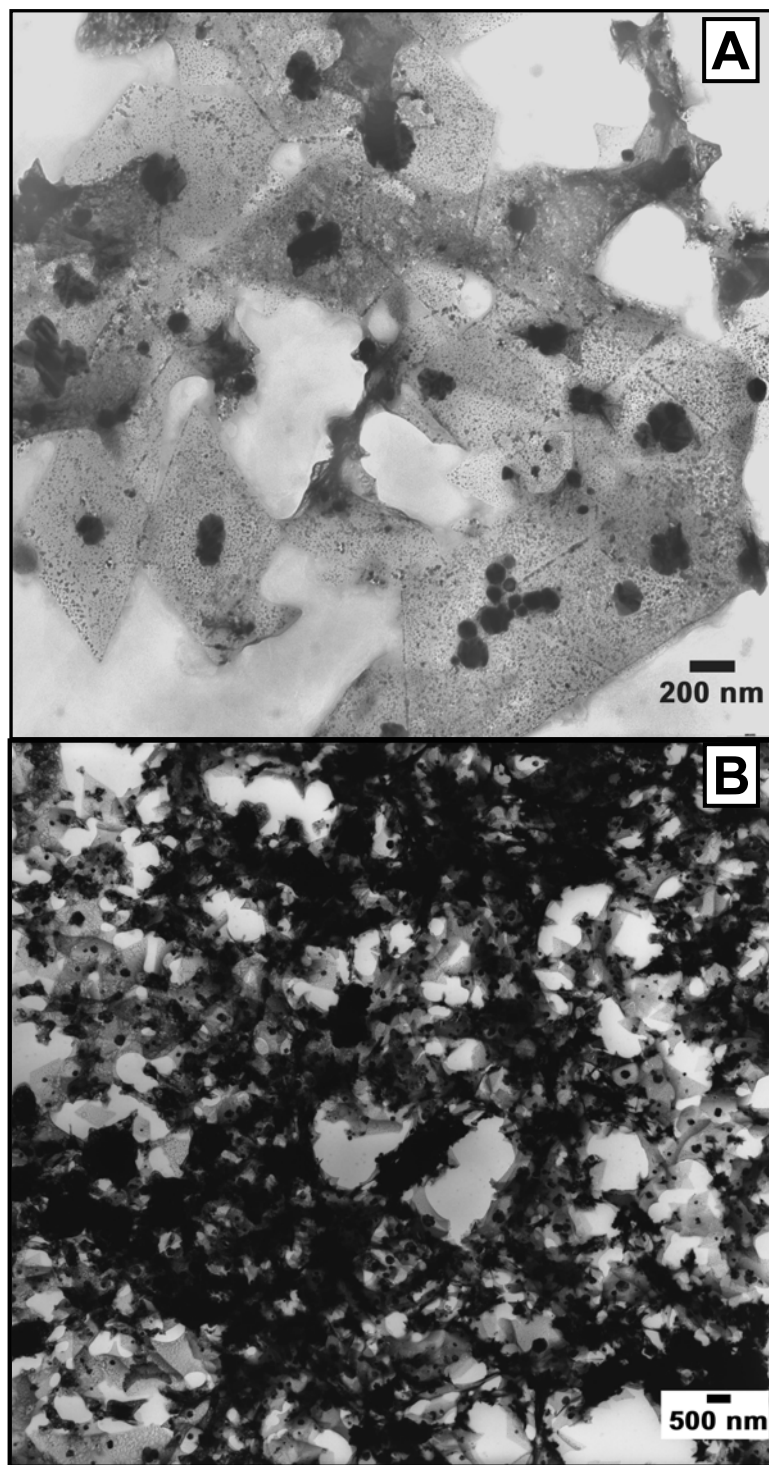


Figure 6-8. TEM image of diamond shaped aggregates of copper particles collected as a precipitate at the aqueous – oil interface during the liquid – liquid extraction of the AOT surfactant followed by re-dispersion in acetone. Synthesis was performed in compressed propane / AOT – $\text{Cu}(\text{AOT})_2$ / $W = 3$ reverse micelles with $[\text{HCl}] = 4.2 \times 10^{-2}$ M.

orientations. The internal structure of these diamond-shaped assemblies is of significant interest and will be investigated in depth in future studies with focus on determining the origin of these intricate structures. We have observed that the experimental conditions that favor the formation of diamond-shaped assemblies of copper nanoparticles requires both the synthesis of copper nanoparticles within a compressible solvent based reverse micelle microemulsion with $W = 3$ and the presence of chloride ions at concentrations of 4.2×10^{-2} M and 4.2×10^{-3} M. In our previous investigations of copper nanoparticle synthesis within compressed propane and supercritical ethane based AOT microemulsions in the absence of chloride ions, the formation of the diamond-shaped copper particle assemblies was not observed. Similarly, in the isooctane liquid phase microemulsion system discussed previously with the addition of chloride ions, the formation of the diamond-shaped assemblies was not observed. Thus, the formation of these interesting structures requires the use of a compressed fluid as the bulk solvent and the presence of low concentrations of chloride ions, however the exact mechanism of formation is still under investigation. The question remains whether the diamond-shaped particle assemblies are synthesized in the observed geometry in solution or if the assemblies are the result of some type of crystallization that occurs during the depressurization (solvent decompression) during particle collection process. The differences observed in the UV-vis absorbance spectra with and without Cl^- suggest the formation of copper nanoparticles with geometries or structures other than spherical particles; however this observation is not conclusive for the formation of the diamond-shaped structures. In the same respect, it is difficult to rule out the effects of depressurization that occur during particle collection, including rapid removal of the

propane solvent and a significant temperature drop due to the Joule-Thompson effect during solvent expansion. The solvent removal and temperature drop are both occurrences which would promote crystallization and the formation long range ordering of the copper nanoparticles into the defined diamond-shaped geometry.

Another interesting property of the diamond-shaped copper nanoparticle assemblies is the stability of the structure formed. After particle synthesis and removal of the compressed solvent by depressurization, the precipitated particle / surfactant matrix left in the reaction vessel was re-dispersed in isooctane with 0.01 M dodecylamine, followed by a liquid – liquid extraction of the AOT surfactant using a 50% ethanol / water solution by methods similar to particle collection in the liquid isooctane phase. The TEM images in Figure 6-7 were obtained from copper nanoparticle synthesis in the compressed propane / $\text{Cu}(\text{AOT})_2$ – AOT / $W = 3$ reverse micelle system with $[\text{HCl}] = 4.2 \times 10^{-2}$ M at 20°C and 310 bar. The particles in Figure 6-7a and 6-7b were collected by the spray technique through capillary tubing during depressurization for two separate experiments at identical experimental conditions. Figure 6-7b demonstrates the overlap of two diamond-shaped structures. The TEM images in Figure 6-7c and 6-7d were obtained from samples prepared by placing a droplet of the isooctane solution with 0.01 M dodecylamine and the re-dispersed particle / surfactant matrix resulting from the same experiment as Figure 6-7b. Figure 6-7c and 6-7d demonstrate the consistency of the overall diamond-shape geometry, as well as the variation in the size and shape of the larger center particle. Interestingly, the size of the central particle corresponds to the size of the diamond-shaped structure. Comparison of the two particle collection techniques demonstrates that well defined and isolated structures are obtained

by the spray process while the re-dispersed samples result in agglomeration of the diamond-shaped aggregates. The observed agglomerations may be due to the precipitation of the surfactant / particle matrix during depressurization or possibly an effect of the droplet collection technique used for collection of the re-dispersed solutions. Following re-dispersion, the liquid – liquid extraction method for the removal of the AOT surfactant was implemented and upon which, a significant amount of precipitation from the isooctane phase occurred at the interface of the two liquids. Prior to the precipitation, the isooctane phase exhibited a cloudy, red-brown color and after precipitation the isooctane phase appeared clear with a very slight red tint having negligible UV-vis absorbance and no copper particles on the TEM grid. The cause of the precipitation is likely the partitioning of ethanol from the aqueous phase into the isooctane phase. Ethanol addition has been used extensively and effectively in the precipitation of dodecanethiol stabilized metallic particles from organic phases in size selective particle fractionations^{68,74}. The precipitate was isolated from the liquid phases and re-dispersed in acetone. The TEM images in Figure 6-8 were obtained by the droplet collection method of the acetone precipitate dispersion, demonstrating the extent of the diamond-shaped structure synthesis and the stability of the structures to withstand extensive solution processing. The synthesis of the diamond-shaped structures is reproducible and from our observations a majority of the nanoparticles synthesized exist in the diamond-shaped structure.

Several modifications to the experimental procedure were examined in order to gain a better understanding of the underlying mechanism for the formation of these structures. The particle collection process was performed for the compressed propane /

$\text{Cu}(\text{AOT})_2 - \text{AOT} / \text{W} = 3$ reverse micelle system with $[\text{HCl}] = 4.2 \times 10^{-2} \text{ M}$ at 20°C and 310 bar, without the introduction of the hydrazine reducing agent, as well as immediately following hydrazine reduction while the microemulsion exhibited the deep blue color. In both cases, the presence of diamond-shaped structures was not observed. This suggests that the diamond-shaped structures are either synthesized as such in solution or that the presence of copper particles is necessary for the formation of the structures on depressurization. In addition, spherical particles synthesized in isooctane with HCl and reagent concentrations equivalent to those in the propane synthesis were collected by nebulizer spray and diamond-shaped structures were not formed. The fine mist produced by the nebulized particle solution simulates the compressed propane spray process in that the isooctane is quickly evaporated from the atomized solution coupled with a temperature drop due to solvent evaporation. Interestingly, the effects of the chloride ion on particle geometry from the isooctane microemulsion was evidenced by the observation of copper nanorods at the lower water content ($\text{W} = 3$) and not with higher water content ($\text{W} = 5$ or 10). This suggests that the low water content necessary for copper nanoparticle synthesis in compressed propane³¹ may facilitate the formation of the diamond-shaped assemblies within the microemulsion system.

EDS analysis was also performed on the diamond-shaped copper nanoparticle assemblies. Figure 6-9a presents the EDS spectrum from the presented sample in Figure 6-7b where the sample was collected by the propane spray technique on a nickel TEM grid. The EDS measurement shows evidence of Ni from the grid bars of the TEM grid, Cu from the nanoparticles, and S, Na, and O from the AOT surfactant. Interestingly, the presence of Cl is not observed. Figure 6-9b presents the EDS spectra for copper particles

collected on a copper grid after the liquid – liquid extraction of the AOT surfactant, corresponding to Figure 6-10c,d and demonstrating the effective removal of the AOT surfactant. Again, the presence of Cl was not observed.

Another aspect to take into consideration is the concentration of HCl. High concentrations of HCl (0.42 M) within the micelle core resulted in the inability to synthesize copper nanoparticles, as also observed in the isooctane study. Particle synthesis was achieved with low HCl concentrations of 4.2×10^{-3} M within the micelle core as demonstrated with the UV-vis absorbance spectra in Figure 6-6 and the TEM images in Figure 6-10. The diamond-shaped assembly of copper nanoparticles was again observed with this low HCl concentration (4.2×10^{-3} M) in propane. It is important to note, however, that particle synthesis in propane with no HCl present resulted in dispersed spherical particles and the diamond-shaped assemblies were not observed. Figure 6-10a presents the TEM image of the sample collected by the spray process following synthesis in the compressed propane / $\text{Cu}(\text{AOT})_2 - \text{AOT} / \text{W} = 3$ reverse micelle system with $[\text{HCl}] = 4.2 \times 10^{-3}$ M at 20°C and 310 bar. The copper particles in Figure 6-10b were collected by the droplet method of the particle / surfactant matrix re-dispersed in isooctane + 0.01 M dodecylamine. The copper particles in Figure 6-10c and 6-10d were collected using the particle nebulizer and a solution of the particle precipitate resulting from the liquid – liquid extraction procedure, dispersed in acetone. TEM analysis of copper particles synthesized at the lower HCl concentration (4.2×10^{-3} M vs 4.2×10^{-2} M) reveals several interesting observations, particularly the absence of the large particle located in the center of the diamond-shaped structure. From our study, a few occurrences of the large center particle were observed, but for the most part, the

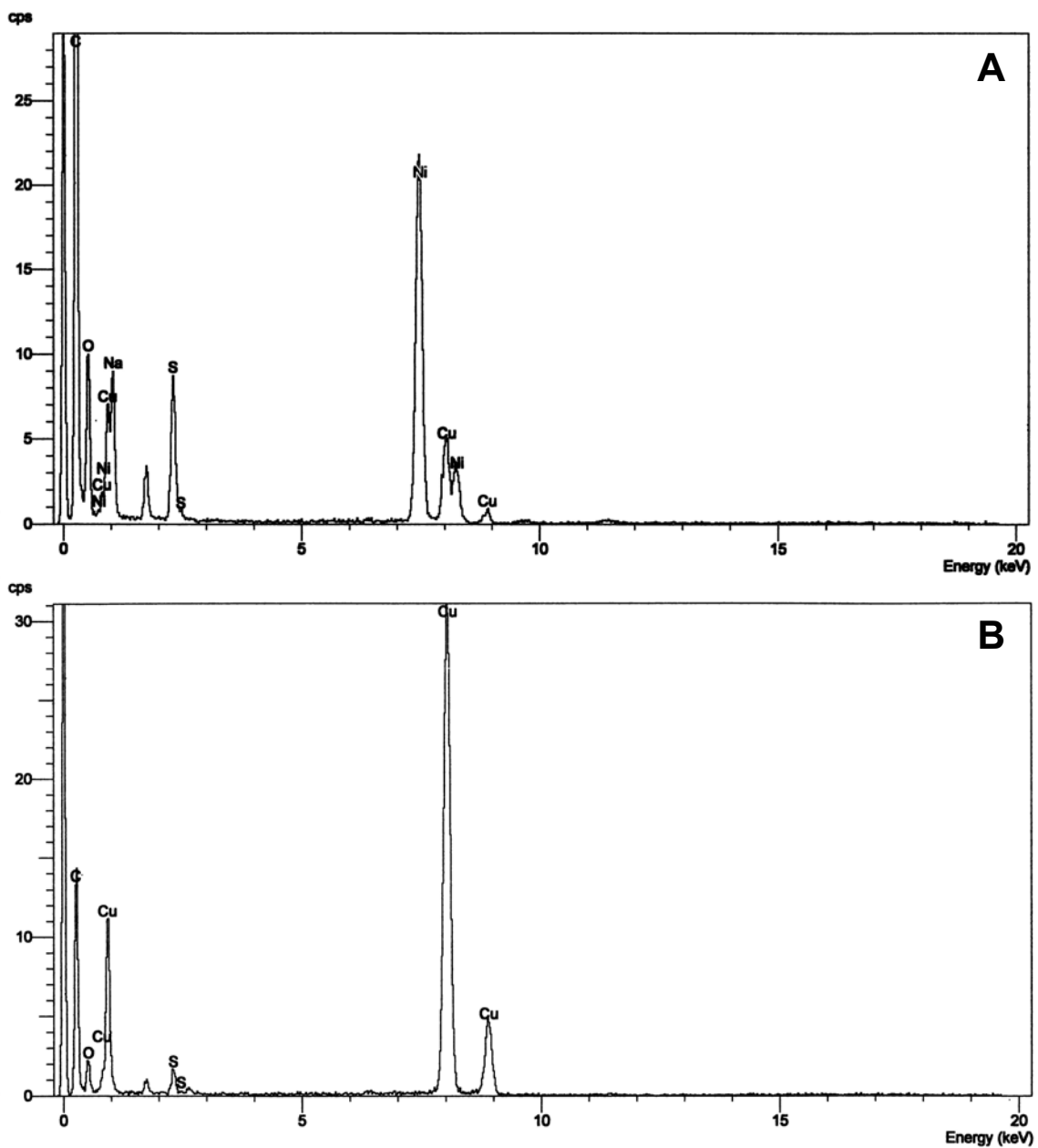


Figure 6-9. EDS spectra measured from diamond shaped assemblies of copper nanoparticles collected by a) spray technique following synthesis in compressed propane, on a nickel TEM grid (Figure 7a) and b) by the droplet method on a copper grid of particles re-dispersed in acetone following precipitation during the liquid – liquid extraction of the AOT surfactant (Figure 10c).

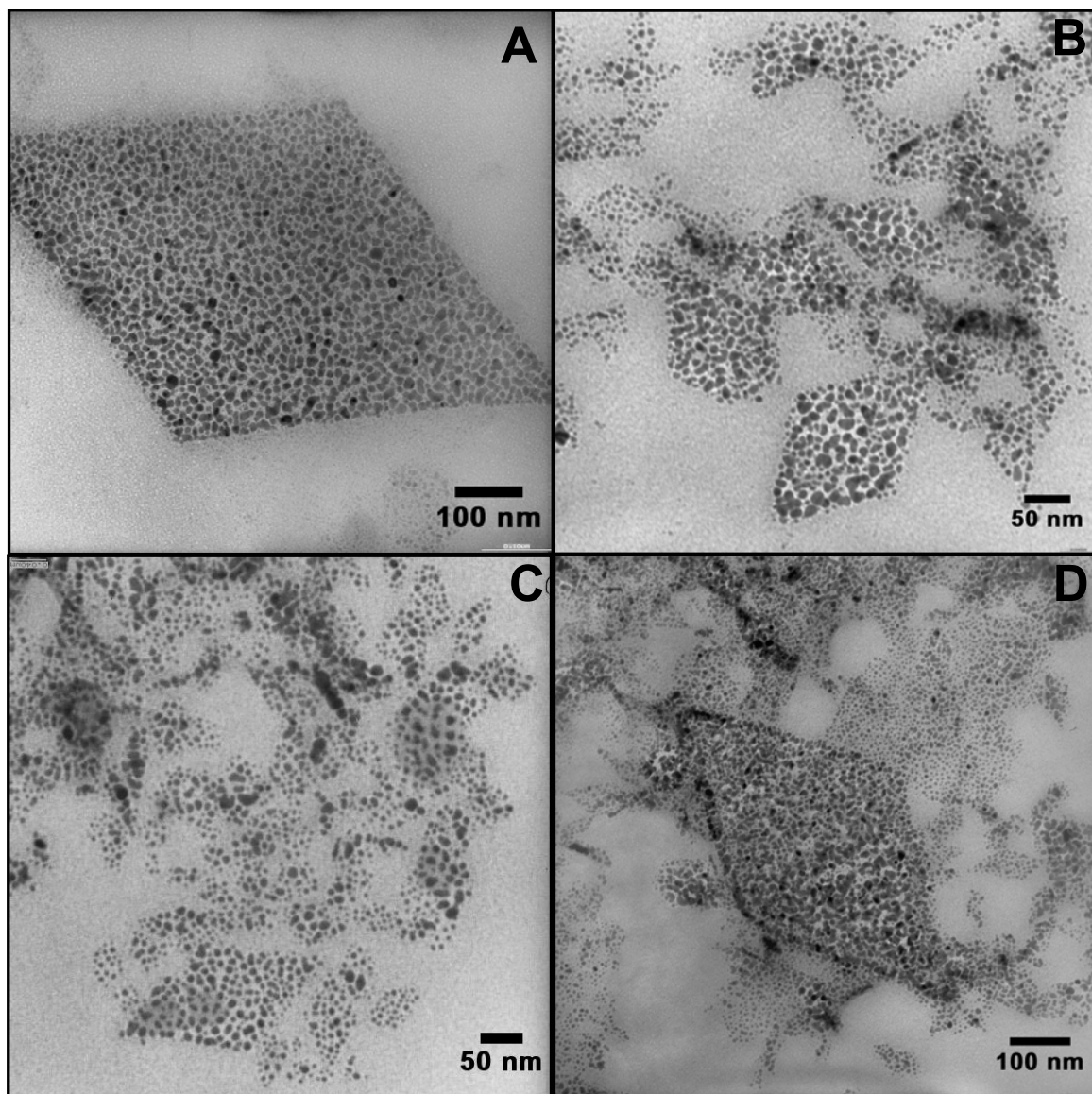


Figure 6-10. TEM images of copper nanoparticles synthesized in compressed propane / AOT – Cu(AOT)₂ / W = 3 reverse micelles with [HCl] = 4.2 x 10⁻³ M and collected by a) spray process, b) re-dispersion in isoctane + 0.01 M dodecylamine, and c,d) by precipitation during the liquid – liquid extraction of the AOT surfactant and re-dispersed in acetone.

large particle was absent. Another observation is the apparent decrease in the defined diamond-shaped geometry and an increase in the occurrence of isolated individual particles. The particle collection process described for the synthesis with $[\text{HCl}] = 4.2 \times 10^{-2} \text{ M}$ was also applied to the synthesis with $[\text{HCl}] = 4.2 \times 10^{-3} \text{ M}$ and similar results were observed with one exception. During the liquid – liquid extraction process, precipitation to the liquid interface was observed to a lesser extent. The cloudy, red-brown isooctane phase became clear, but retained the red-brown color. UV-vis absorbance analysis resulted in spectrum b in Figure 6-6 and TEM analysis resulted in the observation of mostly spherical copper nanoparticles and a few diamond-shaped particle assemblies with little structure. The UV-vis absorbance spectrum b is characteristic of spherical copper nanoparticles dispersed in solution with the characteristic absorbance band at 566 nm. Comparison of the spectra in Figure 6-6 and assuming that the 600 nm wavelength peak in spectrum c is representative of diamond-shaped copper nanoparticle assemblies dispersed in solution, spectrum a (lower HCl concentration) appears to exhibit characteristics of both spectra b and c with a broad peak centered at 600 nm and a small shoulder at 566 nm. This would suggest the presence of both diamond-shaped assemblies and independent spherical copper nanoparticles dispersed in compressed propane, 3 hours after copper reduction with $[\text{HCl}] = 4.2 \times 10^{-3} \text{ M}$ within the micelle cores. This suggestion corresponds with the observations made in the TEM analysis of the synthesized nanomaterials for this lower HCl concentration.

The results observed for copper nanoparticle synthesis with $[\text{HCl}] = 4.2 \times 10^{-3} \text{ M}$ demonstrates an effect of Cl^- concentration on the formation of diamond-shaped copper nanoparticle assemblies. UV-vis analysis and the inability to obtain diamond-shaped

geometries prior to and immediately following copper reduction suggests that the diamond-shaped copper nanoparticle assemblies are synthesized in their observed geometries while dispersed within the compressed propane / AOT reverse micelle system. Conversely, the inability to synthesize the diamond-shaped copper nanoparticle assemblies in conventional alkane liquid solvents, such as isooctane, demonstrates that the use of a compressed fluid as the bulk phase is required for the synthesis, from which solvent removal by depressurization is required for particle collection and TEM analysis. At this point, conclusive evidence of the governing factor which promotes the formation of diamond-shaped copper nanoparticle assemblies is not available, however further investigations will examine this novel method of nanomaterial production.

6-4. CONCLUSIONS

This study has demonstrated the effects of chloride ion on the synthesis of copper nanoparticles within the AOT reverse micelle system utilizing both liquid isooctane and compressed propane as the bulk solvent. Copper nanoparticle synthesis can be achieved with the addition of HCl to the micelle core at concentrations which are effectively buffered by the AOT surfactant. The concentration of chloride ion affects the particle growth rate in liquid isooctane as well as the effects of particle dispersing ligands. The addition of chloride ion to particle synthesis in compressed propane has a significant effect on the geometry and structure of the copper nanomaterials produced. As a result of HCl addition to the compressed propane / $\text{Cu}(\text{AOT})_2 - \text{AOT} / \text{W} = 3$ reverse micelle system at 20°C and 310 bar, the consistent formation of diamond-shaped copper nanoparticle assemblies is observed. Synthesis of the diamond-shaped assemblies

requires both the use of compressed propane as the bulk solvent and the presence of HCl within the AOT reverse micelles at concentrations low enough to be effectively buffered and high enough to promote interactions with the particle surfaces. The copper nanoparticle assemblies exhibit unique structure and retain their structure through repeated solvent processing. Future studies will further investigate the physical properties and mechanism of synthesis for the copper nanoparticle assemblies, as well as the ability to selectively separate and assemble the diamond-shaped copper nanoparticle structures for potential applications.

6-5. REFERENCES

- (1) Brust, M.; Kiely, C. J. *Colloid Surf. A-Physicochem. Eng. Asp.* 2002, 202, 175-186.
- (2) Brust, M.; Fink, J.; Bethell, D.; Schiffrin, D. J.; Kiely, C. J. *Chem. Soc.-Chem. Commun.* 1995, 1655-1656.
- (3) Wang, Z. L. *Adv. Mater.* 1998, 10, 13-+.
- (4) Collier, C. P.; Vossmeier, T.; Heath, J. R. *Annu. Rev. Phys. Chem.* 1998, 49, 371-404.
- (5) Murray, C. B.; Kagan, C. R.; Bawendi, M. G. *Annu. Rev. Mater. Sci.* 2000, 30, 545-610.
- (6) Parviz, B. A.; Ryan, D.; Whitesides, G. M. *Ieee Transactions on Advanced Packaging* 2003, 26, 233-241.
- (7) Shipway, A. N.; Katz, E.; Willner, I. *ChemPhysChem* 2000, 1, 18-52.
- (8) Maillard, M.; Giorgio, S.; Pileni, M. P. *J. Phys. Chem. B* 2003, 107, 2466-2470.
- (9) Gou, L. F.; Murphy, C. J. *Nano Lett.* 2003, 3, 231-234.
- (10) Gou, L. F.; Murphy, C. J. *Journal of Materials Chemistry* 2004, 14, 735-738.
- (11) Murphy, C. J. *Science* 2002, 298, 2139-+.
- (12) Sun, Y. G.; Xia, Y. N. *Science* 2002, 298, 2176-2179.
- (13) Sun, Y. G.; Mayers, B.; Xia, Y. N. *Adv. Mater.* 2003, 15, 641-646.
- (14) Pinna, N.; Weiss, K.; Urban, J.; Pileni, M. P. *Adv. Mater.* 2001, 13, 261-+.
- (15) Pileni, M. P.; Lalatonne, Y.; Ingert, D.; Lisiecki, I.; Courty, A. *Faraday Discussions* 2004, 125, 251-264.
- (16) Pileni, M. P. *Comptes Rendus Chimie* 2003, 6, 965-978.
- (17) Sun, Y. A.; Xia, Y. N. *Adv. Mater.* 2003, 15, 695-699.
- (18) Sun, Y. G.; Mayers, B.; Xia, Y. N. *Nano Lett.* 2003, 3, 675-679.
- (19) Filankembo, A.; Pileni, M. P. *Applied Surface Science* 2000, 164, 260-267.
- (20) Ziegler, K. J.; Doty, R. C.; Johnston, K. P.; Korgel, B. A. *J. Am. Chem. Soc.* 2001, 123, 7797-7803.
- (21) Liu, C. M.; Guo, L.; Xu, H. B.; Wu, Z. Y.; Weber, J. *Microelectron. Eng.* 2003, 66, 107-114.
- (22) Wang, C. Y.; Zhou, Y.; Chen, Z. Y.; Cheng, B.; Liu, H. J.; Mo, X. J. *Colloid Interface Sci.* 1999, 220, 468-470.
- (23) Wang, W.; Liu, Z.; Liu, Y.; Xu, C.; Zheng, C.; Wang, G. *Appl. Phys. A-Mater. Sci. Process.* 2003, 76, 417-420.

- (24) Zhao, Q. T.; Hou, L. S.; Huang, R.; Li, S. Z. *Mater. Chem. Phys.* 2004, 85, 180-183.
- (25) Lu, X. M.; Hanrath, T.; Johnston, K. P.; Korgel, B. A. *Nano Lett.* 2003, 3, 93-99.
- (26) Holmes, J. D.; Johnston, K. P.; Doty, R. C.; Korgel, B. A. *Science* 2000, 287, 1471-1473.
- (27) Sun, Y. G.; Yin, Y. D.; Mayers, B. T.; Herricks, T.; Xia, Y. N. *Chem. Mat.* 2002, 14, 4736-4745.
- (28) Sun, Y. G.; Mayers, B.; Herricks, T.; Xia, Y. N. *Nano Lett.* 2003, 3, 955-960.
- (29) Ziegler, K. J.; Harrington, P. A.; Ryan, K. M.; Crowley, T.; Holmes, J. D.; Morris, M. A. *Journal of Physics-Condensed Matter* 2003, 15, 8303-8314.
- (30) Filankembo, A.; Giorgio, S.; Lisiecki, I.; Pileni, M. P. *Journal of Physical Chemistry B* 2003, 107, 7492-7500.
- (31) Kitchens, C. L.; Roberts, C. B. *Industrial & Engineering Chemistry Research* 2004.
- (32) Kitchens, C. L.; McLeod, M. C.; Roberts, C. B. *J. Phys. Chem. B.* 2003, 107, 11331-11338.
- (33) Cason, J. P.; Khambaswadkar, K.; Roberts, C. B. *Ind. Eng. Chem. Res.* 2000, 39, 4749-4755.
- (34) Cason, J. P.; Roberts, C. B. *J. Phys. Chem. B* 2000, 104, 1217-1221.
- (35) Cason, J. P.; Miller, M. E.; Thompson, J. B.; Roberts, C. B. *J. Phys. Chem. B* 2001, 105, 2297-2302.
- (36) Shah, P. S.; Hanrath, T.; Johnston, K. P.; Korgel, B. A. *Journal of Physical Chemistry B* 2004, 108, 9574-9587.
- (37) Shah, P. S.; Johnston, K. P.; Korgel, B. A. In *Supercritical Carbon Dioxide: Separations and Processes*, 2003; Vol. 860, pp 339-352.
- (38) Shah, P. S.; Novick, B. J.; Hwang, H. S.; Lim, K. T.; Carbonell, R. G.; Johnston, K. P.; Korgel, B. A. *Nano Lett.* 2003, 3, 1671-1675.
- (39) Zhang, J. L.; Han, B. X.; Liu, J. C.; Zhang, X. G.; He, J.; Liu, Z. M.; Jiang, T.; Yang, G. Y. *Chem.-Eur. J.* 2002, 8, 3879-3883.
- (40) Johnston, K. P.; Shah, P. S. *Science* 2004, 303, 482-483.
- (41) Yan, D.; Jennings, G. K.; Weinstein, R. D. *Ind. Eng. Chem. Res.* 2002, 41, 4528-4533.
- (42) Weinstein, R. D.; Yan, D.; Jennings, G. K. *Ind. Eng. Chem. Res.* 2001, 40, 2046-2053.
- (43) Sun, Y.-P.; Atorngitjawat, P.; Meziari, M. J. *Langmuir* 2001, 17, 5707-5710.
- (44) Sun, Y. P.; Rollins, H. W.; Guduru, R. *Chem. Mat.* 1999, 11, 7-+.
- (45) Long, D. P.; Blackburn, J. M.; Watkins, J. J. *Adv. Mater.* 2000, 12, 913-915.
- (46) Blackburn, J. M.; Long, D. P.; Cabanas, A.; Watkins, J. J. *Science* 2001, 294, 141-145.
- (47) Cabanas, A.; Blackburn, J. M.; Watkins, J. J. *Microelectron. Eng.* 2002, 64, 53-61.

- (48) Ohde, H.; Ohde, M.; Bailey, F.; Kim, H.; Wai, C. M. *Nano Letters* 2002, 2, 721-724.
- (49) Ye, X. R.; Zhang, H. F.; Lin, Y. H.; Wang, L. S.; Wai, C. M. *Journal of Nanoscience and Nanotechnology* 2004, 4, 82-85.
- (50) Ye, X. R.; Lin, Y. H.; Wang, C. M.; Engelhard, M. H.; Wang, Y.; Wai, C. M. *Journal of Materials Chemistry* 2004, 14, 908-913.
- (51) Lisiecki, I.; Bjorling, M.; Motte, L.; Ninham, B.; Pileni, M. P. *Langmuir* 1995, 11, 2385-2392.
- (52) Hasegawa, M. *Langmuir* 2001, 17, 1426-1431.
- (53) Lisiecki, I.; Pileni, M. P. *Journal of Physical Chemistry* 1995, 99, 5077-5082.
- (54) Fletcher, P. D. I.; Howe, A. M.; Robinson, B. H. *Journal of the Chemical Society-Faraday Transactions I* 1987, 83, 985-1006.
- (55) Bagwe, R. P.; Khilar, K. C. *Langmuir* 1997, 13, 6432-6438.
- (56) Bagwe, R. P.; Khilar, K. C. *Langmuir* 2000, 16, 905-910.
- (57) Towey, T. F.; Khanlodhi, A.; Robinson, B. H. *Journal of the Chemical Society-Faraday Transactions* 1990, 86, 3757-3762.
- (58) Kellay, H.; Meunier, J.; Binks, B. P. *Phys. Rev. Lett.* 1993, 70, 1485-1488.
- (59) Kellay, H.; Meunier, J. *Journal of Physics-Condensed Matter* 1996, 8, A49-A64.
- (60) Binks, B. P.; Kellay, H.; Meunier, J. *Europhys. Lett.* 1991, 16, 53-58.
- (61) Rabie, H. R.; Vera, J. H. *Langmuir* 1995, 11, 1162-1169.
- (62) Rabie, H. R.; Vera, J. H. *Fluid Phase Equilibria* 1996, 122, 169-186.
- (63) Peck, D. G.; Johnston, K. P. *J. Phys. Chem.* 1991, 95, 9549-9556.
- (64) Kunieda, H.; Shinoda, K. *Journal of Colloid and Interface Science* 1979, 70, 577-583.
- (65) Ghosh, O.; Miller, C. A. *Journal of Physical Chemistry* 1987, 91, 4528-4535.
- (66) Lisiecki, I.; Pileni, M. P. *Langmuir* 2003, 19, 9486-9489.
- (67) Legrand, J.; Petit, C.; Pileni, M. P. *Journal of Physical Chemistry B* 2001, 105, 5643-5646.
- (68) Brust M.; Walker M.; Bethell D.; Schiffrin D.J.; R., W. *JOURNAL OF THE CHEMICAL SOCIETY-CHEMICAL COMMUNICATIONS* 1994, 7, 801-802.
- (69) McLeod, M. C.; McHenry, R. S.; Beckman, E. J.; Roberts, C. B. *J. Phys. Chem. B* 2003, 107, 2693-2700.
- (70) Shah, P. S.; Holmes, J. D.; Johnston, K. P.; Korgel, B. A. *J. Phys. Chem. B* 2002, 106, 2545-2551.
- (71) Pileni, M. P. *Langmuir* 1997, 13, 3266-3276.
- (72) Lisiecki, I.; Billoudet, F.; Pileni, M. P. *Journal of Physical Chemistry* 1996, 100, 4160-4166.
- (73) Creighton, J. A.; Eadon, D. G. *Journal of the Chemical Society-Faraday Transactions* 1991, 87, 3881-3891.
- (74) Sigman, M. B.; Saunders, A. E.; Korgel, B. A. *Langmuir* 2004, 20, 978-983.

CHAPTER 7

7. CONCLUSIONS AND RECOMMENDATIONS OF FUTURE WORK

7-1. CONCLUSIONS

This dissertation reflects the work performed on investigating metallic nanoparticle synthesis within microemulsion systems, utilizing both conventional liquid solvents as well as tunable, compressed and supercritical fluid solvents. This research has provided an increased understanding of metallic nanoparticle synthesis within the AOT reverse micelle system. In the initiation of this research, it was perceived that the AOT spherical reverse micelles acted as a somewhat rigid template for the formation of the nanoparticles within the aqueous micelle cores. After extensive investigation of the nanoparticle synthesis process, convincing arguments have been made that the synthesis of copper nanoparticles within the AOT microemulsion is governed by a directed assembly mechanism where the AOT surfactant acts to sterically stabilize the synthesized particles in solution during the growth process until an ultimate particle size is achieved. The role of the AOT surfactant is two-fold. Initially, the surfactant forms a thermodynamically stable, reverse micelle microemulsion with nano-sized water pools dispersed within the bulk organic solvent. These aqueous environments act as nano-reactors for the chemical reduction of the metallic precursors and the metallic nanoparticle synthesis. Secondly, the surfactant acts as a stabilizing agent, effectively

dispersing synthesized particles in solution and preventing agglomeration. The steric stabilization of the copper particles in solution by the AOT surfactant during synthesis is significant in that interactions between the surfactant tails and bulk solvent determine the maximum particle size that can be dispersed in solution, as demonstrated by the total interaction energy modeling results. Based on the “bottom up” type synthesis methods used, the ability to control the maximum particle size dispersible in solution by adjusting the bulk solvent conditions allows for control over the ultimate particle size synthesized. The ability to tailor metallic nanoparticle synthesis using thermodynamics to control the nanoparticle growth rate and more so, the particle size is itself intriguing based on the fact that conventional “top down” methods for particle size control consist of a physical nature, eg. grinding, sonication etc.

The use of compressed and supercritical fluids as the bulk solvent takes full advantage of the adjustable solvent – surfactant tail interactions through changes in temperature and pressure, with applications to particle dispersion and size control. Other advantages of particle synthesis within compressed fluids include the ease of solvent removal by simply depressurizing and novel particle collection techniques. Particle spray coating techniques have been demonstrated as an effective method of particle deposition with the absence of wetting effects observed with deposition involving the drying of conventional liquid solvents. Also, following depressurization and the rapid removal of the bulk solvent, a surfactant – particle matrix is precipitated in the reaction vessel. The formation of this surfactant – particle matrix provides effective means for transport and handling of the stabilized nanoparticles which can later be re-dispersed for application.

The steric stabilization of the copper nanoparticles by the AOT surfactant is believed to also play a role in the particle growth kinetics where interactions between the surfactant head group and particle surface effectively suppress the particle growth rate as compared to the synthesis of silver and gold nanoparticles by the same methods. The slower growth rate of the copper nanoparticles is significant because it affords the ability to easily study the particle growth kinetics by UV-vis absorbance spectroscopy, however it is remarkable that the copper growth rate is much slower than other metals and would provide an interesting future study. Other aspects which contribute to the kinetics of copper nanoparticle synthesis are related to interfacial properties of the micelle surfactant monolayer, specifically the bending elasticity and micelle rigidity. Comparison of the particle growth rates observed in this research with the measurements of the intermicellar exchange rates and other micelle kinetics studies by other researchers have demonstrated remarkably similar trends investigated as a function of the bulk solvent properties, water content, temperature, and the addition of salts and cosolvents. The use of Neutron Spin Echo spectroscopy to measure the properties of the AOT monolayer assembled in reverse micelles demonstrated the same trends observed in the nanoparticle growth kinetics studies as well as those reported in the literature determined by other methods. NSE is a relatively new technique that has found application in the study of micelle dynamics. The work presented in this dissertation is the first high pressure NSE study using compressible near-critical fluids and included the design and construction of a high pressure vessel and temperature control system.

The molecular structure of AOT is an inverted cone shape with a packing parameter greater than 1 and thus AOT self assembles in solution to form a minimum energy geometry of spherical reverse micelles. It is thought that a similar driving force directs the assembly of spherical nanoparticles. In the literature, researchers have used various surfactant / polymer systems as templates in attempt to synthesize nanomaterials with specific geometries. Various anionic species such as Cl^- and Br^- have been demonstrated to promote the synthesis of nanorods and nanocubes by interacting with specific crystalline faces on the nanoparticles, direct growth in specific directions. The results from this study investigated the synthesis of copper nanoparticles in the presence of chloride ions utilizing both liquid isooctane and compressed propane as the bulk solvent. Particle synthesis within the isooctane – AOT reverse micelle system was shown to be influenced by the Cl^- concentration. Specifically, the particle growth rate and the interactions of stabilizing ligands with the particle surface were affected by the presence of Cl^- . At low water contents, $W = 3$, the synthesis of copper nanorods was observed. The addition of chloride ion to particle synthesis in compressed propane has a significant effect on the geometry and structure of the copper nanomaterials produced. As a result of HCl addition to the compressed propane reverse micelle system at 20°C and 310 bar, the consistent formation of diamond-shaped copper nanoparticle assemblies was observed. Synthesis of the diamond-shaped assemblies requires both the use of compressed propane as the bulk solvent and the presence of HCl within the AOT reverse micelles at concentrations low enough to be effectively buffered and high enough to promote interactions with the particle surfaces. The copper nanoparticle assemblies exhibit unique

structure and retain their structure through repeated solvent processing. Future studies will further investigate the physical properties and mechanism of synthesis for the copper nanoparticle assemblies, as well as the ability to selectively separate and assemble the diamond-shaped copper nanoparticle structures for potential applications.

Overall, the goal of this research: to gain an increased understanding of metallic nanoparticle synthesis within microemulsion systems was accomplished and exceeded. This research has demonstrated the effects of various components of the microemulsion system on copper nanoparticle synthesis as well as the advantages of emulsion based nanoparticle synthesis. The advantages of using compressed solvents were also investigated which range from the tunable solvent properties to novel particle collection methods to the synthesis of unique assemblies of particles. This work has encompassed several disciplines of study beyond chemical engineering including: Materials science in the analysis of the nanomaterials by TEM, Mechanical engineering in the design of high pressure vessels and a high pressure fiber optic reflectance probe, Fundamental thermodynamics in the use of compressed and supercritical solvents as well as the application of the interaction energy model, Interfacial science for the work with surfactants and microemulsions, Fundamental science from the neutron scattering studies, and most importantly chemistry / chemical engineering in understanding the synthesis and stabilization of nanoparticles and the production of novel nanomaterials with applications to the advancement of the nanotechnology field.

7-2. FUTURE WORK

The recommended future work for this project includes the continued use of compressed and supercritical fluids for the synthesis and processing of metallic nanomaterials by emulsion based methods as well as other techniques. The use of gas expanded liquids (GXL's) as a new adjustable solvent phase for the synthesis and processing of nanomaterials is also recommended. Continued investigation of the effects of chloride ions and other ionic species on the formation of nanomaterials with unique uniform geometries is also an area of interest. The application of nanomaterials is also a natural progression of this research. To this point, a majority of the research in the field of nanotechnology has concentrated on the synthesis of nanomaterials. The future of nanotechnology lies in the application of these materials and one avenue of research is the functionalization of nanoparticles and the ability to manipulate the assembly of nanoparticles in arrays with specific ordering and functionality. The use of various chelating agents may be an area of interest.

7-2a. Continued Investigation of Synthesis within Tunable Solvents

As discussed previously, the adjustable solvent properties of compressed and supercritical fluids can be utilized to control the particle sizes which can be synthesized or dispersed in solution. The work of Johnston et al. demonstrated the size selective dispersion of dodecanethiol stabilized silver particles using supercritical ethane. Compressed and supercritical fluids have demonstrated attractive solutions for the synthesis of nanomaterials, as presented in this dissertation, as well as solutions for particle processing, including size selective separation and deposition methods. The

compressed solvents are attractive based on the adjustable solvent properties, in addition to the ease of solvent removal, increased transport properties, and decreased surface tensions as compared to conventional liquid solvents. GXL's are also attractive reaction media because of the adjustable solvent conditions but in a manner different from SCF's. GXL's consist of an organic liquid solvent which has a high affinity for the dissolution of a gas, typically carbon dioxide. The addition of carbon dioxide to an organic solvent such as hexane, acts to swell the liquid phase and in doing so, change the properties of the bulk solvent. The amount of CO₂ dissolved in the hexane phase is controlled by the pressure of the system and thus the properties of the gas expanded liquid can be controlled with the CO₂ pressure. Preliminary experiments have shown that the addition of CO₂ to dodecanethiol stabilized metallic nanoparticles dispersed in hexane promotes the size selective precipitation of the particles from solution where the average particle diameter dispersed in solution decreases with increasing pressure as CO₂ is added to the system causing the organic phase to swell. Similarly, the tunable properties of the GXL's may influence the size of metallic nanoparticles synthesized as was observed in the compressed alkane solvents. The advantages of using GXL's includes the adjustable bulk solvent, as with the compressed and SCF's, however the GXL's have solvent properties more closely resembling conventional liquid solvents. This provides the ability to investigate the effects of tunable solvent properties at much lower pressures with values less than the vapor pressure of the expanding gas.

7-2b. Particle Deposition Applications

As discussed previously, compressed and SCF's offer advantages in the methods of particle collection and particle deposition on surfaces. GXL's also have potential of being advantageous in particle processing, post synthesis. The work from this dissertation has convincingly demonstrated a direct relationship between particle dispersibility and the solvent interactions with the particle stabilizing agent tail group. The advantage of using tunable solvents is the ability to adjust this solvent – tail interaction and thus control particle dispersibility. The composition of the dispersed particles also plays a role in the interparticle attractive van der Waals forces and thus affects the particle dispersibility. Using these tools which influence particle dispersion, the deposition of particles from solution in a desired manor can be achieved. The extent of this deposition control can be extended to the use of multiple metallic species, particles of varying sizes and alteration of the stabilizing ligand. The application of using multiple metallic species (eg. a mixture of monodispersed copper and silver particles of the same size) is based on the differences in van der Waals attractive forces for different materials resulting in particle precipitation of the two materials at different solvent conditions. For the case of 8 nm diameter copper and silver particle dispersed in compressed propane, as the pressure is slowly decreased a point would be reached when the silver particles precipitate out of solution. The copper particles should precipitate at a lower pressure as a result of a decreased interparticle attractive force between copper particles as opposed to silver due to the lower Hamaker constant of copper. This method of particle deposition would theoretically result in the formation of a bimetallic double layer of

particles with each layer 8 nm thick. Similar methods of particle deposition can be achieved using particles of differing sizes where the larger particles would precipitate first due to the increased interparticle van der Waals attraction. Another method would involve the use of particles with different stabilizing agents having varying strengths of interaction with the bulk fluid and thus as the bulk fluid solvent strength is decreased, the particles with the less favorable solvent interaction would precipitate first. Manipulation of these components of the particle dispersions in conjunction with the thermophysical properties of the bulk fluid may enable the directed assembly of multi layered nanoparticle arrays with specific 3 dimensional structures.

7-2c. Anion Effects on Nanomaterial Synthesis within Compressible Fluids

The synthesis of the diamond shaped copper nanoparticle assemblies is interesting on many levels. First of all, the geometry of the structures is very defined and reproducible. The exterior parallelogram structure is very ordered while the arrangement of nanoparticles on the interior is disordered with the exception of the large agglomeration of particles at the center which only occurs reproducibly with higher Cl⁻ concentrations. The formation of the diamond shaped assemblies is exclusive to synthesis with compressed propane as the bulk solvent and the presence of HCl within the AOT reverse micelles at concentrations low enough to be effectively buffered and high enough to promote interactions with the particle surfaces. The structure was also found to be dependant on the concentration of chloride ion and robust enough to withstand rapid solvent removal, multiple redispersions, and liquid – liquid extraction of the excess surfactant. Further investigation on the formation of these novel structures is

required to determine the influence of ionic species on the formation of nanomaterials with unique structures and geometries. High Resolution TEM analysis is required to further determine the structure, crystallinity, and physical properties of these assemblies in attempt to determine the mechanism of formation as well as any potential for application. Additional experimental studies should examine the effects of temperature and pressure as well as application to SCF ethane and other compressed solvents. The use of ionic species other than HCl should be investigated, including HBr, NaCl, NaBr, and the chloride and bromide salts of cationic co-surfactants such as CTAC and CTAB. The synthesis reproducibility and ability to withstand repeated solvent processing enables these structures to undergo deposition investigations in order to form ordered arrays of these structures aligned either axially or closely packed for potential application.

7-2d. Nanoparticle Functionalization

The ability of AOT to act as an effective stabilizing agent during particle synthesis is also significant in that the surfactant can be easily replaced by more conventional capping ligands and stabilizing agents with a desired chemical functionality in the tail region. The functionality of the capping ligand can be specifically designed for a desired application ranging from dispersion in aqueous versus organic phases, adhesion to a particular surface, or assembly and the formation of particle arrays. The mechanism of particle synthesis via AOT steric stabilization has similarities to the recently developed and much popularized method of silver and gold nanoparticle synthesis using a two phase method with a phase transfer catalyst and thiol capping ligands. This method, developed by Brust and co-workers is a simple solution based synthesis that effectively produces

large quantities of relatively monodispersed particles and has been used quite extensively in recent investigations of particle deposition techniques and the formation of highly ordered, uniform particle arrays. In order to obtain the uniform particle arrays, a thorough size selective precipitation process is necessary to obtain a very narrow size distribution of particles. Also the process is limited to the functionality associated with the thiol capping agent present during synthesis. The reverse micelle method of particle synthesis has the advantage of affording the ability to use capping agents with varying functionality. The post synthesis size selective precipitation process to obtain highly monodispersed particles is also applicable to the microemulsion process.

Proposed future work involves the use of the microemulsion technique for nanoparticle synthesis followed by the selective functionalization of the particle surface. Suggested functional groups include azobenzene compounds, hydrophilic species, ligands with specific terminating functional groups, and ligands with dual functionality with hydrophobic and hydrophilic components. Ligands of varying lengths may be used to adjust the interparticle spacing of the deposited particle. The azobenzene compounds have the unique ability to go through a photo induced cis-trans rearrangement transition. It is believed that this rearrangement would enable the extension and collapse of the ligand tail groups providing for switchable particle dispersion with the application of UV illumination. The use stabilizing ligands with hydrophilic functionality may enable the formation of an aqueous dispersion of nanoparticles, as well as the arrangement of particles at an oil interface with a high degree of order. The ability to direct the assembly of particle arrays may be achieved through specific functionalization of the terminating

groups. Ligands with terminating benzene groups could take advantage of the planar structure and preferential stacking of the ring structures with respect to each other. Ligands terminating with siloxane groups may find applications in attaching to silicate substrates in ordered arrays for electronics applications. Ligands terminating with functionalities capable of hydrogen bonding are also of interest for the formation of interconnected arrays of particles. This may be achieved with the use of carboxylic acid terminated ligands or by the mixing of a particle solution with alcohol terminated ligands and a particle solution with an ether dithiol ligand. Preliminary investigation of this type of mixture resulted in instantaneous particle precipitation, potentially due to the formation of a hydrogen bonded network of particles. Further analysis may lead to reversible interconnected networks which are responsive to temperature or the addition of CO₂ to disrupt the hydrogen bonding. Copper nanoparticles dispersed in solution are notoriously susceptible to oxidation and it has been suggested that the use xanthalate ligands, with two adjacent thiol groups, will inhibit particle oxidation and actually enables aqueous phase synthesis of copper nanoparticles at ambient conditions. This method of particle synthesis has also been examined and requires further investigation.

7-2e. Initial Stages of Copper Nanoparticle Synthesis

Finally, it has been observed that for particle synthesis within the compressed solvents, the initial solution color change from light blue to deep blue to light brown is extended and the deep blue color can persist on the order an hour. This deep blue solution exhibits an intense, broad UV-vis absorbance peak centered at 630 nm. It has been suggested that this solution color and UV-vis absorbance peak is possibly indicative

of copper nanoparticles in the 1 to 2 nm diameter range which exhibit quantum confinement properties similar to the CdS and CdSe nanoparticles which fluoresce different colors depending on the particle size. Another possibility is the formation of 1 to 2 nm CuO semiconductor nanoparticles which were previously thought to be unstable and nonexistent with length scales below ~20 nm. Further investigation of the initial stages of copper nanoparticle synthesis within the compressible solvents may result in the formation of another novel nanomaterial unattainable by alternate methods of synthesis.

APPENDIX A

A. RESEARCH METHODS

A-1. SYNTHESIS OF $\text{Cu}(\text{AOT})_2$ AND AgAOT

A-1a. Synthesis of $\text{Cu}(\text{AOT})_2$ Batch Method

This method is very similar to the method used by Cason previously¹. The method by Cason was adapted from the method introduced by Pileni².

- Get 2 500 ml Flasks.
- CuII SO_4 , AOT, Na Resin, H^+ Resin, HPLC Water, Ethanol.
- Make 1 L of 50/50 ethanol / water solution (may use 20% ethanol solution).
- CuSO_4 solution 1 M solution 50 g CuSO_4 in 200 ml of Water in flask 1.
- Mix 20g AOT in 300 ml of ethanol / water solution.
- Add 20g of Na Resin to Cu solution in flask 1. Cover and stir for 40 minutes.
- Remove from stir and let settle, pour off liquid. Add 200 ml of ethanol / water solution to blue resin and stir for 1 to 1.5 hours.
- After stirring, check PH and adjust to 7 by adding a few drops of 10N NaOH, stir for 30 minutes. Recheck pH and repeat as needed. Do not add NaOH too quickly.

If solution is too basic → add HCl

If solution is too acidic → add 10N NaOH

- Once AOT solution (flask 2) is dissolved add 14 to 15 g H^+ resin. Cover and stir for 1 hour.
- Once Cu solution (flask 1) is at pH 7 pour off only liquid down sink with lots of water.
- Add 200 ml of ethanol / water solution and stir for 20 minutes. Check pH between 6 – 7 and pour off liquid (or vacuum filter with filter flask).
- Take AOT solution (flask 2) and let settle. Pour off only the liquid onto blue resin to perform exchange $\text{H}^+ \text{AOT} \rightarrow \text{Cu}(\text{AOT})_2$ (do not let H^+ resin go into blue resin, may want to vacuum filter).
- Cover and stir for 1 hour.
- After conversion pour off liquid and dry
- Use a RotoVap if available. If not then use vacuum oven.
- Once dry in round bottom flask from Rotovap.
 - Be sure it is completely dry.
 - Dissolve $\text{Cu}(\text{AOT})_2$ in Isooctane and let settle or filter to remove any insoluble particulates.

- Continue to dry and when solution becomes very viscous, pour into flask and continue to dry in vacuum oven. Do not over heat to help avoid burning.
- This method works well but can only achieve ~75% conversion.
- Conversion is measured by creating aqueous solution and analyzing at soils lab by doing a trace analysis and find the ratio of Cu to Na.

A-1b. Synthesis of $\text{Cu}(\text{AOT})_2$ Using Columns

This method was adjusted from the batch method mentioned previously in attempt to obtain a better conversion of NaAOT to $\text{Cu}(\text{AOT})_2$. The solution analysis report demonstrates that this method is much more efficient with increased conversion.

- Dissolve 20g AOT in 300 ml of 25% ethanol/water solution (0.15M solution).
- Dissolve 50g CuSO_4 in 200 ml water \rightarrow 1.0 m solution
- H^+ resin \rightarrow 1.7 mmol H^+ /ml resin, 0.7g/ml resin.
- Use 50% excess of H^+ resin
20g AOT \rightarrow 27.8g H^+ resin.
- Na resin \rightarrow 2.4 mmol/ml resin, 0.7g/ml
- Use 300% excess Na resin.
20g AOT \rightarrow 26.28g Na resin.
- Get two 50 ml graduated burrets to use as columns and pack the bottom with a little bit of glass wool. (a double A battery works nicely to pack down the glass wool).
- Take each of the resins in a beaker already massed out and add one volume equivalent of water.
- Mix the resin and water to make a slurry and pour into the columns and let them drain.
- Add a little glass wool to the top to keep resin in place.
- Equilibrate the H^+ resin column with three bed volume equivalents of 25% ethanol / water solution.
- Then pass the AOT solution over the H^+ resin at a slow drip rate and collect the H^+ AOT.
- Check the pH of the H^+ AOT effluent and should be between 0 and 1.
- Wash the column with 25% Ethanol solution until pH is between 4 and 5.
- Equilibrate the Na resin column with three bed volumes of water.
- Pour the CuSO_4 solution over the Na resin at a slow drip rate and then wash the column with water until the effluent is clear (~250ml).
- Save the CuSO_4 solution collected.

- Pass the H^+ AOT solution over column 2 (Cu resin) at a slow drip rate (pH ~4 to 5).
- Pass the $CuSO_4$ solution from before over the bed again.
- Pass the AOT solution over the column again to make sure the exchange is complete.
- Wash the column with three bed volumes of 25% ethanol solution.
- Collect the $Cu(AOT)_2$ and wash and Rotovap to dry.
- Dissolve the dry $Cu(AOT)_2$ in Isooctane and filter out particulates (just let settle and separate).
- Continue drying in Rotovap or vacuum oven.

A-1c. Column Regeneration

- H^+ Resin: Wash column with two bed volumes of 1N HCl or nitric acid (when using Ag), then wash with DI water until pH ~5.
- Na Resin: Wash column with three bed volumes of 0.5 N NaOH at a flow rate of 1 ml/min per cm^2 cross second area. Conversion is complete when pH is greater than 9. Rinse with four bed volumes of DI water.

Specifications on Various Resins Used

H^+ Resin	Na Resin	Anionic Resin
AG 50W-X8	Bio-Rex 70	AG 4x4
Cat # 143-5441	Cat # 142-5822	Cat # 143-3341
Capacity 1.7 meq/ml resin	2.4 meq/ml resin	0.8 meq/ml
Density 0.8g/ml	0.7g/ml	0.7g/ml

Selectivities

$H^+ = 1.0$	$Na^+ = 1.5$	$Cu^{2+} = 2.9$
$Cu^+ = 5.3$	$Ag^+ = 7.6$	

- Can use selectivities to determine % excess needed or also the # of bed volumes for regeneration. (See biorad booklet.)

Things to keep in mind when working with Ion Exchange

- Keep in mind the selectivity of different Ions.
Eg. When have Cu ions on resin and pass through H^+ AOT and resin have a strong affinity for the Cu ion and will compete.
- General Rule use 30% excess capacity.
- Pay attention to pH.
- Try not the use more than 25% ethanol because it may degrade resin.
- For equilibration use three to four bed volumes for bulk solvent to be used.
- Try not to let the bed go dry. Keep wet.
- Use as little glass wool as possible.

A-1d. Synthesis using an Anion Exchange Resin

This alternate method was attempted to remove the SO_4^{2-} anion from the product. This method was unsuccessful due to a higher selectivity for the surfactant than the SO_4^{2-} anion on the resin.

A-1e. Synthesis of Silver AOT using Columns

This method is similar to the copper column method with the substitution of Ag^+ for Cu^{2+} .

- Using AgNO_3 with a 2:1 ratio of Ag to AOT.
- Create 1M AgNO_3 solution with water.
0.15 M AOT solution with 25% ethanol / water solution.
For this run use 5.67g AgNO_3
- $5.67\text{g AgNO}_3 = 0.0334 \text{ mol Ag NO}_3$
- $0.0334 \text{ mol AgNO}_3 = 7.41\text{g AOT}$
- $7.41\text{g AOT mol AOT} = 0.1113 \text{ L } 25\% \text{ ethanol solution}$
- $0.0334 \text{ mol Ag NO}_3 = 33.4 \text{ ml water}$
Na Resin: $33.4 \text{ mmol AgNO}_3 \rightarrow 9.74\text{g Na resin}$
 H^+ Resin: $0.0167 \text{ mol AOT} \rightarrow 15.7\text{g H}^+ \text{ Resin at } 100\% \text{ excess}$
- Dissolve 5.67g AgNO_3 in 33.4ml water
- Dissolve 7.41g AOT in 111.3mL 25% ethanol solution
- Set up column 1 with 9.74g Na resin
- Set up column 2 with 15.7g H^+ resin.
- Equilibrate columns and then.....
- Pass AgNO_3 solution through column 1 (Na resin). Repeat two more times passing AgNO_3 solution over Na resin three times.
- Wash column 1 with two bed volume equivalents of 25% ethanol solution.
- Pass AOT solution over column 2 (H^+ resin) to obtain H^+AOT solution.
- Wash with two bed volume equivalents of 25% ethanol solution and collect.
- Pass H^+AOT solution over column 1 (Ag resin) to obtain AgAOT . Wash with two bed volume equivalents of 25% ethanol solution.
- Collect solution and dry by Rotovap as before.

Column Regeneration

- H^+ Resin: same as before
- Na Resin: same as before only use more volume of NaOH because there is a higher selectivity for Ag.

A-1f. Synthesis of Cu(AOT)₂ by the Eastoe Method

This synthesis method was later obtained from the work by Eastoe et al.³ where the synthesis of Cu(AOT)₂ was performed without the use of ion exchange resins and rather simply used the natural preferential selectivity of copper over sodium on the AOT head group. The synthesis is as follows.

- Create 250 ml saturated aqueous solution of Cu(NO₃)₂.
- Create 125 ml of 1M AOT solution in ethanol and mix the two solutions. Mixing is best done in a 500ml separation funnel, venting frequently.
- Add 50 ml of diethyl ether to the solution to extract the Cu(AOT)₂ from the ethanol / water solution containing excess Cu(NO₃)₂ and NaNO₃.
- Mix vigorously for several minutes, venting frequently and allow to settle and separate into two phases. The upper phase will contain the diethyl ether and Cu(AOT)₂
- Collect the upper phase and wash twice with one volume equivalent of water to remove any residual NO₃⁻ anion.
- Dry the Cu(AOT)₂ solution in a vacuum oven. Purification by dissolving in isooctane, filtering and re-drying was not found to be necessary.
- This method is by far much simpler and requires less time and resources than the ion exchange resin methods.
- A similar method was also performed to synthesize AgAOT, successfully.

A-1g. Method for Determining Conversion

The conversion of AOT surfactant to Cu(AOT)₂ and AgAOT by the methods mentioned previously was determined by sending surfactant solutions to the Auburn University Soils Testing Laboratory where a trace solution analysis was performed.

- Make solutions ~100 ppm Cu. Addition of small amount of ethanol may be necessary to dissolve surfactant.
- May also add standards of CaCl or KCl salts at known amounts to back out true concentrations. Salt Concentration ~ 1x10⁻³ m
- Elements detected by soils test. Ca, K, Mg, P, Cu, Fe, Mn, Zn, B, Al, Ba, Co, Pb, Na.

A-2. RESULTS

The results dated March 18, 2002 are for three different batches of Cu(AOT)₂ synthesized by the Batch method discussed previously. The Copper to Sodium ratio ranges from 3.4 to 2.3 and given that two AOT molecules are required to form one Cu(AOT)₂ molecule, the AOT conversion is ~ 85% and the percent of Cu(AOT)₂ in the product is ~75 mol percent.

For the results dated August 29, 2002, samples A and B were synthesized by the batch method with results similar to the previous test. Sample C was synthesized by the column method discussed previously. As can be seen by the increase in Cu concentration and the decrease in Na concentration, the column method is much improved with an AOT conversion of 94% and the product having 88 mol percent $\text{Cu}(\text{AOT})_2$. Sample D was AgAOT synthesized by the column method. The solution analysis was unable to test for silver however the limited amount of Na present would prove that the conversion was successful. Sample E was simply a standard solution that contained the original AOT in solution.

The results dated March 13, 2003 correspond to $\text{Cu}(\text{AOT})_2$ synthesized by the Eastoe method. Samples #1 and #2 demonstrate an improved Cu to Na ratio over the methods using exchange resins with a AOT conversion of 98.7% and 97.3 mol percent $\text{Cu}(\text{AOT})_2$ in the final product. This analysis also includes a nitrate test to determine the presence of the salt anion, showing the low anion concentration in the product. Sample #3 was again an AOT standard.

From these results it is apparent that the Eastoe method is by far the superior method, not only by the results but also by the ease of the synthesis.

Auburn University

Auburn University, Alabama 36849-5411

College of Agriculture and
Agricultural Experiment Station System

Department of Agronomy and Soils
Telephone: 844-3958
Area Code: 334

Reply: Soil Testing Laboratory
Auburn University
Auburn University, AL 36849-5411

SOLUTION ANALYSIS REPORT

March 18, 2002

NAME : Christopher Roberts/Chris Kitchens
SAMPLE I.D. : Surfactant
LAB I.D. : F32-02
ANALYSIS : Solution
INCLUDES : Minerals/Nitrate-Nitrogen

ppm in solution

	Ca	K	Mg	P	Cu	Fe	Mn
I	32.7	45.4	0.0	1.8	53.8	0.0	0.0
II	31.6	44.9	0.0	1.8	47.8	0.0	0.0
III	31.4	47.4	0.0	1.6	45.9	0.0	0.0

ppm in solution

	Zn	B	Al	Ba	Co	Cr	Pb
I	0.3	0.0	0.1	0.0	0.0	0.0	0.0
II	0.4	0.0	0.0	0.0	0.0	0.0	0.0
III	0.3	0.0	0.1	0.0	0.0	0.0	0.0

ppm in solution

	Na
I	15.8
II	18.2
III	19.7

A LAND-GRANT UNIVERSITY

Auburn University

Auburn University, Alabama 36849-5411

College of Agriculture and
Agricultural Experiment Station System

Department of Agronomy and Soils
Telephone: 844-3958
Area Code: 334

Reply: Soil Testing Laboratory
Auburn University
Auburn University, AL 36849-5411

SOLUTION ANALYSIS REPORT

August 29, 2002

NAME : Christopher Roberts/Chris Kitchens
SAMPLE I.D. : Surfactant
LAB I.D. : 07-02
ANALYSIS : Solution
INCLUDES : Minerals

--- ppm in solution ---

	Ca	K	Mg	P	Cu	Fe	Mn
A	27.5	34.2	0.0	1.9	45.3	0.0	0.0
B	32.4	38.2	0.0	1.8	39.2	0.0	0.0
C	33.3	37.9	0.0	2.8	67.0	0.0	0.0
D	32.9	38.0	0.0	0.3	3.0	0.0	0.0
E	0.0	0.0	0.0	0.0	0.0	0.0	0.0

--- ppm in solution ---

	Zn	B	Al	Ba	Co	Cr	Pb
A	0.4	0.0	0.0	0.1	0.0	0.0	0.1
B	0.4	0.0	0.0	0.0	0.0	0.0	0.2
C	0.6	0.0	0.0	0.1	0.0	0.0	0.2
D	0.4	0.0	0.0	0.1	0.0	0.0	0.0
E	0.2	0.3	0.0	0.1	0.0	0.0	0.0

ppm in solution

	Na
A	20.7
B	24.5
C	9.0
D	5.2
E	54.5

A LAND-GRANT UNIVERSITY

Auburn University

Auburn University, Alabama 36849-5411

College of Agriculture and
Agricultural Experiment Station System

Department of Agronomy and Soils
Telephone: 844-3958
Area Code: 334

Reply: Soil Testing Laboratory
Auburn University
Auburn University, AL 36849-5411

SOLUTION ANALYSIS REPORT

March 13, 2003

NAME : Christopher Roberts/Chris Kitchens
SAMPLE I.D. : Surfactant, 3-4-03
LAB I.D. : F16-03
ANALYSIS : Solution
INCLUDES : Minerals/Nitrate-Nitrogen

--- ppm in solution ---

	Ca	K	Mg	P	Cu	Fe	Mn
#1	28.6	30.1	0.0	1.6	57.0	0.0	0.0
#2	26.9	27.9	0.0	1.1	49.7	0.0	0.0
#3	27.4	27.0	0.0	0.0	0.0	0.0	0.0

--- ppm in solution ---

	Zn	B	Al	Ba	Co	Cr	Pb
#1	0.6	0.0	0.0	0.0	0.0	0.0	0.0
#2	0.5	0.0	0.0	0.0	0.0	0.0	0.0
#3	0.1	0.0	0.0	0.0	0.0	0.0	0.0

--- ppm in solution ---

	Na	NO3-N
#1	1.6	4.7
#2	1.3	3.2
#3	19.2	0.1

A LAND-GRANT UNIVERSITY

A-3. RESEARCH METHODS FOR COPPER NANOPARTICLE SYNTHESIS

A-3a. Copper Nanoparticle Synthesis in Liquids

- Calculate and mass out the desired amount of Cu as copper salt or $\text{Cu}(\text{AOT})_2$ and AOT.

Eg. Bulk solvent = hexane – 50mL

$[\text{AOT}] = 0.1106\text{M} \rightarrow 2.3862\text{g}$

$[\text{Cu}(\text{AOT})_2] = 0.01106\text{M} \rightarrow 0.5825\text{g}$ (assume 75% conv. of $\text{Cu}(\text{AOT})_2$)
for copper salts, the salt should be dissolved in the water before addition to the solution

- Dissolve $\text{Cu}(\text{AOT})_2 + \text{AOT}$ in solvent but use less than final volume.
- Once dissolved then you may want to add some mol sieves to dry out the system to get a more accurate determination of the amount of water in the microemulsion. If mol sieves are added then do not stir the solution much because it will become cloudy from small pieces of the mol sieves breaking off. Let stand for awhile with the sieves.
- Pour solution into a 50mL volumetric flask, careful not to get any mol sieves into the flask.
- Add the desired amount of water for the right W value.
- Add some solvent to the beaker that the surfactants were dissolved in and rinse then add to the volumetric flask to bring the volume. If solvent is very flammable then may want to over shoot mark to account for evaporation during deoxygenating.
- Use red/orange rubber septum to seal the flask and evacuate oxygen from system.
- It is very important to get all the oxygen out of the system to avoid the oxide formation. This is best done by purging the solution with pure Nitrogen gas, bubbling it through the solution using a long needle and a short vent needle.
- The best method used is to begin purging the solution and immerse in a sonication bath for about one to two minutes to de-air the solution and then continue to purge the system with N_2 for another one to two minutes in order to replenish the dissolved air in solution and bring to equilibrium. (Weaker microemulsions with Decane or Dodecane as the bulk solvent are not susceptible to sonicating but can be purged for longer because it is not as volatile.
- The cuvette to be analyzed in the UV must also be purged for ~10 minutes and should be sealed with one of the red/orange rubber septums as well. The septum caps that come with the cuvettes are not gas tight and allow oxygen into the system forming oxides. The long stem cuvettes are best for the reaction.
- Once the cuvette and solution are purged, the reducing agent should be introduced to the 50mL bulk solution and stirred by swirling or spinning. Try to avoid shaking. If reducing agent does not want to go into solution then try sonicating to get good mixing.

- Using a gas tight syringe, pull three ml of solution out of the flask while replacing with N₂ and inject into the cuvette through the septum.
- Wipe the cuvette with a Chem wipe and begin the UV time acquisition.

Reduction Reaction

- As the reaction proceeds, if oxide forms then the absorbance around the 800 nm and will increase dramatically, but regardless as particles form the overall absorbance will grow and eventually some particles will fall out of solution and the overall absorption will fall but the absorbance ratio 566/500 will stay the same.

A-3b. Copper Nanoparticle Production in Compressible Solvents

- The high pressure reactor is equipped with an RTD temperature control device, a pressure transducer, inlet and outlet ports with HiP valves and opposing quartz windows for UV-Vis absorbance measurements. The quartz windows are sealed with nitrile-butyl rubber o-rings on each side and secured with side plate bolted to the reactor. For experiments at elevated temperatures viton o-rings must be used.
- The desired amount of surfactant and a stir bar are added to the reactor and the final reactor plate is sealed with an o-ring and bolted to the reactor. For experiments with high absorbance that require a shorter path length, a quartz window spacer supported by a Teflon insert may be placed between the opposing exterior windows.
- Once the reactor is sealed, evacuate the cell with a vacuum pump and then purge with N₂ and repeat one or two times as desired, making sure to purge completely and remove all oxygen to prevent copper oxidation.
- Before this is done the syringe pump should be filled with the desired solvent and pressurized. Alltech Gas Dryer trap and Oxy-trap may be used to remove the oxygen and water from the solvent.
- For experiments that require the use of a liquid cosolvent, a gas tight syringe with a luer lock 16 gauge needle fitted with a HiP fitting and valve can be used to introduce the desired amount of cosolvent into the evacuated vessel.
- A high pressure Valco six port injection loop should be used to introduce the desired amount of water into the system on filling the vessel with solvent. Nitrogen should be purged through the injection loop prior to use to prevent oxygen from entering the system.
- The cell should then be filled with the solvent from the syringe pump above the de-mixing pressure and allowed to equilibrate to the desired temperature and become one phase.
- Excess reducing agent should be used with the injection loop where excess passes through the loop cleaning it out then while still flowing, turn the loop to trap the desired amount of reducing agent.
- Fill with additional solvent through the injection loop to introduce the reducing agent into the system and bring the vessel to the desired pressure.

- Stir the contents for a few seconds to get it well mixed and a full color change from light blue to dark blue and finally a light brown color indicating a complete reduction of Cu^{2+} to Cu^0 . Remove the vessel from the stir plate and begin the in-situ time resolved UV-Vis measurements.

A-4. PARTICLE COLLECTION METHODS

Deposit on carbon coated grids for TEM Analysis.

Liquids

- Put small drop on grid using a microliter syringe. Surfactant is some times too thick to see particles.
- Use nebulizer to spray fine mist of particles on grids (this process emulates the spray coating process).
- Mix particle solution with an equal volume 20/50 or 50/50 ethanol/water solution to remove excess surfactant. Remove the aqueous phase and deposite particle solution on the TEM grids.
- The above liquid – liquid extraction of the excess surfactant is more effective with the introduction of a particle stabilizing agent such as dodecylamine, undecanoic acid or dodecanethiol.

SCF (under pressure)

- Spray particles onto grids through capillary tubing nozzle when depressurizing.
- After depressurization, then take surfactant and particles that fell out of solution and re-dissolve in another solvent and collect by the liquid methods.
- Selective functionalization can be achieved by redispersing the particle surfactant matrix in a 0.01 M alkane solution with a desired stabilizing agent.

These methods can also be applied to silicon wafers or carbon block for analysis on the AFM.

(1) Cason, J. P.; Miller, M. E.; Thompson, J. B.; Roberts, C. B. *Journal of Physical Chemistry B* **2001**, *105*, 2297.

(2) Lisiecki, I.; Lixon, P.; Pileni, M. P. *Progress in Colloid & Polymer Science* **1991**, *84*, 342.

(3) Eastoe, J.; Fragneto, G.; Robinson, B. H.; Towey, T. F.; Heenan, R. K.; Leng, F. J. *Journal of the Chemical Society-Faraday Transactions* **1992**, *88*, 461.

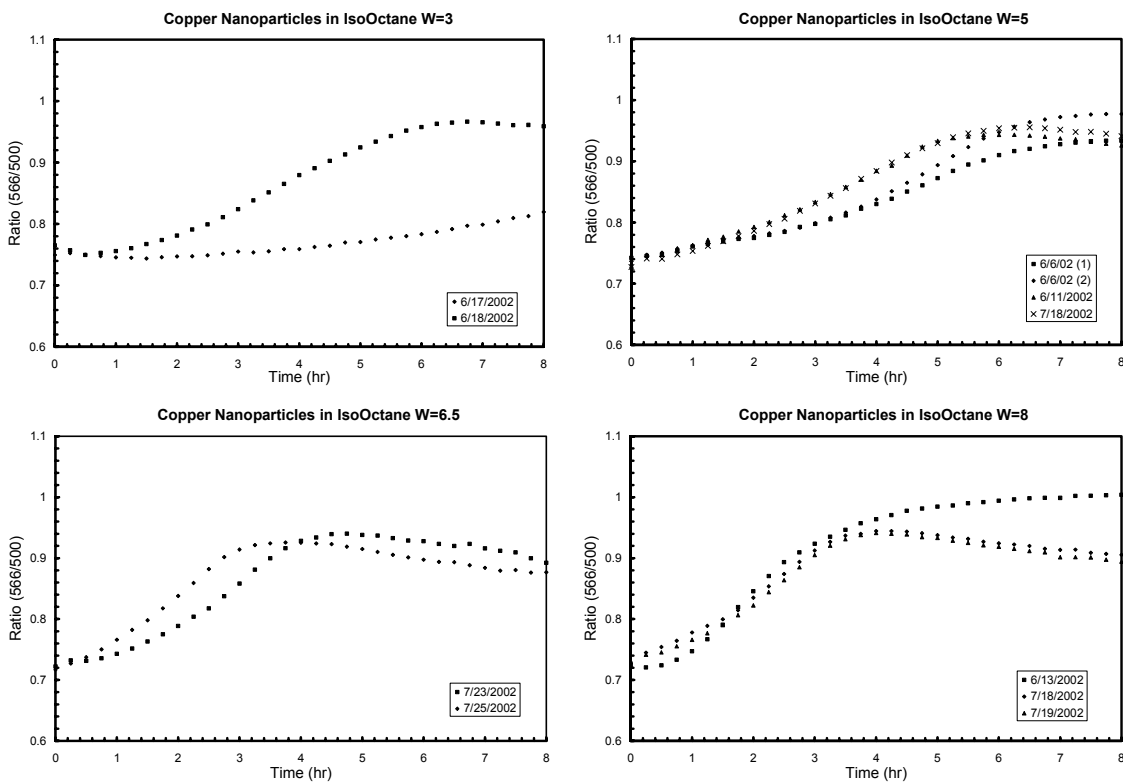
APPENDIX B

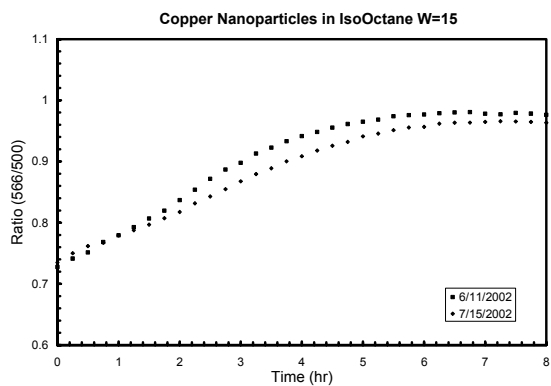
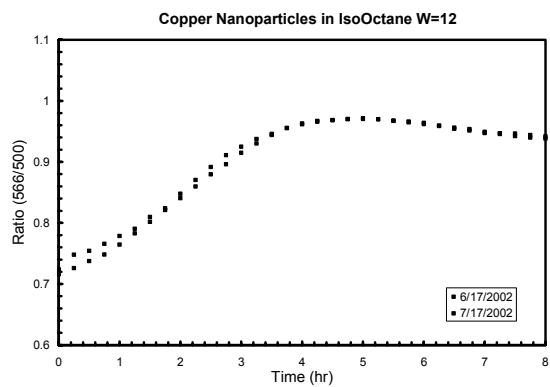
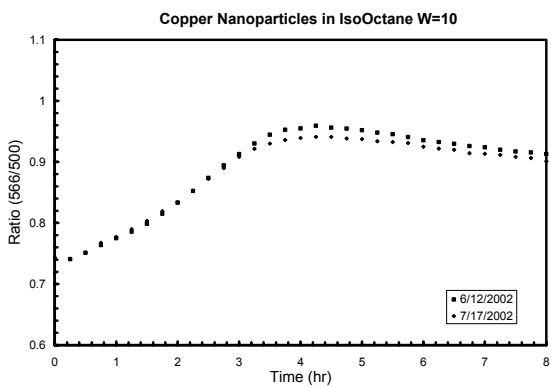
B. SYNTHESIS OF COPPER METALLIC NANOPARTICLES IN AOT REVERSE MICELLE SYSTEMS

B-1. EXPERIMENTAL GROWTH CURVES

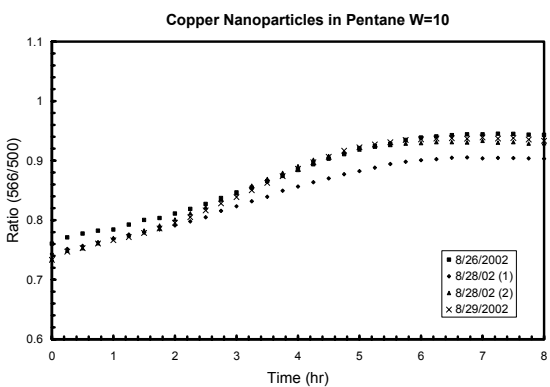
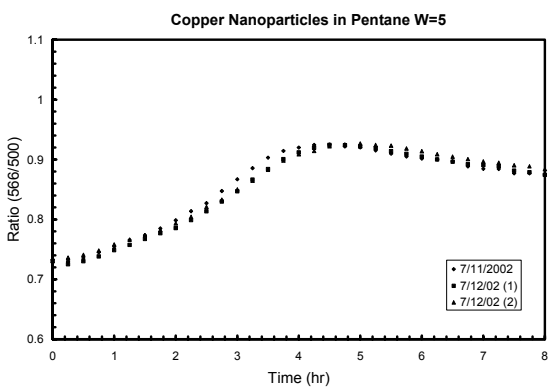
In order to determine the effects of water content, bulk solvent, and the method of introducing the copper ion; the particle growth curves were measured in-situ by UV-Vis absorbance measurements where the ratio of the absorbance at 566 nm and 500 nm can be related directly to the average particle size dispersed in solution. The following plots display the measured absorbance ratio as a function of time. Multiple experiments were performed for each of the experimental conditions and compositions and a regression analysis was performed to obtain the particle growth rate and the ultimate particle size.

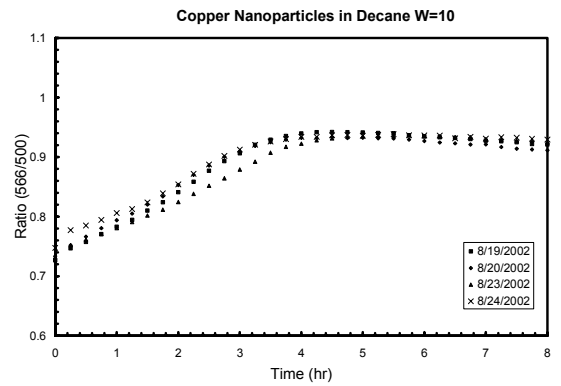
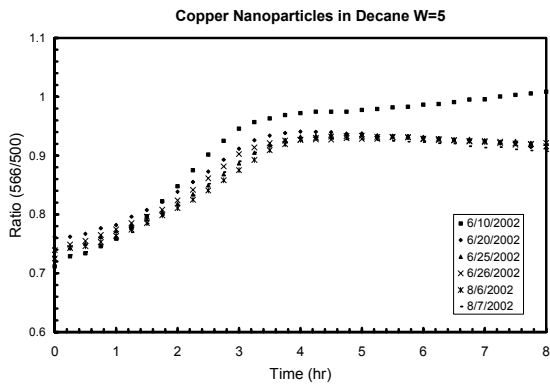
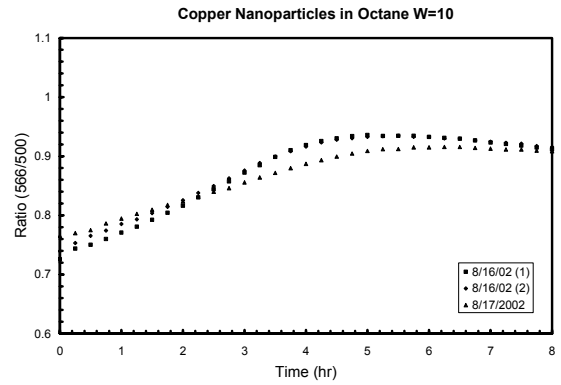
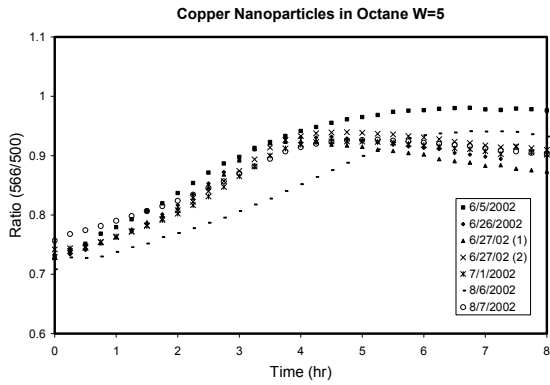
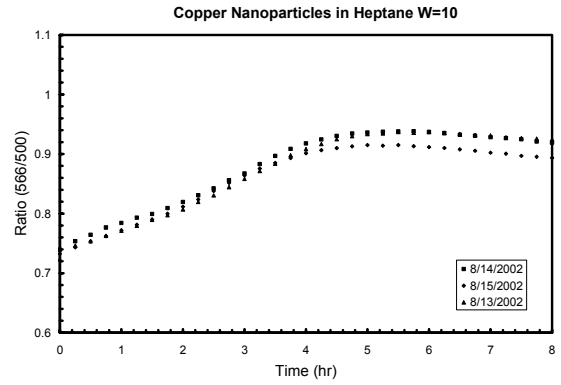
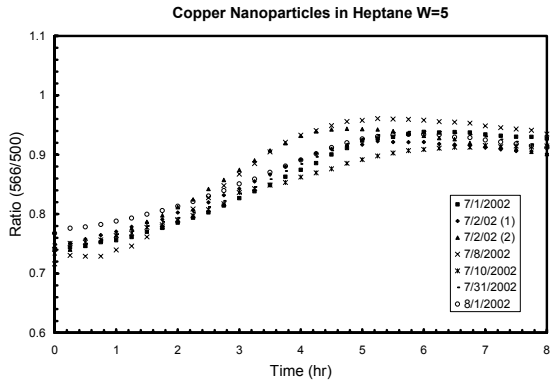
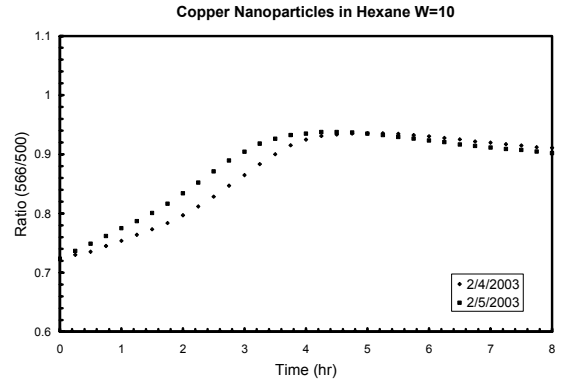
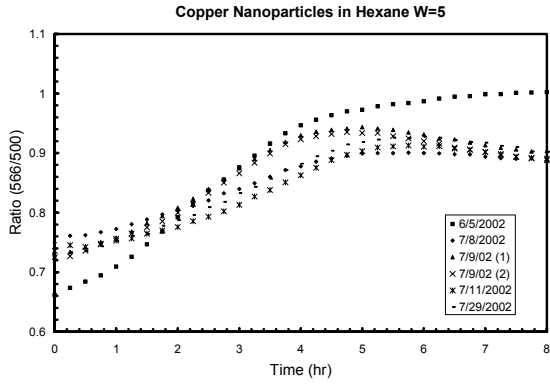
B-1a. Effects of W Value on Particle Growth

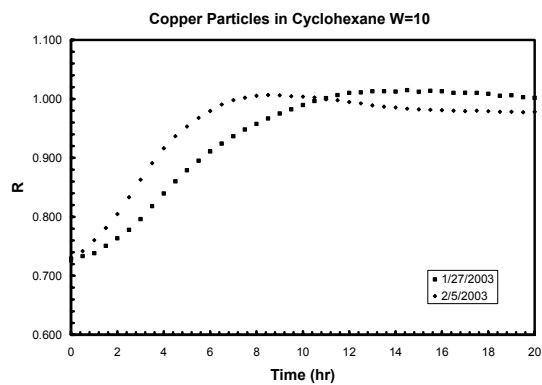
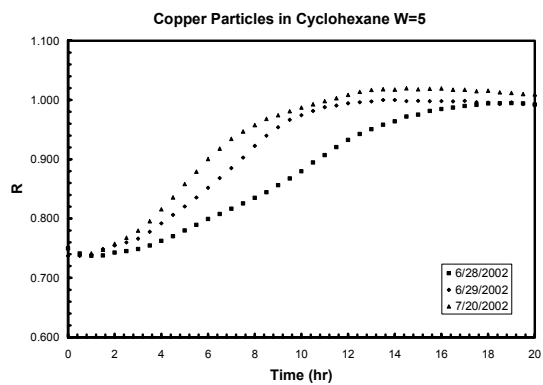
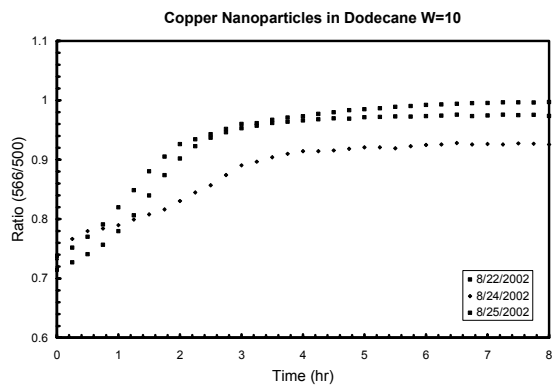
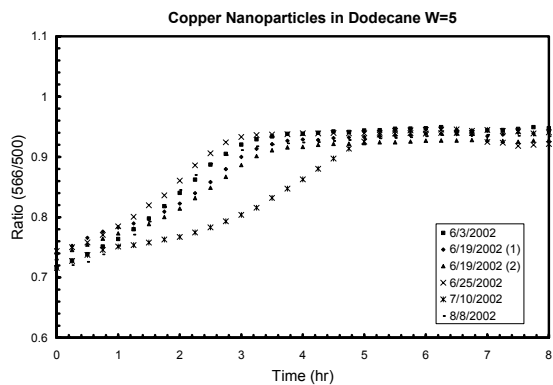




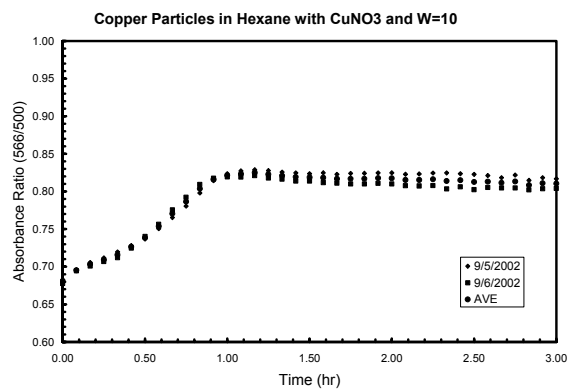
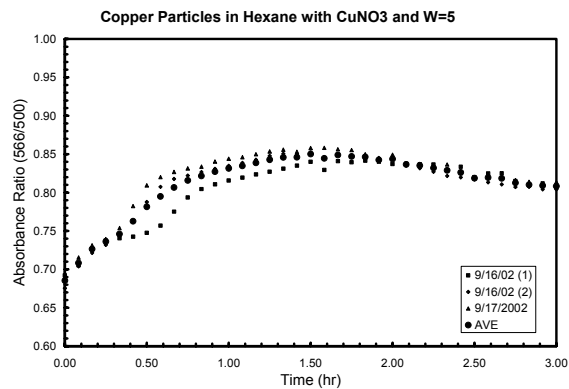
B-1b. Effects of Various Bulk Solvent Types on Particle Synthesis

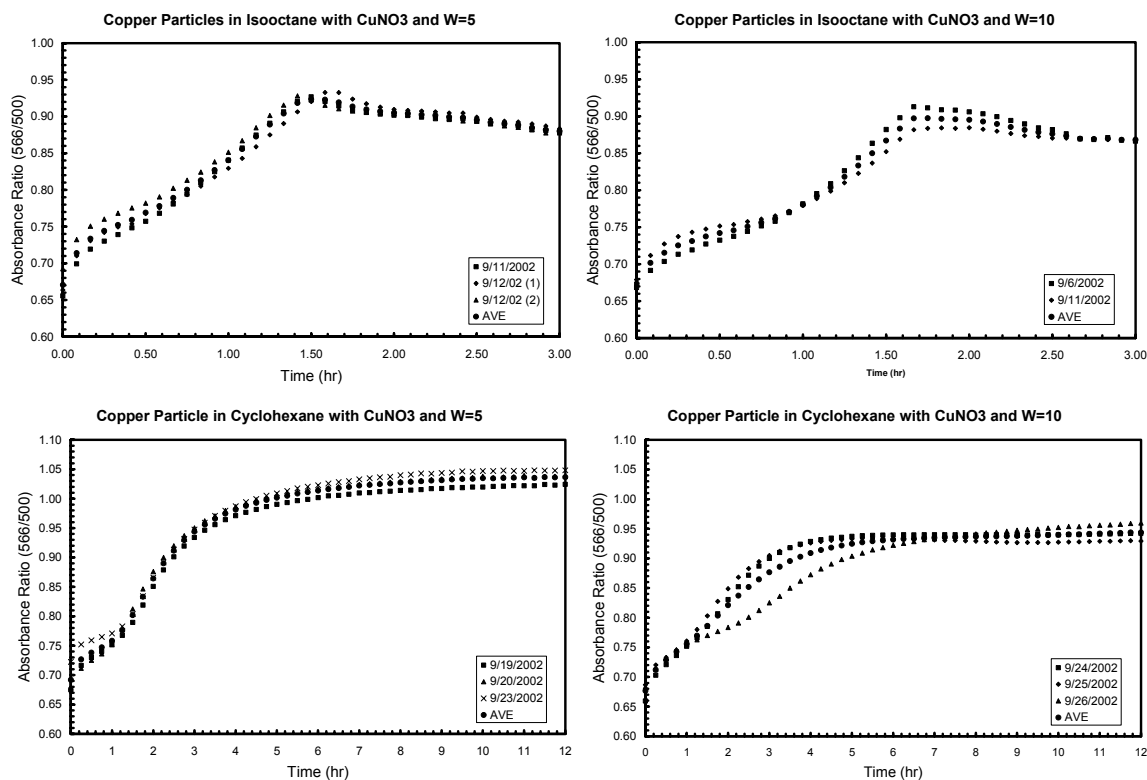






B-1c. Effects of Copper Salt Precursor on Particle Synthesis





B-2. SYNTHESIS OF COPPER METALLIC NANOPARTICLES IN AOT REVERSE MICELLE SYSTEMS EXPERIMENTAL GROWTH CURVES REGRESSION ANALYSIS

The regression analysis on the particle growth was done using the statistical software package Minitab 13¹. A quantitative representation of the relative growth rate is determined from the initial 1 to 6 hours of particle growth depending on the experimental conditions. The growth rates are obtained from the slope of the particle size vs. time plots, where the particle sizes are obtained from the Abs_{566}/Abs_{500} to particle size relationship. The slope was determined by a linear regression analysis of multiple experimental growth curves for each of the bulk solvents and W values. How well the regression analysis fits the particle growth curves is represented by an R^2 value. The error in the particle growth rate represented by the slope is determined from a 95% confidence interval calculated by twice the standard error obtained from the regression analysis¹. The results from the linear regression analysis are listed below including the time length of the initial growth. These results corresponding to the experimental data plotted in the previous section of this appendix and take into account each data set plotted.

B-2a. Effects of Bulk Solvent Type on Particle Synthesis with W =5

Regression Analysis: Pentane versus Time (First 4 hours)

The regression equation is

$$\text{Pentane} = 0.252 + 1.74 \text{ Time Pent}$$

Predictor	Coef	SE Coef	T	P
-----------	------	---------	---	---

Constant	0.2517	0.1761	1.43	0.160	
Time Pen	1.73825	0.07056	24.63	0.000	
S = 0.5113	R-Sq = 93.4%	R-Sq(adj) = 93.2%			
Analysis of Variance					
Source	DF	SS	MS	F	P
Regression	1	158.63	158.63	606.84	0.000
Residual Error	43	11.24	0.26		
Total	44	169.87			

Regression Analysis: Hexane versus Time (First 4 hours)

The regression equation is

$$\text{Hexane} = 0.416 + 1.62 \text{ Time Hex}$$

Predictor	Coef	SE Coef	T	P
Constant	0.4164	0.2065	2.02	0.047
Time Hex	1.62140	0.08273	19.60	0.000

S = 0.8477 R-Sq = 81.4% R-Sq(adj) = 81.2%

Analysis of Variance

Source	DF	SS	MS	F	P
Regression	1	276.04	276.04	384.15	0.000
Residual Error	88	63.23	0.72		
Total	89	339.27			

Regression Analysis: Heptane versus Time (First 5 hours)

The regression equation is

$$\text{Heptane} = 0.884 + 1.36 \text{ Time Hept}$$

Predictor	Coef	SE Coef	T	P
Constant	0.8842	0.1983	4.46	0.000
Time Hep	1.36102	0.06456	21.08	0.000

S = 1.156 R-Sq = 72.4% R-Sq(adj) = 72.3%

Analysis of Variance

Source	DF	SS	MS	F	P
Regression	1	593.92	593.92	444.41	0.000
Residual Error	169	225.86	1.34		
Total	170	819.78			

Regression Analysis: Octane versus Time (First 3.5 hours)

The regression equation is

$$\text{Octane} = 0.451 + 1.96 \text{ Time Oct}$$

Predictor	Coef	SE Coef	T	P
Constant	0.4509	0.1609	2.80	0.007
Time Oct	1.95758	0.07288	26.86	0.000

S = 0.5496 R-Sq = 92.0% R-Sq(adj) = 91.8%

Analysis of Variance

Source	DF	SS	MS	F	P
Regression	1	217.95	217.95	721.46	0.000
Residual Error	63	19.03	0.30		
Total	64	236.98			

Regression Analysis: Decane versus Time (First 3 hours)

The regression equation is

$$\text{Decane} = 1.11 + 1.77 \text{ Time Dec}$$

Predictor	Coef	SE Coef	T	P
Constant	1.1078	0.1539	7.20	0.000
Time Dec	1.77249	0.08704	20.36	0.000

S = 0.7191 R-Sq = 84.5% R-Sq(adj) = 84.3%

Analysis of Variance

Source	DF	SS	MS	F	P
Regression	1	214.42	214.42	414.67	0.000
Residual Error	76	39.30	0.52		
Total	77	253.72			

Regression Analysis: Dodecane versus Time (First 3 hours)

The regression equation is

$$\text{Dodecane} = 0.996 + 2.00 \text{ Time Dod}$$

Predictor	Coef	SE Coef	T	P
Constant	0.9963	0.1675	5.95	0.000
Time Dod	1.99740	0.09476	21.08	0.000

S = 0.7146 R-Sq = 87.6% R-Sq(adj) = 87.4%

Analysis of Variance

Source	DF	SS	MS	F	P
Regression	1	226.91	226.91	444.33	0.000
Residual Error	63	32.17	0.51		
Total	64	259.08			

Regression Analysis: Isooctane versus Time (First 6 hours)

The regression equation is

$$\text{Isooctane} = 0.886 + 1.25 \text{ Time Iso}$$

Predictor	Coef	SE Coef	T	P
Constant	0.8865	0.1746	5.08	0.000
Time Iso	1.24765	0.04988	25.01	0.000

S = 0.8993 R-Sq = 86.5% R-Sq(adj) = 86.3%

Analysis of Variance

Source	DF	SS	MS	F	P
Regression	1	505.90	505.90	625.60	0.000
Residual Error	98	79.25	0.81		
Total	99	585.15			

Regression Analysis: Cyclohexane versus Time (From hour 4 to hour 11)

The regression equation is

$$\text{Cyclohexane} = -1.27 + 1.09 \text{ Time Cyclo}$$

Predictor	Coef	SE Coef	T	P
Constant	-1.273	1.070	-1.19	0.241
Time Cyc	1.0917	0.1371	7.96	0.000

S = 1.987 R-Sq = 59.6% R-Sq(adj) = 58.7%

Analysis of Variance

Source	DF	SS	MS	F	P
Regression	1	250.28	250.28	63.41	0.000
Residual Error	43	169.72	3.95		
Total	44	420.00			

B-2b. Effects of Bulk Solvent Type on Particle Synthesis with W = 10

Regression Analysis: Pentane versus Time (First 5 hours)

The regression equation is

$$\text{Pentane} = 1.48 + 1.16 \text{ Time Pent}$$

Predictor	Coef	SE Coef	T	P
Constant	1.4761	0.1103	13.39	0.000
Time Pen	1.16214	0.03772	30.81	0.000

S = 0.5234 R-Sq = 92.0% R-Sq(adj) = 92.0%

Analysis of Variance

Source	DF	SS	MS	F	P
Regression	1	259.98	259.98	949.07	0.000
Residual Error	82	22.46	0.27		
Total	83	282.45			

Regression Analysis: Hexane versus Time (First 4 hours)

The regression equation is

$$\text{Hexane} = 0.791 + 1.87 \text{ Time Hex}$$

Predictor	Coef	SE Coef	T	P
Constant	0.7913	0.2335	3.39	0.002
Time Hex	1.86592	0.09958	18.74	0.000

S = 0.7111 R-Sq = 91.6% R-Sq(adj) = 91.4%

Analysis of Variance

Source	DF	SS	MS	F	P
Regression	1	177.56	177.56	351.10	0.000
Residual Error	32	16.18	0.51		
Total	33	193.75			

Regression Analysis: Heptane versus Time (First 4 hours)

The regression equation is

$$\text{Heptane} = 1.35 + 1.44 \text{ Time Hept}$$

Predictor	Coef	SE Coef	T	P
Constant	1.35116	0.09880	13.68	0.000
Time Hep	1.43666	0.04213	34.10	0.000

S = 0.3685 R-Sq = 96.0% R-Sq(adj) = 95.9%

Analysis of Variance

Source	DF	SS	MS	F	P
Regression	1	157.90	157.90	1162.84	0.000
Residual Error	49	6.65	0.14		
Total	50	164.55			

Regression Analysis: Octane versus Time (First 4 hours)

The regression equation is

$$\text{Octane} = 1.62 + 1.39 \text{ Time Oct}$$

Predictor	Coef	SE Coef	T	P
Constant	1.6234	0.1148	14.15	0.000
Time Oct	1.39049	0.04893	28.42	0.000

S = 0.4280 R-Sq = 94.3% R-Sq(adj) = 94.2%

Analysis of Variance

Source	DF	SS	MS	F	P
Regression	1	147.91	147.91	807.47	0.000
Residual Error	49	8.98	0.18		
Total	50	156.88			

Regression Analysis: Decane versus Time (First 3.5 hours)

The regression equation is

$$\text{Decane} = 1.46 + 1.85 \text{ Time Dec}$$

Predictor	Coef	SE Coef	T	P
Constant	1.4565	0.1247	11.68	0.000
Time Dec	1.85140	0.06061	30.54	0.000

S = 0.5071 R-Sq = 94.1% R-Sq(adj) = 94.0%

Analysis of Variance

Source	DF	SS	MS	F	P
Regression	1	239.94	239.94	932.94	0.000
Residual Error	58	14.92	0.26		
Total	59	254.85			

Regression Analysis: Dodecane versus Time (First 3 hours)

The regression equation is

$$\text{Dodecane} = 1.13 + 2.31 \text{ Time Dodec}$$

Predictor	Coef	SE Coef	T	P
Constant	1.1279	0.4339	2.60	0.016
Time Dod	2.3131	0.2455	9.42	0.000

S = 1.171 R-Sq = 78.7% R-Sq(adj) = 77.8%

Analysis of Variance

Source	DF	SS	MS	F	P
Regression	1	121.73	121.73	88.80	0.000
Residual Error	24	32.90	1.37		

Total 25 154.62

Regression Analysis: Isooctane versus Time (First 3.5 hours)

The regression equation is

Isooctane = 0.891 + 2.11 Time Iso

Predictor	Coef	SE Coef	T	P
Constant	0.8907	0.1881	4.73	0.000
Time Iso	2.11275	0.09147	23.10	0.000

S = 0.5412 R-Sq = 95.0% R-Sq(adj) = 94.8%

Analysis of Variance

Source	DF	SS	MS	F	P
Regression	1	156.23	156.23	533.46	0.000
Residual Error	28	8.20	0.29		
Total	29	164.43			

Regression Analysis: Cyclohexane versus Time (First 6 hours)

The regression equation is

Cyclohexane = 0.094 + 1.55 Time Cyclo

Predictor	Coef	SE Coef	T	P
Constant	0.0936	0.7377	0.13	0.900
Time Cyc	1.5507	0.1921	8.07	0.000

S = 1.425 R-Sq = 76.5% R-Sq(adj) = 75.3%

Analysis of Variance

Source	DF	SS	MS	F	P
Regression	1	132.26	132.26	65.17	0.000
Residual Error	20	40.59	2.03		
Total	21	172.85			

B-2c. Effects of W Value on Particle Growth for Isooctane Bulk Solvent

Regression Analysis: Iso 3 versus Time (First 6 hours)

The regression equation is

Iso 3 = 1.91 + 0.136 Time 3

Predictor	Coef	SE Coef	T	P
Constant	1.91200	0.04973	38.45	0.000
Time 3	0.13600	0.01421	9.57	0.000

S = 0.1281 R-Sq = 79.9% R-Sq(adj) = 79.1%

Analysis of Variance

Source	DF	SS	MS	F	P
Regression	1	1.5028	1.5028	91.63	0.000
Residual Error	23	0.3772	0.0164		
Total	24	1.8800			

Regression Analysis: Iso 5 versus Time (First 6 hours)

The regression equation is

Iso 5 = 0.895 + 1.24 Time 5

Predictor	Coef	SE Coef	T	P
Constant	0.8946	0.1743	5.13	0.000
Time 5	1.24446	0.04979	24.99	0.000

S = 0.8976 R-Sq = 86.4% R-Sq(adj) = 86.3%

Analysis of Variance

Source	DF	SS	MS	F	P
Regression	1	503.32	503.32	624.70	0.000
Residual Error	98	78.96	0.81		
Total	99	582.28			

Regression Analysis: Iso 6.5 versus Time (First 4 hours)

The regression equation is

Iso 6.5 = 0.633 + 1.91 Time 6.5

Predictor	Coef	SE Coef	T	P
Constant	0.6333	0.2810	2.25	0.031
Time 6.5	1.9054	0.1198	15.90	0.000

S = 0.8556 R-Sq = 88.8% R-Sq(adj) = 88.4%

Analysis of Variance

Source	DF	SS	MS	F	P
Regression	1	185.16	185.16	252.91	0.000
Residual Error	32	23.43	0.73		
Total	33	208.58			

Regression Analysis: Iso 8 versus Time (First 3.5 hours)

The regression equation is

Iso 8 = 0.630 + 2.23 Time 8

Predictor	Coef	SE Coef	T	P
Constant	0.6303	0.1847	3.41	0.001
Time 8	2.23286	0.08984	24.85	0.000

S = 0.6509 R-Sq = 93.5% R-Sq(adj) = 93.3%

Analysis of Variance

Source	DF	SS	MS	F	P
Regression	1	261.75	261.75	617.76	0.000
Residual Error	43	18.22	0.42		
Total	44	279.97			

Regression Analysis: Iso 10 versus Time (First 3.5 hours)

The regression equation is

Iso 10 = 0.912 + 2.11 Tme 10

Predictor	Coef	SE Coef	T	P
Constant	0.9117	0.1902	4.79	0.000
Tme 10	2.10571	0.09246	22.77	0.000

S = 0.5470 R-Sq = 94.9% R-Sq(adj) = 94.7%

Analysis of Variance

Source	DF	SS	MS	F	P
Regression	1	155.19	155.19	518.63	0.000
Residual Error	28	8.38	0.30		
Total	29	163.57			

Regression Analysis: Iso 12 versus Time (First 3.5 hours)

The regression equation is

Iso 12 = 0.676 + 2.34 Time 12

Predictor	Coef	SE Coef	T	P
Constant	0.6763	0.1849	3.66	0.001
Time 12	2.34500	0.08991	26.08	0.000

S = 0.5319 R-Sq = 96.0% R-Sq(adj) = 95.9%

Analysis of Variance

Source	DF	SS	MS	F	P
Regression	1	192.47	192.47	680.25	0.000
Residual Error	28	7.92	0.28		
Total	29	200.39			

Regression Analysis: Iso 15 versus Time (First 3.5 hours)

The regression equation is

Iso 15 = 1.33 + 1.64 Time 15

Predictor	Coef	SE Coef	T	P
Constant	1.3338	0.1788	7.46	0.000
Time 15	1.63786	0.08695	18.84	0.000

S = 0.5144 R-Sq = 92.7% R-Sq(adj) = 92.4%

Analysis of Variance

Source	DF	SS	MS	F	P
Regression	1	93.890	93.890	354.79	0.000

Residual Error	28	7.410	0.265
Total	29	101.300	

B-2d. Effects of Copper Salt on Particle Synthesis

CuNO₃ Effect

Regression Analysis: Hex W=5 versus Hex Time (First hour)

The regression equation is

$$\text{Hex W=5} = 1.08 + 3.56 \text{ Hex Time}$$

Predictor	Coef	SE Coef	T	P
Constant	1.0790	0.1370	7.87	0.000
Hex Time	3.5636	0.2325	15.33	0.000

S = 0.4532 R-Sq = 86.4% R-Sq(adj) = 86.0%

Analysis of Variance

Source	DF	SS	MS	F	P
Regression	1	48.239	48.239	234.91	0.000
Residual Error	37	7.598	0.205		
Total	38	55.837			

Regression Analysis: Hex W=10 versus Hex Time (First hour)

The regression equation is

$$\text{Hex W=10} = 0.691 + 3.15 \text{ Hex Time}$$

Predictor	Coef	SE Coef	T	P
Constant	0.6913	0.1023	6.76	0.000
Hex Time	3.1474	0.1735	18.14	0.000

S = 0.2761 R-Sq = 93.2% R-Sq(adj) = 92.9%

Analysis of Variance

Source	DF	SS	MS	F	P
Regression	1	25.086	25.086	328.98	0.000
Residual Error	24	1.830	0.076		
Total	25	26.916			

Regression Analysis: Iso W=5 versus Iso Time (First 1.5 hours)

The regression equation is

$$\text{Iso W=5} = 0.521 + 4.71 \text{ Iso Time}$$

Predictor	Coef	SE Coef	T	P
Constant	0.5208	0.1494	3.49	0.001
Iso Time	4.7119	0.1701	27.70	0.000

S = 0.5865 R-Sq = 93.3% R-Sq(adj) = 93.2%

Analysis of Variance

Source	DF	SS	MS	F	P
Regression	1	263.88	263.88	767.06	0.000
Residual Error	55	18.92	0.34		
Total	56	282.80			

Regression Analysis: Iso W=10 versus Iso Time (First 1.5 hours)

The regression equation is

$$\text{Iso W=10} = 0.736 + 2.64 \text{ Iso Time}$$

Predictor	Coef	SE Coef	T	P
Constant	0.7358	0.1557	4.72	0.000
Iso Time	2.6358	0.1774	14.86	0.000

S = 0.4993 R-Sq = 86.0% R-Sq(adj) = 85.6%

Analysis of Variance

Source	DF	SS	MS	F	P
Regression	1	55.048	55.048	220.81	0.000
Residual Error	36	8.975	0.249		
Total	37	64.022			

Regression Analysis: Cyclo W=5 versus Cyclo Time (First 1.5 hours)

The regression equation is

$$\text{Cyclo W=5}_1 = 1.22 + 1.32 \text{ Cyclo Time}_1$$

Predictor	Coef	SE Coef	T	P
Constant	1.2217	0.1277	9.57	0.000
Cyclo Ti	1.3229	0.1417	9.34	0.000

S = 0.3246 R-Sq = 82.1% R-Sq(adj) = 81.2%

Analysis of Variance

Source	DF	SS	MS	F	P
Regression	1	9.1872	9.1872	87.20	0.000
Residual Error	19	2.0019	0.1054		
Total	20	11.1891			

Regression Analysis: Cyclo W=10 versus Cyclo Time (First 1.5 hours)

The regression equation is

$$\text{Cyclo W=10}_1 = 1.07 + 1.26 \text{ Cyclo Time}_1$$

Predictor	Coef	SE Coef	T	P
Constant	1.06857	0.07545	14.16	0.000
Cyclo Ti	1.25905	0.08371	15.04	0.000

S = 0.1918 R-Sq = 92.3% R-Sq(adj) = 91.8%

Analysis of Variance

Source	DF	SS	MS	F	P
Regression	1	8.3223	8.3223	226.24	0.000
Residual Error	19	0.6989	0.0368		
Total	20	9.0212			

(1) Kitchens, L. J. *Exploring statistics : a modern introduction to data analysis and inference*; West Pub. Co.: St. Paul, 1987.

APPENDIX C

C. UV-VIS ABSORBANCE DATA TOOLS

C-1. DETAILS ON THE OCEAN OPTICS SD2000 FIBER OPTIC DUEL SPECTROMETER

The Ocean Optics UV-Vis fiber optic spectrometer is a versatile instrument that is capable of recording UV-Vis absorbance measurements in the range of 785nm to 176nm in wavelength on a millisecond time scale. This is done with the use of diffraction gratings where the entire spectrum is recorded at once rather than performing a scan of the wavelength spectra. This allows for the measurement of fast reactions; however there is a trade off in the resolution of the data. To compensate for this and improve the resolution, a duel spectrometer is used where two spectrometers run in parallel are used to divide the spectrum in half and achieve a resolution of less than 0.2 nm. The spectrometer has two channels, a master channel which records the lower half of the spectrum and a slave1 channel which records the upper half of the spectrum.

The spectrometer is set up with a Tungsten / Deuterium light source fed through a 400 micron fiber and a collimating lens then into the sample. A second collimating lens receives the transmitted light and a bifurcated fiber feeds into the two spectrometer channels. The collimating lenses allow for collimated light to pass through the sample and thus measurements can be taken in daylight without having to shield the sample from ambient light.

The software used to run the fiber optic spectrometer is OOI Base32. The software has multiple functionality however this description will go through the setup of a typical time resolved absorbance measurement. The spectrometer is connected to a computer by a USB connection and the software is compatible with Windows 98 and XP. Below describes a typical absorption experiment where both channels are used independently and several measurements are taken at specific time intervals. The output data stores each spectra in a separate file and the data can then be compiled and reduced into a single excel file using the VBA program written by Chris Kitchens.

C-2. UV-VIS TIME RESOLVED MEASUREMENTS USING THE OCEAN OPTICS FIBER OPTIC SPECTROMETER METHOD

- Spectrometer Configuration: Once the software is opened the spectrometer can be configured to tailor to various experiments. On the toolbar, go to Spectrometer and then to Configure. In this window, either the Master or Slave1 channels can be activated or deactivated if you want to look at the upper or lower or both ends of the spectrum.

- It has been observed that for some samples which absorb differently in the UV and Visible ranges that it is better to have two different windows open, one for each channel. For this case, open two spectrum windows and under the window menu choose Tile Vertically. Then highlight Spectrum 1 window and go to Spectrometer → Configure, click on Slave1 and uncheck Channel Enable and OK. Then highlight Spectrum 2 window and go to Spectrometer → Configure, click on Master and uncheck Channel Enable and OK.
- The two windows should now display the entire spectrum. For each of the two windows, the Integration Time should be adjusted in msec such that the Intensity maximum is around 3500 counts (excluding the spike at 656 nm from the UV lamp). The Average value may also be adjusted to suit the particular experiments.
- Collect a Global Dark Spectrum by totally blocking the light path so no light is transmitted and click on the dark light bulb at the top of the screen. Next, collect a background by allowing light to transmit but without the sample and collect the Global Reference by clicking on the yellow light bulb. The Absorbance mode should now be active, the A's turn blue and can be clicked on to go into absorbance collection mode.
- The Spectrometer is now ready to record data but still needs to be set up for time acquisition.
- Open Exploring and create a folder where you would like the data to be stored.*
- Highlight Spectrum 1 window and in the menu bar go to Time Acquisition → Configure → Configure Acquisition. Browse and find the folder recently created and enter the time acquisition file name for the master channel (UV data). This file is to be used later in the data reduction!** Check save full spectrum with each acquisition. Set Initial Delay, Frequency, and Duration.
- Highlight the Spectrum 2 window and repeat the previous step for the Slave1 channel (Vis Data) using a different time acquisition file name.
- The OOIBase32 software also has the ability to set Time Channel Acquisitions – Channels A thru F plus 2 Combinations. For each of the two spectrometer channels the time channels can be set by Time Acquisition → Configure → Configure Time Channels where the wavelengths and channels can be set. (If the Channel is not active then a bad value will be stored.) The Time Channel Configuration can be saved for use in the Data Reduction step later*** and also if these time channels are to be used repetitively then they can be restored. Time Acquisition → Configure → Restore / Save Parameters.
- Activate the Time Acquisition for each window by clicking on the alarm clock so that the play button turns green or go to Time Acquisition → Activate Time Acquisition.
- The measurements are now ready to be run and can be started by clicking the green Play Button.

C-3. DATA COMPILER AND REDUCER

VBA macros were written to compile and process the output from the time resolved absorbance measurements using the Ocean Optics Fiber Optic Spectrometer.

The output from the measurements stores each data acquisition in a separate file as well as the time channel data. This Compiler reads in all the data into a single file, reduces the data and plots the spectra in a single file. The program is fully automated and is fairly user friendly. To use the compiler, open the excel file Ocean Optics Data Compiler or Ocean Optics Data Compiler Copper (includes an Info page which plots the 566nm/500nm Ratio as a function of time). When opening be sure to enable macros. In the menu bar go to Tools → Macro → Macros select Oceanoptics and Run. The macro will proceed as follows.

- The program will ask for the file name to save the compiled data under as an excel file. Enter a file name for the excel file.
- Enter the number of spectra that were collected during the experiment. The folder created previously (refer to *) which contains the raw data will label the individual files with consecutive numbers starting with 00000 and for example, if 37 scans were collected, then the numbers will end with 00036. In this case you would enter 37 in the window.
- The next window will ask for the Time Acquisition File. This is the file name that you entered in the Configure Time Acquisition step previously (refer to **). This file name will have a *.time file extension.
- The program will then ask if a second spectrometer was used and in this case there is the Slave1 channel, so click yes. In the case that both of the spectrometers were used in a single spectrum window then the *.time files for each spectrometer would be the same. In the case that only one of the spectrometers were used then click no.
- Next, select the Time Acquisition File (*.time) for the Slave1 Spectrometer if it is asked for.
- The program will then import the time acquisition data and will ask if the original *.time files should be saved in the excel format. It is suggested that you select **No** for both files.
- The program will then ask if there is a Time Acquisition Parameters File. This is the *.TimeParameters file (refer to ***) that was created under Configure Time Channels and was either saved or restored. If this step was skipped or not saved/restored then select no. If you configured the time channels but did not save the file, you will be able to enter the wavelengths manually.
- If you select Yes the program will ask for the *.TimeParameters file. This file type may not be available initially, so you must select all files under the Files of type: menu and then find the *.TimeParameters file. This will input the headings into the time channels data pages and the same headings can be used for each spectrometer or if separate configurations were used for each of the spectrometers, different headings may be used.
- If there is not a parameters file to use, the headings for each of the spectrometers may be entered manually when prompted.
- Next the program will Import all of the raw data that was stored in the individual files and place it into the single excel worksheet. The program will ask if you want to save the raw data file before the data is reduced. This is up to your preference.

- Next is the data compression step which averages the data to the nearest wavelength and prompts for the wavelength ranges for each spectrometer. Default wavelengths are available.
- The compressed data can then be plotted and the raw data can be removed. (The raw data may have been saved two steps previously so it may not be lost permanently if the final file is saved under a different name.
- For the case of Copper Nanoparticle Experiments there is now the option to create an Info page which will extract the absorbance data at 500nm and 566nm and plot the Absorbance Ratio as a function of time.
- Once the Data Reduction is completed, the file can be saved and the original files can be cleaned up to conserve disk space.

This Concludes the Details on the Ocean Optics Fiber Optic Spectrometer and Data Compiler/Reduction. For more information refer to the instrument manual or VBA code.

C-4. VISUAL BASIC APPLICATIONS FOR EXCEL CODE FOR REDUCING DATA FROM VARIAN CARY 3 UV-VIS SPECTROMETER

VBA macro was written to process the output from the time resolved absorbance measurements using the Varian Cary 3 UV-Vis Spectrometer. In rare cases the output file would miss an absorbance value for a particular wavelength and thus the macro analyses the data to repair these vacancies. The macro also plots the absorbance data in an Excel file and extracts the absorbance values at 500 nm and 566 nm wavelengths and calculates the absorbance ratio and plots the ratio as a function of time. The macro is available upon request.

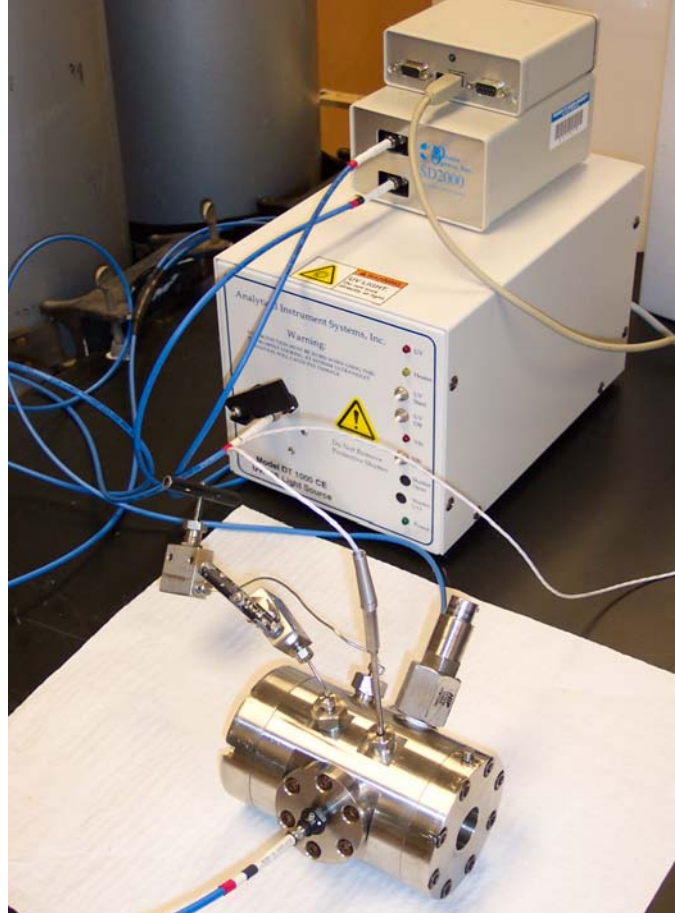
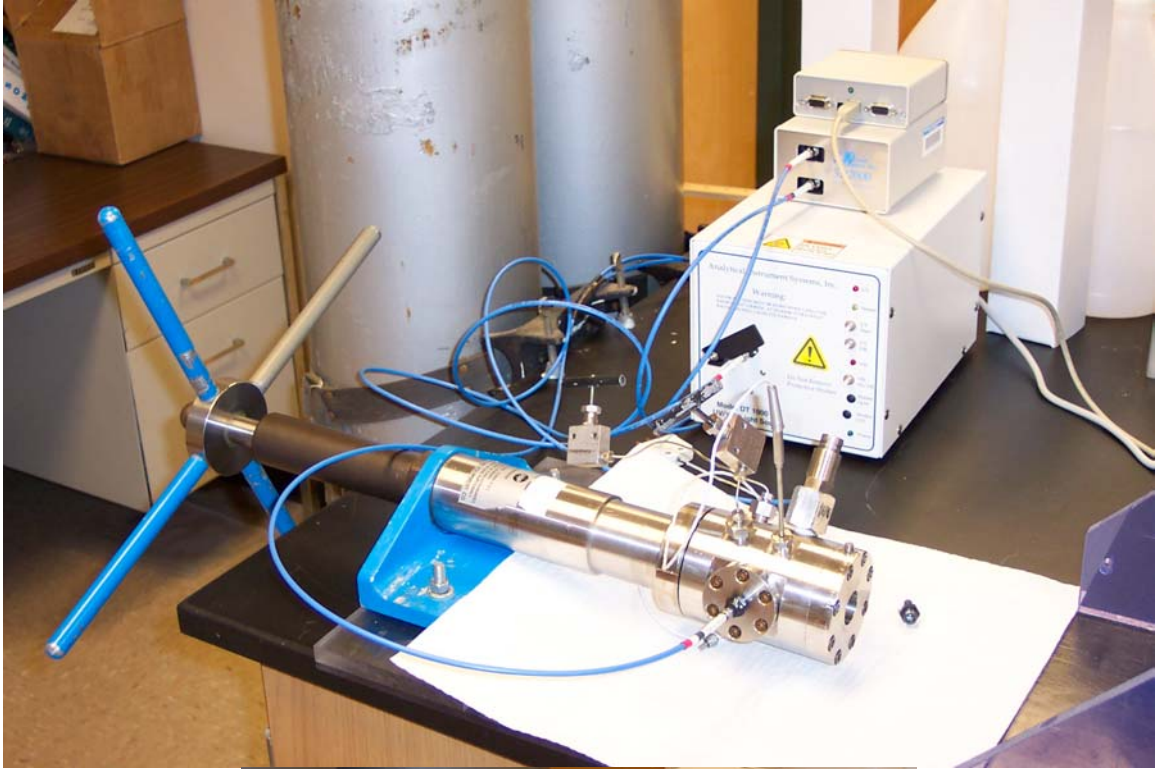
APPENDIX D

D. HIGH PRESSURE VESSELS FOR COMPRESSED AND SUPERCRITICAL FLUID REACTION

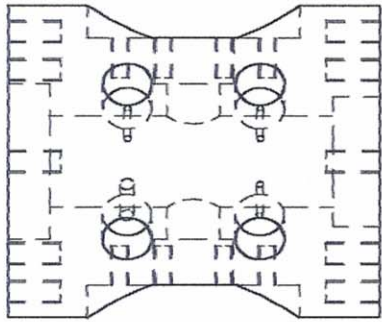
D-1. VARIABLE VOLUME VIEW CELL APPARATUS

In collaboration with Joe Aderholt, our departmental machinist, I was able to design and build a multi-functional, high pressure variable volume view cell. The cell uses a modified high pressure piston displacement hand pump, attached to the cell with a quartz window in the face, such that the entire content of the vessel is visible. The sides of the vessel are equipped with opposing windows which allow for UV-Vis absorption measurements, necessary to monitor the growth of nanomaterials, in-situ. The cell also has input and output valves as well as an RTD temperature controller and a flush mount pressure transducer. The cell has the ability to be used as a constant volume reaction vessel by replacing the modified displacement pump with a back plate giving the vessel a volume of ~30ml. The vessel has been pressure tested up to 10,000 psi at room temperature and has proven very useful in the measurement of critical points and solubility cloud points, in addition to running reactions in compressed and supercritical fluids where the temperature and pressure of the system can be controlled to determine the thermophysical properties of the reaction system. A web cam and ring light have also been adapted to allow digital monitoring of the reaction vessel, which has safety and research advantages.

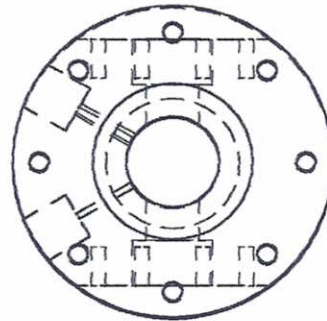
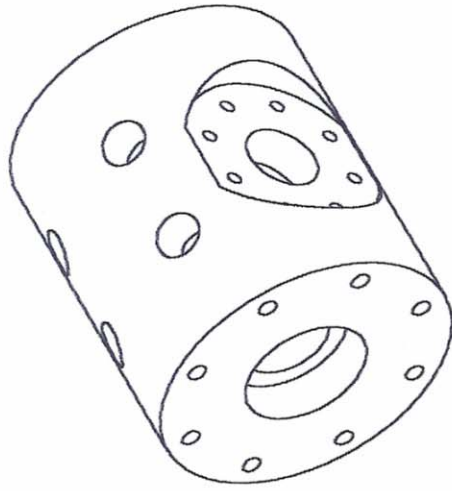




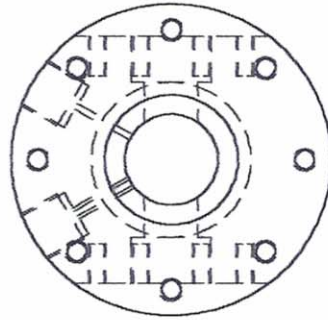
Vessel Body



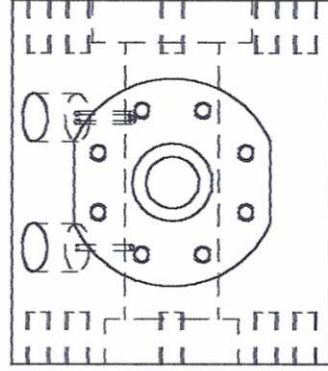
Top View



Back View



Front View

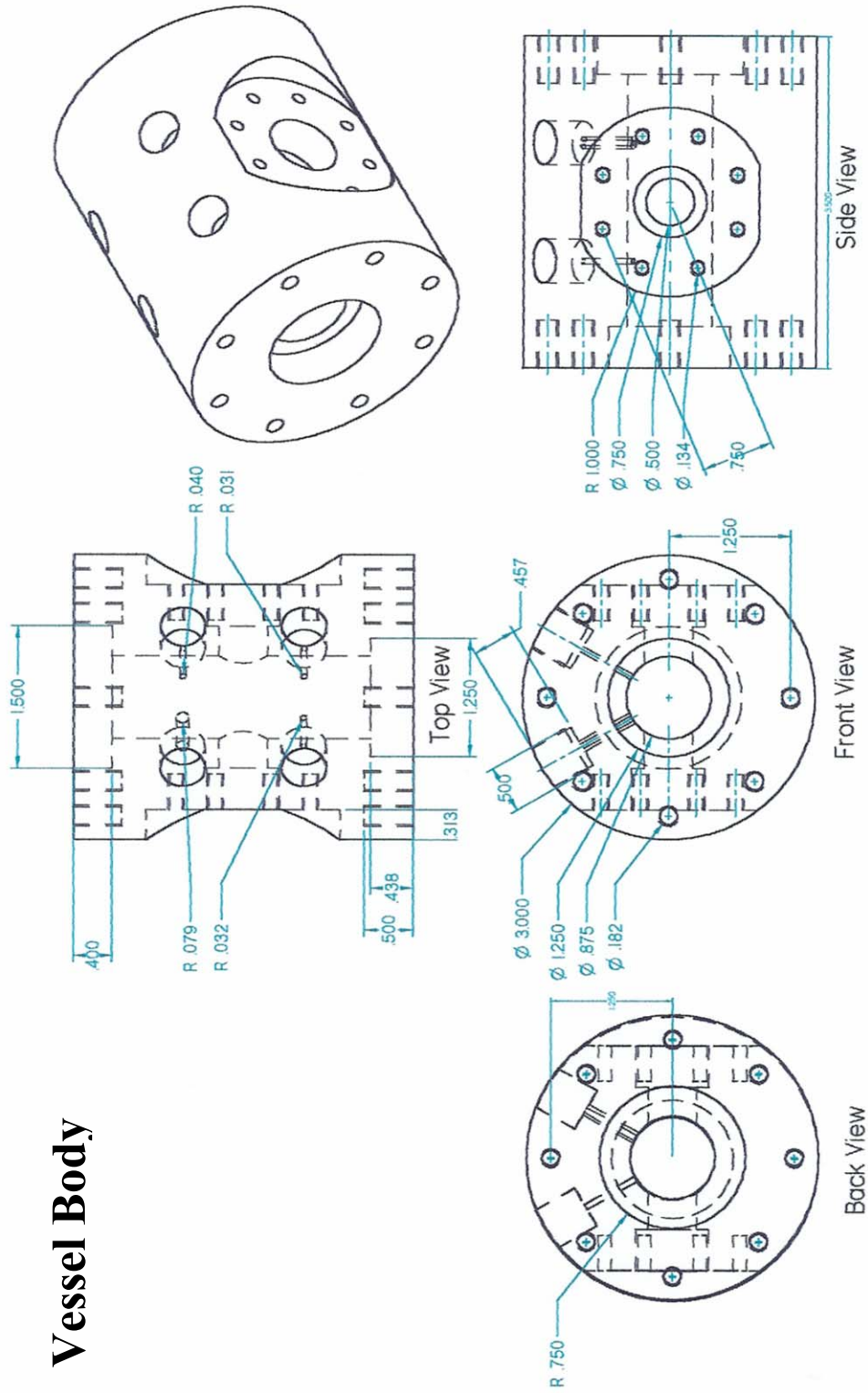


Side View

Page	Chris Kitchens
1	High Pressure Vessel
3/20/02	Super Critical Fluids

SOLID EDGE ACADEMIC COPY

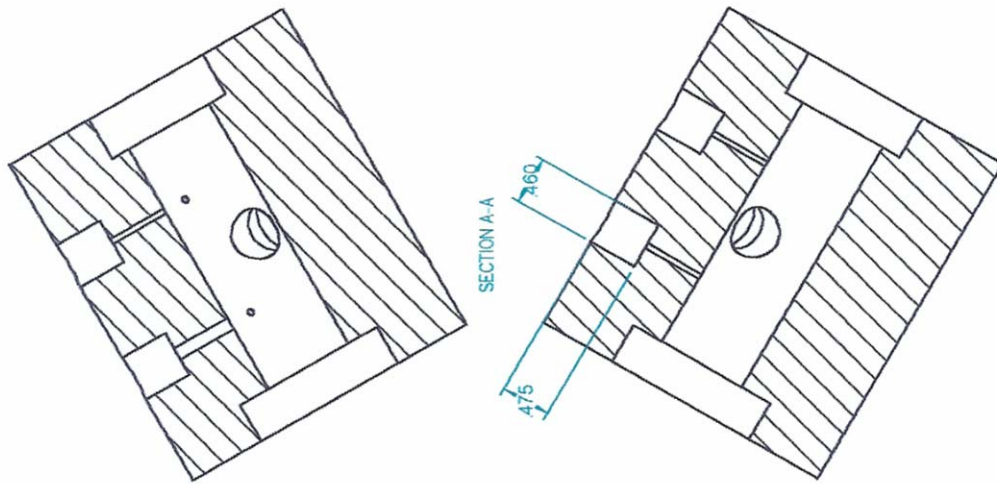
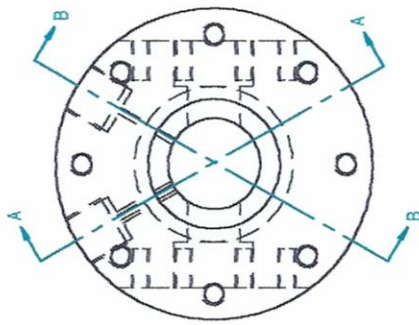
Vessel Body



Page	Chris Kitchens
2	High Pressure Vessel
3/20/02	Super CriticalFluids

SOLID EDGE ACADEMIC COPY

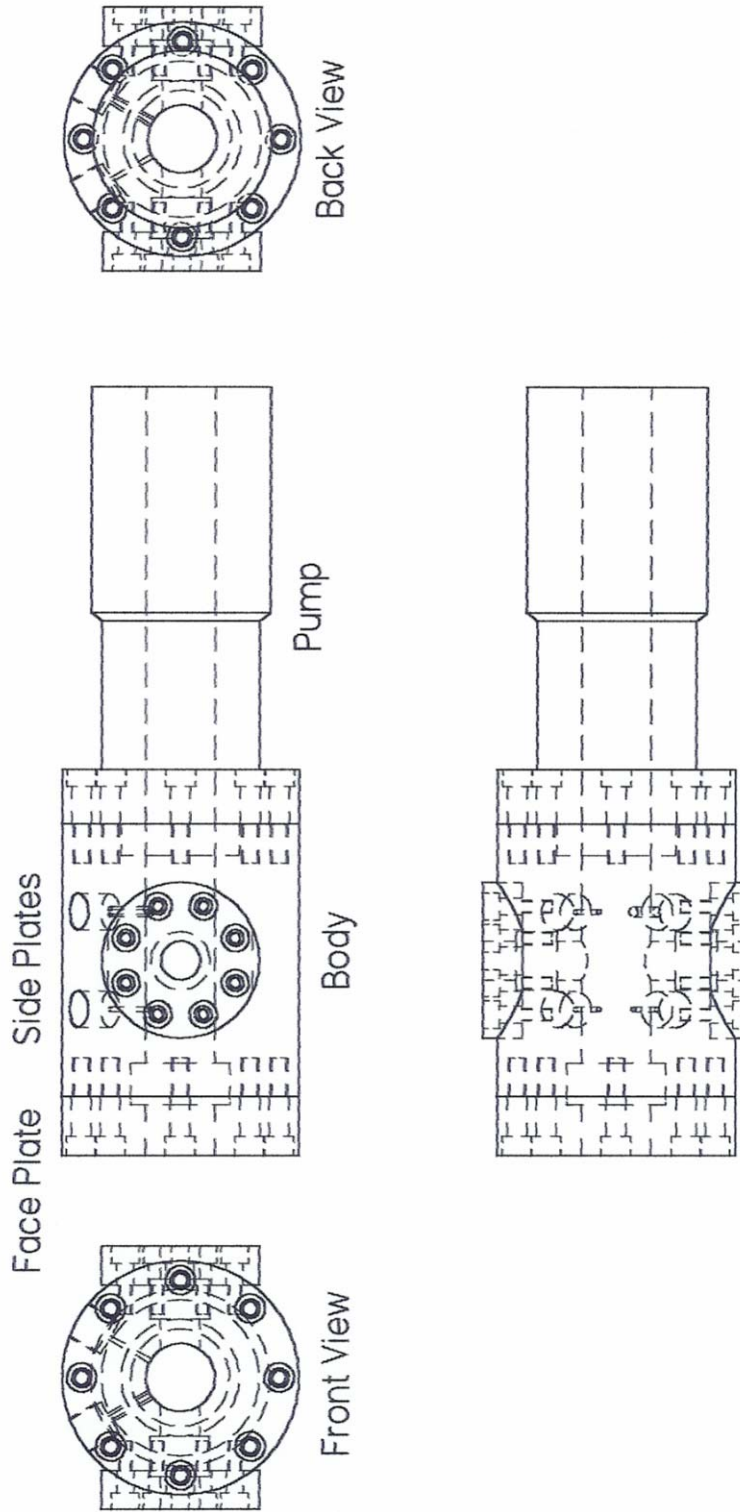
Vessel Body



Page	Chris Kitchens
3	High Pressure Vessel
3/20/02	Super Critical Fluids

SOLID EDGE ACADEMIC COPY SECTION B-B

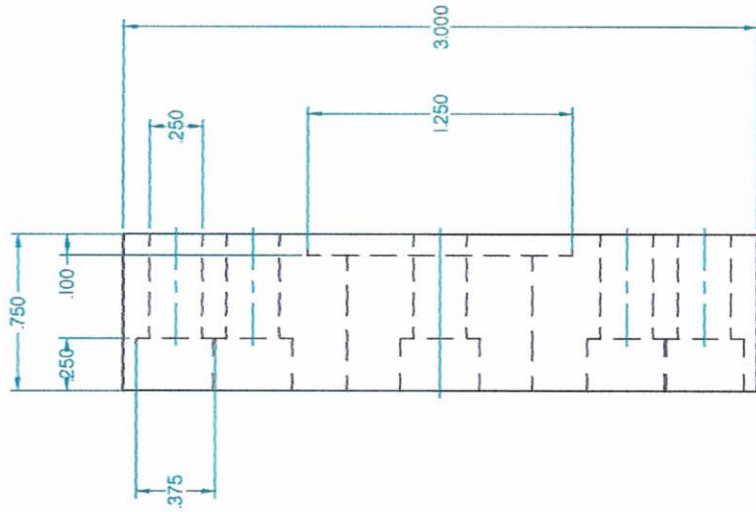
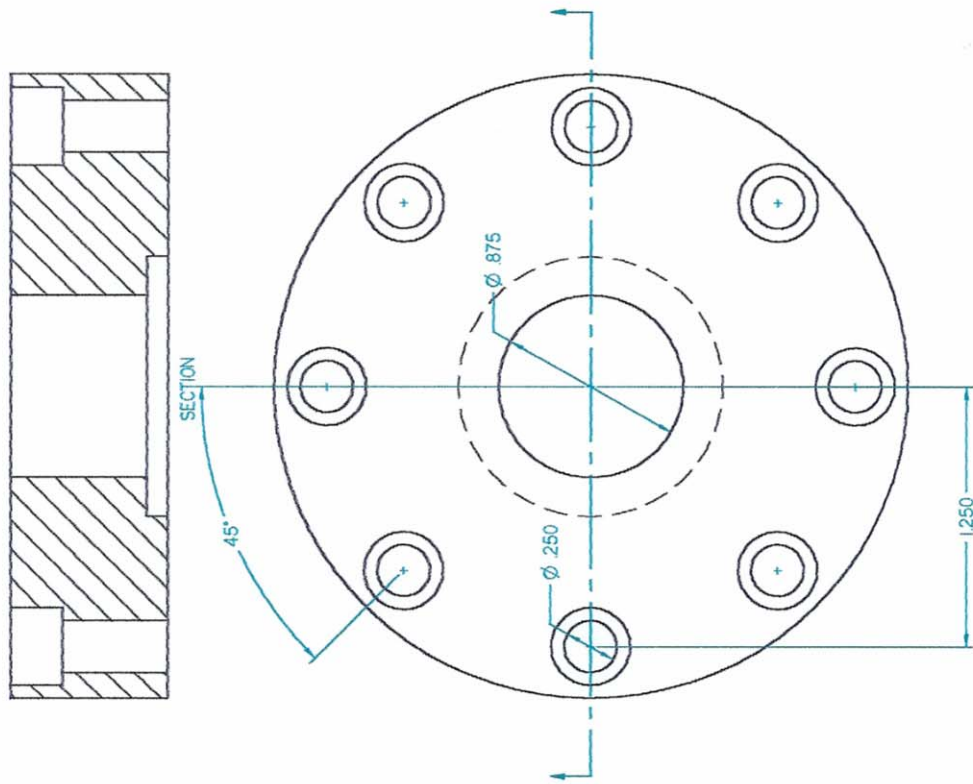
Vessel Assembly



Page	Chris Kitchens
4	High Pressure Vessel
3/20/02	Super Critical Fluids

SOLID EDGE ACADEMIC COPY

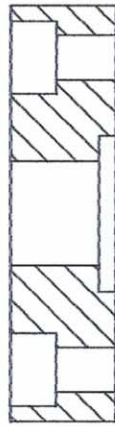
Vessel Face Plate



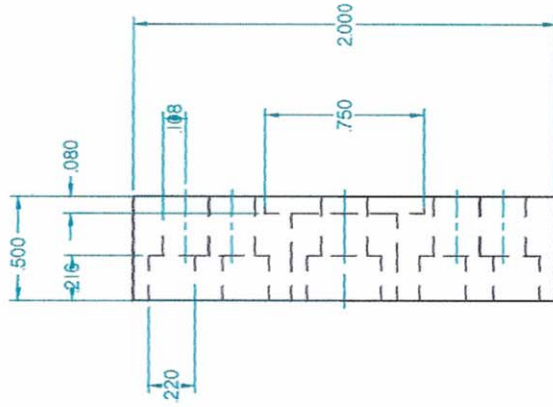
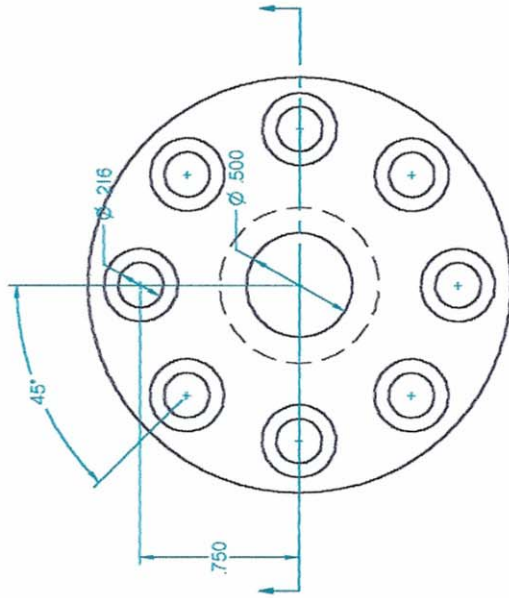
Page	Chris Kitchens
5	High Pressure Vessel
3/20/02	Super Critical Fluids

SOLID EDGE ACADEMIC COPY

Vessel Side Plate



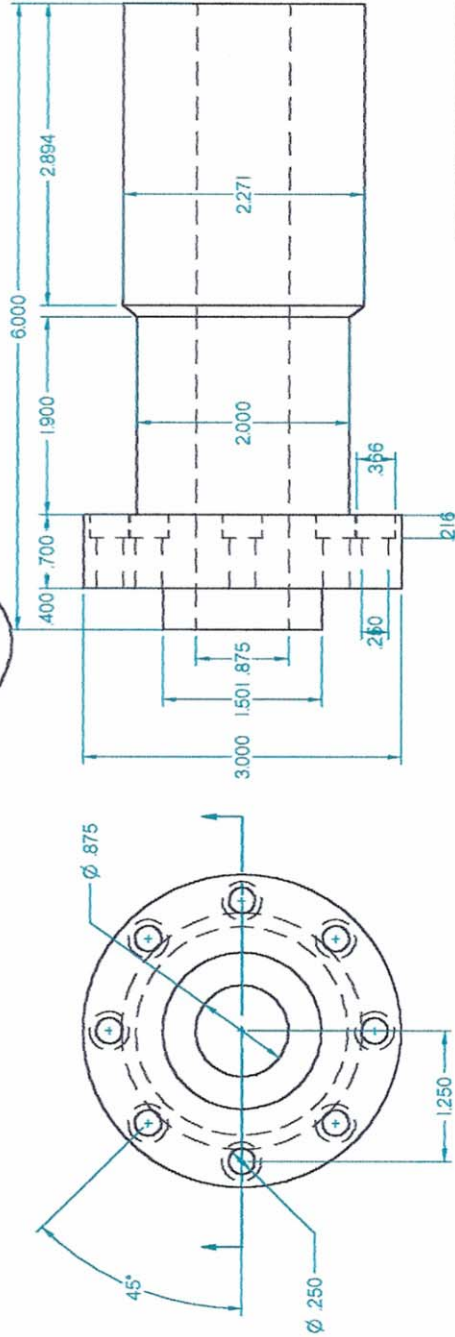
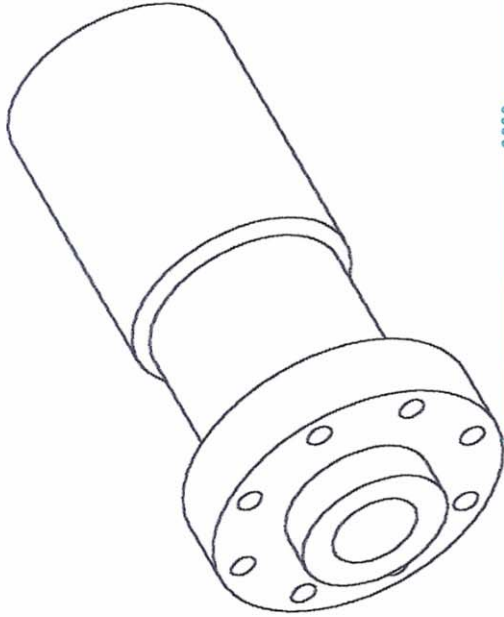
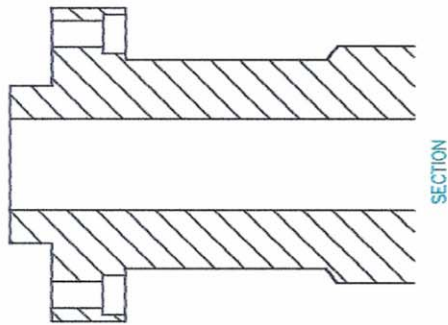
SECTION



Page	Chris Kitchens
6	High Pressure Vessel
3/20/02	Super Critical Fluids

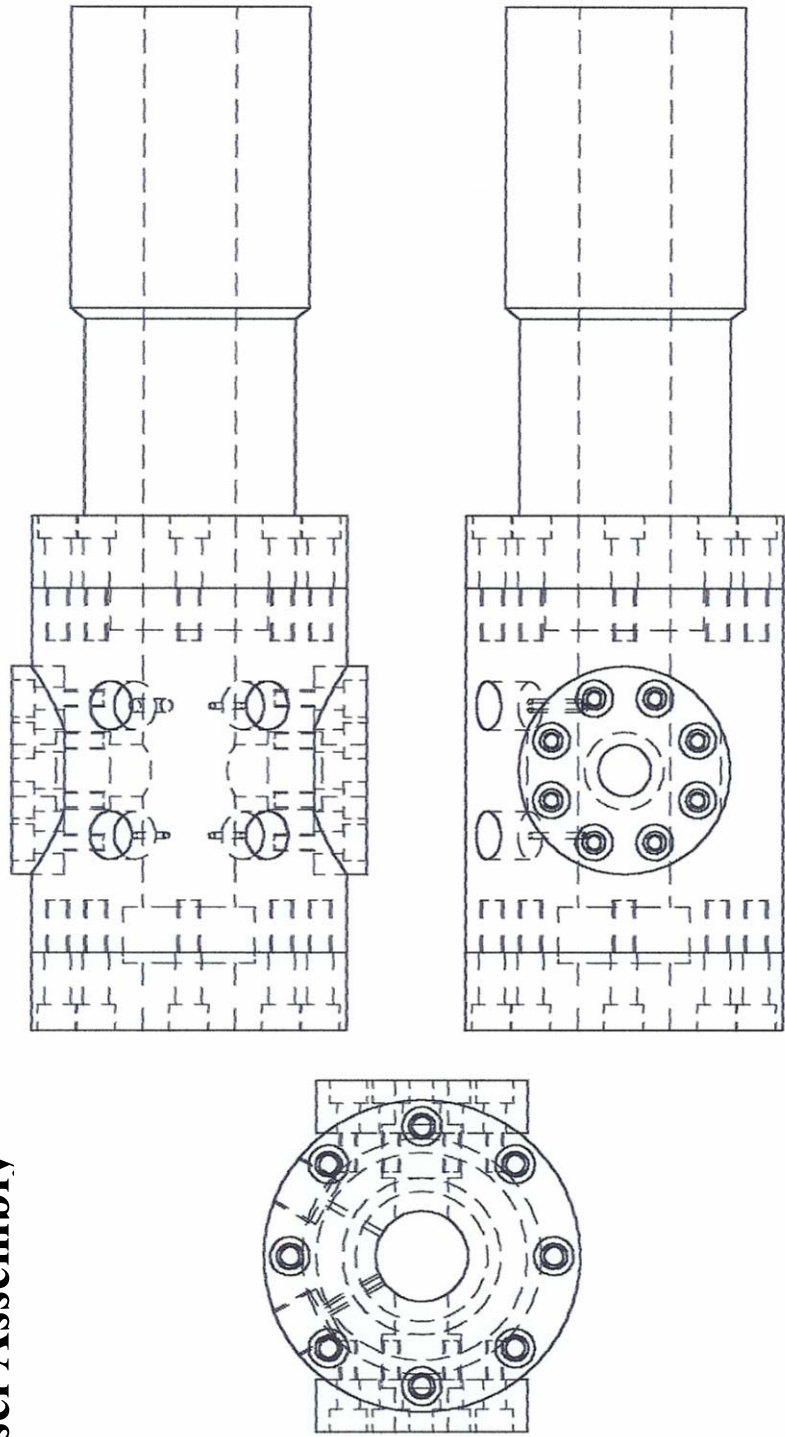
SOLID EDGE ACADEMIC COPY

Variable Volume Piston Displacement Hand



SOLID EDGE ACADEMIC COPY

Vessel Assembly

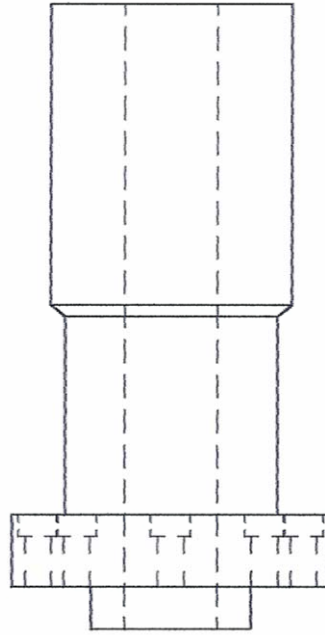
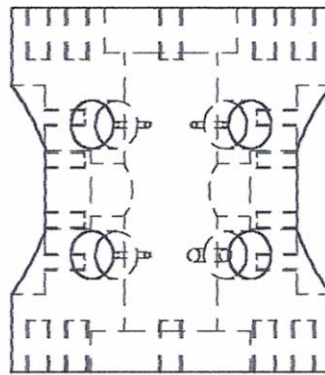
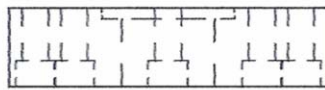


Title	Material
High Pressure Variable Volume Pump	316 Stainless Steel
High Pressure Vessel Side Plates	316 Stainless Steel
High Pressure Variable Volume Cell	316 Stainless Steel
High Pressure Vessel Face Plate	316 Stainless Steel

Page	Chris Kitchens
8	High Pressure Vessel
3/20/02	Super Critical Fluids

ACADEMIC COPY

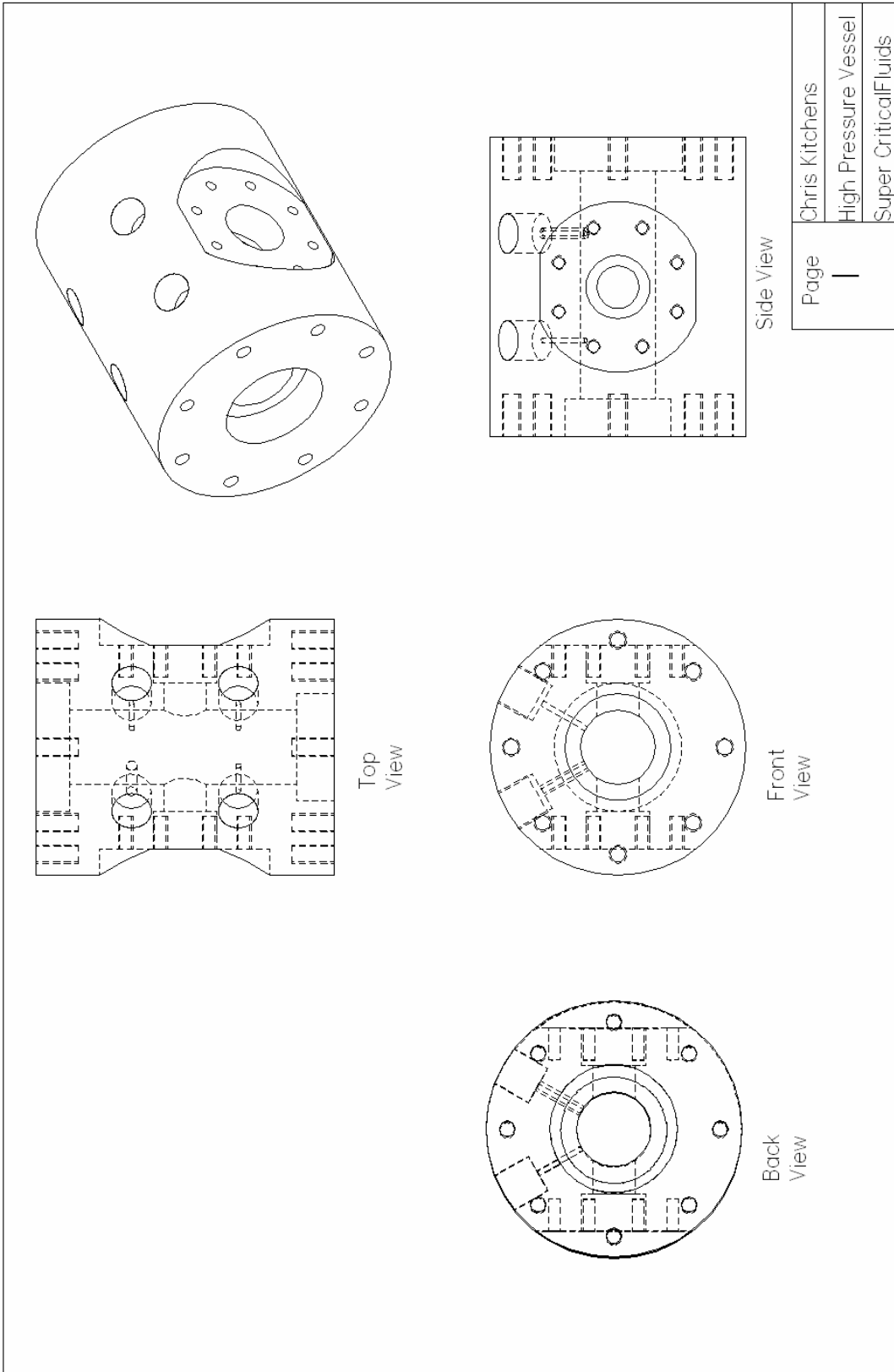
Vessel Assembly



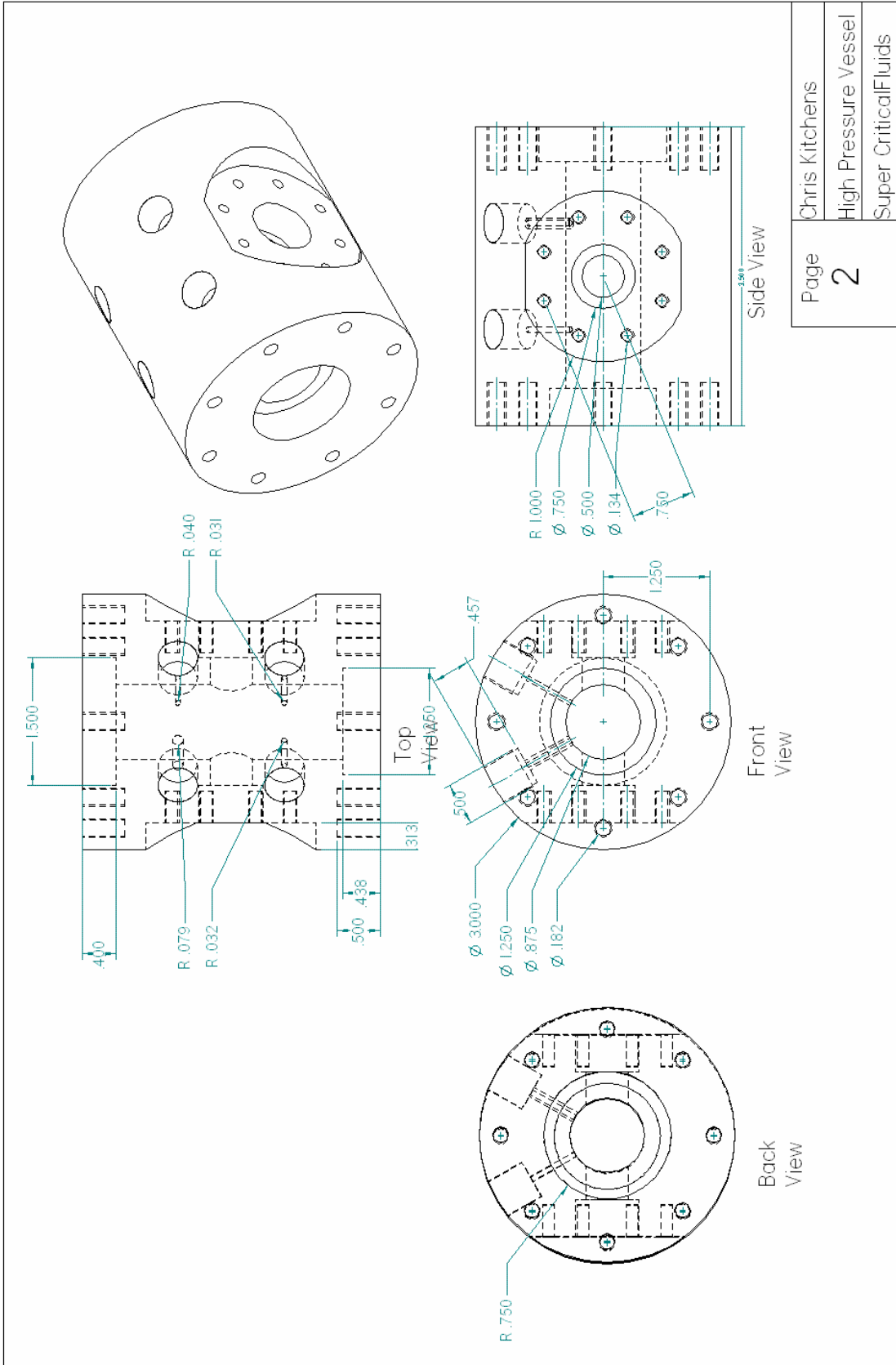
Page	Chris Kitchens
9	High Pressure Vessel
3/20/02	Super Critical Fluids

SOLID EDGE ACADEMIC COPY

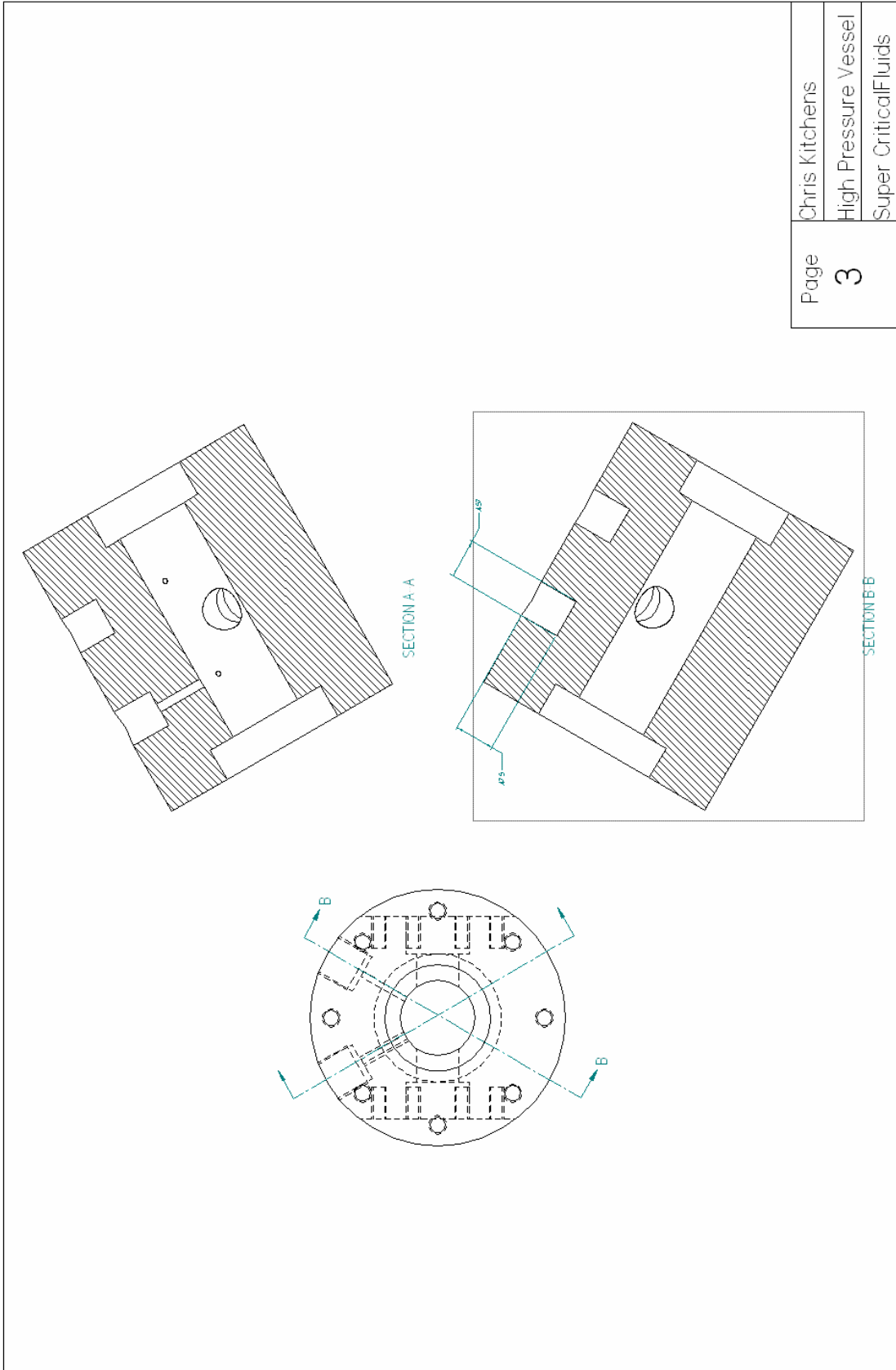
D-2. HIGH PRESSURE VIEW CELL



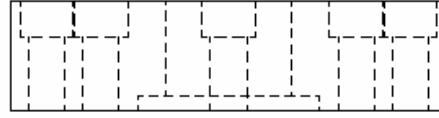
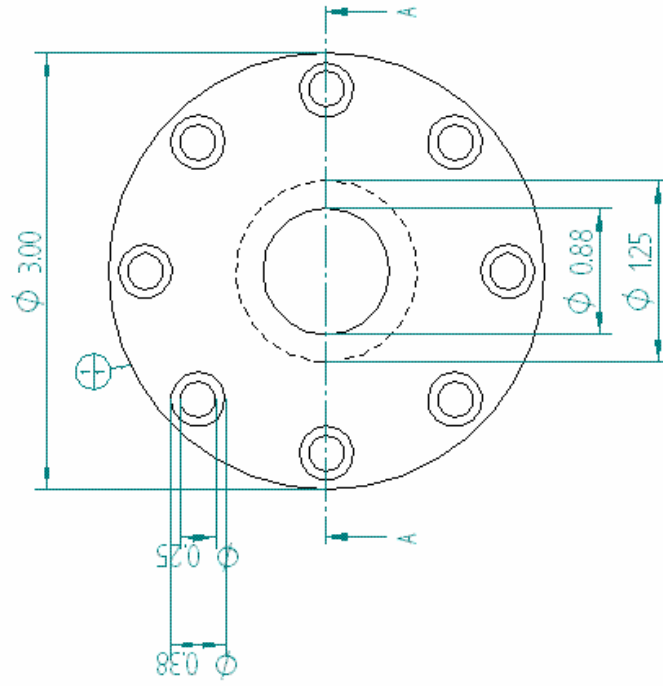
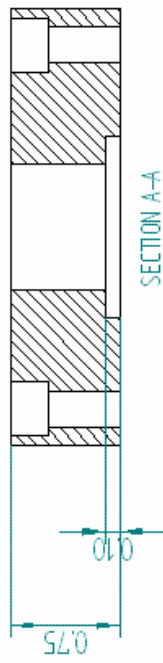
Page	Chris Kitchens
1	High Pressure Vessel
	Super Critical Fluids



Page	Chris Kitchens
2	High Pressure Vessel
	Super Critical Fluids

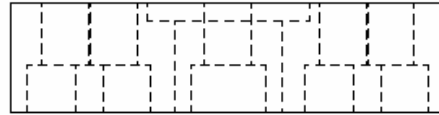
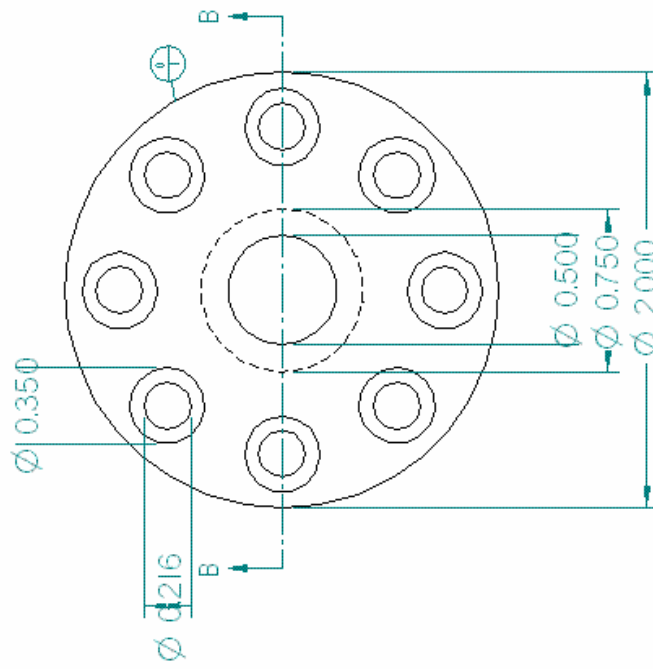
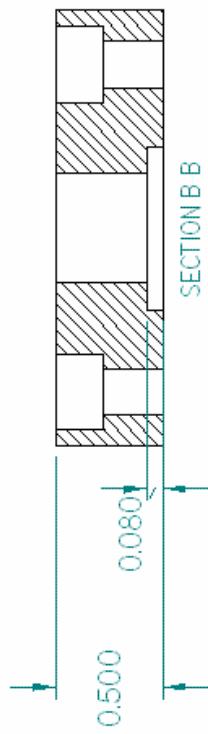


Page	Chris Kitchens
3	High Pressure Vessel
	Super Critical Fluids



Title Material
 Face Plate 316 Stainless Steel

Page	Chris Kitchens
4	High Pressure Vessel
	Super Critical Fluids



Title
High Pressure Vessel
Side Plates

Material
316 Stainless
Steel

Chris Kitchens

Page

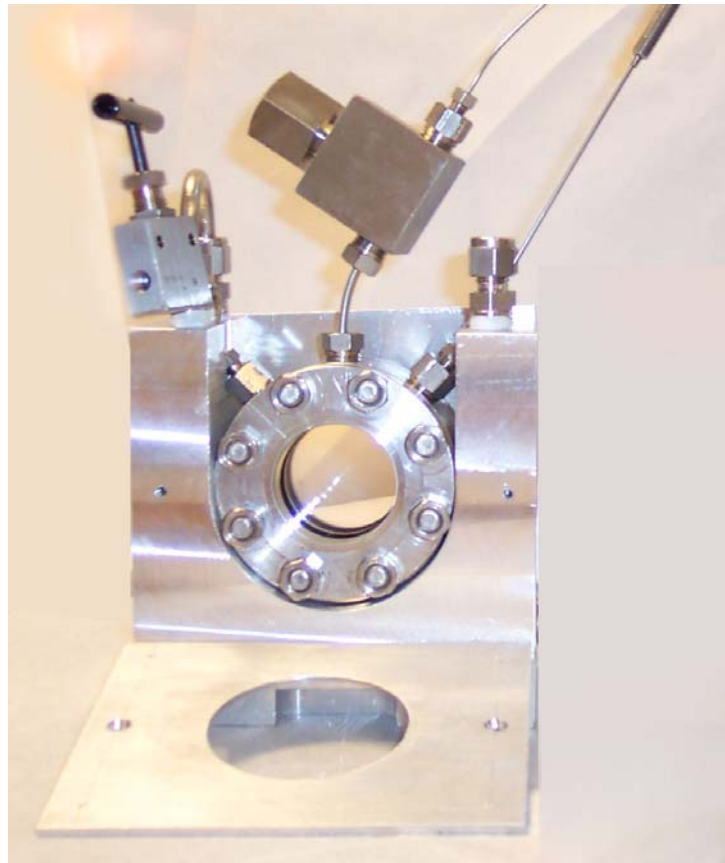
5

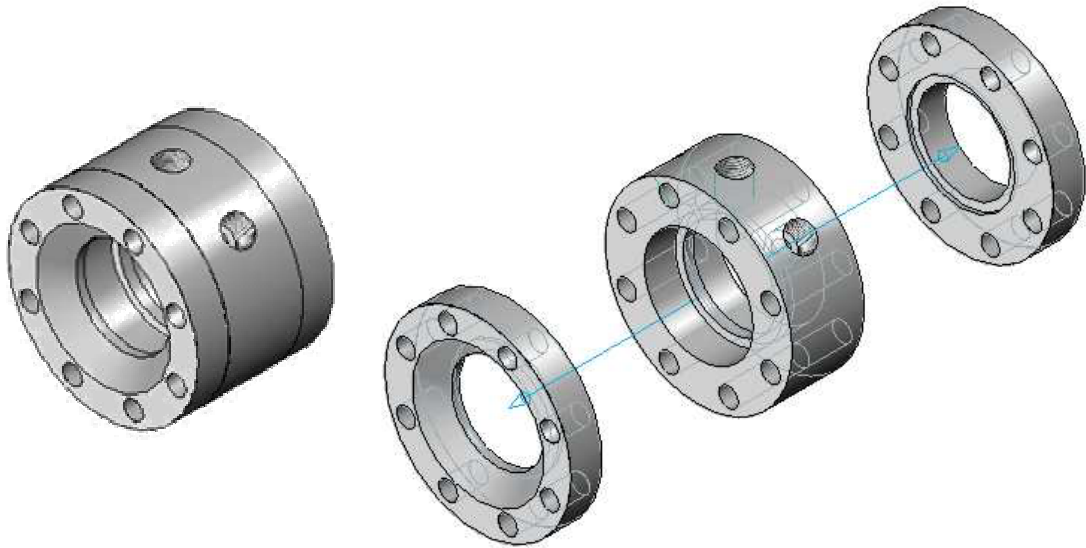
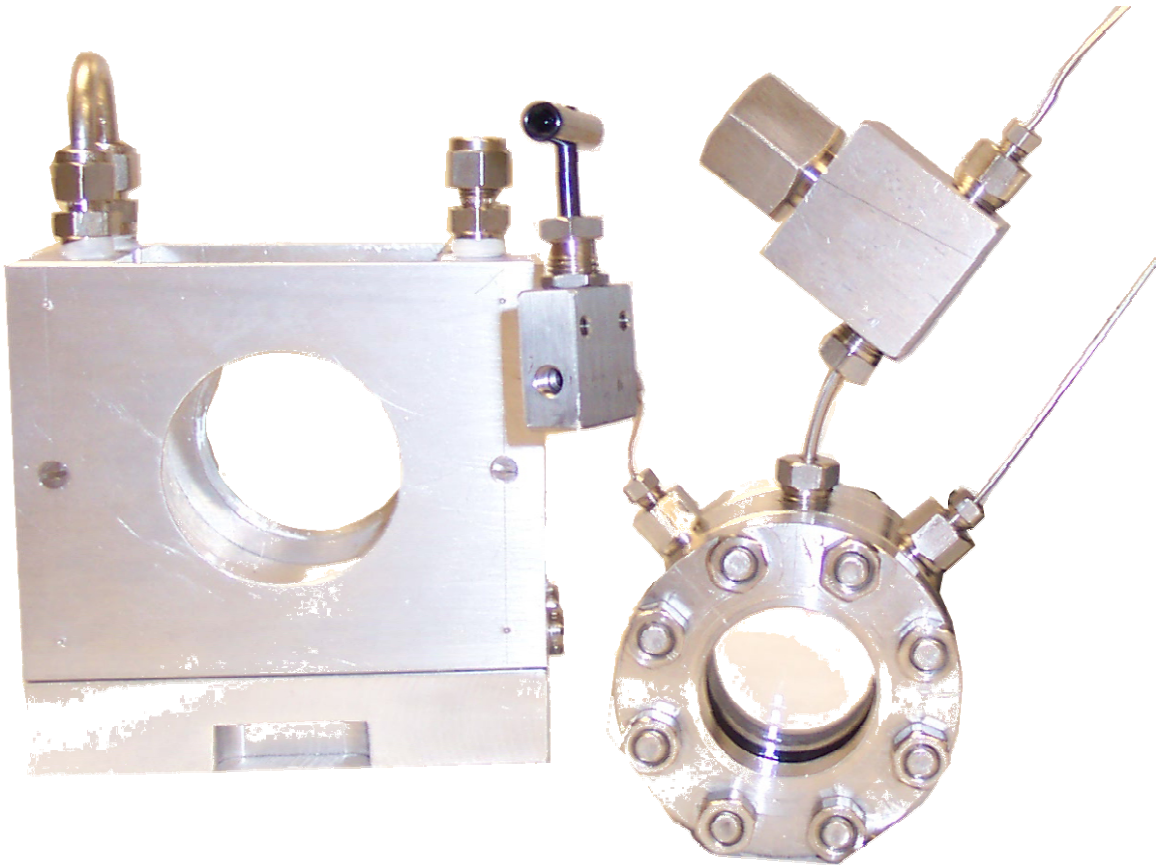
High Pressure Vessel

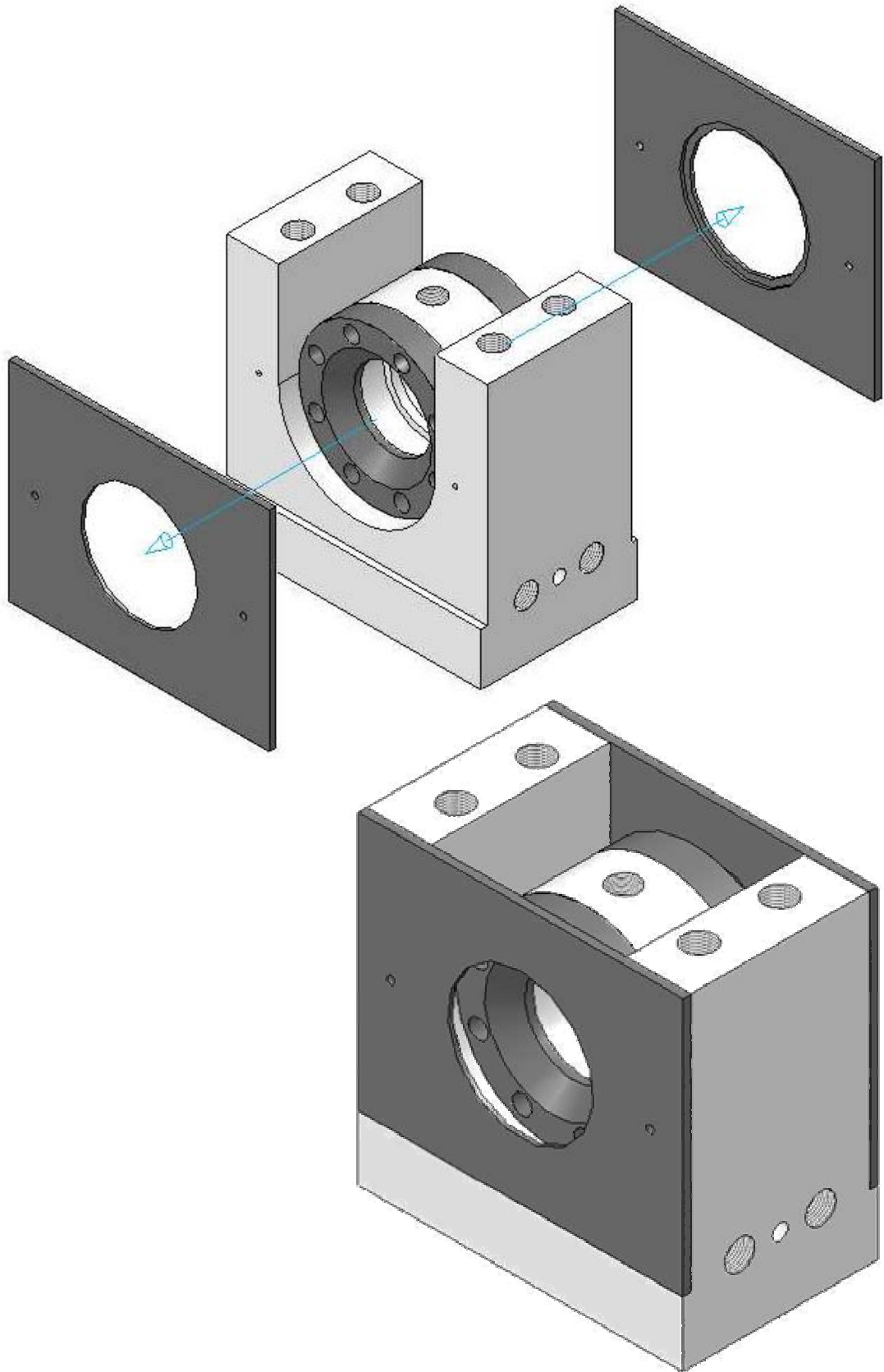
Super Critical Fluids

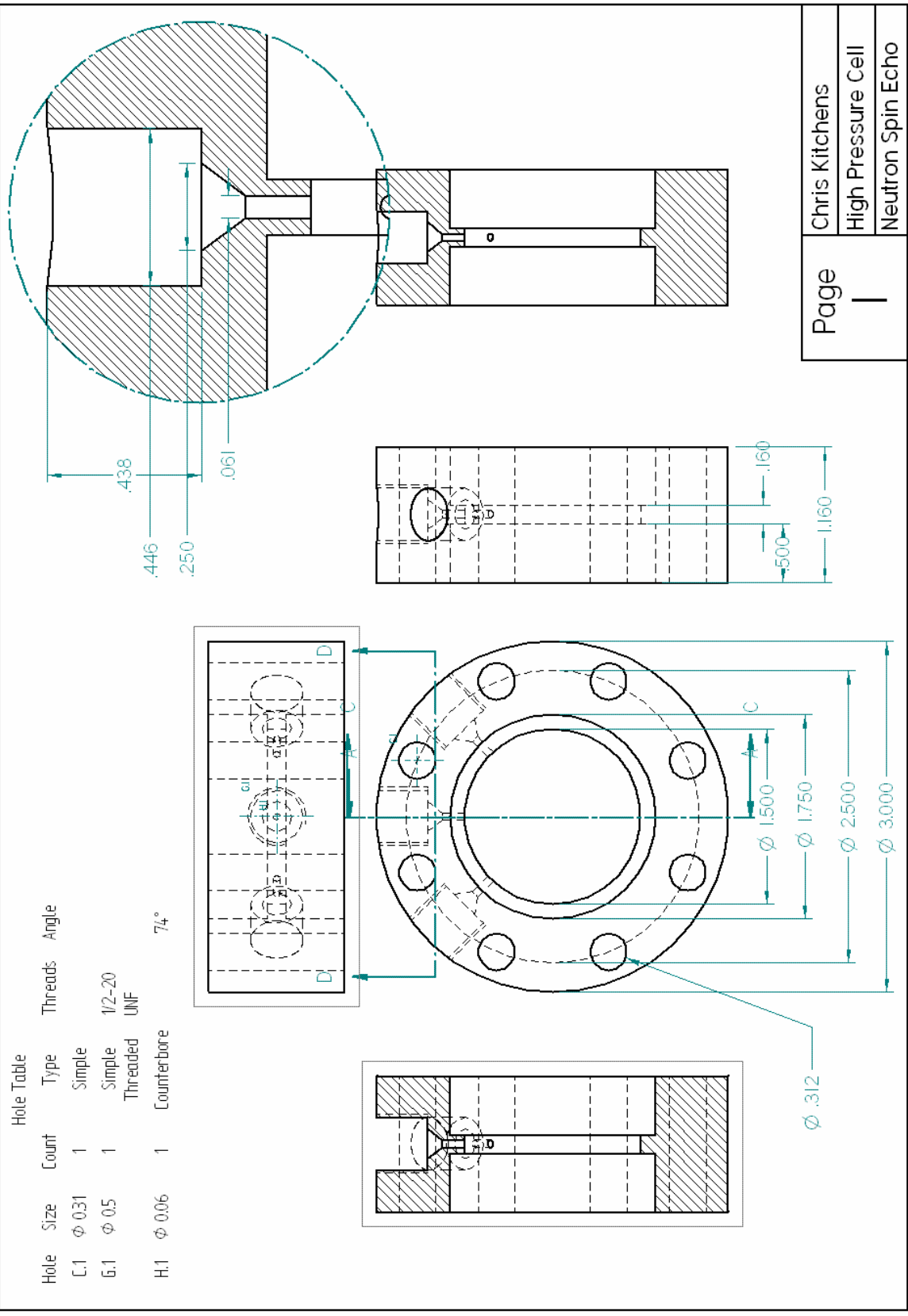
D-3. HIGH PRESSURE NEUTRON SPIN ECHO CELL

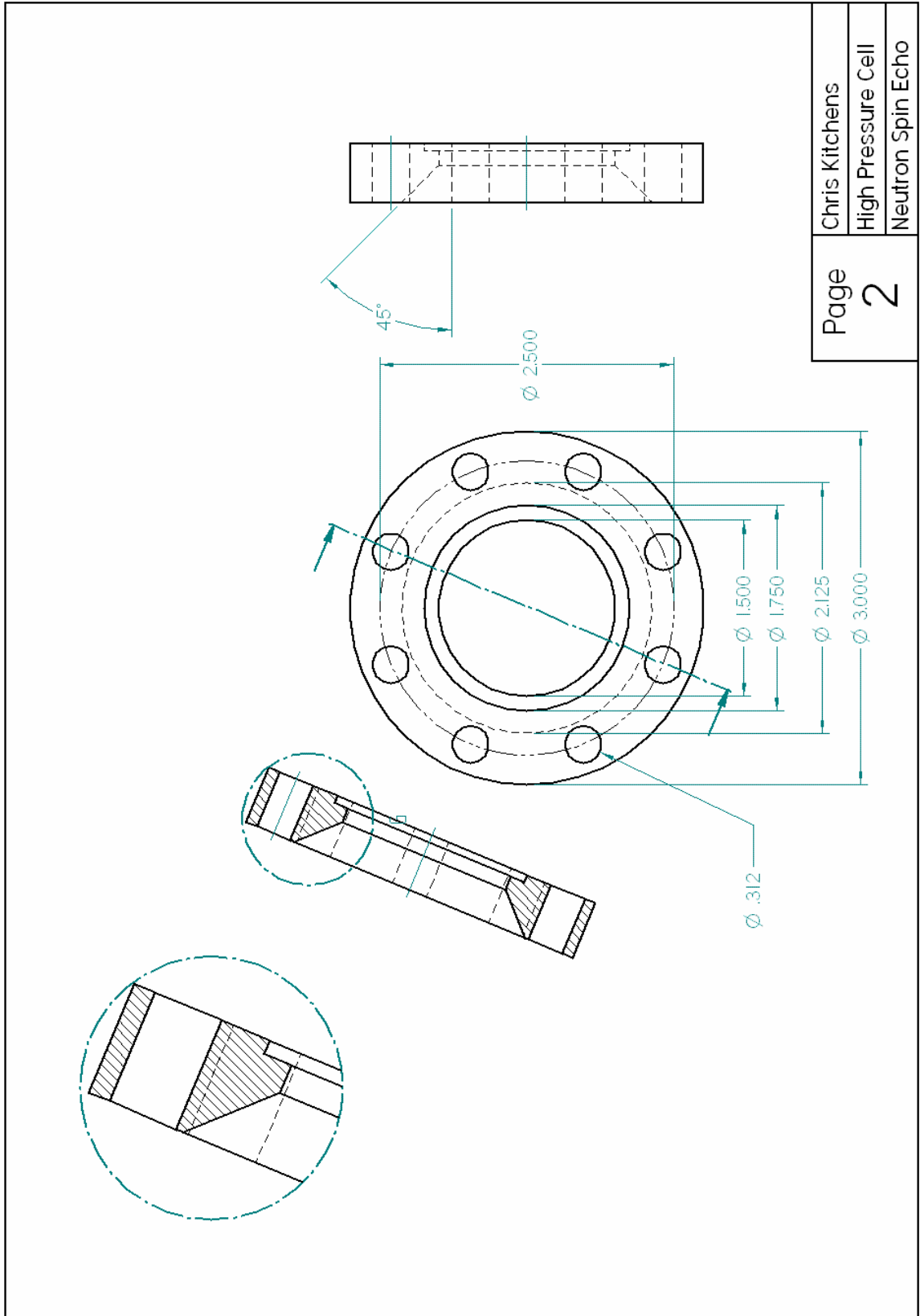
The design and construction of a high pressure vessel was required to perform the Neutron Spin Echo measurements at the NIST Center for Neutron Research. The requirements of the vessel were have a variable path length of 6 mm or less and a sample area accessible by a 35 mm diameter neutron beam. The vessel required 1.75 inch diameter, 0.5 inch thick sapphire windows, inlet/outlet ports, 10,000 psi relief valve, temperature and pressure control and constructed with non-magnetic material (3-16 Stainless Steel). An aluminum temperature control block was constructed and acted as a vessel holder compatible with the NSE instrument. The vessel was pressure tested to 500 bar for 48 hrs without rupture and utilized viton o-rings to seal around the windows.

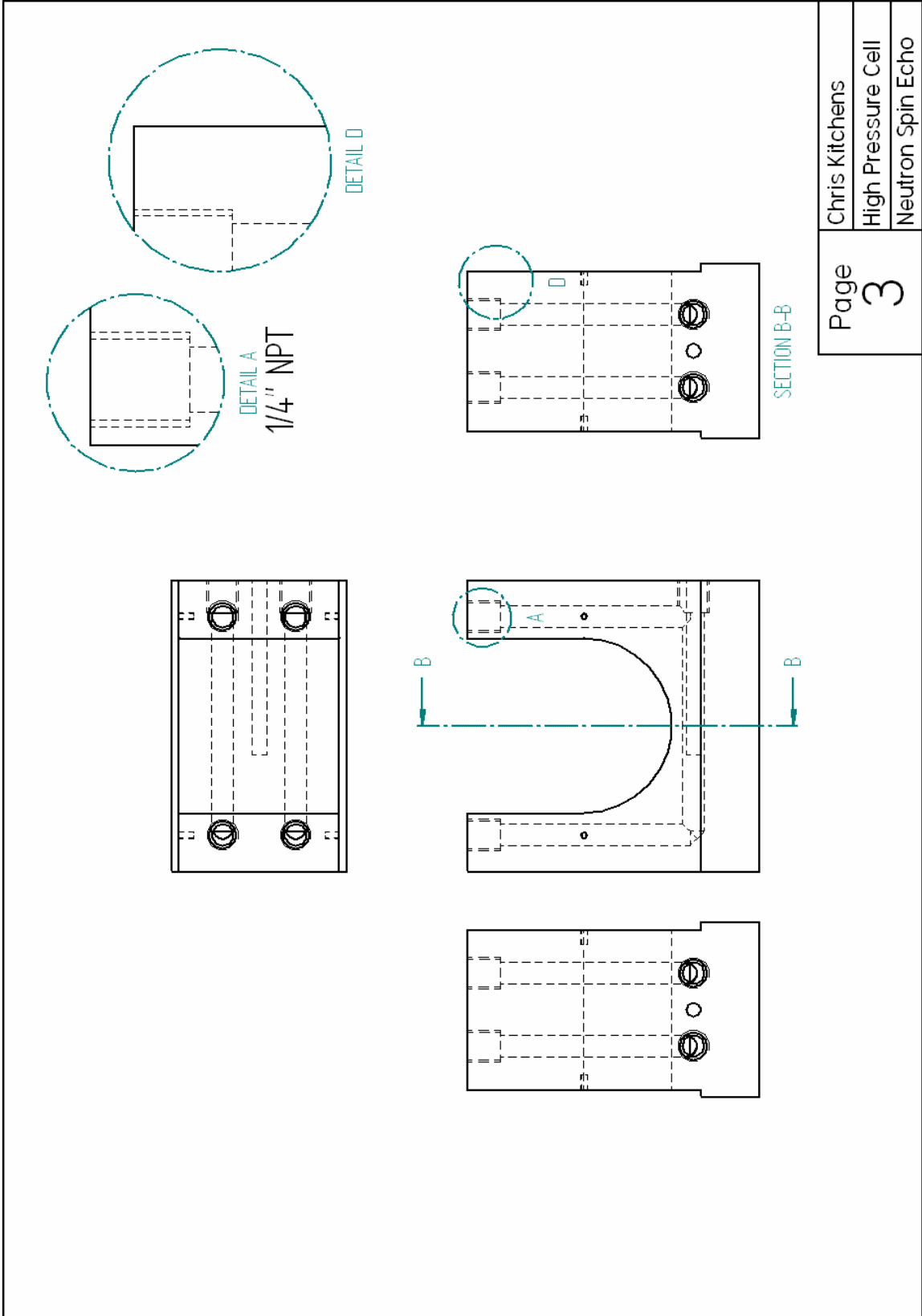


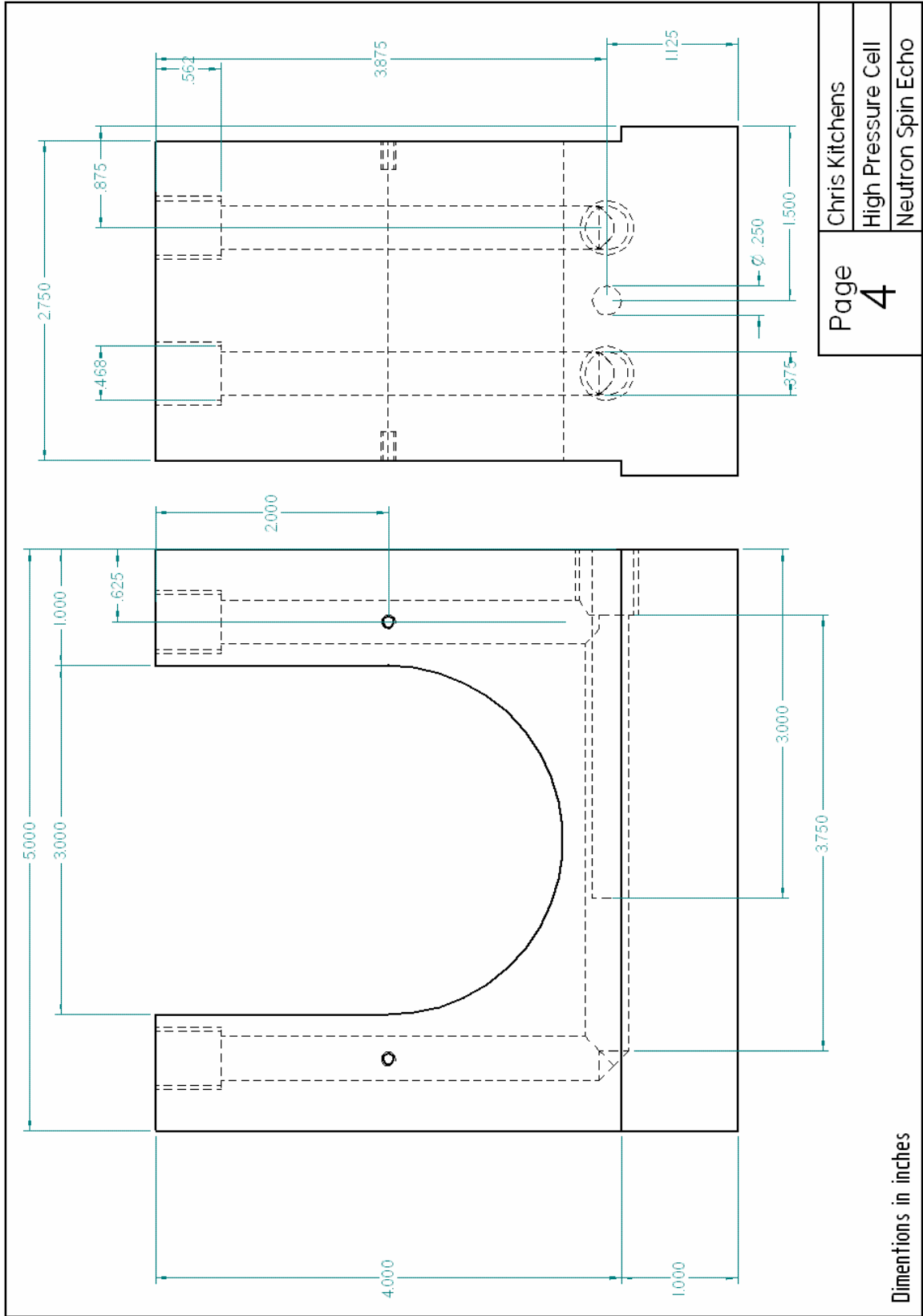




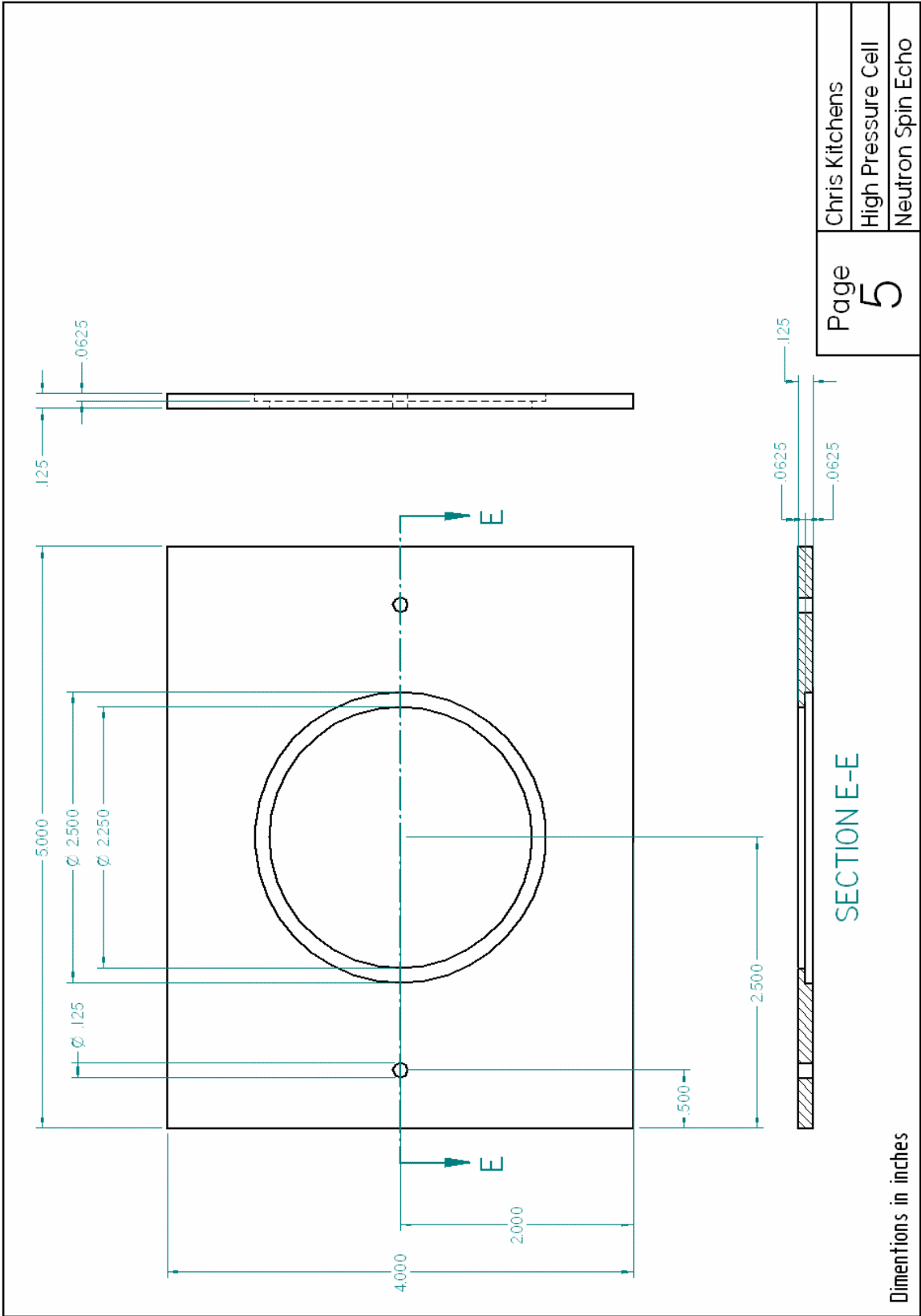








Dimensions in inches

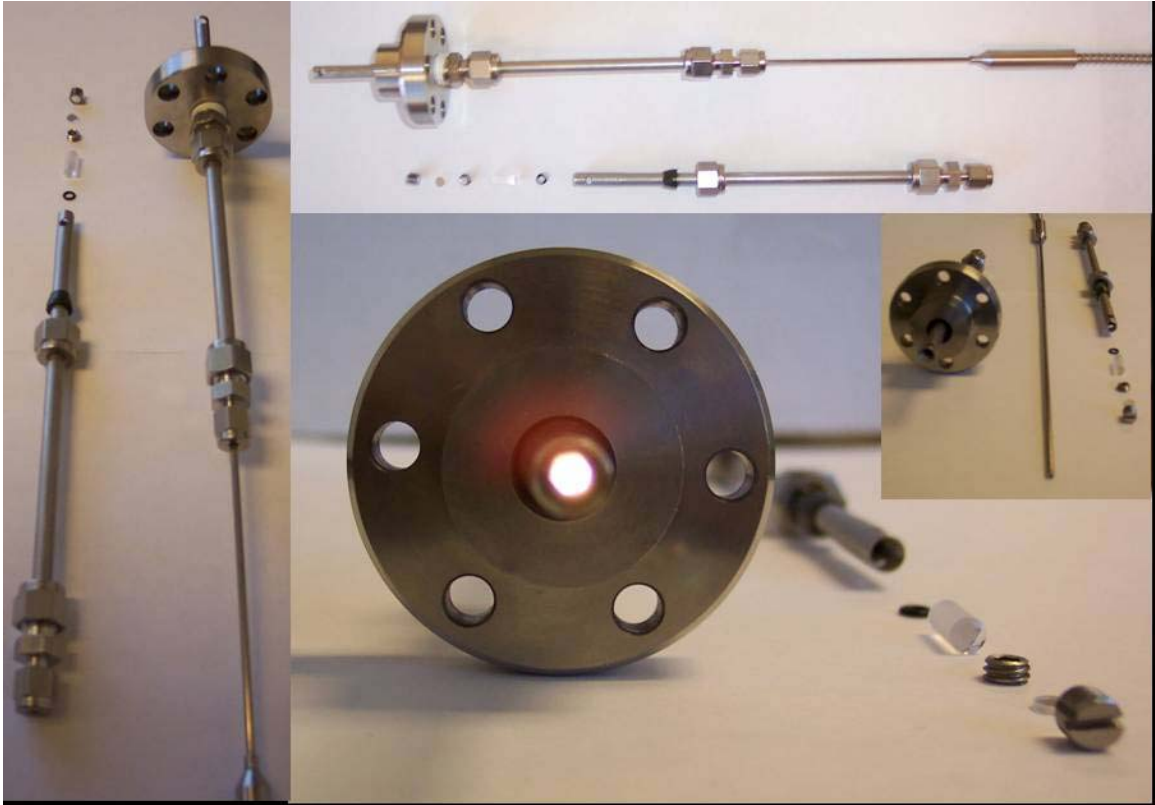


SECTION E-E

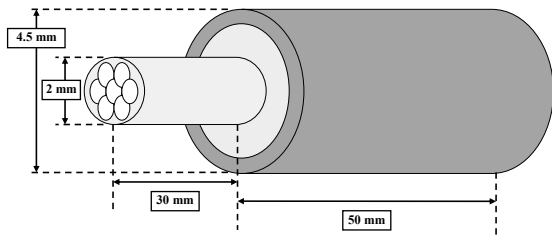
Dimensions in inches

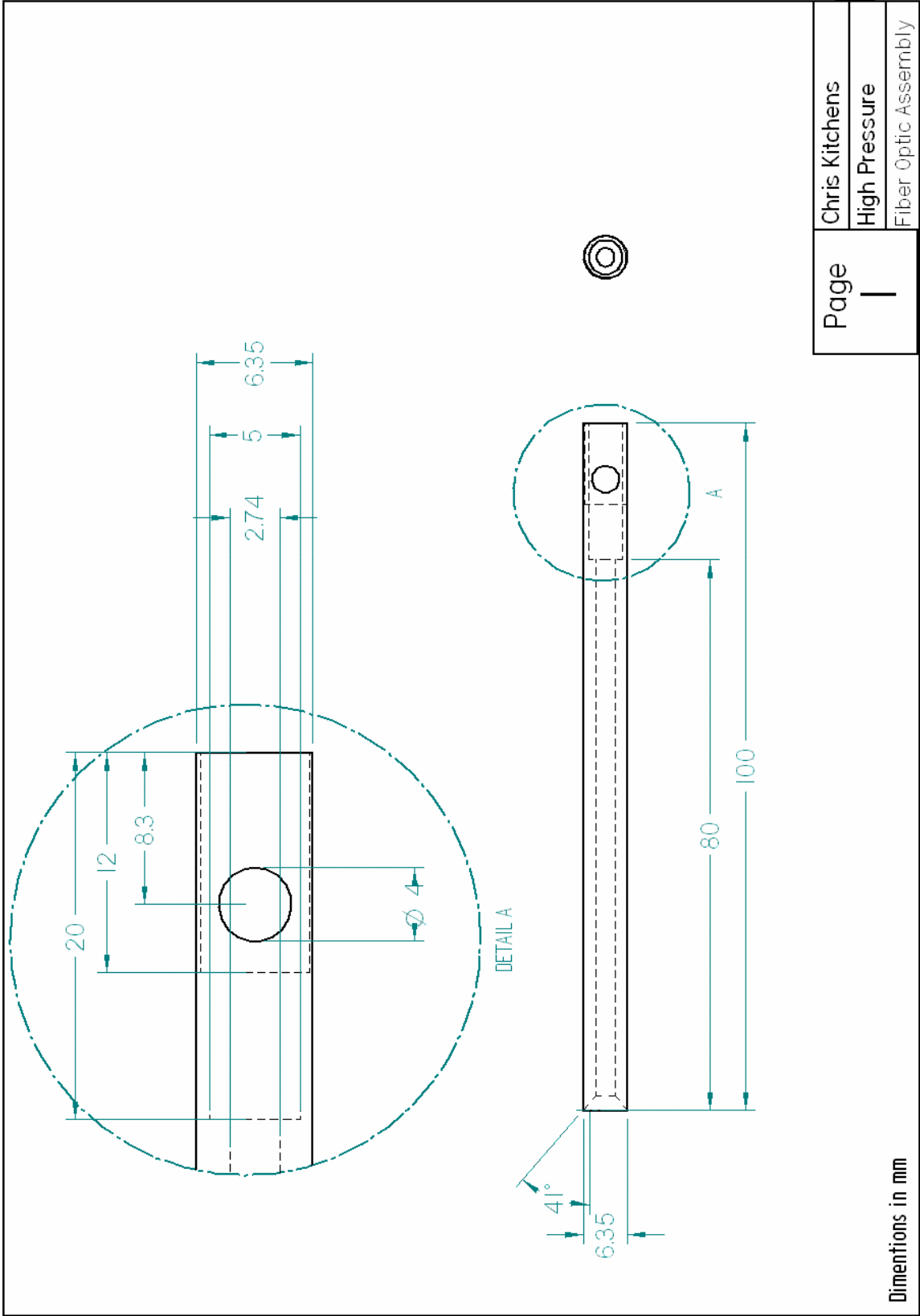
D-4. HIGH PRESSURE FIBER OPTIC PROBE ASSEMBLY

This high pressure fiber optic probe assembly was designed for applications with the Ocean Optics fiber optic UV-vis spectrometer for high pressure absorbance measurements. The probe was designed to act as a reflectance probe where a single fiber within a seven fiber bundle of 400 micron high OH fibers supplies the source light and the remaining six 'read' fibers transmit the reflected light to the dual spectrometer (3 fibers per spectrometer). The fiber assemble was constructed by Polymicro Technologies and consisted of a trifurcated bundle encased within 1/8" OD Stainless Steel encasement. The entire assembly was designed to be contained within 1/4" HiP tubing. The fiber assembly is never exposed to pressure and is held in place by a 1/4" to 1/8" swageloc coupler. The 1/4" tubing housing effectively seals at two points. The first is on the exterior of the 1/4" tubing with swageloc 1/4" fittings and removable Vespel / Graphite ferrules from Alltech. The second pressure seal is made on the inside of the tubing assembly with an o-ring seal. A biconvex sapphire lens serves dual functionality acting as a high pressure window which the system pressure pushes against the o-ring to create the seal. The lens also collimates the light from the fiber and focuses the reflected light to the read fibers. At the end of the probe is a threaded mirror stud which enables a variable path length based on the position of the mirror. The pressure assembly was tested to 7500 psi and is expected to withstand much higher pressures. The assemblt has yet to be utilized for scientific measurement.



Fiber Bundle Assembly

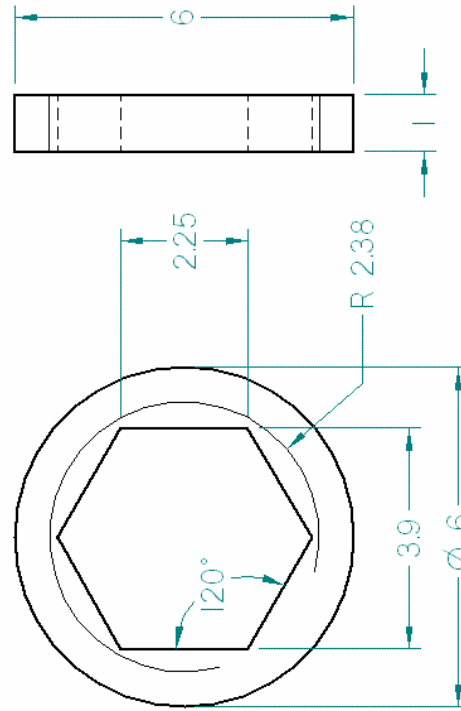
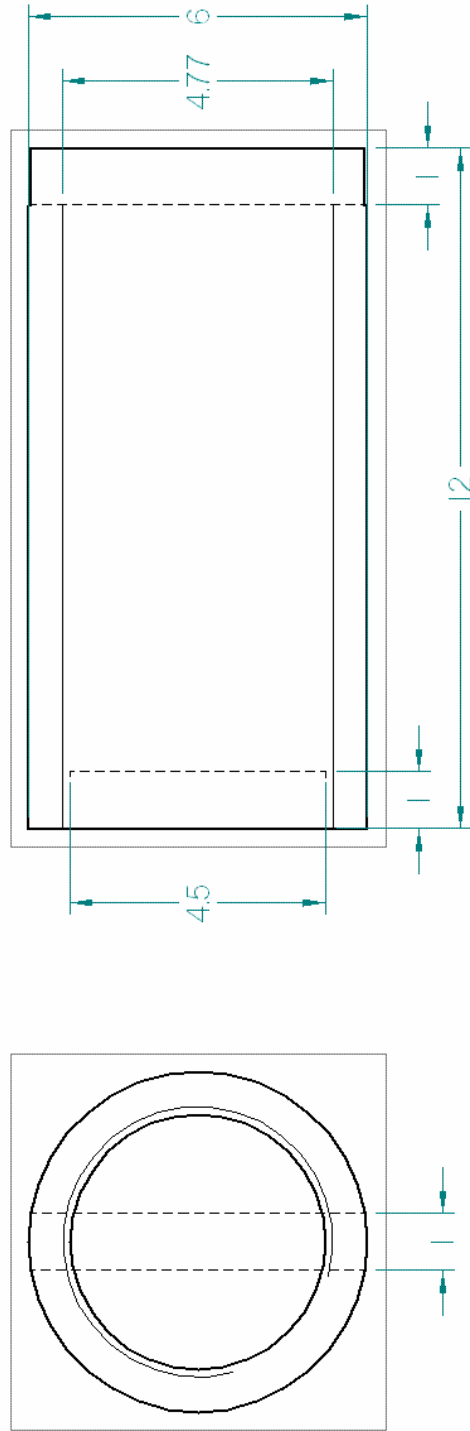




Page	1
Chris Kitchens	
High Pressure	
Fiber Optic Assembly	

Dimensions in mm

Threaded Mirror Stud



Outside Threads - Size M6
Dimensions in mm

Threaded Nut to hold lens in place